

ϕ photo-production from Li, C, Al and Cu
nuclei at $E_\gamma = 1.5\text{--}2.4$ GeV

Takatsugu Ishikawa



A dissertation submitted in partial fulfillment of
the requirements for the degree of

Doctor of Science

Department of Physics
Kyoto University

2005

Abstract

The photo-production of ϕ mesons from Li, C, Al, and Cu nuclei has been measured at the SPring-8/LEPS facility. The high energy photon beam with $E_\gamma = 1.5\text{--}2.4$ GeV has been produced by laser induced backward Compton scattering from 8 GeV electrons in the storage ring, and irradiated the nuclear targets. Charged particles produced at the targets have been detected at forward angles with the LEPS spectrometer. The ϕ meson peaks are clearly observed in the K^+K^- invariant mass distributions for all the targets. The measured mass and width for each target in the momentum range from 1.0 to 2.2 GeV are consistent with those of the free ϕ meson. The slope parameter b obtained by fitting the differential cross section for each nuclear target with a function $d\sigma/dt = C \exp(-bt)$ is consistent with that for the proton target, implying that incoherent ϕ photo-production is dominant. However, coherent ϕ photo-production is also slightly observed in the missing mass m_X distribution for the reaction $\gamma A \rightarrow K^+K^-X$ even at low energies although it is suppressed near the threshold due to the heavy mass of the ϕ meson. After subtracting the coherent contribution, the cross sections give a relation $\sigma_A \propto A^{0.72 \pm 0.07}$. The total cross section of the ϕ -nucleon interaction $\sigma_{\phi N}$ is estimated as 35_{-11}^{+17} mb using the A -dependence of the ϕ photo-production yield with a Glauber-type multiple scattering theory. This value is much larger than $\sigma_{\phi N}$ in free space, suggesting that the ϕ properties might change in the nuclear medium.

Contents

1	Introduction	1
1.1	Physics objectives	1
1.2	Glauber-type multiple scattering theory	5
1.3	Presented Data	7
2	Experiment	8
2.1	Laser-electron photon beam	8
2.1.1	SPring-8 facility	8
2.1.2	LEPS facility	9
2.1.3	Backward Compton scattering	10
2.1.4	Laser injection system	12
2.1.5	Tagging system	14
2.1.6	Materials on the beam line	15
2.2	Target	16
2.3	LEPS spectrometer	17
2.3.1	Upstream veto counter	17
2.3.2	Start counter	18
2.3.3	Aerogel Čerenkov counter	19
2.3.4	Dipole magnet	19
2.3.5	Silicon strip vertex detector (SVTX)	22
2.3.6	Drift chambers	22
2.3.7	TOF wall	24
2.3.8	e^+e^- blocker	24
2.4	Data Acquisition	25
2.4.1	Electronics	25
2.4.2	Trigger	27
2.4.3	Data taking system	28
2.4.4	Obtained data	29
3	Analysis	30
3.1	Program codes	30
3.1.1	Analysis code: LEPSana	30
3.1.2	Monte Carlo simulation code: g3leps	30
3.2	Timings, positions, and resolutions	31
3.2.1	TOF wall	31
3.2.2	RF signals	32
3.2.3	Drift chambers	32
3.3	Determination of the variables	36

3.3.1	Tracking	36
3.3.2	Time of flight	37
3.3.3	Mass	37
3.4	Event Selection	37
3.4.1	Good buffers	37
3.4.2	Number of tracks	37
3.4.3	Particle identification	38
3.4.4	Good tracks	41
3.4.5	Closest distance	42
3.4.6	Vertex	43
3.4.7	Invariant mass	46
3.4.8	Tagger hit	47
3.4.9	Cut statistics	49
3.5	Observed ϕ mesons	49
3.5.1	Mass and width	49
3.5.2	Incident γ energy distribution	53
3.5.3	Momentum distribution of ϕ mesons	53
3.5.4	\bar{t} distribution	55
3.5.5	Scattering angle of K^+ in the helicity frame	59
3.6	Background events	63
3.6.1	Contamination of the start counter events	63
3.6.2	Particle mis-identification	64
3.6.3	Non resonant K^+K^- events	65
3.7	Normalization	66
3.7.1	Effective number of tagger hits	66
3.7.2	Number of target nuclei	69
3.7.3	Attenuation of the photon flux in the target material	69
3.7.4	Efficiency of the data taking system	70
3.7.5	Efficiency of the analyzer	71
3.7.6	Geometrical acceptance	73
3.7.7	Yield for ϕ photo-production from nuclei	73
4	ϕ-N total cross section	75
4.1	Determination of the ϕ - N total cross section	75
4.2	Incoherent and coherent ϕ photo-production	76
4.3	Subtraction of the coherent process contribution	80
4.4	Selection of the kinematical region for incoherent production	85
4.5	Comparison with the theoretical calculations	88
4.6	Why large $\sigma_{\phi N}$ is obtained?	90
5	Conclusion	92
	Acknowledgement	94
	Appendix	96
A	A-dependence of the production cross section	97
A.1	Production cross section for the coherent process	98
A.2	Production cross section for the incoherent process	99

B	Decay angular distribution of the vector meson	102
B.1	General decay angular distribution of the vector meson	102
B.2	Density matrix of linearly polarized photons	103
B.3	Decomposition of the density matrix $\rho(V)$	103
B.4	Density matrix for the s -channel helicity conserving model	104
C	Systematic uncertainty	105
C.1	Different responses of the detector system	105
C.1.1	Acceptance of the particle identification	105
C.1.2	χ^2 probability in the good track cut	108
C.1.3	z -vertex resolution	112
C.1.4	Momentum resolution	116
C.1.5	Efficiency of drift chambers	116
C.1.6	Yield from the start counter	118
C.2	Different kinematical conditions	120
C.2.1	z -vertex dependence of the geometrical acceptance	120
C.2.2	Center of mass energy	124
C.3	Momentum mis-calibration	127
C.4	KK background from $\Lambda(1520)$ photo-production	130
D	Incoherent and coherent ϕ photo-production	132
D.1	Missing mass	132
D.2	ν - q^2 correlation	135
E	ϕ-N total cross section with various cuts	138
E.1	Selecting kinematical region for the incoherent process	138
E.1.1	Excluding one of the four targets for the 30 MeV cut	138
E.1.2	Invariant mass	138
E.1.3	χ^2 probability cut	140
E.1.4	Incident γ energy	140
E.1.5	Momentum of ϕ meson	140
E.1.6	Scattering angle in the γ - N center of mass system	141
E.2	Semi-coherent process	144
F	Description of nuclei	150
F.1	Fermi motion in a nucleus	150
F.1.1	Harmonic oscillator model	150
F.1.2	Comparison to the experimental data	152
F.2	Off-shell correction	153
F.3	Nucleon density distributions	154
G	Miscellaneous	156
G.1	Confirmation of good buffers	156
G.2	Voigt function	158
G.3	Finite element method in TOSCA	159

List of Figures

1.1	e^+e^- invariant mass spectrum for the Pb+Au collision	1
1.2	e^+e^- invariant mass spectrum for the p +Cu reaction	1
1.3	Decrease of the mass predicted by Hatsuda <i>et al.</i>	2
1.4	Broadening of the width predicted by Oset <i>et al.</i>	2
1.5	K^+K^- invariant mass spectrum for the Si+Au collisions	3
1.6	e^+e^- invariant mass spectrum for the p +Cu reaction	3
1.7	Deviation of the A -dependence predicted by the $\sigma_{\phi N}$ in free space	4
1.8	Total cross section of vector mesons in interaction with a nucleon	4
1.9	Effective nucleon number A_{eff}	6
2.1	Layout of the SPing-8 facility	8
2.2	Schematic view of the LEPS facility	9
2.3	Kinematical values of the BCS process	10
2.4	Energy of the BCS photon	11
2.5	Polarization of the BCS photon	11
2.6	Wave length of the Ar laser	12
2.7	Schematic view of the laser operation system	13
2.8	Laser intensity with respect to the direction of the transimission axis	13
2.9	Top view of the tagging system	14
2.10	Energy spectrum of BCS photons measured by the tagging system	15
2.11	Schematic view of the beam line	16
2.12	Target shape	17
2.13	Schematic view of the LEPS spectrometer	18
2.14	Structure of the aerogel Čerenkov counter	19
2.15	Division of the dipole magnet for the field calculation	20
2.16	Relation between the magnetic flux density B and field H	20
2.17	Comparison between the calculated and measured magnetic fields	20
2.18	Magnetic field B_y along the z axis	21
2.19	Structure of the SVTX	22
2.20	Structure of the DC wire planes	23
2.21	Structure of the TOF wall	24
2.22	Schematic view of the e^+e^- blocker	25
2.23	Electronics for the trigger counters	26
2.24	Diagram of the trigger logic	28
3.1	Plastic scintillator of which light signals are recorded in both sides	31
3.2	Threshold for DC widths	33
3.3	Zero timing T_0	33
3.4	Contour of the potential and the drift line	34

3.5	Relation between the drift length and the drift time	34
3.6	Relation between the drift length and the drift time	35
3.7	Residual distributions	35
3.8	Momentum dependence of mass square resolution	38
3.9	Momentum dependence of mass square	39
3.10	Momentum dependence of mass square for the ADC non-saturated events	39
3.11	Particle identification	40
3.12	Particle identification for two track events	41
3.13	Closest distance distributions of K^+K^- tracks in the MC simulation	43
3.14	Closest distance distributions for K^+K^- tracks in the real data	43
3.15	z -vertex distribution of the K^+K^- tracks	44
3.16	(x, y) -vertex distribution of the K^+K^- tracks	45
3.17	K^+K^- invariant mass distributions	46
3.18	Difference between E_γ and E_γ^{KK}	47
3.19	Difference of measured γ energies	48
3.20	K^+K^- invariant mass distributions for non-resonant K^+K^- production in the MC simulation	50
3.21	Fitting with σ as a free parameter in the real data	50
3.22	Fitting with σ as a free parameter in the MC simulation	51
3.23	Fitting with Γ as a free parameter in the real data	52
3.24	π^-p invariant mass distribution	53
3.25	Incident γ energy distribution	54
3.26	Momentum distribution of ϕ mesons	54
3.27	Limit of $ t $ as a function of E_γ	55
3.28	\tilde{t} distribution	56
3.29	Normalized yield R as a function of \tilde{t}	56
3.30	Acceptance as a function of \tilde{t}	57
3.31	Acceptance corrected yield as a function of \tilde{t}	57
3.32	Acceptance corrected yield as a function of \tilde{t}	58
3.33	Scattering angle of K^+ in the helicity frame for the vertically polarized photon data	59
3.34	Scattering angle of K^+ in the helicity frame for the horizontally polarized photon data	60
3.35	Scattering angle of K^+ in the helicity frame for LH ₂	61
3.36	Reaction mechanism of the ϕ photo-production on the nucleon	62
3.37	Fraction of pions identified as kaon	65
3.38	K^+K^- invariant mass distribution for non-resonant KK production	66
3.39	TDC distributions of tagger plastic scintillator	67
3.40	Comparison of the accidental coincidence rate	68
3.41	Efficiency of data taking system	71
3.42	Fraction of the events that cannot be analyzed	72
3.43	A -dependence of the ϕ meson photo-production from nuclei	74
4.1	A_{eff} as a function of $\sigma_{\phi N}$	76
4.2	Missing mass m_X for $\gamma p \rightarrow K^+K^-X$ in the real data of LH ₂	76
4.3	Missing mass m_X of $\gamma A \rightarrow K^+K^-X$ in the real data	77
4.4	Missing mass m_X of $\gamma A \rightarrow K^+K^-X$ for incoherent production in the MC simulation	78
4.5	Missing mass m_X of $\gamma A \rightarrow K^+K^-X$ for coherent production in the MC simulation	78
4.6	Comparison of missing energy distributions between the real and MC simulation data	79
4.7	Coherent to incoherent ratio	81

4.8	Relation between q^2 and t	81
4.9	Coherent differential cross section $d\sigma_{\text{coh}}/dt$	81
4.10	Cross sections for coherent production $\sigma_{\text{coh}}(t > t _{\text{min}})$	82
4.11	Missing energy distribution in Li	83
4.12	A -dependence with subtraction of the coherent ϕ events	83
4.13	Efficiency of the missing energy cut	85
4.14	ϕ - N total cross section $\sigma_{\phi N}$ according to the E_x cut	85
4.15	A -dependence with the 30 MeV missing energy cut	87
4.16	Comparison of P_{out} for the yields after the coherent ϕ events are subtracted	89
4.17	Comparison of $P_{\text{out}}/P_{\text{out}}(\text{Li})$ for the yields after the coherent ϕ events are subtracted	89
4.18	Comparison of P_{out} for the yields in the kinematical region of the incoherent process	90
4.19	Comparison of $P_{\text{out}}/P_{\text{out}}(\text{Li})$ for the yields in the kinematical region of the incoherent process	90
A.1	Definition of the kinematics for the estimation of the production cross sections	97
C.1	Momentum distribution of K^+ and K^-	105
C.2	Passing ratio of the particle identification and the good track cuts	106
C.3	Contamination in the particles detected as K^+ and K^-	107
C.4	Probabilities that μ^+ and μ^- are detected as K^+ and K^-	108
C.5	K^+K^- invariant mass distributions with/without the χ^2 probability cut	109
C.6	χ^2 probability distribution for K^+K^- tracks	110
C.7	χ^2 probability distributions for the K^+K^- tracks as a function of the x, y -global SVTX shifts	110
C.8	Number of K^+K^- tracks passing the good track cut as a function of the x, y -global SVTX shifts	111
C.9	Run dependence of the mean of the χ^2 distributions and the width of z vertex distributions for the start counter	111
C.10	Opening angle dependence of z -vertex resolutions for $\phi \rightarrow K^+K^-$ events in the MC simulation	112
C.11	z -vertex distributions for $\phi \rightarrow K^+K^-$ events in the MC simulation	114
C.12	z -vertex distributions for $\phi \rightarrow K^+K^-$ events in the real data	114
C.13	Opening angle distribution for $\phi \rightarrow K^+K^-$ events	116
C.14	Efficiency of drift chambers	117
C.15	Comparison of the efficiencies with/without the DC TDC width cut	118
C.16	$\pi^+\pi^-$ yield for the start counter	119
C.17	π^+p yield for the start counter	119
C.18	K^+K^- yield for the start counter	120
C.19	Yield as a function of z vertex in the MC simulation	121
C.20	Yield ratio between the real and MC simulation data (1)	122
C.21	Yield ratio between the real and MC simulation data (2)	123
C.22	Fermi momentum distribution for the detected ϕ mesons	124
C.23	Fermi momentum distribution for the produced ϕ mesons	124
C.24	Center of mass distribution for the detected ϕ mesons	125
C.25	Center of mass distribution for all the produced ϕ mesons	125
C.26	Incident γ energy distribution for the detected ϕ meson (MC)	126
C.27	Incident γ energy distribution for the detected ϕ meson for LH ₂ (MC)	126
C.28	Correction factor C_p to the measured momentum	127

C.29	Relation of the momentum correction to the centroid of the KK invariant mass distribution	128
C.30	Comparison of the missing energy distributions with/without momentum correction	128
C.31	Excess of the measured momentum	129
C.32	Comparison between non resonant KK and KK from $\Lambda(1520)$	130
D.1	Missing mass m_X of $\gamma p \rightarrow K^+ K^- X$ for the incoherent process in the MC simulation data	132
D.2	Missing mass m_X of $\gamma p \rightarrow K^+ K^- X$ for the coherent process in the MC simulation data	133
D.3	Missing mass m_X of $\gamma p \rightarrow K^+ K^- X$ for the start counter	133
D.4	Missing mass distributions M_X for $\gamma p \rightarrow K^+ K^- X$	134
D.5	Correlation between missing energy and missing mass m_X of $\gamma p \rightarrow \phi + X$	134
D.6	ν - q^2 correlation for the incoherent process in the MC simulation	135
D.7	ν - q^2 correlation for the coherent process in the MC simulation	136
D.8	ν - q^2 correlation in the real data	136
D.9	ν^2 - q^2 and ν - q^2 correlation for the LH ₂ target in the MC simulation	137
D.10	ν^2 - q^2 and ν - q^2 correlation for the LH ₂ target in the real data	137
E.1	A -dependence for different incident γ energy regions	140
E.2	A -dependence for different ϕ meson momentum regions	141
E.3	Scattering angle in the γ - N CM frame $\cos \theta$ for the incoherent process	142
E.4	Scattering angle in the γ - N CM frame $\cos \theta$ for the real data	142
E.5	Scattering angle in the γ - N CM frame $\cos \theta$ for the coherent process	143
E.6	Missing energy distributions for the $A=2$ semi-coherent process	145
E.7	Missing energy distributions for the $A=3$ semi-coherent process	145
E.8	Missing energy distribution for the $A=4$ semi-coherent process	146
E.9	Missing energy distribution of $\gamma p \rightarrow K^+ K^- p$ for the coherent process	146
E.10	Missing energy distribution of $\gamma p \rightarrow K^+ K^- p$ for the $A=2-4$ semi-coherent process	147
E.11	Missing energy distributions of $\gamma p \rightarrow K^+ K^- p$ for the incoherent process	147
E.12	Missing energy distributions of $\gamma p \rightarrow K^+ K^- p$ in the real data	148
E.13	Efficiency of the missing energy cut for $\gamma p \rightarrow K^+ K^- p$	148
F.1	Comparison of the Fermi motion with $(e, e'p)$ experimental data	152
F.2	Missing energy distribution with and without off-shell correction	153
F.3	Nucleon density distributions in coordinate space	155
G.1	Correlation of the x/y position between SVTX and DC1	156
G.2	Consistency ratio for the x and y positions between SVTX and DC1	158

List of Tables

2.1	Properties of the nuclear targets used	16
2.2	Design parameters of DC	23
3.1	Factors of the intrinsic resolutions to the residuals	35
3.2	Intrinsic resolutions of drift chambers	36
3.3	Number of the tracks	37
3.4	Number of the events after the particle identification cut	40
3.5	Number of the events after the good track cut	42
3.6	Number of events after the closest distance cut	44
3.7	Number of the events after z -vertex cut	45
3.8	Number of the events after x and y vertex cut	46
3.9	Number of the events after the invariant mass cut	47
3.10	Number of tagger hits for $\phi \rightarrow K^+K^-$ events.	48
3.11	Number of the events after the tagger hit cut	48
3.12	Cut statistics	49
3.13	Comparison of the fitting parameters with σ as a free one	51
3.14	Fitting parameters with Γ as a free parameter	52
3.15	Fitting results for the position and width of the $\Lambda \rightarrow \pi^- p$ peak	53
3.16	Summary of b parameters in the \tilde{t} distribution	58
3.17	Probabilities of the contamination due to the vertex cut	63
3.18	Filling pattern of the electron injection beam	67
3.19	Correction parameter for accidental coincidence rate	67
3.20	Effective photon counts with correction	69
3.21	Properties of the nuclear targets used	69
3.22	Attenuation of the photon flux in the target	70
3.23	Averaged efficiency of the data taking system.	70
3.24	Averaged efficiency of the analyzer	72
3.25	Geometrical acceptance (η_{geo})	73
3.26	Fitting parameters for A -dependence	74
4.1	Fitting results for the low $ t $ coherent differential cross section	82
4.2	Estimated number of coherent ϕ events	84
4.3	Fitting results of the yield after the coherent ϕ events are subtracted	84
4.4	Fitting results of the yield with $E_x \geq E_x^{\text{thr}}$	86
4.5	Probability P_{out} with subtraction of the coherent ϕ events	88
4.6	Probability P_{out} in the kinematical region of the incoherent process	90
C.1	Passing ratio of the particle identification and decay in flight cuts	106
C.2	Contamination in the particles detected as K^+ and K^-	107

C.3	Probabilities that μ^+ and μ^- are detected as K^+ and K^-	108
C.4	Number of ϕ events as a function of the χ^2 probability limit	109
C.5	Fitting results of z -vertex resolutions in the MC simulation	113
C.6	Fitting results of z -vertex resolutions in the real data	115
C.7	Comparison of the z -vertex distribution between the real and MC simulation data	115
C.8	$\pi^+\pi^-$ yield for the start counter	119
C.9	π^+p yield for the start counter	119
C.10	K^+K^- yield for the start counter	120
C.11	Fitting parameters with the $\Lambda(1520)$ - KK background	131
E.1	Fitting parameters excluding one of the four targets	138
E.2	Fitting parameters tightening the invariant mass cut	139
E.3	Fitting parameters tightening the χ^2 probability cut	139
E.4	Fitting parameters for different incident γ energies	140
E.5	Fitting parameters different ϕ meson momentum regions	141
E.6	Fitting parameters for different $\cos\theta^*$ cuts	144
E.7	Fitting parameters for various missing energy cuts for the reaction $\gamma p \rightarrow K^+K^-p$	149
F.1	Nucleon density for each state.	152
F.2	Number of nucleons at each state.	152
F.3	Proton and neutron separation energy	153
F.4	Charge density parameters for Li	154
F.5	Charge density parameters for C, Al, and Cu	155
G.1	Run number used for the analysis and analyzed buffers	157

Chapter 1

Introduction

1.1 Physics objectives

The modification of the vector mesons in nuclear matter (a decrease of the mass, a broadening of the width, and so on) is a subject of great interest in hadron physics. The mass of the vector mesons is predicted to decrease in nuclear matter [1, 2, 3]. The properties (mass and width) of the ρ meson in the nuclear medium have been studied of intense both theoretically and experimentally. The experimental

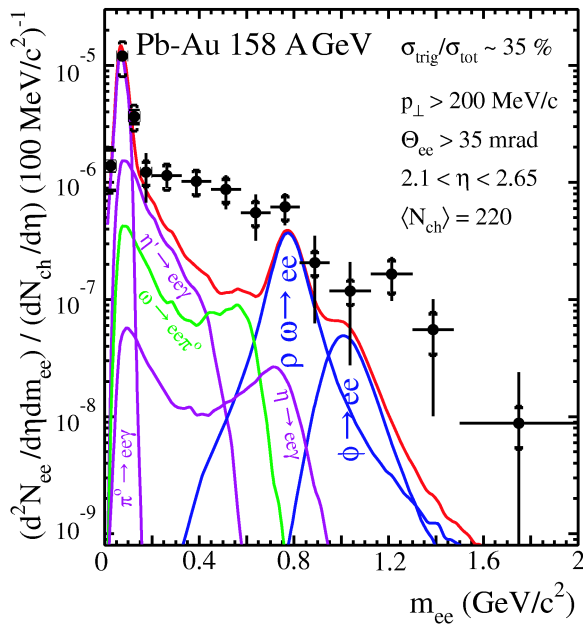


Figure 1.1: e^+e^- invariant mass spectrum for the Pb+Au collision given by Ref. [6]. The mass spectrum is reproduced by the known processes except for the mass region below the ω/ρ peak.

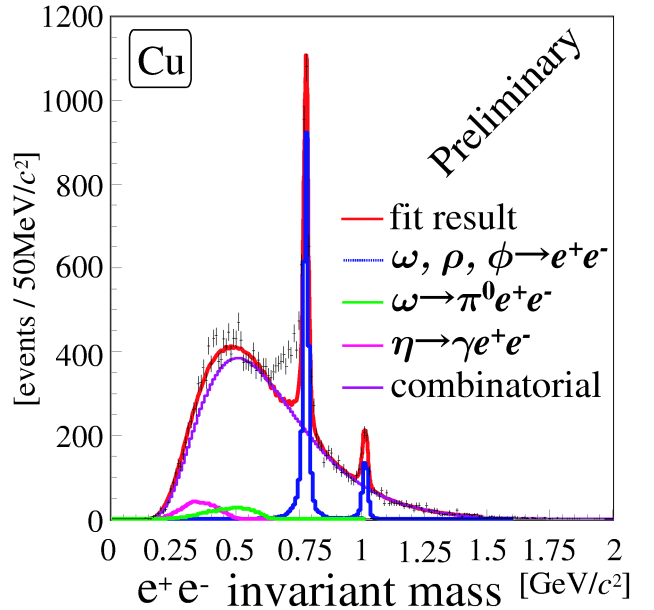


Figure 1.2: e^+e^- invariant mass spectrum for the p +Cu reaction given by Ref. [13]. The mass spectrum is reproduced by the known processes except for the mass region below the ω peak.

data on dilepton production in A - A collisions at the CERN-SPS seem to indicate lowering the mass and broadening the width of the ρ meson in the nuclear medium [4, 5, 6]. Figure 1.1 shows the e^+e^- invariant mass distributions for the Pb+Au collision given by Ref. [6]. The e^+e^- invariant mass distributions for the p +Be, p +Au collisions are reproduced by the known processes to the dilepton

pairs such as the $\pi^0/\eta/\eta' \rightarrow e^+e^-\gamma$, $\rho/\omega/\phi \rightarrow e^+e^-$, and $\omega \rightarrow e^+e^-\pi^0$ reactions. But those for the S+Au, and Pb+Au collisions are not reproduced by these reactions in the mass region below the ω/ρ peak. The ρ contribution is only a fraction of the total mass spectrum, and the difficulty exists in the treatment of the background. An enhancement in the mass region below the ω/ρ peak has been also observed in the p - A reaction at the normal nuclear density [7, 8, 9, 10, 11, 12, 13]. Figure 1.2 shows the e^+e^- invariant mass distribution for the $p + A$ reaction at the KEK-PS given by Ref. [13]. The spectra are not reproduced by the known processes such as the $\eta \rightarrow e^+e^-\gamma$, $\rho/\omega/\phi \rightarrow e^+e^-$, and $\omega \rightarrow e^+e^-\pi^0$ reactions, and the particle mis-identification of π^\pm as e^\pm (the process $\pi^0 \rightarrow e^+e^-\gamma$ is out of the detector acceptance). The same difficulty exists in the treatment of the background.

The ϕ meson is not concealed by other resonances by contrast in the dilepton or $K\bar{K}$ invariant mass spectra. In this regard, many theoretical calculations have been made for the ϕ meson, and a broadening of the width and/or a lowering of the mass are also predicted at the normal nuclear density because of partial restoration of chiral symmetry [14, 16] or the meson-nucleon interaction in the nuclear medium [15, 17, 18, 19, 20, 22, 21, 23]. Figures 1.3 and 1.4 show the examples of the theoretical calculations for the change of the ϕ properties which predict a decrease of the mass and a broadening of the width in the nuclear medium. Figure 1.3 shows an expected mass shift of the ϕ meson as a function of baryon density where the calculations based on the in-medium QCD sum rule have been made by Hatsuda *et al.* [14]. Figure 1.4 shows an expected broadening of the width where the calculations based on the ϕ self-energy with the meson-nucleon interaction in the nuclear medium have been made by Oset *et al.* [20].

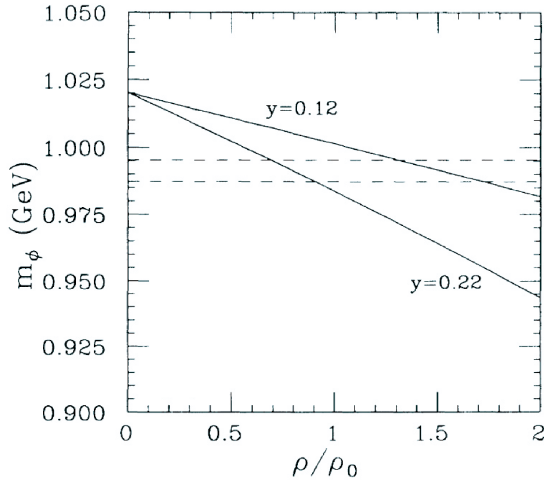


Figure 1.3: Decrease of the mass predicted by Hatsuda *et al.* given in the Ref. [14]. An expected mass shift of the ϕ meson as a function of baryon density are shown where calculations are based on the in-medium QCD sum rule. The value of the mass shift depends on the strange contents in the nucleon $Y = 2\langle s\bar{s} \rangle_N / (\langle u\bar{u} \rangle_N + \langle d\bar{d} \rangle_N)$.

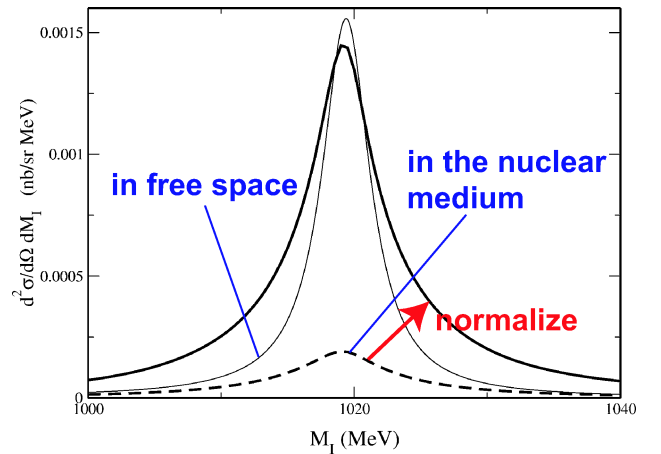


Figure 1.4: Broadening of the width predicted by Oset *et al.* given in the Ref. [20]. The mass spectra of the ϕ meson in the nuclear medium are shown where calculations are based on the meson-nucleon interaction in the nuclear medium.

The mass shift of the ϕ meson has been looked for experimentally in the p - A reaction at the normal nuclear density [7, 8, 9, 10, 11, 12, 13], and also in high energy heavy ion collisions [24, 25]. However, no clear evidence has been observed so far. Figure 1.5 shows the K^+K^- invariant mass

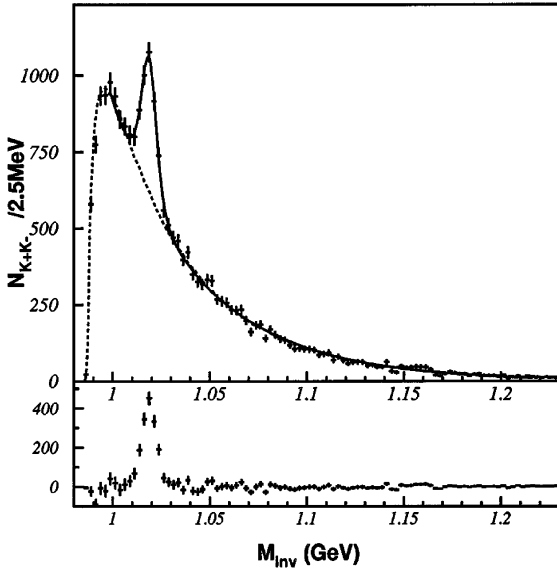


Figure 1.5: K^+K^- invariant mass spectrum for the Si+Au collisions given by Ref. [25]. The mass and width of the ϕ meson is consistent with those of the ϕ meson in free space.

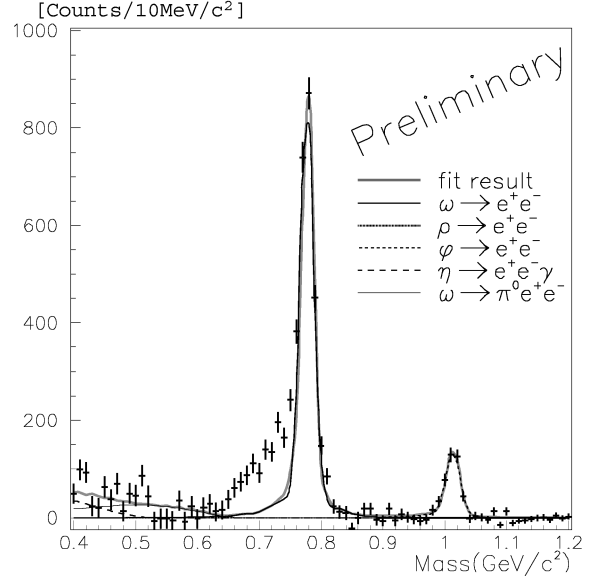


Figure 1.6: e^+e^- invariant mass spectrum for the p +Cu reaction given by Ref. [13]. The mass spectrum is obtained by subtracting the combinatorial background. The excess in the mass region below the ϕ is not observed.

spectrum in the Si+Au collision at BNL-AGS. The measured mass and width are consistent with those of the ϕ meson in free space. Most of produced ϕ mesons decay outside the nucleus due to the small width of the ϕ resonance. Even if all the ϕ mesons decay inside the nucleus, the $K\bar{K}$ invariant mass spectrum might be strongly distorted by the KN and the $\bar{K}N$ interactions [26]. It seems difficult to observe the change of the ϕ properties through the $K\bar{K}$ invariant mass distribution. Figure 1.6 shows the e^+e^- invariant mass spectrum in the p -A reaction at the KEK-PS. The excess in the mass region below the ϕ peak is not observed. The difficulty exists in the treatment of the combinatorial background. Recently, it has been pointed out that the change of the ϕ width can be studied by ϕ photo-production from nuclei [27]. The decrease of photo-produced ϕ meson flux in the nucleus is related to the ϕ width in the nuclear medium.

The total ϕ -nucleon (N) cross section $\sigma_{\phi N}$ should be small since the ϕ meson consists of almost pure $s\bar{s}$ and $s\bar{s}$ is basically absent in a nucleon. If $\sigma_{\phi N}$ in free space is small and $\sigma_{\phi N}$ in the nuclear medium is the same as that in free space, the incoherent ϕ photo-production cross section from a nucleus σ_A^{inc} is approximately proportional to the target mass number A since almost all the produced ϕ mesons are expected to go outside the nucleus without interacting with a nucleon. If $\sigma_{\phi N}$ becomes larger in the nuclear medium, some fraction of the photo-produced ϕ mesons would interact with a nucleon in the nucleus and disappear via inelastic reactions. In this case, the A -dependence sizeably deviates from $\sigma_A \propto A^1$. Figure 1.7 illustrates the deviation of the A -dependence.

The $\sigma_{\phi N}$ in free space is well determined to be 7.7–8.7 mb from the ϕ photo-production cross section on the proton $d\sigma/dt|_{t=0}$ at $E_\gamma = 4.6$ –6.7 GeV, where the energy dependence of the γ - ϕ coupling is assumed to be constant on the basis of the vector meson dominance model (VDM) [28]. A quark model [29] gives a prediction of 13.0 ± 1.5 mb for $\sigma_{\phi N}$ [28]. This value is deduced from the total $\pi^\pm p$ and $K^+ p$ cross sections obtained at the high energy limit. The obtained and predicted

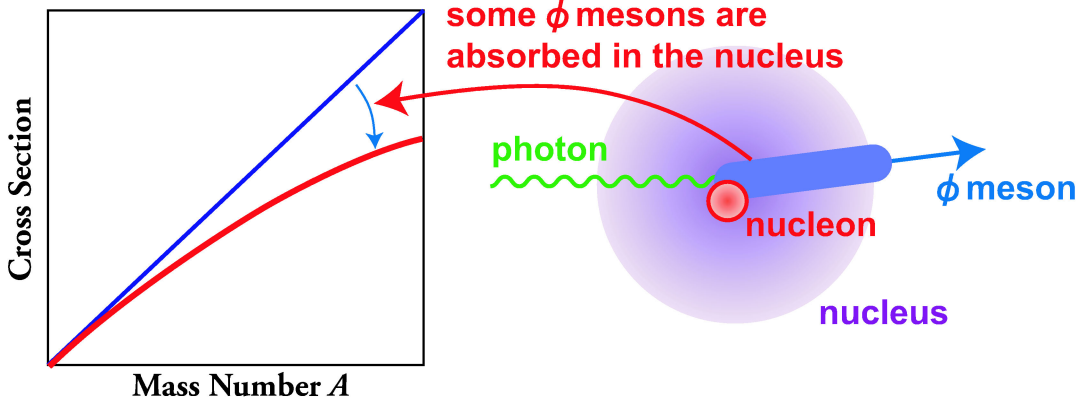


Figure 1.7: Deviation of the A -dependence predicted by the $\sigma_{\phi N}$ in free space. In this figure, the $\sigma_{\phi N}$ in free space is assumed to be 0, and the A -dependence is predicted to be $\sigma_A \propto A^1$. If $\sigma_{\phi N}$ becomes larger in the nuclear medium, some photo-produced ϕ mesons would be absorbed in the nucleus, and the A -dependence sizeably deviates from $\sigma_A \propto A^1$.

values of $\sigma_{\phi N}$ in free space are much smaller than other meson-nucleon total cross sections $\sigma_{\omega N}$, $\sigma_{\rho N}$, and $\sigma_{\eta N}$ (~ 30 mb) [30, 31, 32].

The ϕ - N total cross section $\sigma_{\phi N}$, the real-imaginary ratio of ϕ - N scattering amplitude $\alpha_{\phi N}$, and ϕ - N coupling constant $f_{\phi N}$ are the fundamental parameters to describe ϕ -nucleon scattering. The photo-production from nuclei is the best way to determine these parameters because a nucleus is transparent to the photon probe, and a multi-step process can be negligible. Thus, many measurements of the meson photo-production cross sections from various nuclei have been performed to deduce the total cross section of the mesons in interaction with a nucleon. Figure 1.8 shows the summary of the total

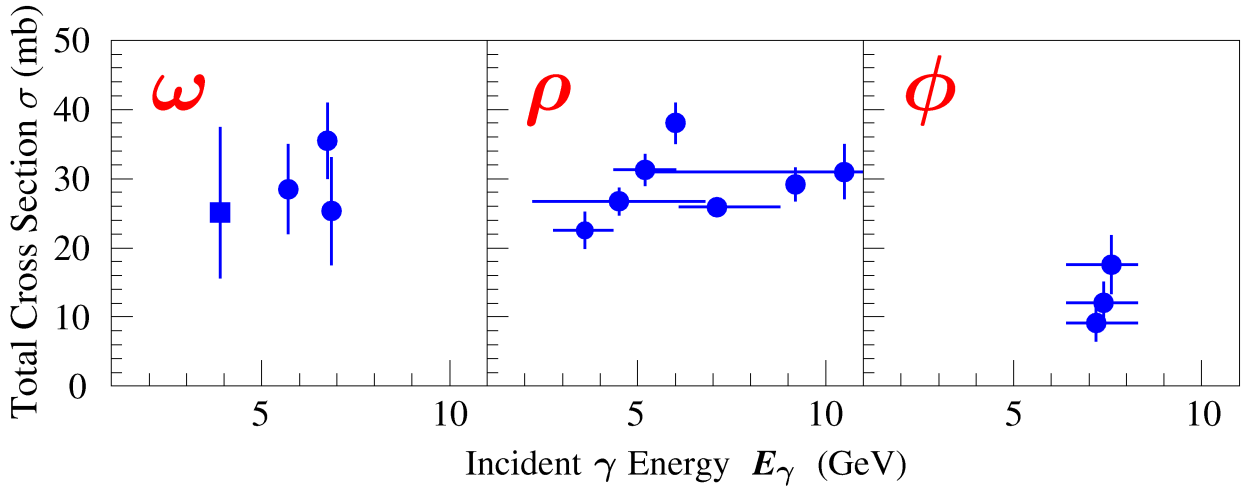


Figure 1.8: Total cross section of vector mesons in interaction with a nucleon. The closed squares show the data determined from the incoherent process, and the closed circles show the data from the coherent one. Only one experiment is reported for the ϕ meson. The horizontal bars show the incident γ energy ranges.

cross sections for vector mesons: $\sigma_{\rho N}$ [33, 34, 35, 36, 37, 38, 39, 40], $\sigma_{\omega N}$ [41, 42, 43, 44], and $\sigma_{\phi N}$ [45].

The $\sigma_{\omega N}$ at $E_\gamma = 3.9$ GeV [43] has been determined from the incoherent process, and the others have been determined from the coherent one.

As for the ϕ mesons, only one measurement of ϕ photo-production from nuclei at high energies (6.4–9.0 GeV) has been performed to determine the fundamental parameters mentioned above [45]. Since coherent ϕ photo-production is dominant at $E_\gamma = 6.4$ –9.0 GeV at forward angles, an optical model of a Glauber-type multiple scattering theory for coherent production has been used [46, 47]. To deduce $\sigma_{\phi N}$ from the A -dependence of the production cross section, the model for coherent production requires three parameters: $\sigma_{\phi N}$, $\alpha_{\phi N}$, and $f_{\phi N}$. A unique solution for $\sigma_{\phi N}$ can not be determined due to the fact that the number of parameters is large. However, at low energies near the ϕ photo-production threshold, coherent production is expected to be suppressed as compared with incoherent production since the momentum transfer $|t|$ is larger even at forward angles where coherent production is expected to be dominantly observed. In the optical model for incoherent production, only one parameter $\sigma_{\phi N}$ is related with the A -dependence. Thus, ϕ -nucleon total cross section $\sigma_{\phi N}$ can be determined with less ambiguities.

1.2 Glauber-type multiple scattering theory

At GeV energies, particle production from nuclei is very useful for obtaining the total cross section of unstable particles and a nucleon. They are produced on one nucleon in the nucleus, and then interact with others before decaying. Thus, the measurements of the production cross section in a wide range of the target mass number A is advantageous to extract the total cross section. The A -dependence of the production cross section is discussed [46, 48, 47] with the following assumptions:

1. the spin and isospin independent interactions,
2. single-step process

$$1 + N \rightarrow 2 + N \quad (1.1)$$

is dominant where 1 and 2 refer to the incident and produced particles, respectively, and

3. the two body process (1.1) is a small part of the total cross section for the particle 1 in interaction with a nucleon.

The production cross section of the incoherent process at forward angles $d\sigma^{\text{inc}}/dt$ is described as

$$\frac{d\sigma^{\text{inc}}}{dt} = \frac{d\sigma_N}{dt} A_{\text{eff}}(A, \sigma_{1N}, \sigma_{2N}) + \int \frac{d\sigma_N(\vec{q}')}{d\Omega'} G(\vec{q}, \vec{q}'; A, \sigma_{1N}, \sigma_{2N}) d^2q' + \dots, \quad (1.2)$$

where A_{eff} stands for an effective nucleon number, σ_N denotes the production cross section on a nucleon, and $G(\vec{q}, \vec{q}'; A, \sigma_{1N}, \sigma_{2N})$ is a correction due to single scattering before and after the production. The A_{eff} is defined as

$$A_{\text{eff}}(A, \sigma_{1N}, \sigma_{2N}) = \frac{1}{\sigma_{2N} - \sigma_{1N}} \int \left\{ \exp(-\sigma_{1N}T(b)) - \exp(-\sigma_{2N}T(b)) \right\} d^2b, \quad (1.3)$$

where σ_{1N} and σ_{2N} denote the total cross sections of the incident and produced particles in interaction with a nucleon, respectively, and $T(b)$ is a thickness function:

$$T(b) = A \int_{-\infty}^{+\infty} \rho(b, z) dz, \quad (1.4)$$

which is estimated assuming the particle 2 goes at an angle of 0° to the momentum direction of the particle 1. The $G(\vec{q}, \vec{q}'; A, \sigma_{1N}, \sigma_{2N})$ is described as

$$G(\vec{q}, \vec{q}'; A, \sigma_{1N}, \sigma_{2N}) = \frac{1}{\sigma_{2N} - \sigma_{1N}} \frac{1}{k^2} \int d^2b \left[\frac{1}{\sigma_{2N} - \sigma_{1N}} \left\{ \exp(-\sigma_{1N}T(b)) - \exp(-\sigma_{2N}T(b)) \right\} \left(|f_{11}(\vec{q} - \vec{q}')|^2 - |f_{22}(\vec{q} - \vec{q}')|^2 \right) + T(b) \left\{ \exp(-\sigma_{1N}T(b)) |f_{11}(\vec{q} - \vec{q}')|^2 - \exp(-\sigma_{2N}T(b)) |f_{22}(\vec{q} - \vec{q}')|^2 \right\} \right], \quad (1.5)$$

where the f_{ij} is the two body scattering or production amplitudes, The f_{ii} denotes the amplitude for scattering of the particle i on a nucleon, and f_{ij} ($i \neq j$) stands for producing j with i incident on a nucleon. The derivation of the incoherent production cross section is reviewed in detail in Appendix A. Assuming that this higher order correction is small, the incoherent production cross section becomes

$$\frac{d\sigma^{\text{inc}}}{dt} = \frac{d\sigma_N}{dt} A_{\text{eff}}(A, \sigma_{1N}, \sigma_{2N}). \quad (1.6)$$

The correction is small for ϕ photo-production since the direct coupling ϕNN lacks due to the Okubo-Zweig-Iizuka (OZI) rule. The ϕ photo-production cross section is proportional to A_{eff} .

The effective nucleon number A_{eff} plays an important role describing the production cross section. In photo-production, the total cross section of the incident photon in interaction with a nucleon (σ_{1N}) is very small (140 μb at $E_\gamma = 1.5\text{--}2.4$ GeV [49]), thus A_{eff} can be described as a function of the target mass number A and the total cross section of the produced particle with a nucleon σ_{2N} . Figure 1.9

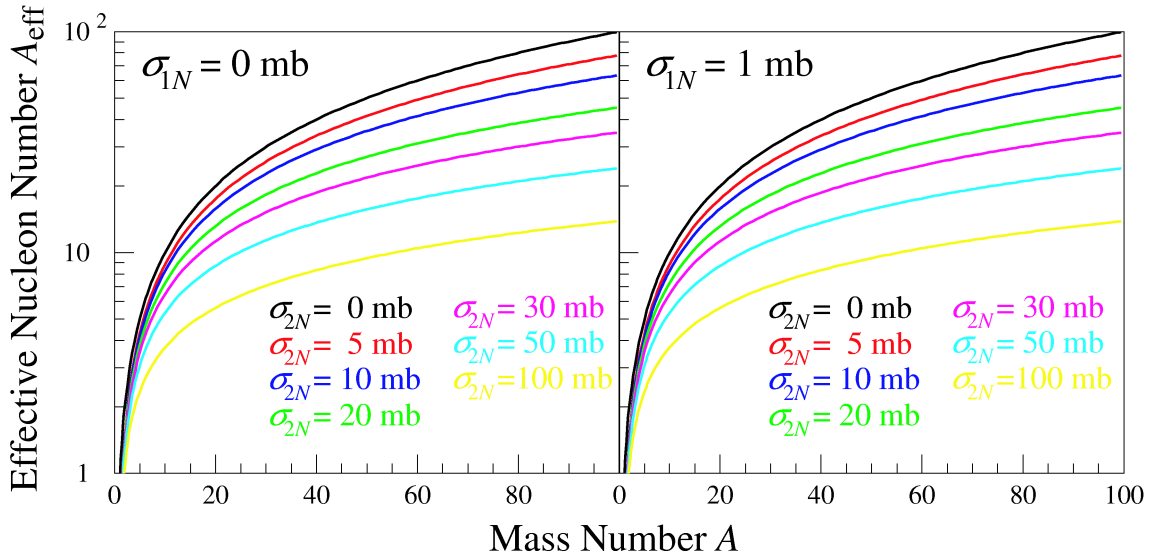


Figure 1.9: Effective nucleon number A_{eff} as a function of A . It is estimated for various σ_{2N} values. The left panel shows A_{eff} for $\sigma_{1N} = 0$ mb, and the right one shows that for $\sigma_{1N} = 1$ mb.

shows A_{eff} for some total cross section values σ_{2N} . Assuming the same $d\sigma_N/dt$ for the proton and the neutron, $\sigma_{\phi N}$ can be derived from the A -dependence of the particle production cross section. The absolute values of the production cross sections are not necessary.

1.3 Presented Data

In this paper, ϕ photo-production from Li, C, Al, and Cu at $E_\gamma = 1.5\text{--}2.4$ GeV is reported. This experiment was carried out at SPring-8/LEPS (C01BL33LEP-6002N, Spokesperson: T. Ishikawa). Before and after this experiment, ϕ photo-production on the proton at $E_\gamma = 1.5\text{--}2.4$ GeV was measured by the LEPS collaboration (C01BL33LEP-6001N, Spokesperson: T. Nakano), and those data are also presented for comparison.

In Chapter 2, the SPring/LEPS facility, detector system, and electronics are described. The procedure of data reduction and event selection, and the mass and width of the observed ϕ mesons are presented in Chapter 3. In Chapter 4, ϕ - N total cross section is estimated from the target mass number A dependence, and the A -dependence is compared with the theoretical calculations. Finally, the work is concluded in Chapter 5.

Chapter 2

Experiment

The differential cross sections of photo-production from nuclei were measured at the SPring-8/LEPS facility. The linearly polarized photons were produced by laser induced backward Compton scattering from 8 GeV electrons in the storage ring. An ultra violet Ar laser was used to generate a photon beam with the maximum energy of 2.4 GeV. The recoil electrons were momentum analyzed by a bending magnet in the storage ring, and were detected by a tagging counter placed at the exit of the bending magnet. Photons with the energy ranging from 1.5 to 2.9 GeV were tagged. Charged particles produced by photo-reactions were momentum analyzed with the LEPS spectrometer system. The SPring-8/LEPS facility and the LEPS spectrometer are described in this chapter.

2.1 Laser-electron photon beam

2.1.1 SPring-8 facility

The Super-Photon Ring-8 GeV (SPring-8) [50, 51] is a third generation synchrotron orbital radiation (SOR) facility, which is optimized to produce a high brightness SOR light source by using insertion devices such as wigglers and undulators. The facility is composed of an injector linear accelerator, a booster synchrotron, and a low emittance and high brightness storage ring. Electrons are

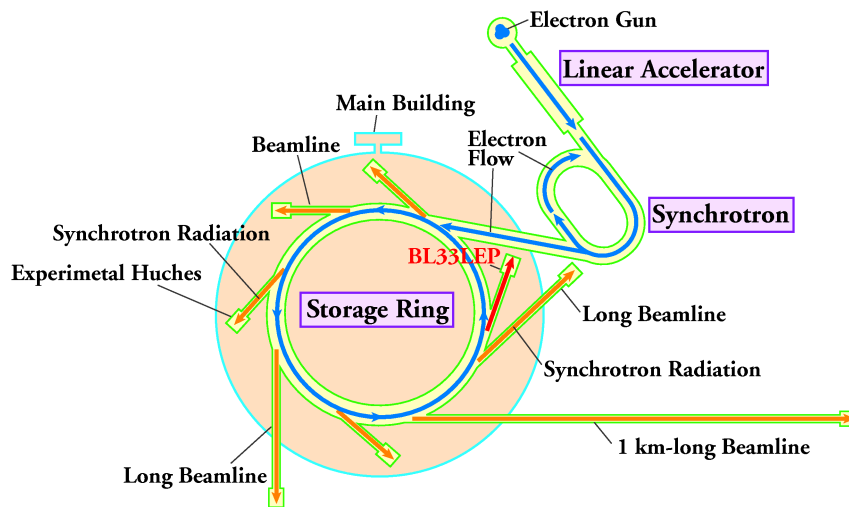


Figure 2.1: Layout of the SPring-8 facility. The SPring-8 facility is composed of a linear accelerator, a booster synchrotron, and a storage ring with 62 photon beam lines.

generated at a thermionic gun, and are accelerated to an energy of 1 GeV in the injector linear accelerator with a length of 140 m, which consists of 26 accelerator columns. The radio frequency (RF) of the linear accelerator is 2856.2403 MHz. The 1 GeV electrons are transported to the booster synchrotron with a circumference of 396.12 m, and are accelerated to 8 GeV. The RF frequency and harmonic number of the synchrotron are 508.58 MHz, and 672, respectively. The 8 GeV electrons are injected to the storage ring with a circumference of 1435.95 m. The RF frequency and harmonic number of the storage ring are 508.58 MHz, and 2436, respectively. Figure 2.1 shows the layout of the SPring-8 facility.

The 8 GeV electrons circulate in the storage ring 2.0878×10^5 times a second. The maximum electron circulating current is 100 mA. Electrons are filled in some of the total 2436 bunches with various filling patterns, where the time interval of the successive bunches is 1.966 nsec. A lifetime depends on the filling pattern, and was about 100 hours in the experiment. The natural emittance is 6.89π nm rad, and the averaged widths are 75 μm and 25 μm in the horizontal and vertical directions, respectively.

The stored electron beam is used to produce photon beams, and there exist 62 beam lines. A laser-electron photon facility has been constructed in the BL33LEP beamline, which is called LEPS (laser-electron photon facility at SPring-8).

2.1.2 LEPS facility

The LEPS facility [52, 54, 55] has been constructed for quark nuclear physics by Research Center for Nuclear Physics (RCNP), Osaka University, by Japan Synchrotron Radiation Institute (JASRI), and by Japan Atomic Energy Research Institute (JAERI). A multi-GeV photon beam is produced by the backward Compton scattering of laser photons from circulating 8 GeV electrons in the storage ring. The LEPS facility consists of an interaction region of laser photons and circulating electrons, a tagging system, a laser hatch, and an experimental hatch. Laser photons are injected to a 7.8 m long straight

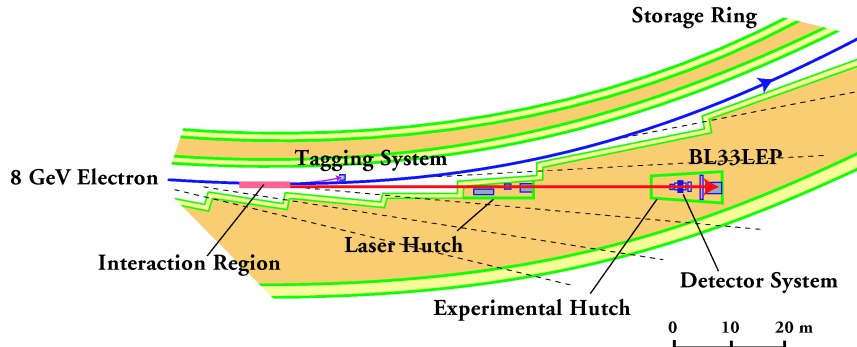


Figure 2.2: Schematic view of the LEPS facility. The LEPS facility consists of an interaction region of laser photons and circulating electrons, a laser hatch, a tagging system, and an experimental hatch.

section between two bending magnets BM1 and BM2 in the storage ring. This straight section is a laser photon-circulating electron interaction region, and some laser photons gain multi-GeV momenta at a direction of electrons via the backward Compton scattering (BCS). The laser injection system is optimized in the laser hatch to minimize the laser spot size in the interaction region to obtain high intensity BCS photon beam. The recoil electrons are momentum analyzed by BM2, and were detected by the tagging system placed at the exit of BM2. The BCS photon beam is provided to the experimental hatch, and irradiates targets. Experiments with the BCS photon beam have started in 2000.

2.1.3 Backward Compton scattering

Compton scattering of a photon by an electron is a simple process in quantum-electro dynamics (QED). Polarized high energy photons are produced by the collision of polarized laser photons with high energy electrons. The energies of produced photons are the same order as those of the electrons. This process is called as backward Compton scattering (BCS).

To discuss the BCS photons quantitatively [56], the kinematics is described as follows. A laser photon with an energy k_1 and an electron with an energy E_e approach one another, where E_e is much larger than k_1 . The photon strikes the electron with an angle of $\theta_1 \simeq 180^\circ$, and is scattered at an angle θ_2 . Figure 2.3 shows the kinematical values of the BCS process. The energy of the scattered

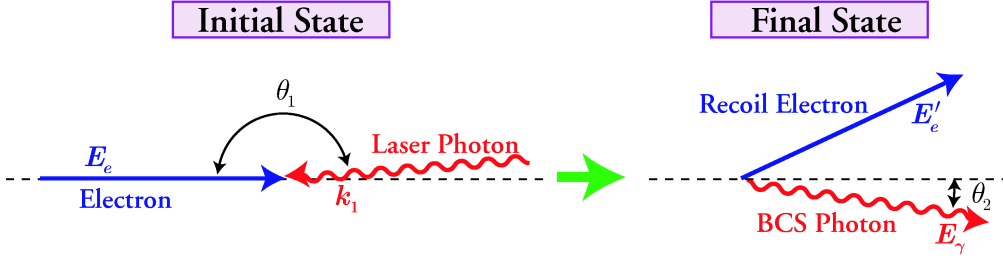


Figure 2.3: Kinematical values of the BCS process. A laser photon with an energy of k_1 strikes an electron with a energy of E_e at an angle θ_1 , the scattered BCS photon at an angle of θ_2 has an energy of E_γ , and the recoil electron has an energy of E'_e .

BCS photon E_γ is

$$E_\gamma = k_1 \frac{1 - \beta \cos \theta_1}{1 - \beta \cos \theta_2 + \frac{k_1(1 - \cos \theta)}{E_e}}, \quad (2.1)$$

where β is an initial velocity of the electron in unit of the speed of the light, and $\theta = \theta_1 - \theta_2$. When $\gamma = E_e/m_e \gg 1$, $\beta \simeq 1$, $\theta_1 \simeq 180^\circ$, and $\theta_2 \ll 1$ are assumed, Eq. (2.1) can be written as

$$E_\gamma = \frac{4E_e^2 k_1}{m_e^2 + 4E_e k_1 + \theta_2^2 \gamma^2 m_e^2}, \quad (2.2)$$

where m_e is the electron mass. The maximum energy of the BCS photon is obtained at $\theta_2 = 0^\circ$. The differential cross section of the BCS process is described [56] as

$$\frac{d\sigma}{dE_\gamma} = \frac{2\pi r_e^2 a}{E_\gamma^{\max}} (\chi + 1 + \cos^2 \alpha), \quad (2.3)$$

where r_e is the classical electron radius, and

$$a = \frac{m_e^2}{m_e^2 + 4E_e k_1}, \quad (2.4)$$

$$\chi = \frac{\rho^2 (1 - a)^2}{1 - \rho(1 - a)}, \quad (2.5)$$

$$\cos \alpha = \frac{1 - \rho(1 + a)}{1 - \rho(1 - a)}, \quad (2.6)$$

$$\rho = \frac{E_\gamma}{E_\gamma^{\max}} \quad (2.7)$$

The polarized BCS photons are produced by using polarized laser photons. Most of the laser polarization is transferred to the BCS photons. The linear, and circular polarizations of BCS photons P_γ^L , P_γ^C are described [56] as

$$P_\gamma^L = P_{\text{laser}}^L \frac{(1 - \cos \alpha)^2}{2(\chi + 1 + \cos^2 \alpha)}, \quad (2.8)$$

$$P_\gamma^C = P_{\text{laser}}^C \frac{(2 + \chi) \cos \alpha}{(\chi + 1 + \cos^2 \alpha)}, \quad (2.9)$$

where P_{laser}^L , P_{laser}^C are the linear, and circular polarizations of laser photons, respectively.

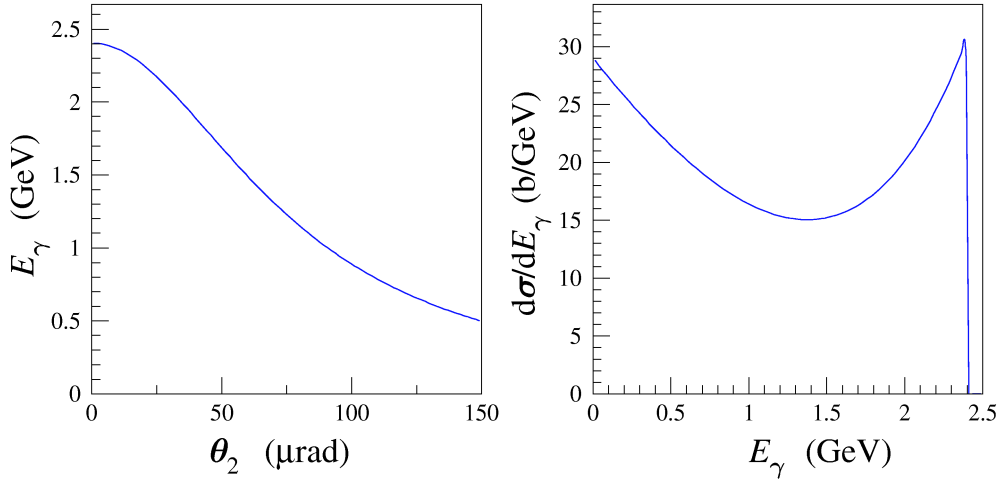


Figure 2.4: Energy of the BCS photon. The left panel shows the energy of the BCS photon as a function of scattering angle. The right panel shows the differential cross section of the BCS process.

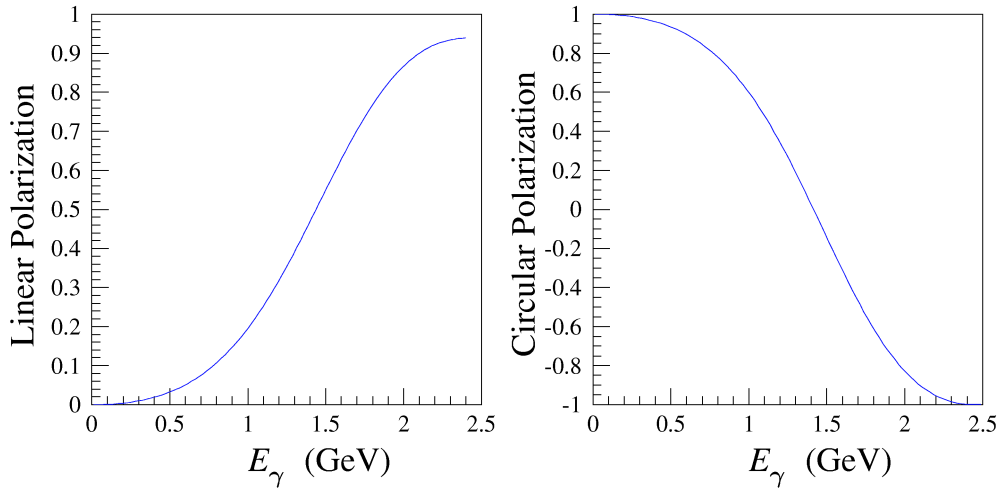


Figure 2.5: Polarization of the BCS photon. The left and right panels show the linear and circular polarization as a function of the BCS photon energy, respectively.

Figure 2.4 shows the energy of the BCS photon as a function of scattering angle θ_2 , the differential cross section $d\sigma/dE_\gamma$ for a laser with a wave length of 351 nm. Here, the circulating electron energy E_e is 7.975 ± 0.003 GeV, the electron mass m_e is 0.51099906 MeV, and the classical electron radius r_e is

2.818 fm. The maximum energy of the BCS photon E_γ^{\max} is 2.4 GeV. The energy distribution for BCS photons is a quasi-flat, and low energy photons are reduced as compared with the Bremsstrahlung photons, of which energy distribution has a $1/E_\gamma$. BCS photons with an energy larger than 1.5 GeV are produced inside a narrow cone (< 0.06 mrad). Figure 2.5 shows the linear, and circular polarizations P_γ^L , P_γ^C as a function of E_γ with a 100% linearly, and circularly polarized laser, respectively. The maximum degree of polarizations are obtained at $E_\gamma^{\max} = 2.4$ GeV, and are 94%, 100% for linear, circular polarization, respectively.

2.1.4 Laser injection system

An ultra violet Ar laser is used to get laser photons. The laser oscillates with a multi-line mode, and the wave length ranges from 333 to 364 nm. Figure 2.6 shows the wave length spectrum of the

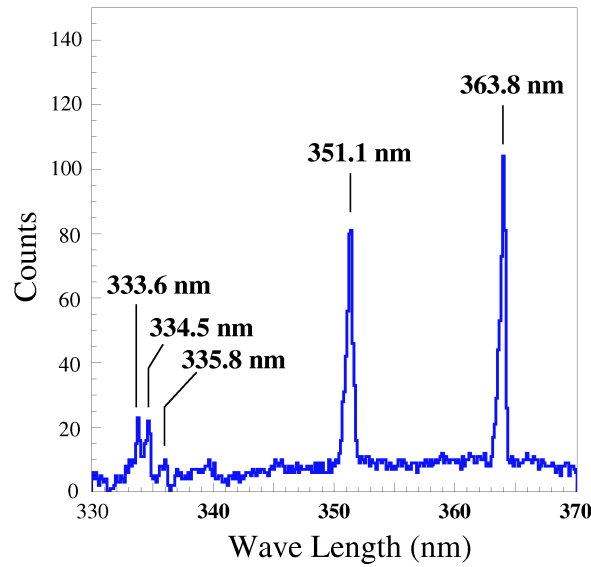


Figure 2.6: Wave length of the Ar laser with a multi-line ultra violet mode. Sharp peaks of 351.1 nm and 363.8 nm are observed.

laser measured by a monochromator. Five peaks of 333.6, 334.5, and 335.8, 351.1, and 363.8 nm are observed, and two peaks of 351.1, and 363.8 nm among them are very sharp. Typical output power of the laser is about 8 W, which corresponds to the $1.42 \times 10^{19} \text{ sec}^{-1}$ since the energy of laser photons with 351 nm is 3.53 eV.

The laser injecting system is composed of the Ar laser, a half wave ($\lambda/2$) plate, and four mirrors, and a polarizer and a photo diode are used for the polarization measurement. Figure 2.7 shows the schematic view of the laser injecting system. The direction of the laser polarity is controlled by a half wave ($\lambda/2$) plate placed just after the laser exit. When a linearly polarized laser is injected on a half wave plate with the polarization plane at an angle θ with respect to the fast axis (optic axis), the polarization plane of the outgoing laser rotates at an angle 2θ after passing through the plate. The fast axis is set at 0° (45°) to get the vertically (horizontally) polarized laser photons since the Ar laser is vertically polarized.

The laser photons travels 40 m before it collides with a circulating electron. A beam expander telescope reduces the divergence angle of the laser beam, and the diameter in the interaction region is minimized to achieve maximum luminosity. The beam expander is placed after the half wave plate.

Four mirrors are used to transport the laser photons to the interaction region in the storage

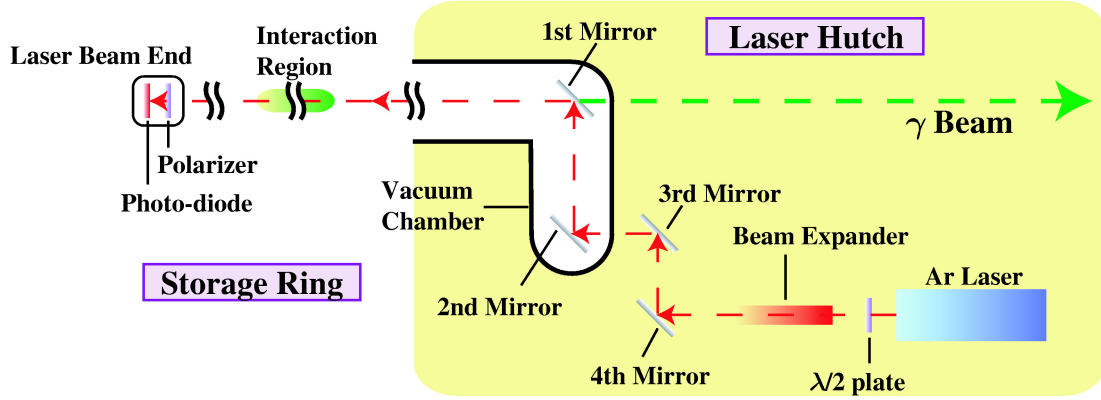


Figure 2.7: Schematic view of the laser operation system. The Ar laser, the $\lambda/2$ plate, and the four mirrors are used for injecting the laser photons to the storage ring. The polarizer and the photo-diode are used for the polarization measurement.

ring. The first and second mirrors are fixed, and the direction and the position of the laser beam are adjusted by the third and fourth mirrors. The first and second mirrors are made of aluminum evaporated silicon, and the third and fourth mirrors are made of quarts. The transmission of the laser photons to the laser beam end is about 40%. Since the reflectivity for the vertically polarized laser photons is higher than that for the horizontally polarized ones, the intensity of the vertically polarized BCS photons is higher than that of the horizontally polarized ones.

The polarization of the laser beam is measured at the laser beam end located downstream of the interaction region. Polarization measurement system consists of a polarizer (glan-laser prism; OptMax PGL8310) and a photo-diode (HAMAMATSU S1406-05). When the laser photons pass through a polarizer, the electric field parallel to the transmission axis of the polarizer survives. Thus

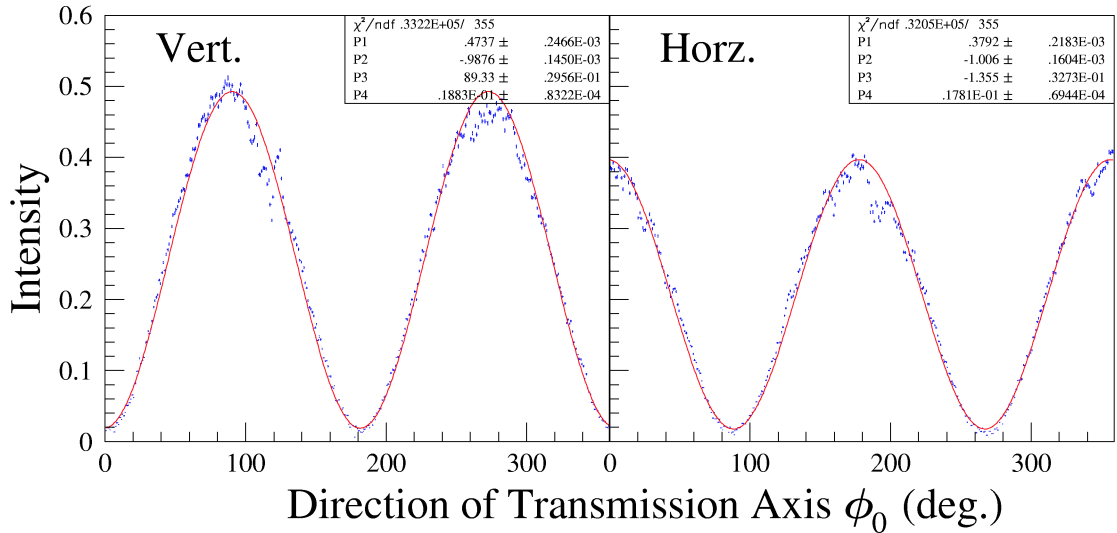


Figure 2.8: Laser intensity with respect to the direction of the transmission axis ϕ_0 . The left and right panels show the vertically and horizontally polarized laser photons.

the intensity of the laser photons after the polarizer I is described as

$$I = I_0 \cos^2 \phi, \quad (2.10)$$

where ϕ is angle between the transmission axis and the direction of the incident laser polarity, and I_0 is the intensity of outgoing laser photons for $\phi = 0$. The intensity of the outgoing laser photons is measured by the photo-diode. Figure 2.8 shows the intensity distribution for the vertically and horizontally polarized laser photons respect to the direction of the transmission axis ϕ_0 . The intensities are proportional to $\cos^2(\phi_0 - 90^\circ)$, and $\cos^2(\phi_0 - 0^\circ)$ for vertically, and horizontally polarized laser photons. The polarization and the direction of polarity ϕ_{laser} is obtained by fitting these distributions with a function described as

$$I = I_0 \cos^2(\phi_0 - \phi_{\text{laser}}), \quad (2.11)$$

2.1.5 Tagging system

The BCS photon energy E_γ is described as

$$E_\gamma = E_e - E'_e, \quad (2.12)$$

where E_e is the circulating electron energy, and E'_e is the recoil electron energy. The E'_e is measured by the tagging system installed at the exit of the bending magnet BM2. Since the momentum of the recoil electron is lower than that of the circulating electrons, the recoil electron bends inward from the normal circulating electron orbit in the storage ring. Therefore, a displacement of the position at the exit of BM2 which the recoil electron passes through corresponds to E'_e .

The tagging system is composed of two plastic scintillator hodoscopes and silicon strip detectors (SSD). Each hodoscope consists of 10 plastic scintillators, and plastic scintillators of a hodoscope are stacked with two layers. Odd and even number ones are placed downstream and upstream with an overlap of 1.0 mm, respectively. Each plastic scintillator is a rectangular parallelepiped of

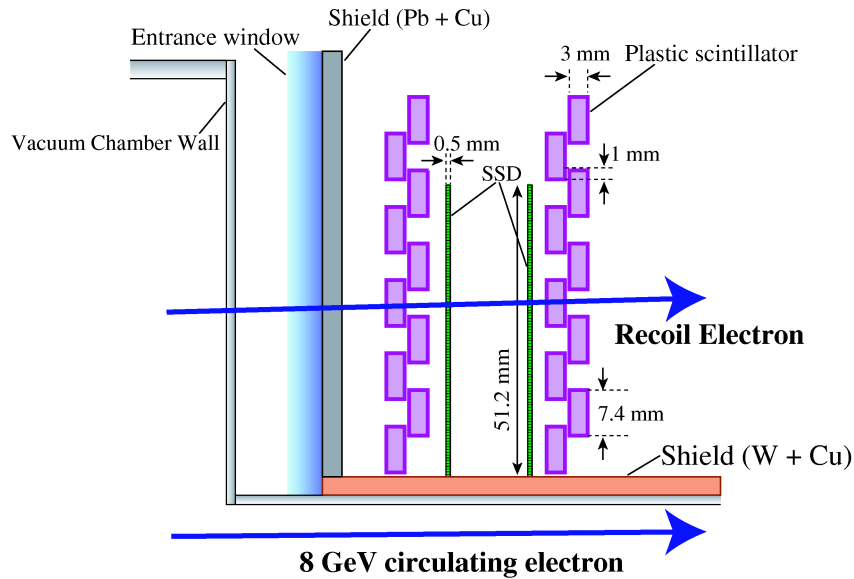


Figure 2.9: Top view of the tagging system. The tagging system is placed at the exit of BM2, and is composed of two plastic scintillator hodoscopes and two SSD's.

7.4 (W) \times 3.0 (T) \times 10.0 (H) mm³, and a photo-multiplier tube (HAMAMATSU R1635P) is coupled to it through a light guide. Two SSD's are installed between the two hodoscopes. Each SSD is a rectangular parallelepiped of 51.2 (W) \times 0.5 (T) \times 10.0 (H) mm³, which has 512 strips in total with a strip pitch of 100 μ m. Figure 2.9 shows the top of the tagging system.

Basically precise hit positions are measured by the SSD. To suppress the background events due to the X rays and electro-magnetic showers, hit information of the associated plastic scintillators is also used with the track which joins hit strips of the two SSD's. It is also required to suppress the background events that only one hit is found at each SSD in the area between the line successive fired scintillators covers on the upstream hodoscope and the one on the downstream hodoscope. This requirement causes three dips at 1.74, 1.94, and 2.14 GeV by suppressing the events that recoil electrons pass through four plastic scintillators. The BCS photon energy ranging from 1.5 to 2.9 GeV can be measured by the tagging system [57]. Figure 2.10 shows the energy spectrum of BCS photons

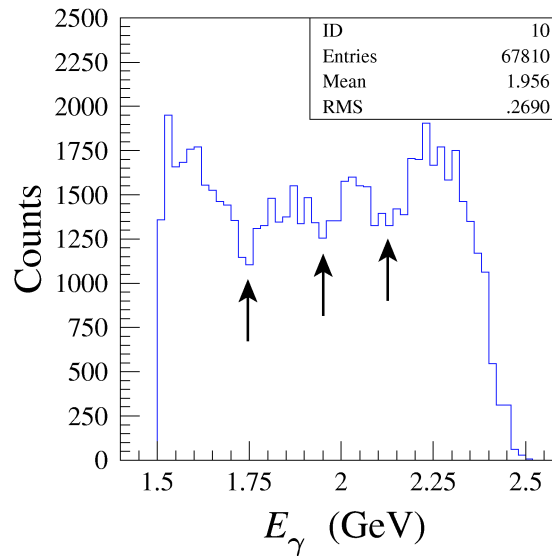


Figure 2.10: Energy spectrum of BCS photons measured by the tagging system. Three dips at 1.74, 1.94, and 2.14 GeV shown by the arrows are caused by the suppression of the events that recoil electrons pass through four plastic scintillators.

measured by the tagging system. The BCS photon energy resolution is about 15 MeV (σ), which is mainly determined by the energy and angular spreads of the circulating electron, and the performance of the bending magnet BM2 as a momentum analyzer.

2.1.6 Materials on the beam line

The BCS photons travel from the collision point to the laser hutch (36 m) and to the experimental hutch (70 m). The first mirror, windows of vacuum chambers, and a X ray absorber are placed on the photon beam line, and photon beam flux is attenuated because some photons mainly converts to e^+e^- pairs. The first mirror is made of aluminum evaporated silicon. It is 6 mm thick and is tilted by 45° from the beam line. The windows are set at the exit of the vacuum chamber of the storage ring, and at the entrance and exit of the vacuum chamber which joins the laser and the experimental hutches. Each window is a 0.55 mm thick aluminum plate. The X ray absorber is introduced so that detectors of the spectrometer work well, which is made of lead sheets, and is 1.5 mm in total. A simple estimation of the transmission of the BCS photons from the interaction region to the target

point is about 72%. However, the measured transmission is 58%. Figure 2.11 shows the schematic

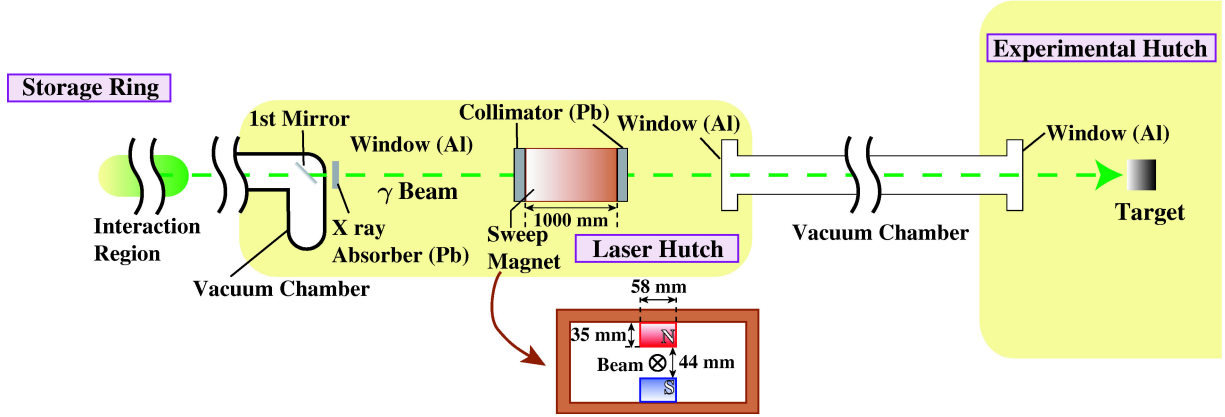


Figure 2.11: Schematic view of the beam line. The first mirror, windows of vacuum chamber, and a X ray absorber are set on the beam line. The e^+e^- pairs created in the materials on the beam line are removed by a sweep magnet.

view of the beam line.

The e^+e^- pairs created in the material on the beam line or the residual gas in the vacuum chamber of the storage ring is removed by a sweep magnet with a magnetic field of 0.6 T at the center as shown in Figure 2.11. The sweep magnet is composed of two permanent magnets and an iron yoke. Each permanent magnet is a rectangular parallelepiped of 58 (W) \times 1000 (L) \times 35 (H) mm³. A gap between two magnets are 44 mm. The lead collimators with diameters of 20 and 25 mm is set upstream and downstream of the sweep magnet. Electrons and positrons with a momentum below 2.1 GeV are blocked by the downstream collimator.

2.2 Target

The nuclear targets used in the experiment were lithium (Li), carbon (C), aluminum (Al), and copper (Cu) with thicknesses of 100 mm, 36 mm, 24 mm, and 3 mm, respectively. All the targets used were natural. Table 2.1 shows the properties of the nuclear targets used. The densities of the Li, Al, and Cu targets are the values in the property sheet [49] since the measured ones are consistent with these values. On the other hand, the density of the C target is a measured value. The Li target block

Table 2.1: Properties of the nuclear targets used. The Li target was a block, and each of the other three targets was divided into three pieces.

Target	Mass Number A	Thickness ξ [cm]	Density ρ [g/cm ³]
Li	6.941	10.0	0.534
C	12.011	3 \times 1.20	1.730
Al	26.982	3 \times 0.80	2.702
Cu	63.546	3 \times 0.10	8.92

was placed in a target box filled with Ar gas. The windows of the target box were sealed with 50 μ m Aramid sheets. To minimize the difference of the acceptances among different target thicknesses and to avoid a systematic error caused in the acceptance correction, each of the other three targets was set

by dividing into three pieces with the same center of gravity and standard deviation of the position along the photon beam direction as those of the Li target. Figure 2.12 shows shapes of the nuclear

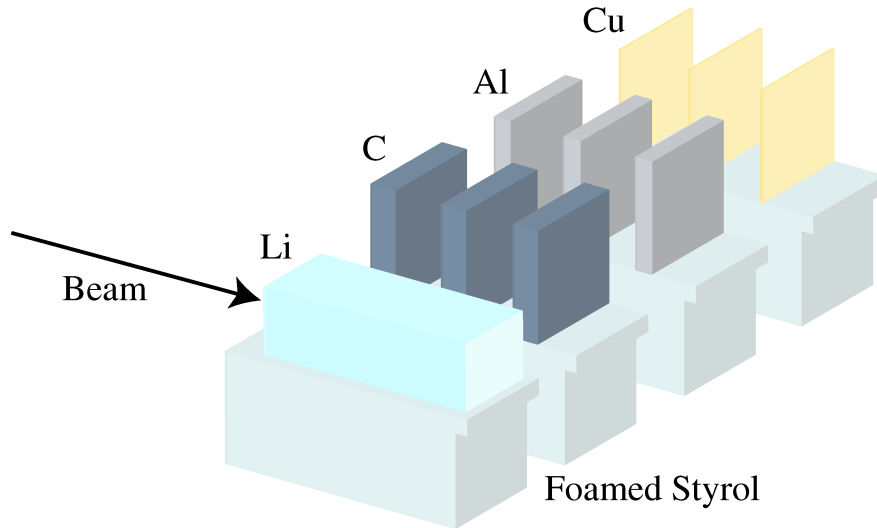


Figure 2.12: Target shape. The target used in the experiment were Li, C, Al, and Cu. The Li target block was set on a formed styrol. Each of the other three targets was set by dividing into three pieces, and was set on a formed styrol.

targets used. To avoid the systematic errors due to the change of the beam conditions, targets were exchanged every two hours.

2.3 LEPS spectrometer

Charged particles produced at the target are detected at forward angles with the LEPS spectrometer. The LEPS spectrometer is located in the experimental hutch, which consists of a plastic scintillator located at the exit of the vacuum chamber (upstream veto counter), a plastic scintillator behind the target (start counter), a silica aerogel Čerenkov counter, a dipole magnet, a silicon-strip vertex detector (SVTX), three multi-wire drift chambers (DC1, DC2, and DC3), and a plastic scintillator hodoscope placed downstream of the tracking detectors (TOF wall). Charged particles produced upstream of the experimental hutch are vetoed by the upstream veto counter. The SVTX, DC1, DC2 and DC3 are used to track charged particles through the dipole magnet. A time of flight of each track is measured by the start counter and the TOF wall. Electrons and positrons produced at very forward angles are blocked by lead bars inside the gap of the magnet, and are vetoed by a silica aerogel Čerenkov counter. Figure 2.13 shows the schematic view of the LEPS spectrometer.

2.3.1 Upstream veto counter

Some photons produces charged particles mainly by the e^+e^- pair production in air, and in the residual gas and the widows of the vacuum chamber downstream of the sweep magnet. These charged particles are identified by the upstream veto counter, and vetoed online. The upstream veto is made of a plastic scintillator, and a rectangular parallelepiped of $190\text{ (W)} \times 5\text{ (T)} \times 200\text{ (H)}\text{ mm}^3$. The 2 inch diameter photo-multiplier tube (HAMAMATSU H7195) is coupled to the scintillator through a light guide.

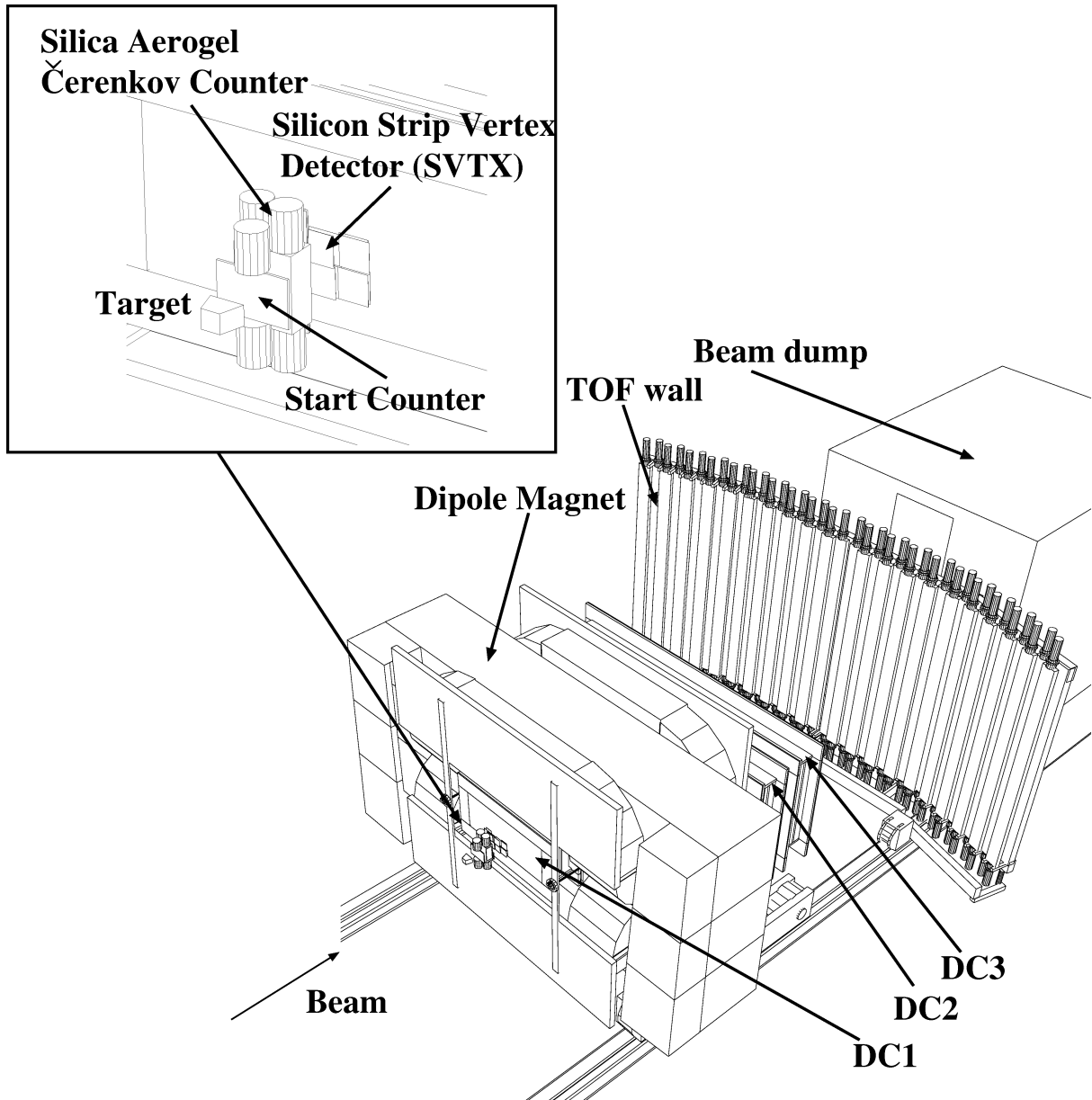


Figure 2.13: Schematic view of the LEPS spectrometer. The LEPS spectrometer consists of a dipole magnet, a silicon-strip vertex detector (SVTX), three multi-wire drift chambers (DC1, DC2, and DC3), a plastic scintillator behind the target (start counter), a silica aerogel Čerenkov counter, and a plastic scintillator hodoscope placed downstream of the tracking detectors (TOF wall).

2.3.2 Start counter

Charged particles produced at a target is detected by the start counter. The start counter is made of a plastic scintillator, and a rectangular parallelepiped of $150\text{ (W)} \times 5\text{ (T)} \times 94\text{ (H)}\text{ mm}^3$. Since the magnetic leakage field of the dipole magnet is a few mT which the start counter is located at, the fine mesh photo-multiplier tubes (HAMAMATSU H6614-01) with a diameter of 2 inch are coupled directly to the scintillator from the top and bottom. The start signal for the time of flight measurement is produced by the start counter.

2.3.3 Aerogel Čerenkov counter

Main background events for the measurement of hadronic reactions are the e^+e^- pairs produced in the target, the start counter, air downstream of the upstream veto counter, and the downstream surface of the upstream veto counter itself. These e^+e^- events are vetoed online by an aerogel Čerenkov counter. In the aerogel Čerenkov counter, two sheets of silica aerogel radiators with a refractive index of 1.03, which are rectangular parallelepipeds of $110\text{ (W)}\times 25\text{ (T)}\times 110\text{ (H)}\text{ mm}^3$, are filled in the box with a rectangular parallelepiped of $120\text{ (W)}\times 60\text{ (T)}\times 110\text{ (H)}\text{ mm}^3$. The box is made of black paper, and Gortex sheets are spreaded on its inside surface as a random reflector. The magnetic leakage field is also a few mT which the counter is placed at, fine mesh photo-multiplier tubes (HAMAMATSU H6614-01) with a diameter of 2 inch are used to read out Čerenkov-photon signals. Two tubes are coupled directly to the counter from the top, and the other two are coupled from the bottom. Figure 2.14 shows the structure of the aerogel Čerenkov counter. Since the refractive index of the

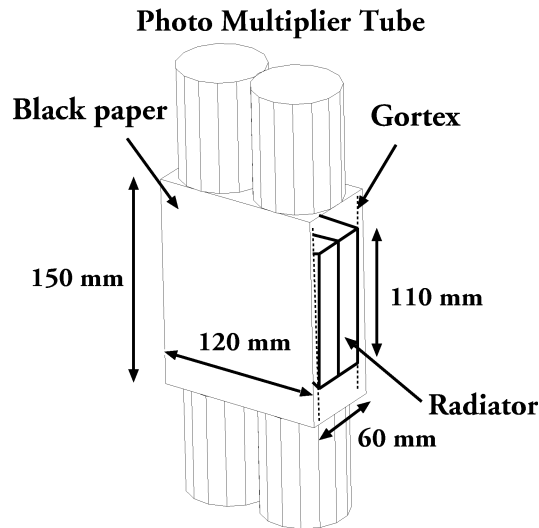


Figure 2.14: Structure of the aerogel Čerenkov counter. Two sheets of silica aerogel radiators with a refractive index of 1.03, are filled in the box.

radiators are 1.03, a charged particle with velocity faster than $1/1.03$ emits a Čerenkov light. The events that includes electrons, positrons, charged pions with momenta higher than 0.57 GeV, or charged kaons with momenta higher than 2.00 GeV are rejected in the trigger level.

2.3.4 Dipole magnet

Charged particles are momentum analyzed by a dipole magnet, which is placed at the center in the experimental hutch. The aperture of the magnet is $1350\text{ (W)}\times 550\text{ (H)}$. The length between the pole edges is 600 mm. The Vector Fields TOSCA 6.6 package in the OPERA-3D suite [58] is used to calculate the magnetostatic field of the magnet. A finite element method is used in TOSCA, which obtains solutions of partial differential or integral equations that cannot be solved by analytic method. The method is based on divisions of domain to solve the equation into small finite elements, and within each finite element a simple polynomial is used to approximate the solution. The finite element method used in TOSCA is described in Appendix G.3.

In the magnetostatic field calculation of the LEPS dipole magnet, each finite element was a hexahedron, and divided regions of the dipole magnet are shown in Figure 2.15. Each region is

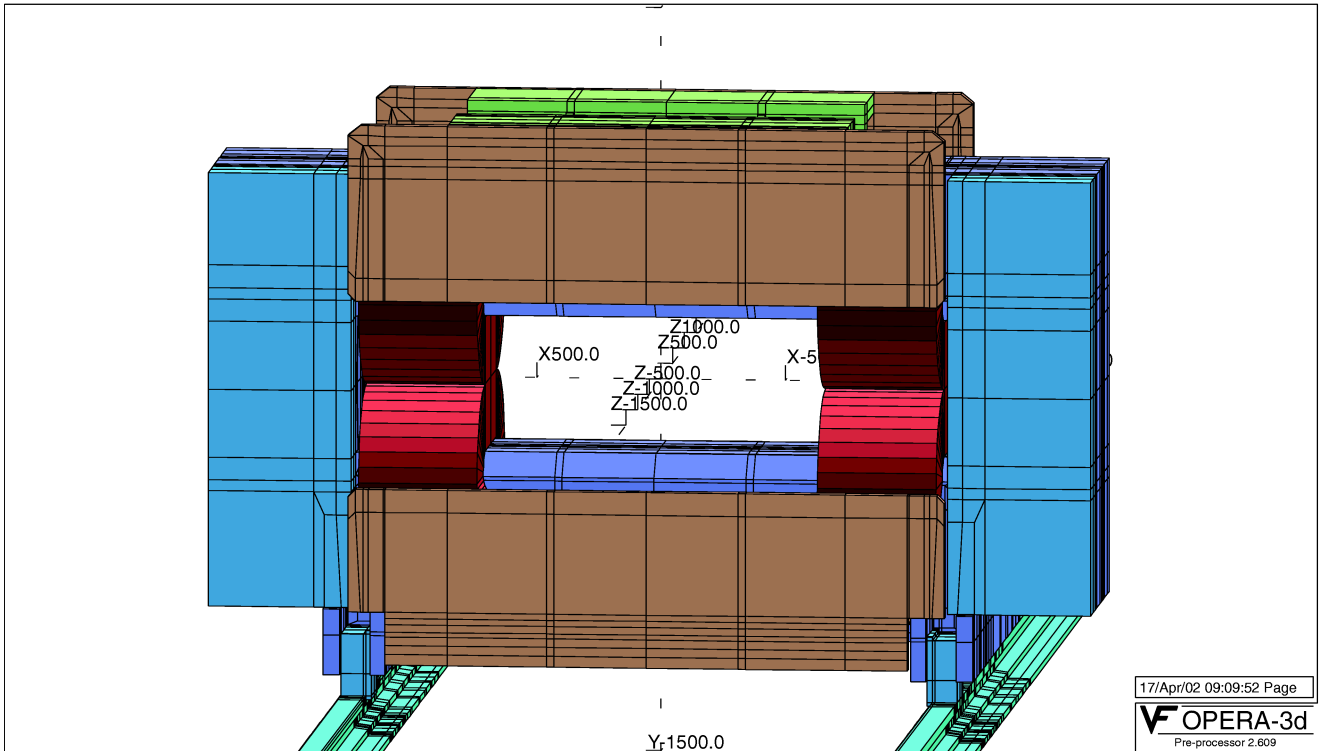


Figure 2.15: Division region of the dipole magnet for the field calculation. Each region is further divided into small finite elements. Coils are filled in red, and an iron yoke is filled in blue.

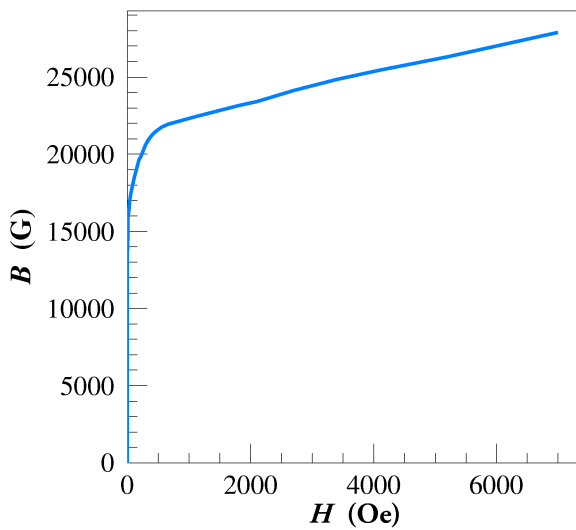


Figure 2.16: Relation between the magnetic flux density B and field H of the iron yoke.

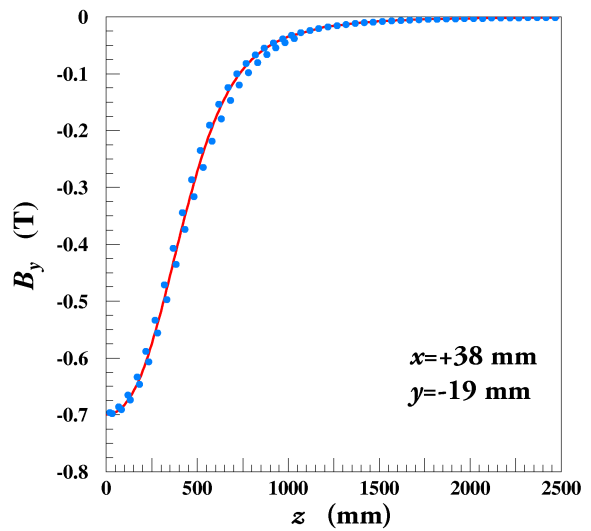


Figure 2.17: Comparison between the calculated and measured magnetic fields.

further divided into small finite elements. Number of divisions to the elements were increased step by step. When the maximum difference in all the domain between the current and the previous steps becomes less than 0.3 mT, the results of the current step was adopted as a final one. Figure 2.16

shows the relation between magnetic flux density B and magnetic field H of the iron yoke for the field calculation¹, and Figure 2.17 shows the comparison between the calculation and the measured field with a hole probe. Figure 2.18 shows the magnetic field B_y along the z axis. The origin

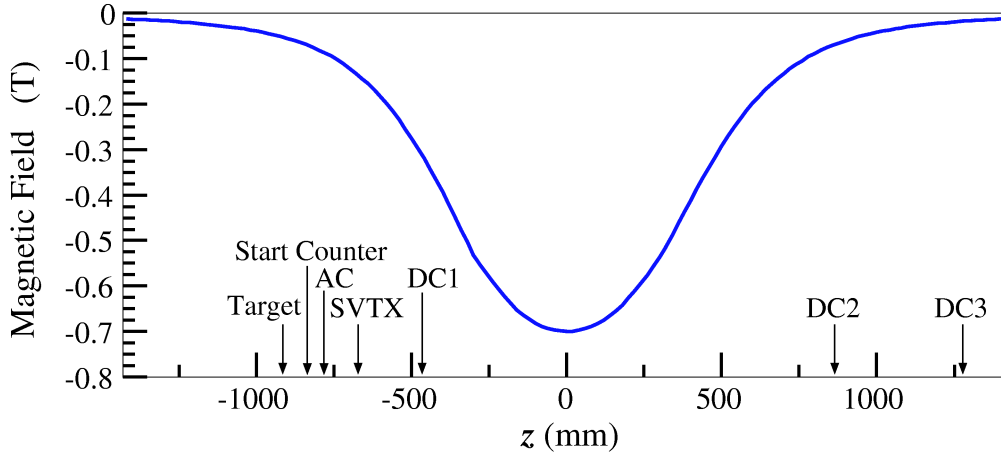


Figure 2.18: Magnetic field B_y along the z axis. The central position of the target, the start counter, aerogel Čerenkov counter (AC), the silicon strip vertex detector (SVTX), and three drift chambers (DC1, DC2, and DC3) are shown by the arrows.

$(x, y, z) = (0, 0, 0)$ is the center of the dipole magnet.

Trajectories of charged particles are determined by a silicon strip vertex detector, three drift chambers, and a plastic scintillator hodoscope.

¹In this thesis, the magnetic flux density B is often called by the magnetic field since only the density in the air region is need to analyze momenta of charged particles.

2.3.5 Silicon strip vertex detector (SVTX)

Positions close to the target are measured by a silicon strip vertex detector (SVTX) with a high precision. The SVTX consists of sixteen silicon strip detectors (SSD) with a pitch of $120\ \mu\text{m}$. Two SSD layers are stacked in all the effective region, one of which measures x positions and the other measures y positions. The SVTX has a diamond-shaped hole with a size of $10\times 10\ \text{mm}^3$ for the BCS photon beam path. Figure 2.19 shows the structure of the SVTX.

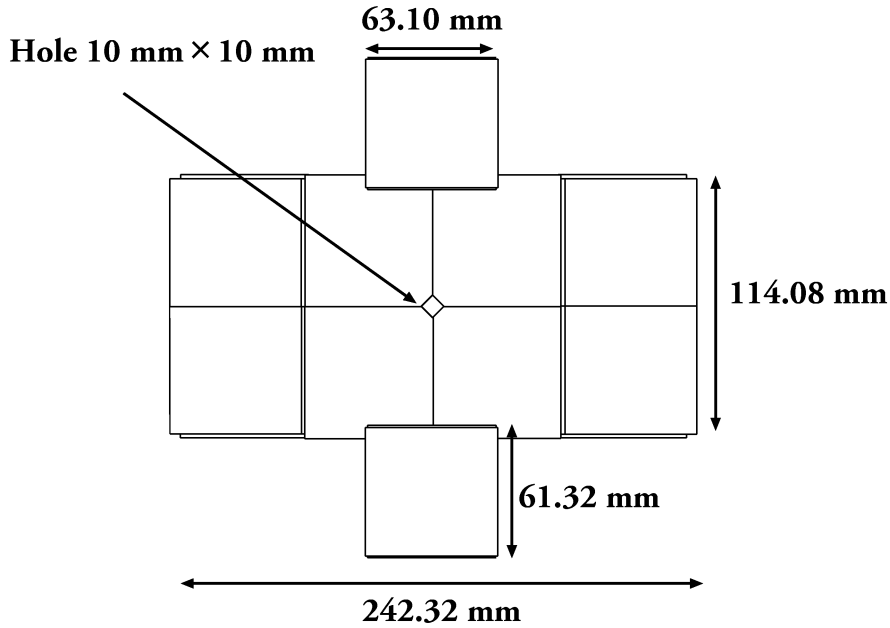


Figure 2.19: Structure of the SVTX. The SVTX consists of sixteen SSD with a strip pitch of $120\ \mu\text{m}$ with a diamond-shaped hole in the center.

2.3.6 Drift chambers

Positions upstream and downstream of the dipole magnet which charged particles pass through are measured by three drift chambers (DC1, DC2, and DC3). The DC1 is placed just behind the SVTX upstream of the magnet. The DC1 has six wire planes which are X'' , V , U' , U , X' , and X wire planes from the upstream side. The DC2 and DC3 are placed downstream of the magnet. The design of the DC2 and DC3 are the same, and have five wire planes which are V , U' , U , X' , and X wire planes from the upstream side. Wires of the X , X' , and X'' planes are strained in the vertical direction. Wires of the U , U' planes in DC1, those of the V plane in DC1, those of the U , U' planes in DC2 and DC3, those of the V plane in DC2 and DC3 are inclined by $+45^\circ$, -45° , $+30^\circ$, -30° , with respect to the vertical direction, respectively. Sense wires of each plane in DC1 are positioned with a $12\ \text{mm}$ spacing, and those in DC2 and DC3 are positioned with a $20\ \text{mm}$ spacing. Sense wires are surrounded by field wires arranged with a honeycomb shape. The X - X' and U - U' planes are doublet, and the wires of X' and U' planes are shifted by a half wire spacing of the plane. Shield wires are installed outside the field wires in order to arrange the electric field. Figure 2.20 shows the structure of the DC wire planes. Sense wires of DC1 are made of gold plated tungsten (Au-W) with a diameter of $25\ \mu\text{m}$, and those of DC2 and DC3 are made of Au-W with a diameter of $30\ \mu\text{m}$. The field and shield wires are made of gold plated alloy of beryllium and copper (Au-BeCu) with a diameter of

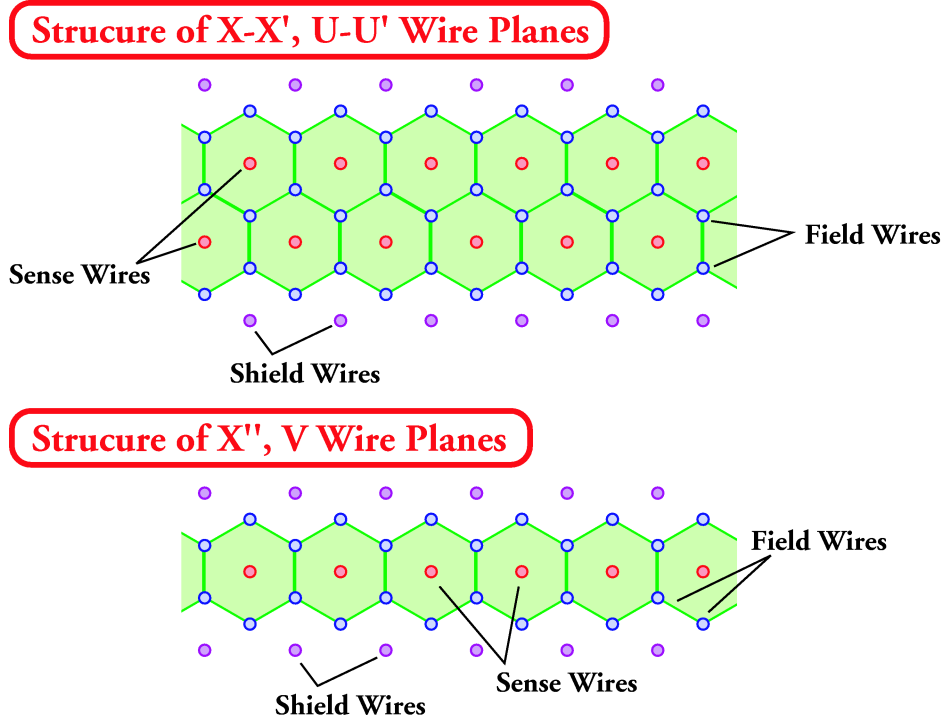


Figure 2.20: Structure of the DC wire planes. The upper panel shows the structure of doublet $X-X'$ and $U-U'$ wire planes, and the lower one shows the structure of X'' and V planes.

100 μm . The windows are made of mylar with a thickness of 125 μm . The design parameters are summarized in Table 2.2. The gas mixture used to operate DC is 70% argon and 30% isobutane with

Table 2.2: Design parameters of DC. The orientation is an inclination angle of the wires with respect to the vertical direction. The wire spacings for $X-X'$ and $U-U'$ planes in this table are the one two planes are treated as one plane. The location z shows the center position of each DC where $z = 0$ is defined as the center of dipole magnet.

	Plane	Orientation	#Sense wires	Wire spacing (mm)	location z
DC1	$X-X'$	0°	48×2	6	-466.0
	$U-U'$	$+45^\circ$	48×2	6	
	V	-45°	48	12	
	X''	0°	48	12	
DC2	$X-X'$	0°	104×2	10	860.5
	$U-U'$	$+30^\circ$	78×2	10	
	V	-30°	79	20	
DC3	$X-X'$	0°	104×2	10	1260.5
	$U-U'$	$+30^\circ$	78×2	10	
	V	-30°	79	20	

a little isopropyl alcohol. The position resolution of DC1 is about 130 μm . and that of DC2 and DC3 is about 200 μm . The typical supplied high voltages are -2000 V, -2400 V, and -2700 V to the shield, the DC1 field, and other DC field wires, respectively.

2.3.7 TOF wall

A time of flight for each charged particle is measured by a plastic scintillator hodoscope (TOF wall). The TOF wall located downstream of DC3. Each scintillator is a rectangular parallelepiped of $120\text{ (W)} \times 40\text{ (T)} \times 2000\text{ (H)}\text{ mm}^3$. Two photo multiplier tubes (HAMAMATSU H7195) are coupled to each scintillator through a light guide from the top and bottom. There exists a gap of 40 mm between the central two scintillators for the photon beam path. Sideway scintillators are aligned in the planes yawed by $\pm 15^\circ$. Figure 2.21 shows the structure of the TOF wall. The center of the TOF wall is $z = 3151.5\text{ mm}$, where the location of $z = 0$ is the center of the dipole magnet.

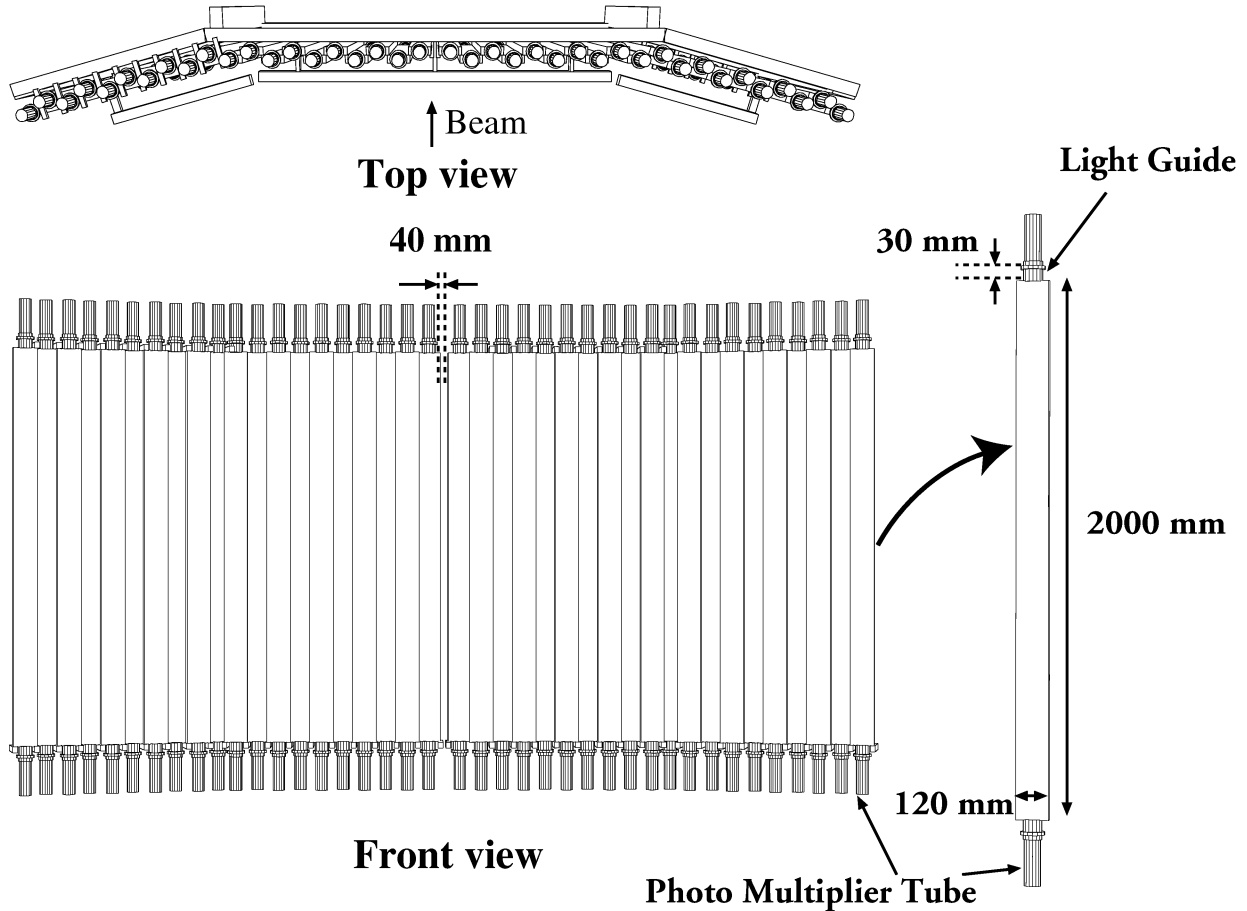


Figure 2.21: Structure of the TOF wall. The upper panel shows the top view of the TOF wall, and the lower one shows the front view.

2.3.8 e^+e^- blocker

Most of e^+e^- pairs produced at the target and at the start counter are scattered at very forward angles. Since the magnetic flux goes from the bottom to the top, these particles spread in the median plane. Low energy electrons and positrons with momenta lower than 1 GeV are blocked by lead bars inside the gap of the magnet (e^+e^- blocker). Each lead bar is a rectangular parallelepiped of $440\text{ (W)} \times 100\text{ (T)} \times 40\text{ (H)}\text{ mm}^3$, and the gap of the two bars is 155 mm. Two lead bars are supported by a V-shaped thin SUS bar with a thickness of 5 mm. The center of lead bars are -7 mm in the y -direction. Figure 2.22 shows the schematic view of the e^+e^- blocker.

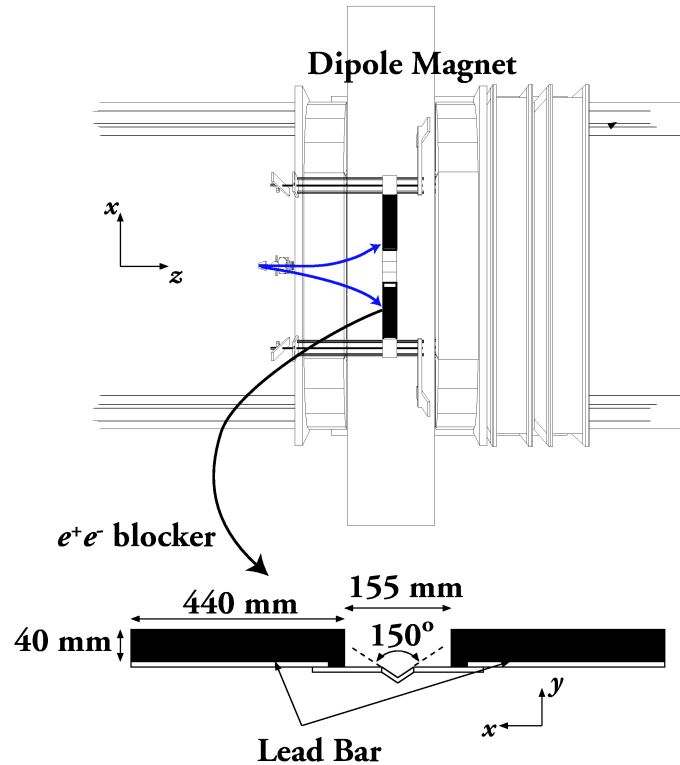


Figure 2.22: Schematic view of the e^+e^- blocker. The upper panel shows the place the e^+e^- blocker is set at, and the lower one shows the structure of the e^+e^- blocker.

2.4 Data Acquisition

2.4.1 Electronics

In this subsection, the electronics for each detector system is described [59, 60]. Figure 2.23 shows the electronics for the trigger counters.

Tagging System

Signals from the plastic scintillator hodoscopes in the tagging system are divided. The charges of the analog signals are read out by the LeCroy 4300B (FERA: Fast Encoding & Readout ADC) modules, of which gate width is set at 150 nsec. The timings of the discriminated signals are read out by the LeCroy FASTBUS 1877S, of which time resolution is 0.5 nsec a channel and of which dynamic range is 1 μ sec.

The VA chips are used for reading out SSD signals. The silicon strips and the VA chips are mounted on a printed circuit. The circuit is connected to a repeater card which contains adjustable bias supply for the VA chips, and buffer amplifier for analog signals. Analog signals from the VA chip are sent to a flash ADC module through the repeater card.

Upstream veto counter

Signals from the upstream veto counter are divided. The charges are read out by FERA, and the timings are read out by the LeCroy FASTBUS 1875A, of which time resolution is 0.025 nsec a channel

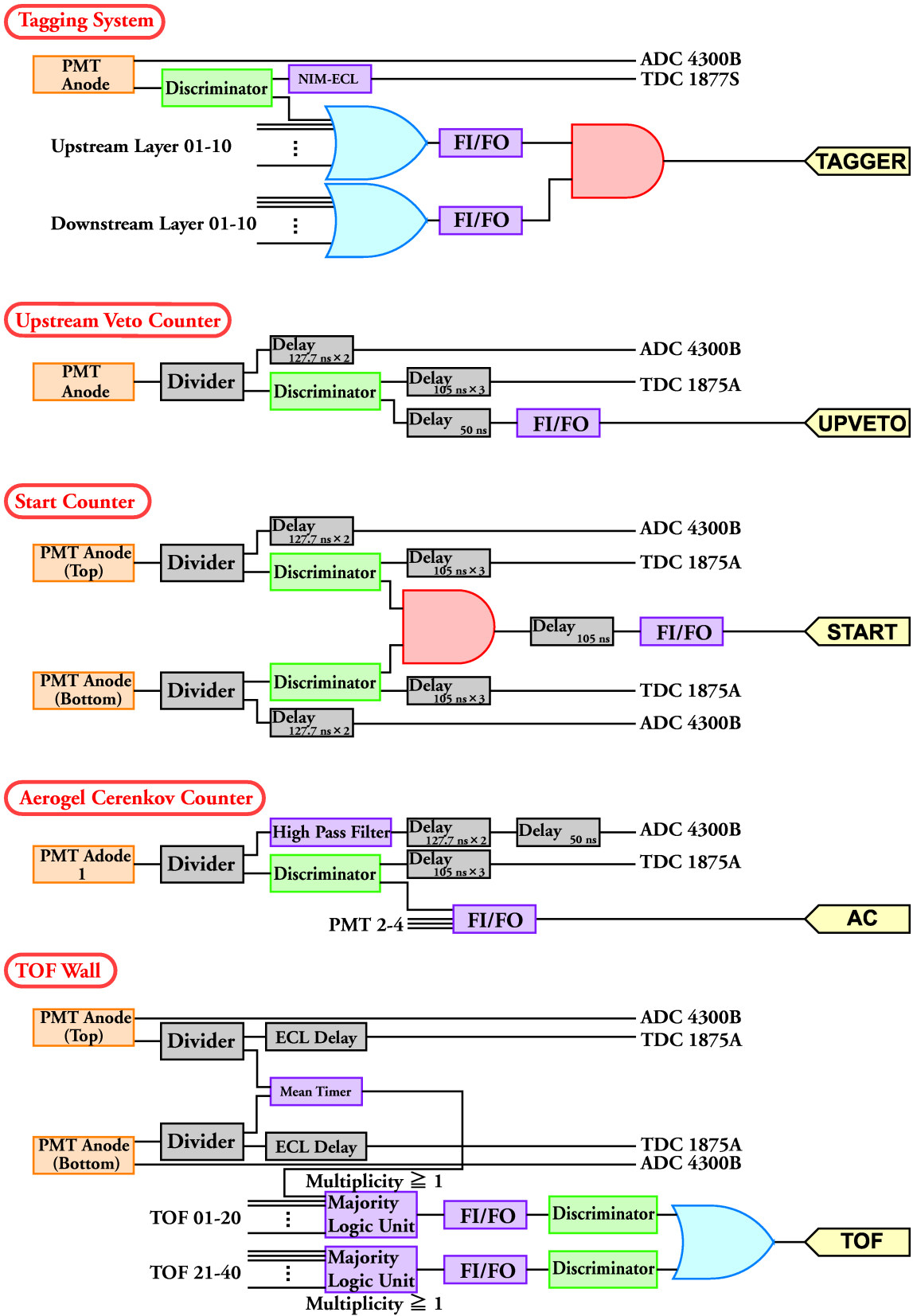


Figure 2.23: Electronics for the trigger counters. Trigger signals are formed from the logic signals of the tagging system, the upstream veto counter, the start counter, the aerogel Čerenkov counter, and the TOF wall.

and of which dynamic range is 100 nsec.

Start counter

Signals from the start counter are divided, and the charges are read out by FERA, and the timings are read out by the LeCroy 1875A.

Aerogel Čerenkov counter

Signals from the aerogel Čerenkov counter are divided, and the charges are sent to FERA through a high pass filter, and the timings are read out by the LeCroy 1875A.

Silicon strip vertex detector (SVTX)

The readout system for the silicon strip detectors are the same as that for SSD in the tagging system.

Drift chambers

Signals from the wires are amplified and discriminated by a pre-amplifier card and an amplifier and discriminator card. The timing of the signals are read out by the LeCroy 1877S.

TOF wall

Signals from the TOF wall are divided, and the charges are read out by FERA, and the timings are read out by the LeCroy 1875A.

RF signal

A radio frequency (RF) of 508.58 MHz is used in the 8 GeV storage ring to accelerate electrons to 8 GeV which lose some energies due to the synchrotron radiation. A start timing for a time of flight measurement is defined by the RF signal instead of the start counter one in order to achieve high timing resolution. An interval of the successive RF signals is 1.966 nsec. The timing of the RF signal is read out by the LeCroy 1875A and the LeCroy 1877S through prescalers (DIGITAL LABORATORY 17K32 508-MHz 30 bit). The RF signal is prescaled with a factor 1/87. One output of the prescaled signal is sent directly to the LeCroy 1875A, and another is sent with a 86 nsec delay. The other is further prescaled with a factor 1/28, of which three outputs are sent to the LeCroy 1877S with 0, 1.8, and 3.6 μ sec delays. The data read out by the LeCroy 1877S is used to investigate accidental rates in the tagging system.

2.4.2 Trigger

Trigger signals are formed from logic signals of the plastic scintillator hodoscope in the tagging system (TAGGER), the upstream veto counter (UPVETO), the start counter (START), the aerogel Čerenkov counter (AC), and the TOF wall (TOF). The trigger logics are described as

$$\text{Hadron Trigger} : (\text{TAGGER} \otimes \overline{\text{UPVETO}}) \otimes (\text{START} \otimes \overline{\text{AC}}) \otimes \text{TOF} \quad (2.13)$$

$$e^+e^- \text{ Trigger} : (\text{TAGGER} \otimes \overline{\text{UPVETO}}) \otimes \text{START} \otimes \text{TOF} \quad (2.14)$$

Each logic signal is formed as follows.

TAGGER: The TAGGER signal is coincidence signals of plastic scintillator hodoscope signals, each of which is summed signal of plastic scintillator signals in a hodoscope.

UPVETO: The UPVETO signal is a logic signal of the upstream veto counter.

START: The START signal is a coincidence signal of the top and bottom photo-multiplier tube signals

AC: The AC signal is a summed signal of four photo-multiplier tube signals.

TOF: The TOF signal is a summed signal of 40 scintillators, each of which is a coincidence signal of the top and bottom photo-multiplier tube signals.

The trigger timing is defined by the delayed start counter signal. Figure 2.24 shows the diagram of the trigger logic.

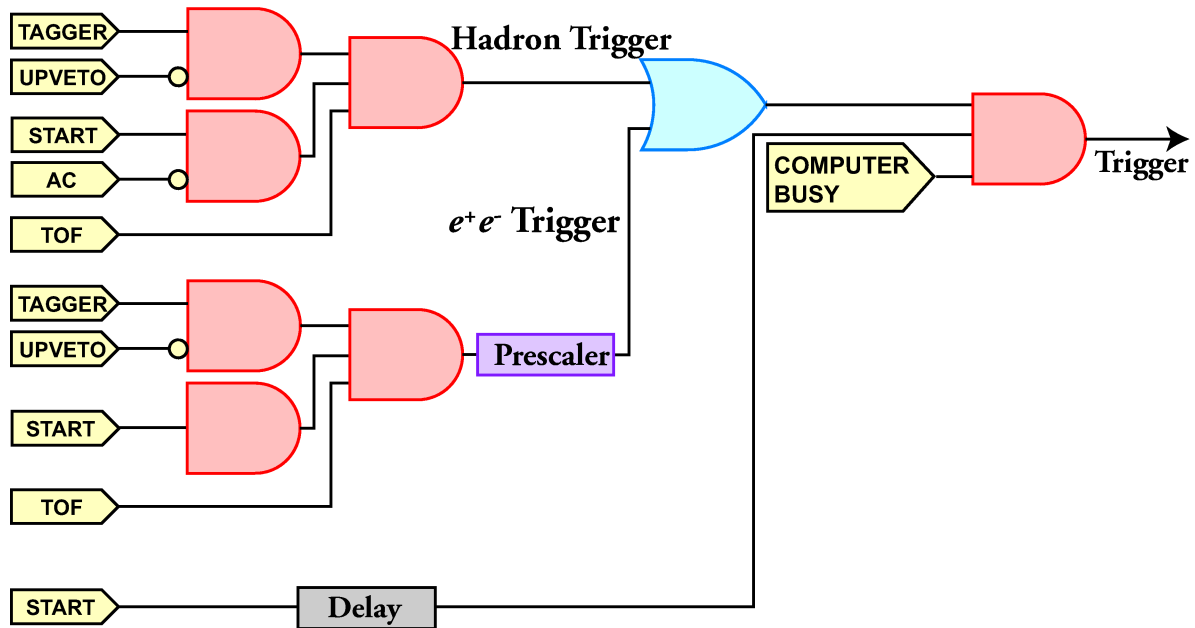


Figure 2.24: Diagram of the trigger logic. The hadron and e^+e^- triggers are described. The trigger timing is defined by the delayed start counter signal. The trigger signal provides the ADC gate, the common start signals for the TDC 1875A, and the common stop signals for the TDC 1877S.

2.4.3 Data taking system

The data taking system is divided into three subsystems. The first one processes the FERA modules in the CAMAC system. The digitized data are collected with a universal I/O module (UIO) with an 8 MB memory in a VME system through the LeCroy 4301 (FERA driver). The UIO module is designed as a buffer sequencer for reading out and buffering of the data. The buffered data are transferred to the Sun Microsystems Force 7V in the VME system. The second one processes the FADC modules in a VME system. The digitized data are transferred to another Force 7V through another UIO module. The third one processes the FASTBUS TDC modules. The Next-Generation FASTBUS (NGF) is used as a buffer sequencer and interface module. The digitized data are transferred to the other Force 7V through NGF. All the buffer sequencer works double buffer mode to reduced the dead time. During a readout sequence of a buffer by the Force 7V, digitized data are stored in another buffer. The data of the three subsystems are collected by the COMPAQ Alpha Server 1200. The dead time of the data taking system was typically 10 % under the condition with a trigger rate of 150 Hz.

2.4.4 Obtained data

The experiment was carried out from the 8th to the 20th November in 2001. The vertically and horizontally polarized photon data were collected in similar amount. About 40 % of the data were junk because serious troubles took place — one of the majority logic modules were out of order, the ring buffer of the TDC1877S sometimes became working abnormally, and so on. The number of hadron triggers which could be used was 8.0, 10.0, 17.1, and 27.8×10^6 for Li, C, Al, and Cu, respectively. The rate of the tagging system was typically 800 kHz, and 600 kHz for the vertically and horizontally polarized BCS photons, respectively. The hadron trigger rate was 100–150 Hz, and the prescaled e^+e^- trigger rate was about 10 Hz.

Chapter 3

Analysis

In this chapter, data reduction is described, which contains reconstruction of charged particle tracks, selection of the ϕ events, and the mass and width of the observed ϕ events.

3.1 Program codes

3.1.1 Analysis code: LEPSana

Raw data by the data taking system is processed by an analysis code LEPSana. The LEPSana has been developed by the LEPS collaboration. The digitized ADC and TDC data of the detectors are processed and the BCS photon beam energy, momenta, positions, and masses of charged particles are extracted. The output of the program are written in NTUPLE format [61] and further analysis is done by accessing output NTUPLE files in the physics analysis workstation (PAW) [63]. The calibration of the detectors and the determination of the parameters have been done beforehand. Processing of the TOF wall data requires timing offsets and gains of plastic scintillators, and that of the tagging system data requires timing offsets and gains of the plastic scintillator hodoscopes. Processing of the drift chamber data requires the timing offsets, the relations of drift times to drift lengths, and position resolutions.

3.1.2 Monte Carlo simulation code: g3leps

The acceptance of the LEPS spectrometer, the resolution of the physical values were studied by a Monte Carlo simulation code g3leps. The g3leps has been developed by the LEPS collaboration, and which is based on the CERN library [62] including GEANT 3.21 [64]. It simulates a generation of particles from the ϕ photo-production, processes during passage of the particles through the experimental apparatus taking into account decay in flight, energy loss, multiple scattering of the particles. The ϕ mesons were produced so that the s -channel helicity should be conserved, which discussed in Appendix B. A harmonic oscillator model was used to determine momentum of a nucleon in a nucleus, which is discussed in Appendix F.1. The GHEISHA package was used to simulate hadronic interactions. The measured resolution and efficiency of the silicon strip vertex detector (SVTX) and the drift chambers, timing resolution of the TOF wall counters were implemented in g3leps. A realistic beam shape of the polarized BCS photon beam, and its resolution were implemented very well. Generated data of the events by the simulation code were analyzed by the exactly same process as the real data were analyzed by the LEPSana. The output of the program are also written in NTUPLE format [65].

3.2 Timings, positions, and resolutions

3.2.1 TOF wall

Consider a charged particle passes through y apart from the center of the plastic scintillator at a time t_0 . The timings when light reach the top and bottom side photo-multiplier tubes (PMT) t_T and t_B are described as

$$\begin{aligned} t_T &= t_0 + \frac{L/2 - y}{v}, \text{ and} \\ t_B &= t_0 + \frac{L/2 + y}{v}, \end{aligned} \quad (3.1)$$

where v is an effective speed of light in a plastic scintillator. The t_0 can be determined by averaging the times t_T and t_B . Figure 3.1 shows the variables for determining timings. The timing of a

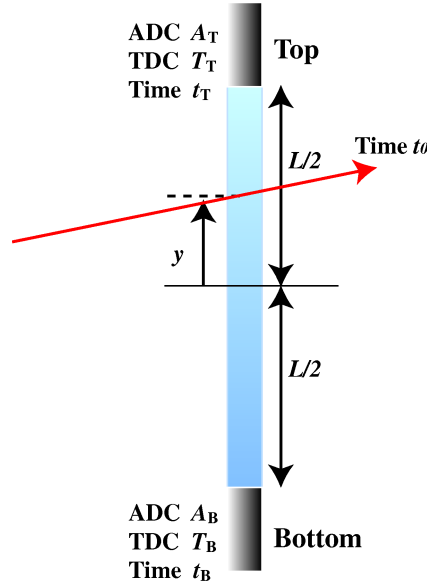


Figure 3.1: Plastic scintillator of which light signals are recorded in both sides. The t_0 stands for the timing when the charged particle penetrate the plastic scintillator with a length L at the position y . The t_T denotes the timing when light reaches the top side PMT, A_T and T_T stand for the measured ADC and TDC values in the top side, respectively. The t_B , A_B , and T_B are defined for the bottom side in the same manner as the top side.

discriminated signal depends on a pulse height. The t_T and t_B are determined by the TDC values T_T , T_B , and the ADC values A_T , A_B in the top and bottom signals, respectively (a pulse height dependent time walk correction).

$$\begin{aligned} t_T &= \left(T_T + \frac{2a_T}{\sqrt{A_T}} + T_T^0 \right) \times 0.025 \text{ nsec/channel}, \text{ and} \\ t_B &= \left(T_B + \frac{2a_B}{\sqrt{A_B}} + T_B^0 \right) \times 0.025 \text{ nsec/channel}, \end{aligned} \quad (3.2)$$

where a_T and a_B are coefficients for the pulse height correction, and T_T^0 and T_B^0 are the timing offsets. Therefore, the t_0 is determined by

$$t_0 = \left(\frac{T_T + T_B}{2} + \frac{a_T}{\sqrt{A_T}} + \frac{a_B}{\sqrt{A_B}} + T_0 \right) \times 0.025 \text{ nsec/channel}, \quad (3.3)$$

where $T_0 = (T_T^0 + T_B^0)/2$. The three parameters a_T , a_B , and T_0 are obtained for each TOF counter [66]. From Eq. (3.1), the hit position y is described as

$$y = v \frac{t_B - t_T}{2} = v \left(\frac{T_B - T_T}{2} + \frac{a_B}{\sqrt{A_B}} - \frac{a_T}{\sqrt{A_T}} + T_{\text{diff.}} \right) \times 0.025 \text{ nsec/channel}, \quad (3.4)$$

where $T_{\text{diff.}} = (T_B^0 - T_T^0)/2$. The effective speed of light v and $T_{\text{diff.}}$ were obtained by the hit position predicted by the downstream drift chamber positions [66].

3.2.2 RF signals

The circulating electrons are bunched according to a RF signal, and the arrival time of a BCS photon at the target position is synchronized with the RF signal. Since the common start signals of TDC modules are provided by the start counter. The timings of the RF signals depend on pulse heights of the start counter photo multiplier tubes. The corrected RF timing $T_{\text{RF}}^{\text{corr.}}$ is determined with the top and bottom TDC values T_T^{SC} , T_B^{SC} , and the ADC values A_T^{SC} , A_B^{SC} of the start counter as

$$T_{\text{RF}}^{\text{corr.}} = T_{\text{RF}} + \frac{1}{2} \left(T_T^{\text{SC}} + T_B^{\text{SC}} + \frac{a_T^{\text{SC}}}{\sqrt{A_T^{\text{SC}}}} + \frac{a_B^{\text{SC}}}{\sqrt{A_B^{\text{SC}}}} + \frac{b_T^{\text{SC}}}{A_T^{\text{SC}}} + \frac{b_B^{\text{SC}}}{A_B^{\text{SC}}} \right), \quad (3.5)$$

where T_{RF} is obtained TDC of the RF signal, and a_T^{SC} , a_B^{SC} , b_T^{SC} , and b_B^{SC} are coefficient for the pulse height correction. The corrected timing $T_{\text{RF}}^{\text{corr.}}$ is used for determining a time of flight, and its resolution is about 150 psec [66].

3.2.3 Drift chambers

The edge timings of signals are recorded for each wire of the drift chambers, and each recorded timing has a flag whether it is leading or trailing. In the experiment, six timings of edges were recorded at most. An ideal signal has basically two edges, one leading and one trailing ones, but signals are raised associating with a true one as electric noises. The timing of a raised signal is delayed, or a raised signal has a shape like a spike. At first, a threshold for an interval between the leading and trailing edges (width) is set to reject signals which have spike-like shapes. Figure 3.2 shows the width distributions together with thresholds. The signals with narrower widths than the thresholds are rejected. The first signals are selected for each wire among the signals that are not rejected by the thresholds for the widths.

A drift time t_{drift} is determined from a timing offset T_0 , and a timing of an leading edge of the first hit (T) as

$$t_{\text{drift}} = -(T - T_0) \times 0.5 \text{ nsec/channel}. \quad (3.6)$$

T_0 is determined by fitting the right edge of the timing T distribution with a Gaussian convoluted step function since charged particles come with a uniform distribution in a local region. Figure 3.3 shows the T distributions together with a fitted Gaussian convoluted step function at T_0 .

The drift time t_{drift} is translated to the drift length x_{drift} (x - t curve) as

$$x_{\text{drift}} = c_1 t_{\text{drift}} + c_2 t_{\text{drift}}^2 + c_3 t_{\text{drift}}^3, \quad (3.7)$$

where c_1 , c_2 , and c_3 are the parameters for the x - t curve, and monotonous increase is required for x_{drift} . The parameters are determined plane by plane. Given parameters $c_1^{(n)}$, $c_2^{(n)}$, and $c_3^{(n)}$ for all the planes, a straight line fitting in three dimensional space is made where the hit information in the plane of interest is not used. The fitting is made with the positions at SVTX and DC1 if the plane of

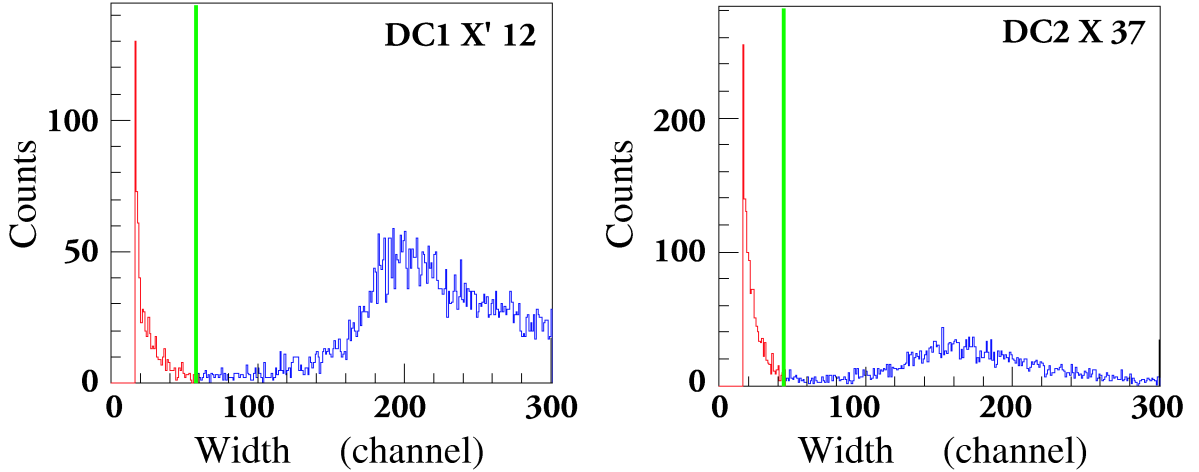


Figure 3.2: Threshold for DC widths. The hits with a short interval between the leading and trailing edges (width) corresponds to an electric noise. The cut points are shown in the line.

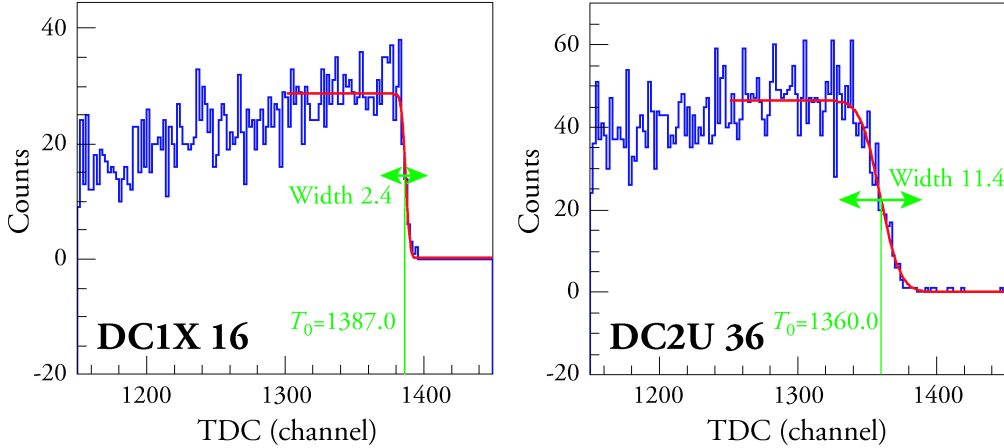


Figure 3.3: Zero timing T_0 . T_0 is determined by fitting with a Gaussian convoluted step function.

interest is that of DC1, otherwise the fitting is made with the positions at DC2 and DC3. The drift length is obtained by the fitting line as a function of t_{drift} for the plane of interest. The parameters $c_1^{(n+1)}$, $c_2^{(n+1)}$, and $c_3^{(n+1)}$ for the plane of interest are obtained by fitting with Eq. (3.7), and those for the other planes are determined in the same way.

The simulation code GARFIELD Ver. 5.10 [67] has been used to determine initial parameters $c_1^{(0)}$, $c_2^{(0)}$, and $c_3^{(0)}$. The supplied high voltage for the field wires were -2400 V, -2700 V, and -2700 V for DC1, DC2, and DC3, respectively. The -2000 V of high voltage is supplied for all the shield wires. The mixed gas of 70% argon and 30% isobutane was used. Figure 3.4 shows the contour of the electric potential and the drift line to the wire for electrons, which are obtained by the simulation. Figure 3.5 shows the relation between the drift length and the drift time for DC's obtained by the simulation. Figure 3.6 shows the relation between the drift length and the drift time in the real data.

The difference between the drift lengths predicted by the fitting line and translated from the drift time is called residual. Two kind of residuals are given whether the plane of interest is included or not on the straight line fitting in three dimensional space. The width of the residual distributions σ_{inc}

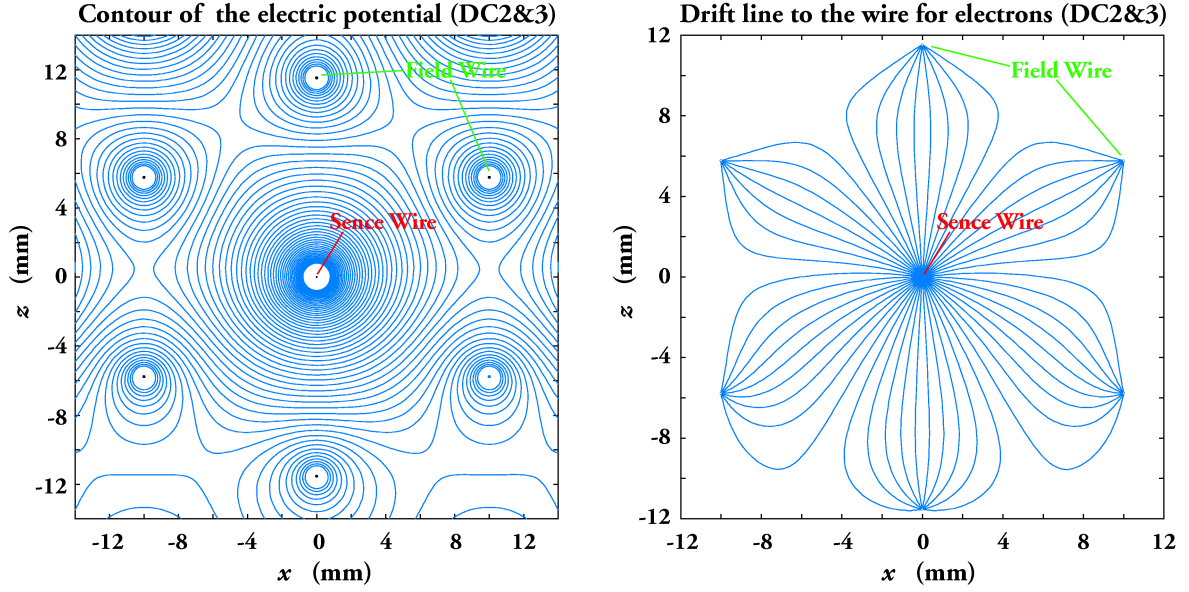


Figure 3.4: Contour of the potential and the drift line calculated by GARFIELD. The left panel shows the contour plot of the electric potential and the right one shows the drift line to the wire for electrons.

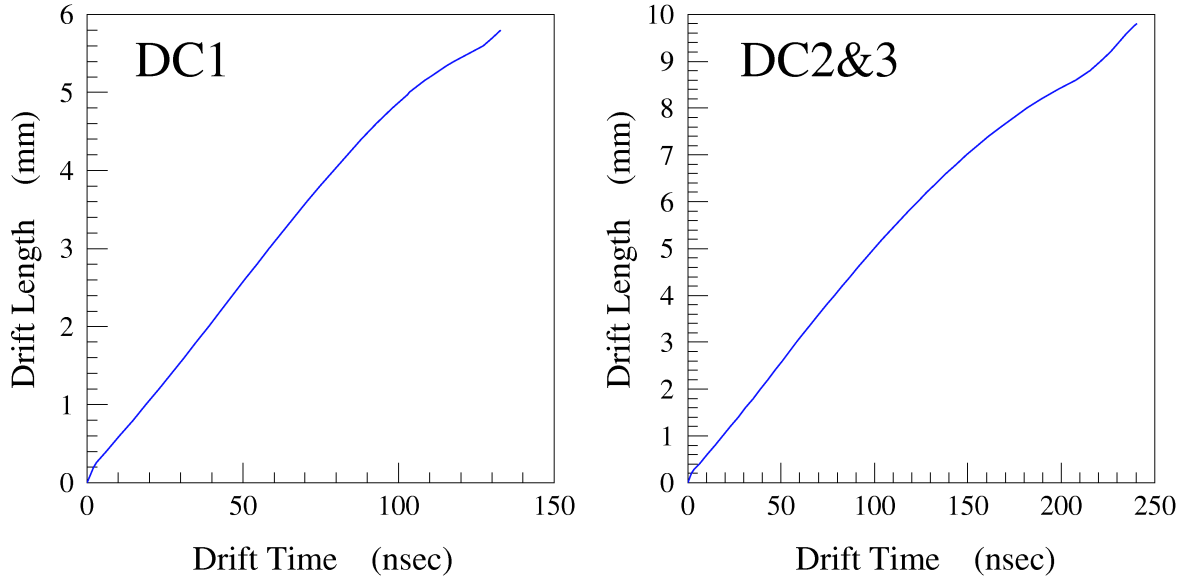


Figure 3.5: The relations between the drift length and the drift time calculated by GARFIELD. The left panel shows that of DC1, and the right one shows that of DC2 and DC3.

and σ_{exc} are determined for including the plane of interest and excluding it, respectively. Figure 3.7 shows the residual distributions. The σ_{inc} and σ_{exc} are found to be proportional to the intrinsic position resolution obtained by a simple simulation. In the simulation, the particles go along a line, and positions are measured at DC planes. The measured positions are smeared out according to the intrinsic resolution. The straight line fittings in three dimensional space are made with the measured positions, and the residual is obtained. Table 3.1 shows the factor of the intrinsic resolutions to the

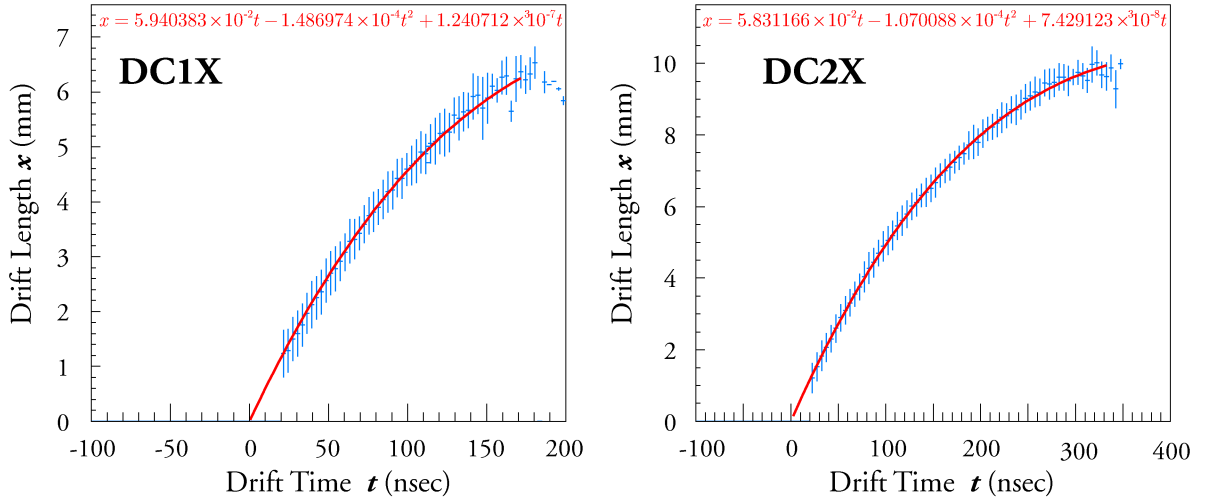


Figure 3.6: Relation between the drift length and the drift time. The drift length is obtained by the straight line fitting in three dimensional space.

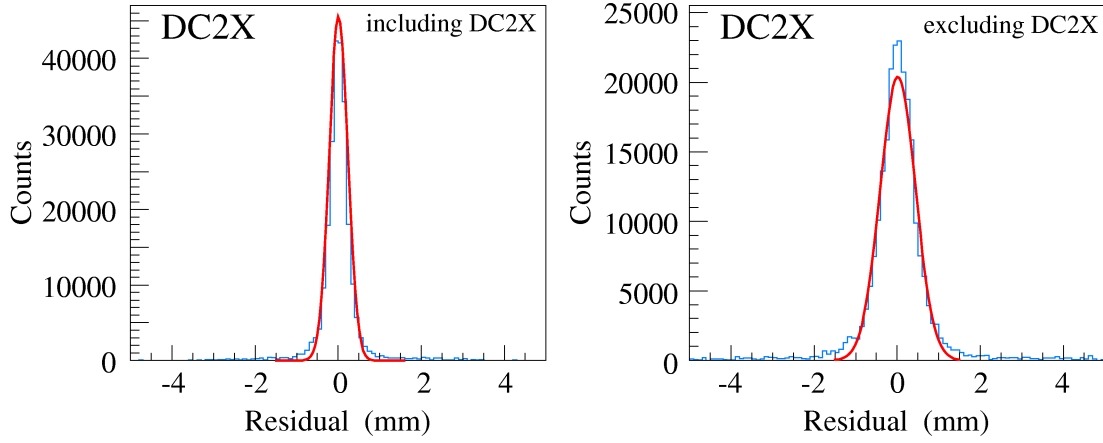


Figure 3.7: Residual distributions. The left and right panels show the residual distributions under the conditions that the plane of interest is included and excluded in the straight line fitting, respectively.

Table 3.1: Factors of the intrinsic resolutions to the residuals. The r_{inc} and r_{exc} denote the factor of the intrinsic resolutions to the residuals for the straight line fitting including and excluding the plane of interest.

	X	X'	U	U'	V	X''
$r_{\text{inc}}(\text{DC1})$	0.688	0.764	0.756	0.768	0.689	0.521
$r_{\text{inc}}(\text{DC2})$	0.726	0.701	0.718	0.688	0.559	—
$r_{\text{inc}}(\text{DC3})$	0.685	0.717	0.688	0.721	0.686	—
$r_{\text{exc}}(\text{DC1})$	1.424	1.278	1.300	1.282	1.430	1.920
$r_{\text{exc}}(\text{DC2})$	1.390	1.459	1.371	1.433	1.767	—
$r_{\text{exc}}(\text{DC3})$	1.421	1.362	1.432	1.374	1.392	—

residuals including and excluding the plane of interest r_{inc} and r_{exc} for each plane determined by the simulation, respectively. Thus, the intrinsic position resolution for each plane is determined as

$$\sigma = \frac{1}{2} \left(\frac{\sigma_{\text{inc}}}{r_{\text{inc}}} + \frac{\sigma_{\text{exc}}}{r_{\text{exc}}} \right). \quad (3.8)$$

Table 3.2 shows the intrinsic resolutions of drift chambers.

Table 3.2: Intrinsic resolutions of drift chambers.

	X	X'	U	U'	V	X''
DC1	0.191	0.192	0.180	0.176	0.219	0.207
DC2	0.215	0.213	0.241	0.242	0.503	—
DC3	0.232	0.232	0.250	0.240	0.435	—

3.3 Determination of the variables

3.3.1 Tracking

A trajectory of a charged particle is determined by hit positions at the silicon strip vertex detector (SVTX), the three drift chambers (DC1, DC2, and DC3), and the TOF wall counters. Since the DC3 does not cover all the aperture of the dipole magnet, the hit information of the TOF wall is used instead of DC3 in case that no hit information is found in DC3. The determining process of the trajectory is called as 'tracking'.

On the first stage of the tracking, clusters in each detector are searched. A cluster in SVTX is comprised of a hit in the x layer and one in the y layer. A cluster in DC1 is composed of more than four wires in the six planes of DC1, and that in DC2 and DC3 is composed of more than three wires in the five planes of DC2 and DC3. Each cluster in DC's does not include more than two hits in the same plane.

On the second stage, straight line fittings in three dimensional space are carried out upstream and downstream of the magnet separately. The hit information that each fired wire has is a drift distance, and an ambiguity exists whether the particle passes through in the left (up) side or the right (down) side. The side that the particle passes through is solved in this stage. The best 30 combinations of clusters are selected in each stream in terms of χ^2 . This combination of clusters in each stream is called 'track'.

On the third stage, the initial values for the Kalman filter method are determined. Among the combination of the upstream and downstream tracks, the consistency is required so that the projections of the upstream and downstream tracks crosses in the x - z plane, and that the slopes in the y - z plane dy/dz are not so different between the upstream and downstream tracks. The initial values of positions x , y and the directions dx/dz , dy/dz at SVTX are obtained from the upstream track, and those of momentum p and charge q are estimated by the bending radius at the cross point of the upstream and downstream tracks.

The final stage determines trajectories with the Kalman filter method that performs a least square fit to the measured hit positions including the effects of multiple scattering and energy loss. The background hits (outliers) are removed on this stage [66]. In the tracking analysis, the sign of the charge, the absolute momentum, the momentum vector, the path length from the target to the TOF wall, and vertex points are obtained

3.3.2 Time of flight

A time of flight T_{TOF} is described by the start time T_{START} and the stop time T_{STOP} as

$$T_{\text{TOF}} = T_{\text{STOP}} - T_{\text{START}} \quad (3.9)$$

The T_{STOP} is determined by the time of the TOF wall counters, and the T_{START} is determined by the RF signals instead of the start counter's to achieve high resolution for the time of flight measurement.

3.3.3 Mass

Mass of a charged particle m is determined with a momentum p , a path length L , and a time of flight T_{TOF} as

$$m^2 = E^2 - p^2 = p^2 \left\{ \left(\frac{E}{p} \right)^2 - 1 \right\} = p^2 \left(\frac{1}{\beta^2} - 1 \right), \quad (3.10)$$

where β is a velocity of the particle in unit of the speed of the light as

$$\beta = \frac{L/T_{\text{TOF}}}{c} \quad (3.11)$$

3.4 Event Selection

The various cuts that were used to select the $\phi \rightarrow K^+K^-$ events are discussed.

3.4.1 Good buffers

In the experiment, serious troubles of the data taking system have happened, and only the good buffers are used. The confirmation of good buffers is described in Appendix G.1.

3.4.2 Number of tracks

The number of charged particles was required to be larger than 1 to select the $\phi \rightarrow K^+K^-$ events. Table 3.3 shows the number of tracks for each target,

Table 3.3: Number of the tracks

#Tracks	Li		C		Al		Cu	
	Vert.	Horz.	Vert.	Horz.	Vert.	Horz.	Vert.	Horz.
0	507713	385784	645325	405656	900796	824051	1152587	1485740
1	2093165	1685429	2711223	1856318	3569146	3731602	6691196	5898745
2	77038	62848	91483	62847	112137	114199	181200	157175
3	1866	1421	2059	1309	2373	2234	3537	2734
4	20	23	35	16	34	26	40	54
Sum	2679802	2135505	3450125	2326146	4584486	4672112	8028560	7544448

3.4.3 Particle identification

Particle identification was made by the reconstructed mass. The mass resolution was momentum dependent, and parameterized as

$$\sigma_{m^2}^2 = 4m^4 \left(1 + \left(\frac{m}{p} \right)^2 \right) a_1^2 + 4m^4 p^2 a_2^2 + 4p^2 (p^2 + m^2) \left(\frac{c}{L} a_3 \right)^2, \quad (3.12)$$

where a_1 , a_2 , and a_3 are parameters, m is the nominal value of the mass, and c is the speed of light, p is measured momentum, and L is the path length between the start counter and the TOF wall. The first and second terms in Eq. (3.12) correspond to the measured momentum resolution as

$$\left(\frac{\sigma_{p^2}}{p} \right) = \frac{a_1^2}{\beta^2} + p^2 a_2^2. \quad (3.13)$$

The first term in Eq. (3.13) shows the contribution of the multiple scattering, and the second one shows the momentum analysis resolution of the spectrometer. The last term in Eq. (3.12) shows the timing resolution of the time of flight measurement. Figure 3.8 shows the resolution of the mass square for the proton. The resolution of the mass square was determined by the width of a Gaussian function fitted to the measured mass square distribution. Red lines show the parameterization in Eq. (3.12) with the resolutions of the detector systems, which reproduces the measured one as well. Here L is fixed to 4100 mm. Figure 3.9 shows measured mass square of the proton, which the corrections of the flight length and the energy deposit at the scintillator of the TOF wall have been applied, together with the lines of the particle data group (PDG) value for the proton mass square [49]. In the low momentum regions, the measured mass squares are smaller than the nominal value. In the case that the ADC of the top or bottom side in the TOF wall counters is saturated, the timing of the TOF counters are not estimated correctly due to the wrong pulse height corrections. Figure 3.10 shows

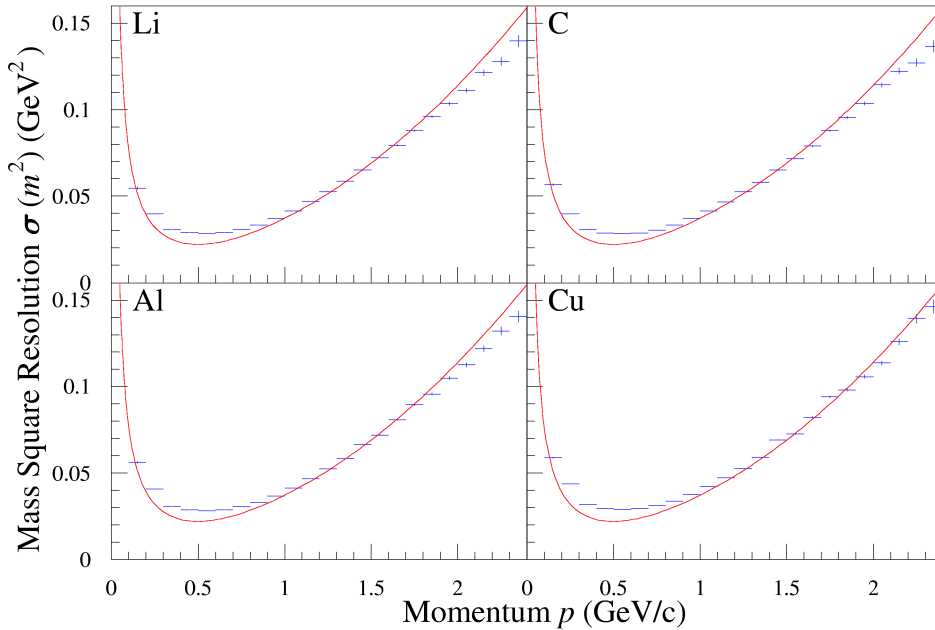


Figure 3.8: Momentum dependence of mass square resolution for the proton. The red lines show the estimated mass square resolution with the parameterization in Eq. (3.12).

the mass square of the proton for the ADC non-saturated events, and there are no dips in the low momentum region.

Kaons were identified within 4σ of the mass resolution, which was momentum dependent and is about 30 MeV for kaons with momentum of 1 GeV. Figure 3.11 shows two dimensional plot

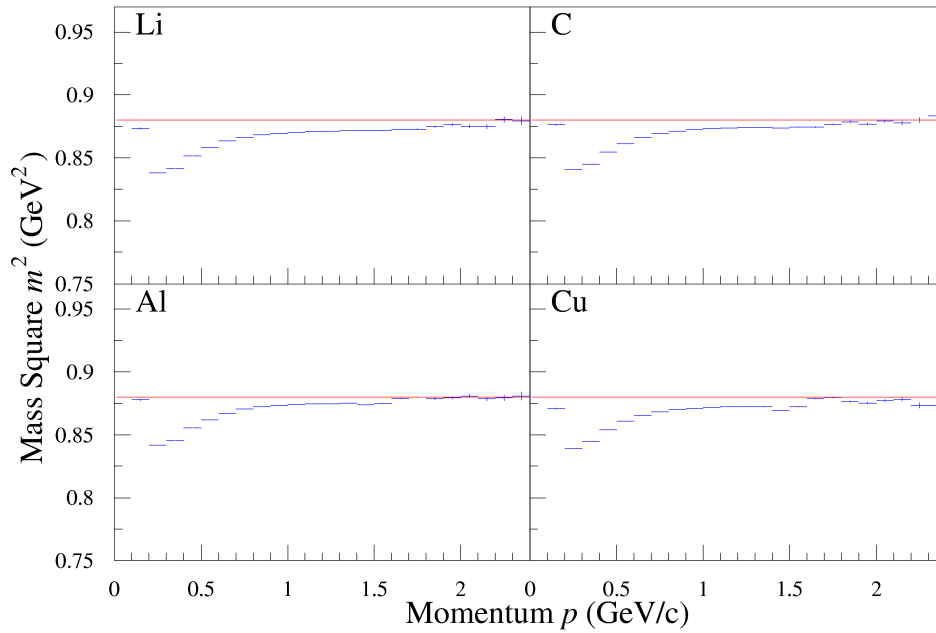


Figure 3.9: Momentum dependence of mass square for the proton. The red lines show the nominal mass square of the proton.

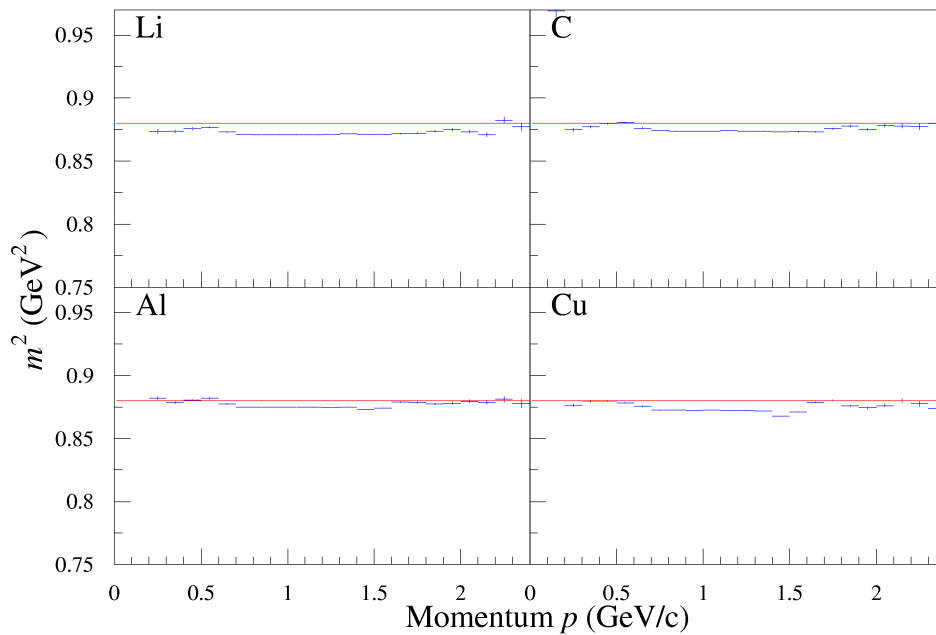


Figure 3.10: Momentum dependence of mass square for the ADC non-saturated events. The red lines are same as Figure 3.9.

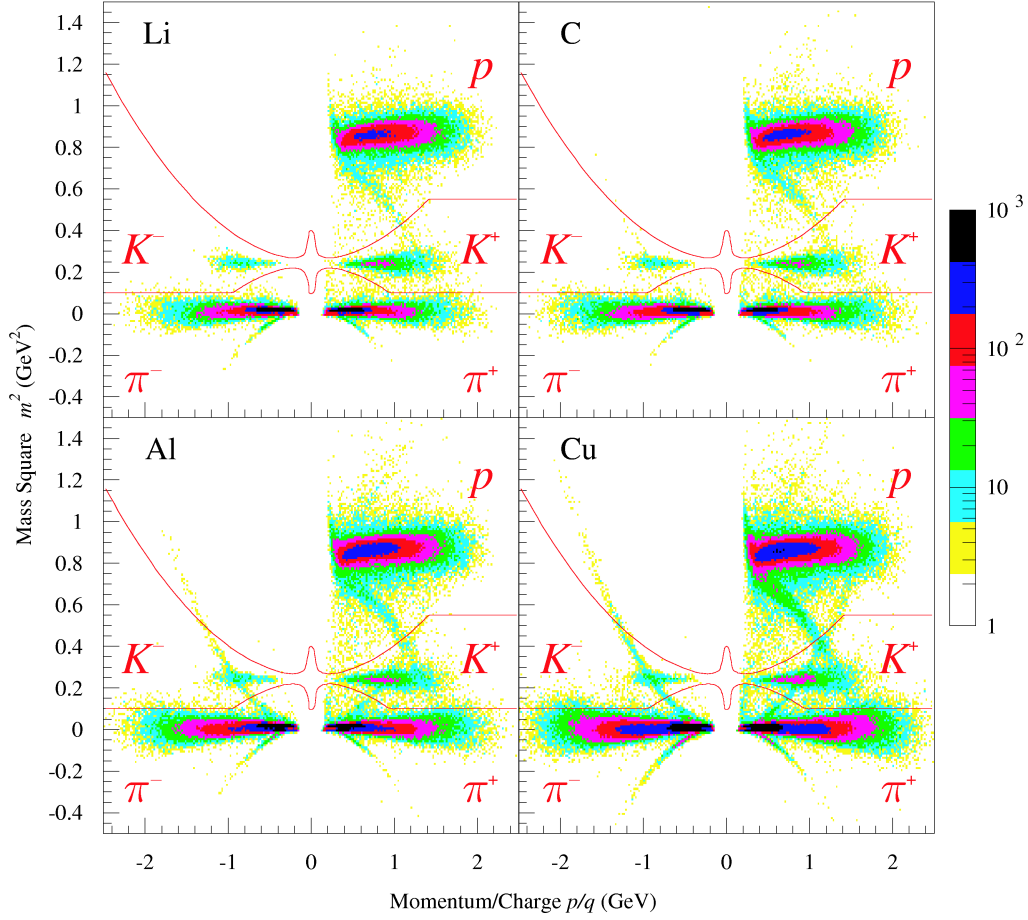


Figure 3.11: Particle identification. The boundaries for kaon identifications are shown in the red lines

between measured mass square m^2 and measured momentum divided by charge p/q together with kaon identification boundaries. The inclined loci correspond to the accidental coincidence with the charged particles associate with successive RF bunches. The time of flight of these particles are mis-measured by 1.966 nsec. When the events in which the number of tracks are larger than 1 are selected, these loci disappear as shown in Figure 3.12. The proton accidental coincidence tracks are still observed in heavier targets, but contamination of these tracks appear in the higher momentum than that of charged kaons decaying from ϕ mesons as discussed in Appendix C.1.1. The difference between the measured and nominal mass squares in the low momentum region does not affect the acceptance of the particle identification. It is because the energy loss of a kaon in the TOF counters is basically smaller than that of a proton. It is also because the difference of the mass square is smaller

Table 3.4: Number of the events after the particle identification cut.

#Tracks	Li		C		Al		Cu	
	Vert.	Horz.	Vert.	Horz.	Vert.	Horz.	Vert.	Horz.
2	489	428	457	346	413	469	467	456
3	16	18	20	10	16	14	20	15
4	0	0	1	0	0	0	0	0
Sum	505	446	478	356	429	483	487	471

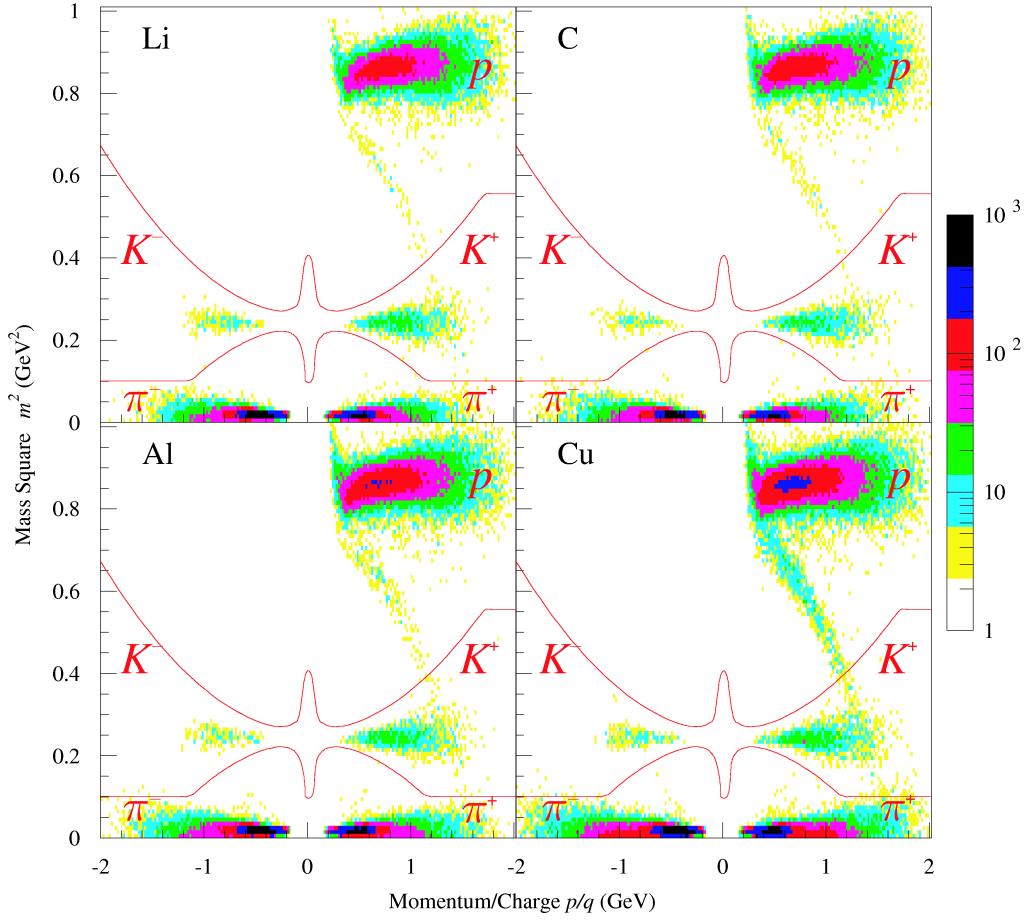


Figure 3.12: Particle identification for two track events. The boundaries for kaon identifications are shown in the red lines

than the twice of the resolution in the low momentum region even for the proton.

The condition where at least one K^+ and one K^- should exist is required. Table 3.4 shows the number of events which survived after the particle identification cut.

3.4.4 Good tracks

Three conditions are required for a good track described below.

High χ^2 probability

The χ^2 probability is used to select good tracks to eliminate background events. The χ^2 probability is defined as

$$\text{Prob}(\chi^2, \text{ndf}) = \int_{\chi^2}^{\infty} f(\chi'^2, \text{ndf}) d\chi'^2, \quad (3.14)$$

where f is the standard χ^2 distribution with a number of degree of freedom ndf. A χ^2 probability higher than 0.02 is required for a good track.

Consistency of the hit position at the TOF counter

It is required that a fired TOF counter corresponding to the track exists, that the counter is the same or adjacent ones predicted by the tracking, and that the difference between y positions measured by the TOF counter and predicted by the tracking is less than 80 mm.

Number of outliers

In the case that χ^2 probability becomes higher when a hit is removed from the track, the hit is judged as a background hit (outlier). Number of outliers in processing Kalman filter method is required to be less than 7.

The following conditions are the summary of the requirements for a good track

- χ^2 probability is higher than 0.02,
- a fired TOF counter corresponding to the track exists,
- a fired TOF counter is the same or adjacent ones predicted by the tracking,
- the difference between y positions measured by the TOF counter and predicted by the tracking is less than 80 mm, and
- number of outliers is less than 7.

The events that had at least one good K^+ and one good K^- tracks were selected, and this cut removes decaying K^+ and K^- tracks in flight.

Table 3.5 shows that the number of events which survived after the good track cut.

Table 3.5: Number of the events after the good track cut.

#Tracks	Li		C		Al		Cu	
	Vert.	Horz.	Vert.	Horz.	Vert.	Horz.	Vert.	Horz.
2	300	255	257	209	235	270	267	254
3	10	11	6	3	7	4	10	9
Sum	310	266	263	212	242	274	277	263

3.4.5 Closest distance

The K^+K^- tracks decaying from ϕ mesons should come to a point, namely closest distance of them should be zero. The calculated closest distance from the tracking information is not always zero due to the finite tracking resolution, the effect of multiple scattering, and so on. Figure 3.13 shows the closest distance distribution of the K^+K^- tracks decaying from ϕ meson in the Monte Carlo simulation (MC) data. Almost all the events concentrated around the closest distance of 0 mm, yet few events were scattered in the larger region. Figure 3.14 shows the closest distance distribution for each target in the real data.

In order to discard the K^+K^- tracks that are not originated from a point, the closest distance of these is required to be less than 5 mm. Although the calculated closest distance of the K^+K^- tracks decaying from ϕ mesons in the MC simulation can have larger values. A few events that the K^+K^- tracks comes from one vertex point do not pass this closest distance cut, yet this cut kill the almost no K^+K^- tracks decayed from ϕ mesons. Table 3.6 shows number of events after the closet distance cut is applied.

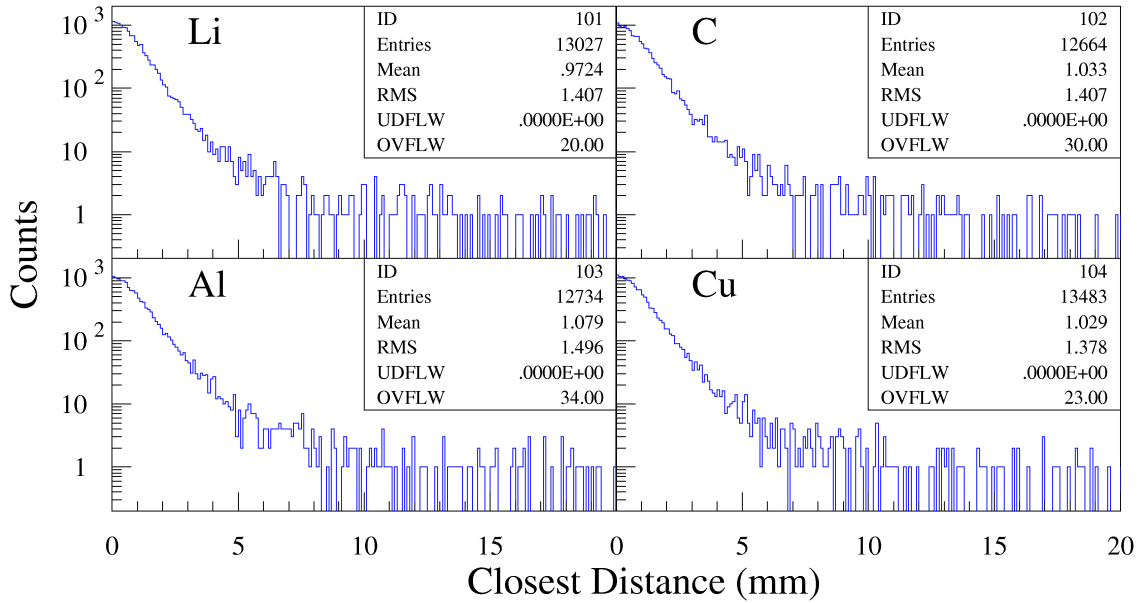


Figure 3.13: Closest distance distributions of K^+K^- tracks in the MC simulation. Events concentrate at 0 mm in the closest distance distributions.

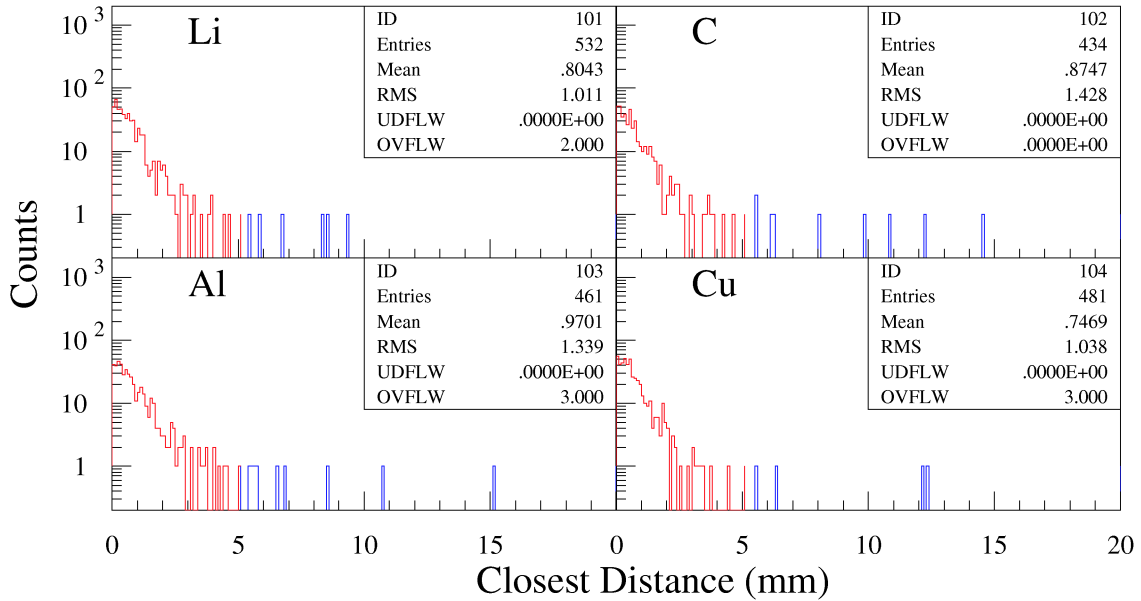


Figure 3.14: Closest distance distributions for K^+K^- tracks in the real data. Measured closest distance distributions are similar to those in the MC simulation.

3.4.6 Vertex

Because the full width of ϕ meson is a few MeV, it decays during tens of fm flight, and the vertex point of K^+K^- tracks can be treated as the same as the produced point of ϕ meson. The vertex points should be in the target volume except for smearing out by the finite resolution.

Figure 3.15 shows z coordinate of the vertex position (z -vertex) for the K^+K^- tracks. Li target

Table 3.6: Number of events after the closest distance cut.

#Tracks	Li		C		Al		Cu	
	Vert.	Horz.	Vert.	Horz.	Vert.	Horz.	Vert.	Horz.
2	298	249	249	203	226	262	257	249
3	10	10	6	3	7	4	10	9
Sum	308	259	255	206	233	266	267	258

consists of one block, and C, Al, and Cu targets are divided into three sheets and each sheet was placed every 35 mm spacing in z coordinate so that the center and standard deviation of target volume in z coordinate should be the same shown in Figure 2.12. In order to discard the events from the start counter, z -vertex is required as

$$\begin{aligned}
 -990. \leq z < -863. & \text{ for Li} \\
 -990. \leq z < -872. & \text{ for C, Al, and Cu.}
 \end{aligned}
 \tag{3.15}$$

Each boundary of upstream side is determined so that this cut should not kill the events whose z -vertex is smeared out by the resolution, and that of downstream side is determined to be center between downstream edge of the downstream sheet of the target and upstream edge of the start counter (a common boundary is adopted for C, Al, and Cu). Small opening angle events have poor resolution on z -vertex, the survived events after this cut can be contaminated by the events from the start counter. The estimation of the contamination is discussed in Subsection 3.6.1. Table 3.7 shows

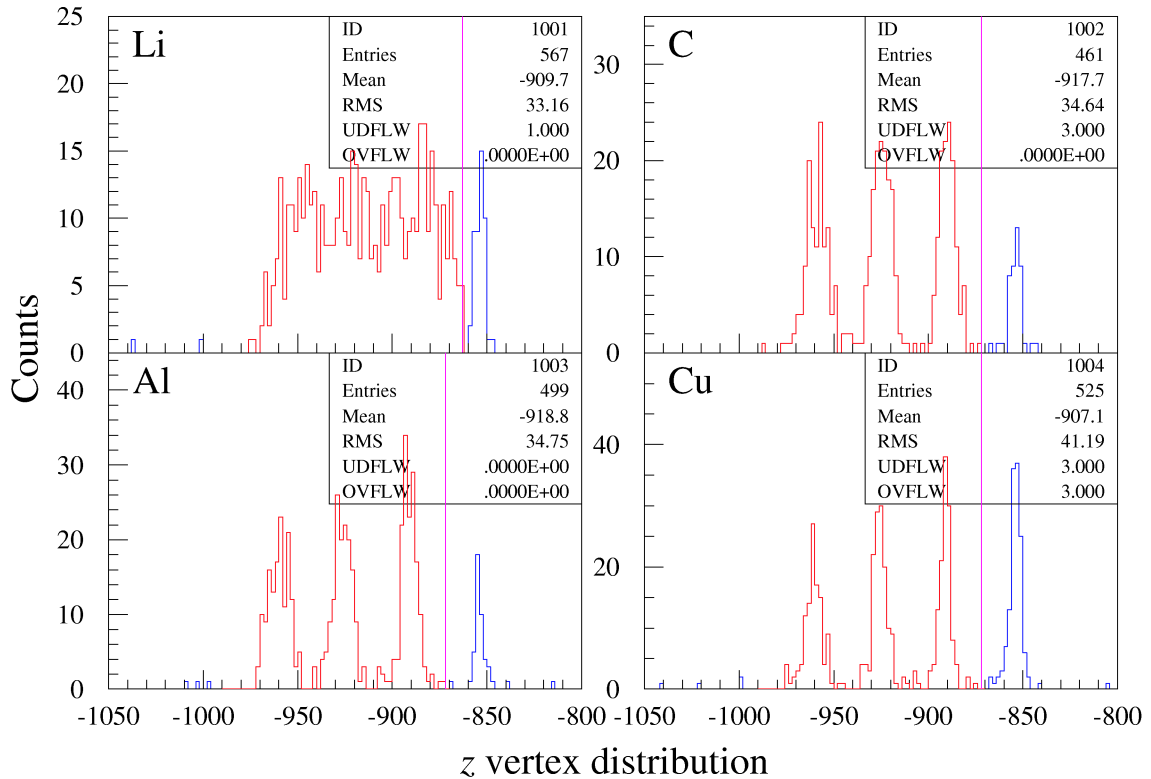


Figure 3.15: z -vertex distribution of the K^+K^- tracks. The events associate with the target and the start counter are separated clearly.

the number of events after the z -vertex cut is applied. Figure 3.16 shows the (x, y) coordinate of the

Table 3.7: Number of the events after z -vertex cut

#Tracks	Li		C		Al		Cu	
	Vert.	Horz.	Vert.	Horz.	Vert.	Horz.	Vert.	Horz.
2	267	232	223	182	204	239	190	176
3	8	101	6	1	5	3	5	7
Sum	275	242	229	183	209	242	195	183

vertex position after the z -vertex cut is applied where red rectangles show the target size. In order to discard the events that come from other than target, x and y vertex is required as

$$\begin{aligned}
 -20. \leq x < +20., \quad -15. \leq y < +15. \quad \text{for Li} \\
 -25. \leq x < +25., \quad -25. \leq y < +25. \quad \text{for C, Al, and Cu.}
 \end{aligned}
 \tag{3.16}$$

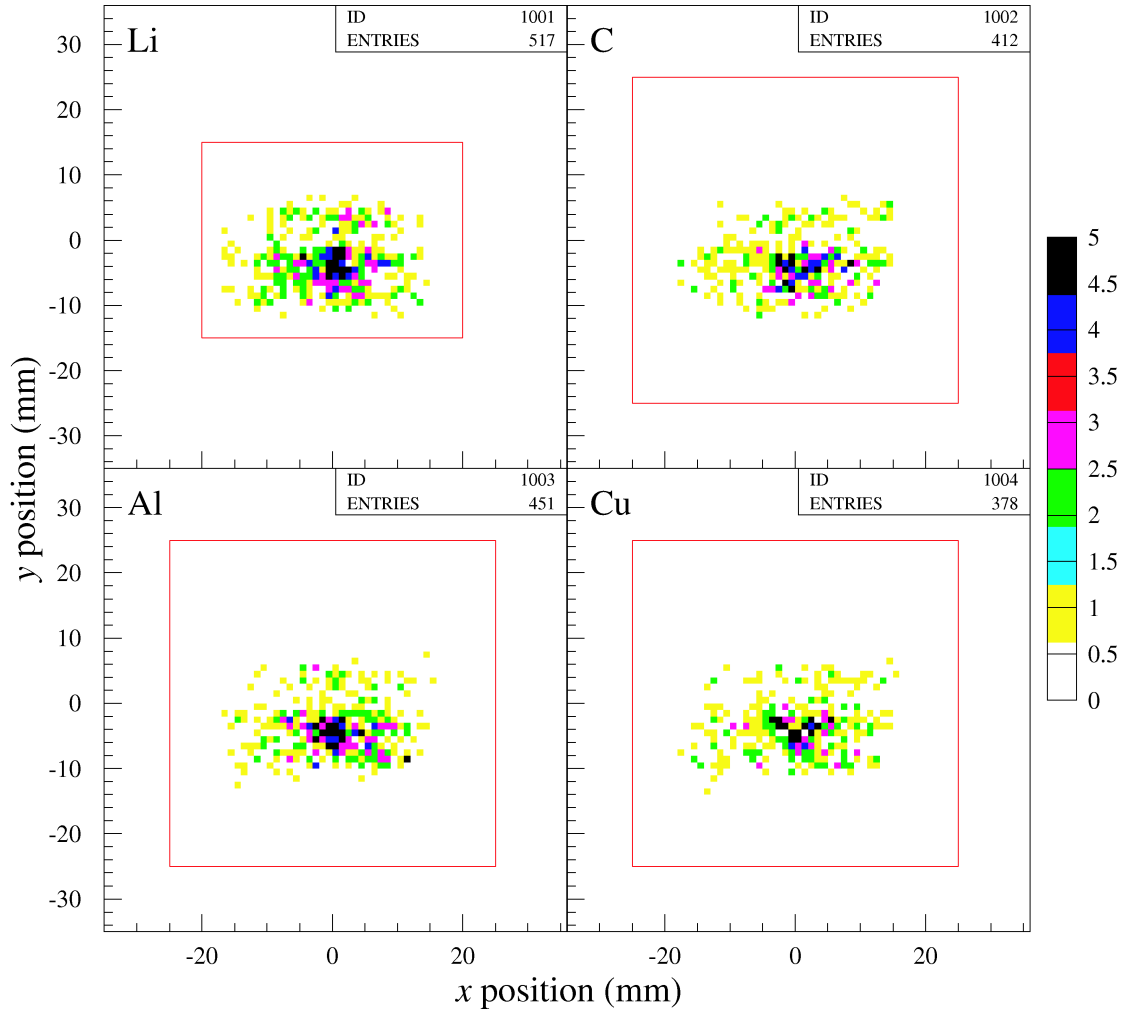


Figure 3.16: (x, y) -vertex distribution of the K^+K^- tracks. All the events are within the target region.

Table 3.8 shows the number of events after x and y vertex cut is applied (No event comes from other than target area).

Table 3.8: Number of the events after x and y vertex cut

#Tracks	Li		C		Al		Cu	
	Vert.	Horz.	Vert.	Horz.	Vert.	Horz.	Vert.	Horz.
2	267	232	223	182	204	239	190	176
3	8	101	6	1	5	3	5	7
Sum	275	242	229	183	209	242	195	183

3.4.7 Invariant mass

The events of ϕ photo-production are identified by the K^+K^- invariant mass distribution. Since momenta of kaons were measured, K^+K^- invariant mass $m_{K^+K^-}$ is described as

$$m_{K^+K^-}^2 = \left(\sqrt{(m_{K^+})^2 + |\vec{p}_{K^+}|^2} + \sqrt{(m_{K^-})^2 + |\vec{p}_{K^-}|^2} \right)^2 - |\vec{p}_{K^+} + \vec{p}_{K^-}|^2. \quad (3.17)$$

where m_K stands for the kaon mass (0.493677 GeV [49]), p_{K^+} and p_{K^-} are the measured K^+ and K^- momenta with a energy loss correction, respectively. Figure 3.17 shows the K^+K^- invariant mass distributions.

The cut condition $1005 \leq m_{K^+K^-} < 1035$ MeV is required for the K^+K^- invariant mass. Note that the mass and width of the ϕ meson in free space is 1019.456 ± 0.020 MeV and 4.26 ± 0.05 MeV,

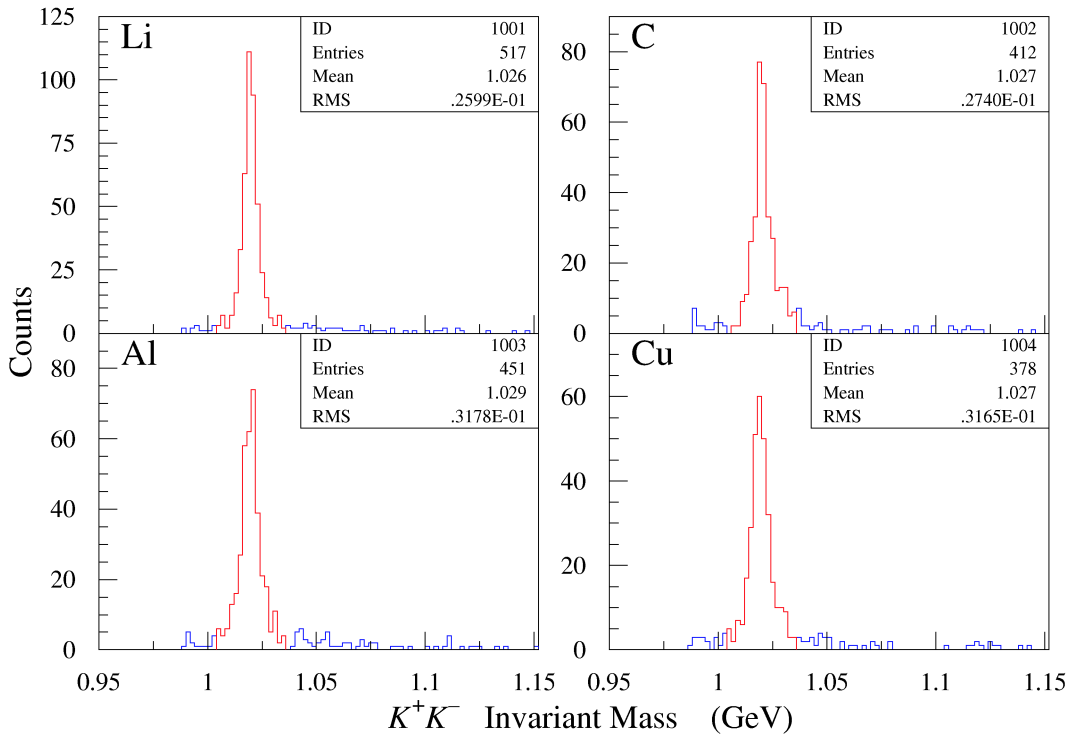


Figure 3.17: K^+K^- invariant mass distributions. The ϕ meson peaks are observed clearly.

respectively [49].

Table 3.9 shows the number of events after the invariant mass cut is applied.

Table 3.9: Number of the events after the invariant mass cut

#Tracks	Li		C		Al		Cu	
	Vert.	Horz.	Vert.	Horz.	Vert.	Horz.	Vert.	Horz.
2	229	197	182	148	165	191	157	143
3	6	8	2	1	3	1	3	5
Sum	235	205	184	149	168	192	160	148

3.4.8 Tagger hit

When the number of tagger hits are greater than 1, some treatment is needed to determine incident γ energies. As for the events with two tagger hits, if two measured γ energies are close, the incident γ energy E_γ can be determined just averaging as

$$E_\gamma = \frac{1}{2}(E_\gamma^{(1)} + E_\gamma^{(2)}), \quad (3.18)$$

where $E_\gamma^{(1)}$ and $E_\gamma^{(2)}$ are the incident γ energy candidates corresponding to the first and second tagger hits. If the target is a proton at rest, E_γ can be calculated analytically from the K^+K^- track

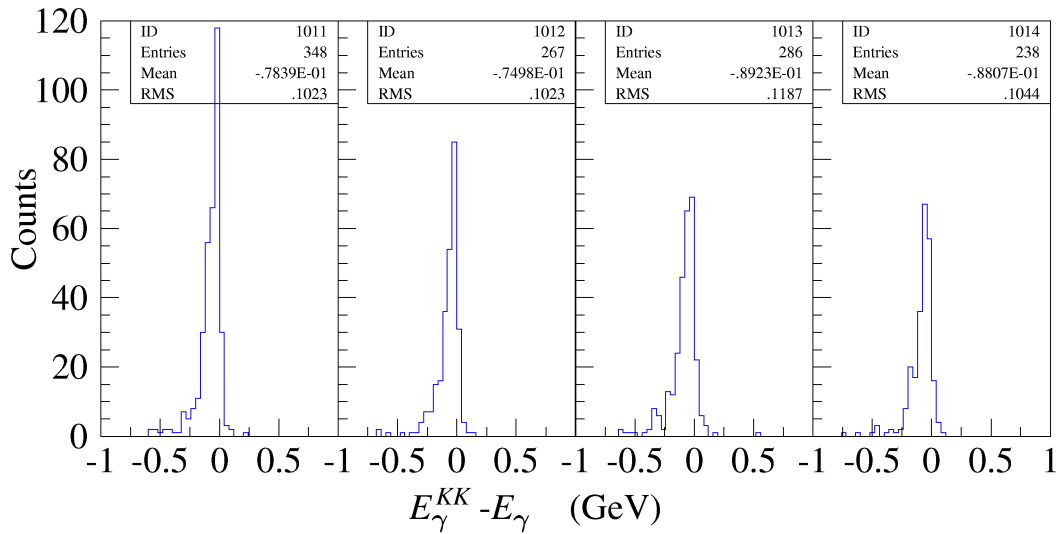


Figure 3.18: Difference between E_γ and E_γ^{KK}

information assuming elastic ϕ photo-production on the proton at rest as

$$E_\gamma^{KK} = \frac{2m_p E_{KK} - m_{KK}^2}{2(m_p - E_{KK} + p_z^{KK})}, \quad (3.19)$$

where m_p is a proton mass, and m_{KK} , E_{KK} , and p_z^{KK} stand for invariant mass, total energy, and z -component of the momentum for K^+K^- system. Figure 3.18 shows the difference between measured E_γ and calculated E_γ^{KK} for single tagger hit events. The r.m.s. of the $|E_\gamma^{KK} - E_\gamma|$ distributions are

0.077, 0.075, 0.090, and 0.091 for each nuclear target. The distributions have larger width (r.m.s. ~ 0.08 GeV/c), this is because the target is not a proton at rest and the calculated E_{γ}^{KK} is smeared due to the Fermi motion. While Figure 3.19 shows the difference of two measured γ energies for the two

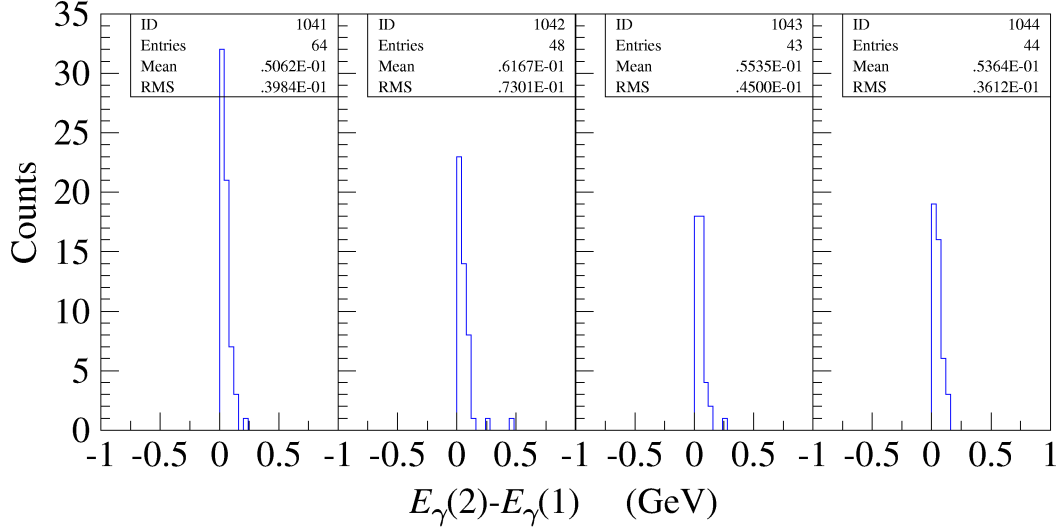


Figure 3.19: Difference of measured γ energies

tagger hit events. The r.m.s. of the $\left|E_{\gamma}^{(2)} - \frac{1}{2}(E_{\gamma}^{(1)} + E_{\gamma}^{(2)})\right|$ or $\left|E_{\gamma}^{(1)} - \frac{1}{2}(E_{\gamma}^{(1)} + E_{\gamma}^{(2)})\right|$ distributions are 0.038, 0.037, 0.045, and 0.046 for each nuclear target. The number of tagger hits for $\phi \rightarrow K^+K^-$

Table 3.10: Number of tagger hits for $\phi \rightarrow K^+K^-$ events.

#Tagger Hits	${}^6\text{Li}$ +start counter	C+start counter	Al+start counter	Cu+start counter
0	25 (5.3 \pm 1.0%)	18 (4.8 \pm 1.1%)	25 (6.3 \pm 1.2%)	28 (6.7 \pm 1.2%)
1	374 (78.6 \pm 1.9%)	296(79.4 \pm 2.1%)	317(79.6 \pm 2.0%)	327 (78.6 \pm 2.0%)
2 ($\Delta E_{\gamma} < 0.2$)	69 (14.5 \pm 1.6%)	51(13.7 \pm 1.8%)	47(11.8 \pm 1.6%)	54 (13.0 \pm 1.6%)
others	8 (1.7 \pm 0.6%)	8 (2.1 \pm 0.8%)	9 (2.3 \pm 0.7%)	7 (1.7 \pm 0.6%)
Sum	476	373	398	416

events without the vertex cuts are shown in Table 3.4.8. The fraction of single tagger hit events is the same for each target. In order to obtain good resolution on missing mass or t value, only single tagger hit events were selected. Table 3.11 shows the number of events after the tagger hit cut is applied.

Table 3.11: Number of the events after the tagger hit cut

#Tracks	Li		C		Al		Cu	
	Vert.	Horz.	Vert.	Horz.	Vert.	Horz.	Vert.	Horz.
2	184	154	143	122	135	148	122	111
3	4	6	2	0	2	1	1	4
Sum	188	160	145	122	137	149	123	115

3.4.9 Cut statistics

Table 3.12 shows the number of events after the various cuts discussed above have been applied together with rejection factors. The rejection factor is defined as

$$\text{Rejection Factor} = \frac{\# \text{Events Before the Cut}}{\# \text{Events After the Cut}} \quad (3.20)$$

All the cuts discussed in this section is called as standard ϕ cut.

Table 3.12: Cut statistics. Each cell shows the number of survived events in the cut together with the rejection factor in the parentheses.

Cut	Li		C		Al		Cu	
	Vert.	Horz.	Vert.	Horz.	Vert.	Horz.	Vert.	Horz.
Hadron Trigger	4508781	3540759	6021008	3934454	8767596	8395717	15260359	12536868
Analyzed	2679802	2135505	3450125	2326146	4584486	4641570	8028560	7544448
	(1.68)	(1.66)	(1.75)	(1.69)	(1.91)	(1.81)	(1.90)	(1.66)
Particle Identification	505	446	478	356	429	483	487	471
	(5310)	(4790)	(7220)	(6530)	(10690)	(9610)	(16490)	(16020)
Good Track	310	266	263	212	242	274	277	263
	(1.63)	(1.68)	(1.82)	(1.68)	(1.77)	(1.76)	(1.76)	(1.79)
Closest Distance	308	259	255	206	233	266	267	258
	(1.01)	(1.03)	(1.03)	(1.03)	(1.04)	(1.03)	(1.04)	(1.02)
z -vertex	275	242	229	183	209	242	195	183
	(1.12)	(1.07)	(1.11)	(1.13)	(1.11)	(1.10)	(1.37)	(1.41)
(x, y) -vertex	275	242	229	183	209	242	195	183
	(1.00)	(1.00)	(1.00)	(1.00)	(1.00)	(1.00)	(1.00)	(1.00)
Invariant Mass	235	205	184	149	168	192	160	148
	(1.17)	(1.18)	(1.25)	(1.23)	(1.24)	(1.26)	(1.22)	(1.24)
Tagger Hit	188	160	145	122	137	149	123	115
	(1.25)	(1.28)	(1.27)	(1.22)	(1.23)	(1.20)	(1.30)	(1.29)
Analyzed ϕ Events	188	160	145	122	137	149	123	115

3.5 Observed ϕ mesons

3.5.1 Mass and width

The mass and width of ϕ meson is determined from the K^+K^- invariant mass shown in Figure 3.17. The clear ϕ meson peaks are observed for all the targets at 1.02 GeV/ c^2 with small number of background events. The shape of these background distributions is assumed to be the same as the KK invariant mass distribution for non-resonant KK production, which is calculated in the Monte Carlo simulation for the three body phase space of the reaction $\gamma N \rightarrow K^+K^-N$. Figure 3.20 shows the KK invariant mass distribution for the non-resonant KK production. The fitting by means of the maximum likelihood method [69] with a sum of a Voigt function, or a Gaussian convoluted Breit-Wigner (Lorentzian) function, and the non-resonant K^+K^- background distribution is made. The fitting function is described as

$$M(x) = cV(x) + bB(x) = c\Gamma/2 \int_0^\infty \exp(-at^2 - \beta t) \cos \gamma t \, dt + bB(x), \quad (3.21)$$

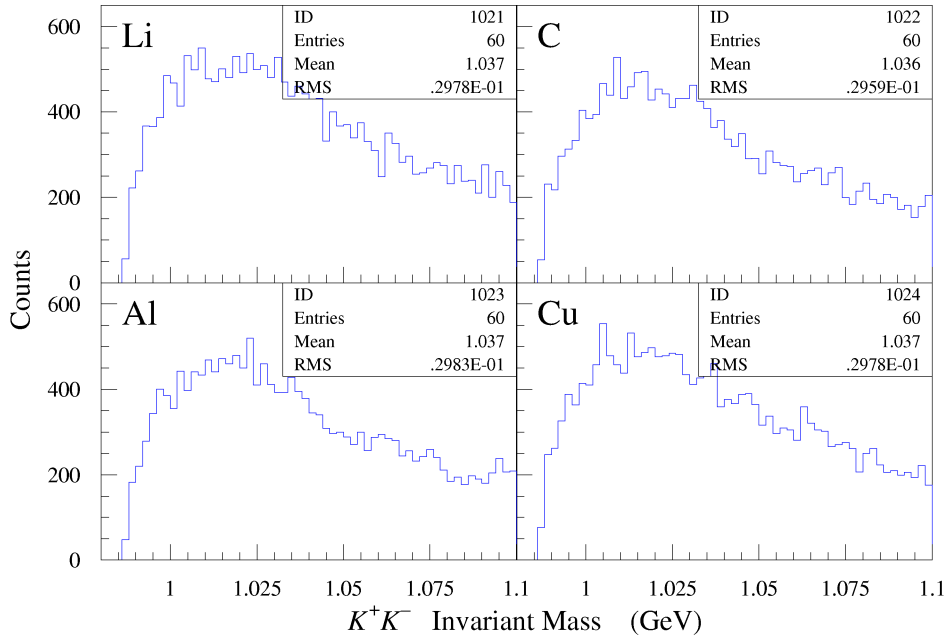


Figure 3.20: K^+K^- invariant mass distributions for non-resonant K^+K^- production in the MC simulation

where $\alpha = \sigma^2/2$, $\beta = \Gamma/2$, and $\gamma = \mu_G + \mu_L - x = m - x$ discussed in Appendix G.2, and the full width of ϕ meson Γ is fixed to be the PDG value of 4.26 MeV [49]. $B(x)$ stands for KK invariant

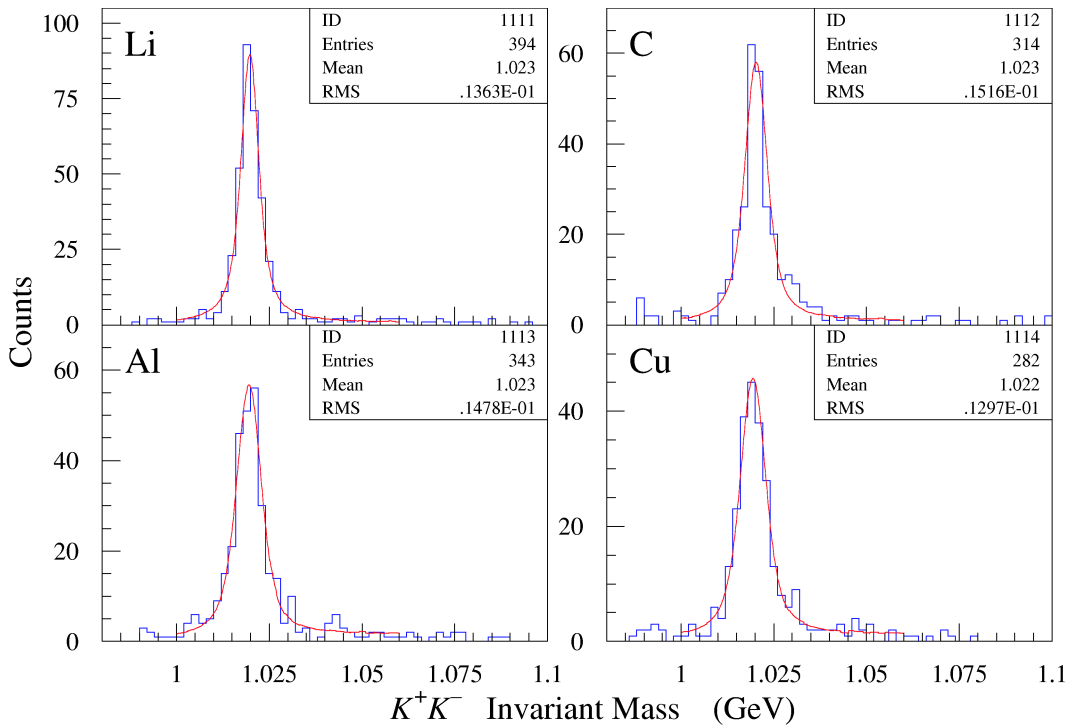
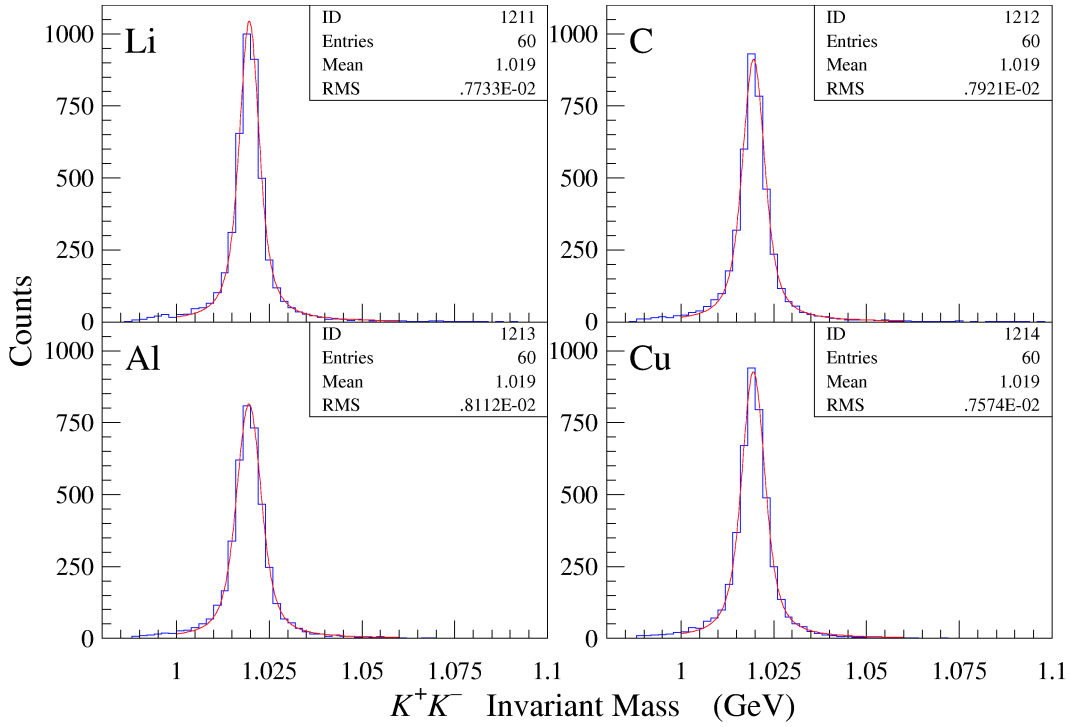


Figure 3.21: Fitting with σ as a free parameter in the real data

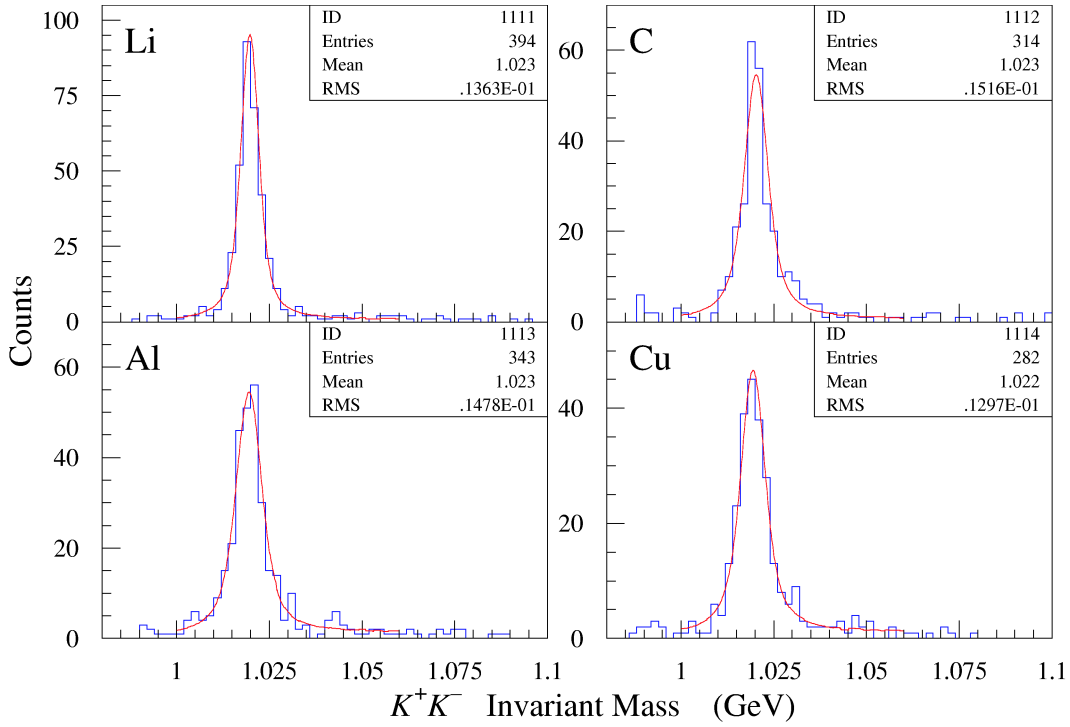
Figure 3.22: Fitting with σ as a free parameter in the MC simulation

mass distribution for the non-resonant K^+K^- production. The fitting region is between 1.00 and 1.06 GeV/c^2 . Figures 3.21, 3.22 show K^+K^- invariant mass distributions with the standard cut except for the invariant mass one in the real data, and in the MC simulation, respectively. Table 3.13 shows the fitting results. The centroid m and Gaussian width σ (resolution) is consistent for each

Table 3.13: Comparison of the fitting parameters with σ as a free one

Target	c	m	σ	b
Li (real)	110.6 ± 6.3	1.0197 ± 0.0002	0.0013 ± 0.0004	0.0015 ± 0.0006
C (real)	84.0 ± 5.8	1.0201 ± 0.0003	0.0020 ± 0.0005	0.0019 ± 0.0008
Al (real)	87.9 ± 5.9	1.0195 ± 0.0003	0.0023 ± 0.0004	0.0034 ± 0.0009
Cu (real)	72.6 ± 5.4	1.0193 ± 0.0003	0.0024 ± 0.0004	0.0026 ± 0.0008
Li (MC)	$140.7 \pm 3.1 \times 10^{+1}$	1.0195 ± 0.0001	0.0016 ± 0.0001	0.0000 ± 0.0005
C (MC)	$133.2 \pm 2.3 \times 10^{+1}$	1.0195 ± 0.0001	0.0019 ± 0.0001	0.0000 ± 0.0008
Al (MC)	$129.1 \pm 2.8 \times 10^{+1}$	1.0194 ± 0.0001	0.0023 ± 0.0001	0.0000 ± 0.0006
Cu (MC)	$139.8 \pm 2.1 \times 10^{+1}$	1.0194 ± 0.0001	0.0021 ± 0.0001	0.0000 ± 0.0004

target between the real data and the MC simulation. The differences of Gaussian widths σ for different targets are thought to be explained by multiple scattering in the target material and so on, and are reproduced very well in the MC simulation. Treating Γ as a free parameter instead of σ provides an important test. The fitting is also made under the condition that the resolution Gaussian width σ is fixed to be the predicted values 1.6, 1.9, 2.3, and 2.1 MeV for Li, C, Al, and Cu, respectively, which are obtained by the previous fitting to the MC simulation. In this case, the full width of ϕ meson Γ is a free parameter. The fitting results of the natural width Γ are 3.4 ± 0.4 , 5.0 ± 0.7 , 4.9 ± 0.8 , and

Figure 3.23: Fitting with Γ as a free parameter in the real data

4.9 ± 0.8 MeV for Li, C, Al, and Cu, respectively. The values of the mass and width are consistent with the nominal mass and full width of ϕ meson in free space within error bars¹. No significant

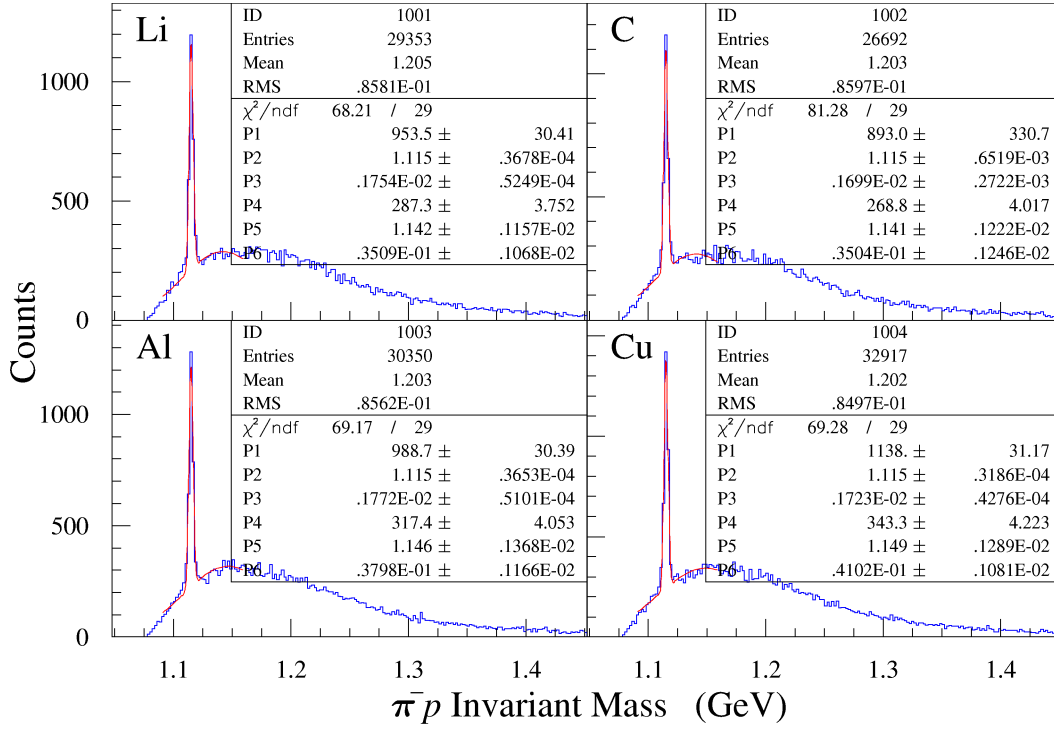
Table 3.14: Fitting parameters with Γ as a free parameter

Target	c	m	Γ	b
Li (real)	139.5 ± 15.9	1.0197 ± 0.0002	0.0034 ± 0.0004	0.0015 ± 0.0007
C (real)	73.7 ± 9.6	1.0201 ± 0.0003	0.0050 ± 0.0007	0.0013 ± 0.0009
Al (real)	79.1 ± 11.0	1.0195 ± 0.0003	0.0049 ± 0.0008	0.0029 ± 0.0008
Cu (real)	65.0 ± 9.5	1.0193 ± 0.0003	0.0049 ± 0.0008	0.0023 ± 0.0009

modification in nuclei can be observed in this situation. This is because the momentum of observed ϕ mesons ranges from 1.0 to 2.2 GeV discussed in Subsection 3.5.3, and almost all the ϕ mesons decay outside the nucleus ($\gtrsim 95\%$).

The Λ is observed in π^-p invariant mass distributions. The observed width of the peak corresponds to the overall resolution of the spectrometer including the energy loss and multiple scattering effects because this decay is weak one and its natural width is very narrow. Figure 3.24 shows the invariant mass distribution of π^-p , and the lines are the best fit results by applying a Gaussian with a linear background. Table 3.15 shows the fitting results for the position and width of the peaks for each target with the PDG peak position [49]. No significant difference can be observed in the width of $\Lambda \rightarrow \pi^-p$ peak, this shows the difference of the energy loss and multiple scattering effects in the target material for various targets is small as expected.

¹Note that the mass and width of the ϕ meson in free space is 1019.456 ± 0.020 MeV and 4.26 ± 0.05 MeV, respectively [49].

Figure 3.24: π^-p invariant mass distribution. Clear Λ peaks are observed for all the targets.Table 3.15: Fitting results for the position and width of the $\Lambda \rightarrow \pi^-p$ peak

target	peak (MeV/ c^2)	width (MeV/ c^2)
Li	1115.27 ± 0.03	1.70 ± 0.05
C	1115.10 ± 0.04	1.60 ± 0.05
Al	1115.07 ± 0.03	1.74 ± 0.05
Cu	1115.21 ± 0.03	1.71 ± 0.05
PDG	1115.683 ± 0.006	

3.5.2 Incident γ energy distribution

Figure 3.25 shows incident γ energy distributions for the events in which the ϕ meson is observed. Red lines show the contribution of the non-resonant KK background events. The estimation of the amount of background events is discussed in the Subsection 3.6.3. The ϕ meson yields monotonously increase as the incident γ energy increases. Averaged incident γ energy is $\langle E_\gamma \rangle = 2.2$ GeV for each nuclear target.

3.5.3 Momentum distribution of ϕ mesons

Figure 3.26 shows the momentum distribution of the ϕ mesons. Red lines show the contribution of the non-resonant KK background events. The averaged momentum of the detected ϕ mesons is $\langle P_\phi \rangle = 1.8$ GeV for each nuclear target.

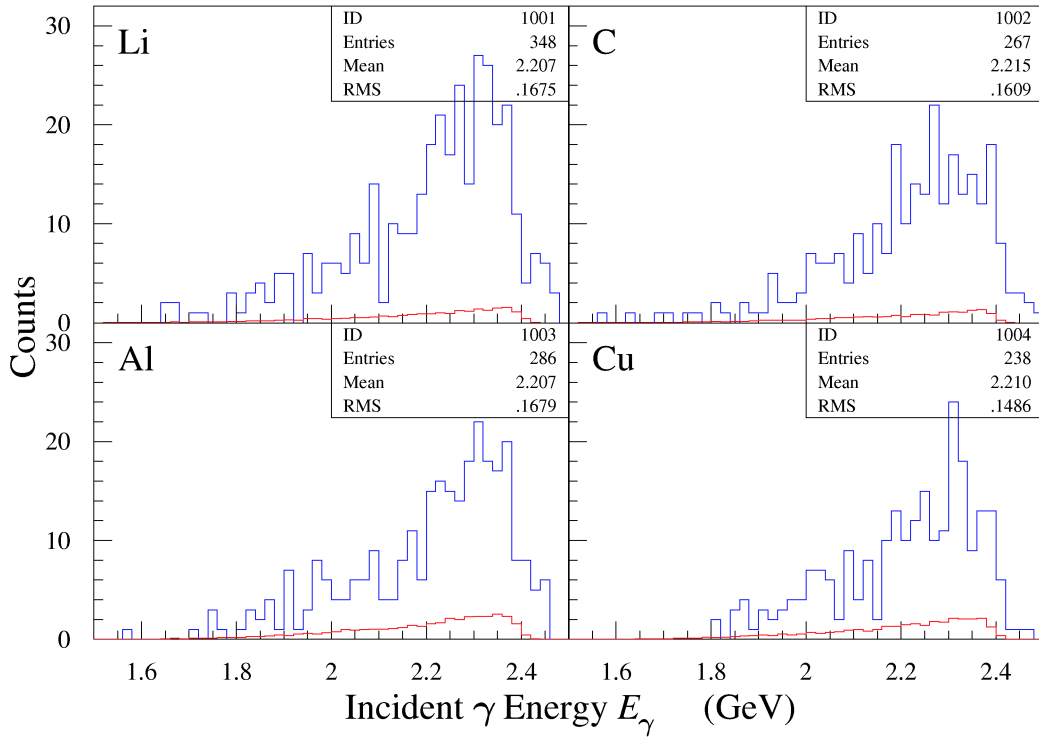


Figure 3.25: Incident γ energy distribution. The red lines show the estimated non-resonant K^+K^- background events. Averaged incident γ energy is $\langle E_\gamma \rangle = 2.2$ GeV.

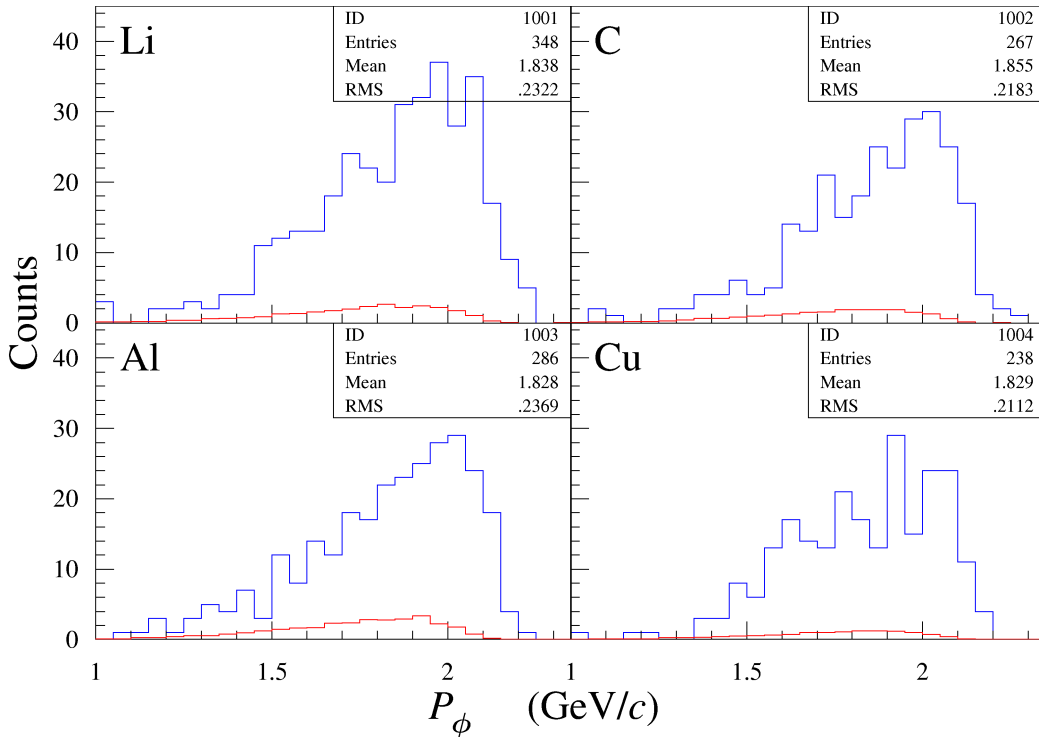


Figure 3.26: Momentum distribution of ϕ mesons. The red lines show the estimated non-resonant K^+K^- background events. Averaged momentum is $\langle P_\phi \rangle = 1.8$ GeV.

3.5.4 \tilde{t} distribution

Near the threshold of ϕ photo-production, the minimum momentum transfer square for the incoherent production (production on the nucleon) varies drastically as the incident γ energy E_γ changes. Figure 3.27 shows the limit of the momentum transfer square $|t|$ as a function of incident γ energy E_γ .

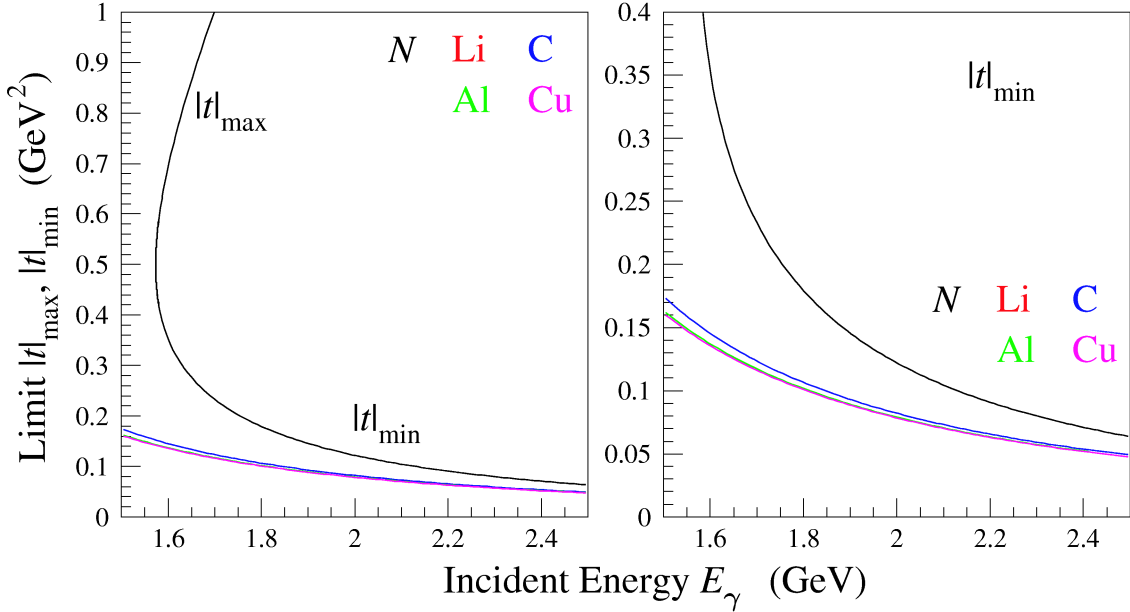


Figure 3.27: Limit of $|t|$ as a function of E_γ . The left panel shows $|t|_{\min}$ and $|t|_{\max}$ for the proton and the nuclear targets used, and the right panel shows the zoomed one in $|t| = 0.0\text{--}0.4 \text{ GeV}^2$.

Since the $|t|_{\min}$ varies drastically as E_γ changes, the variable $\tilde{t} = |t| - |t|_{\min}$ is introduced. Figure 3.28 shows \tilde{t} distribution without any acceptance correction. Here $|t|_{\min}$ is obtained from the incident γ energy and the reaction target is assumed to be a nucleon at rest. The fitting with an exponential function is made, and the fitting region is between $t = 0.0$ and 0.5 GeV^2 . The slopes are similar values -8.0 ± 0.6 , -8.5 ± 0.7 , -7.2 ± 0.6 , and -8.2 ± 0.7 for Li, C, Al, and Cu, respectively. This implies the incoherent process is dominant for all the targets. In order to suppress the acceptance difference between vertically and horizontally polarized γ beam data, normalized yields are obtained by averaging vertically and horizontally polarized photon data as

$$R = \frac{1}{2} \left\{ \frac{N_\phi^V}{\eta_{\text{DAQ}}^V N_\gamma^V} + \frac{N_\phi^H}{\eta_{\text{DAQ}}^H N_\gamma^H} \right\} \quad (3.22)$$

Figure 3.29 shows normalized \tilde{t} distribution. Figure 3.30 shows the acceptance with respect to \tilde{t} for the incoherent process of each nuclear target, where $|t|_{\min}$ is obtained by assuming that the target is a nucleon at rest. No significant difference is seen in the positive \tilde{t} region for all the targets.

Figure 3.31 shows acceptance corrected \tilde{t} distribution. Since the acceptance is determined averaging in a finite region, observed \tilde{t} distributions by the Monte Carlo simulation is adjusted to real ones. The fitting to the exponential function

$$\frac{d\sigma}{d\tilde{t}} = C \exp(-b\tilde{t}) \quad (3.23)$$

is applied for each target, and the fitting region is $\tilde{t} = 0.00$ and 0.50 . The fitting error of the slope is too large, and the fitting the data combined for all the target is also applied. Figure 3.32 shows acceptance

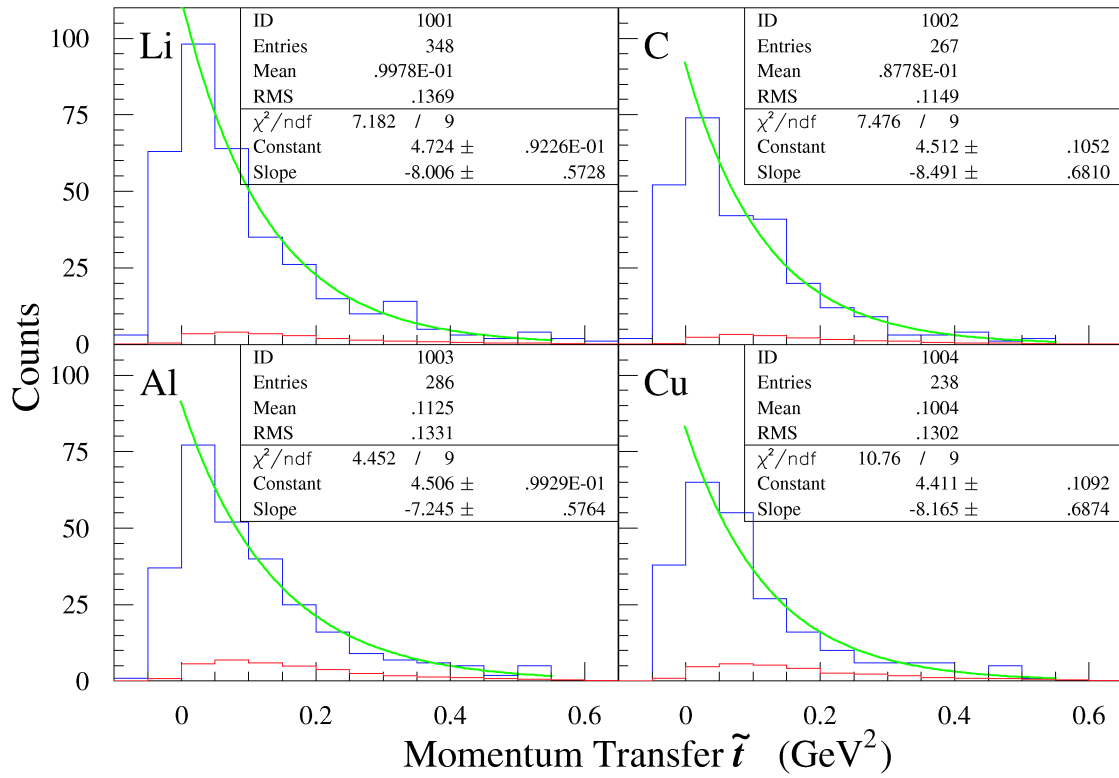


Figure 3.28: \tilde{t} distribution. The distributions are fitted with an exponential function as shown in the green lines. The red lines show the estimated non-resonant K^+K^- background events.

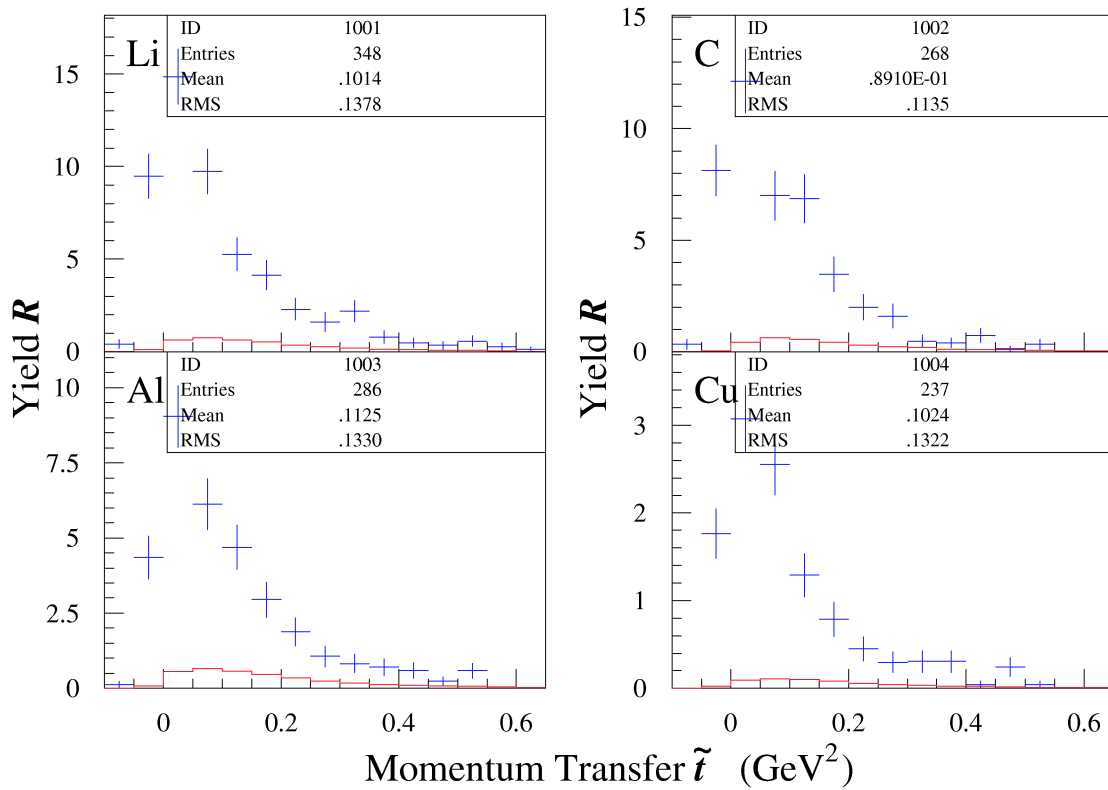


Figure 3.29: Normalized yield R as a function of \tilde{t} . The red lines show the estimated non-resonant K^+K^- background events.

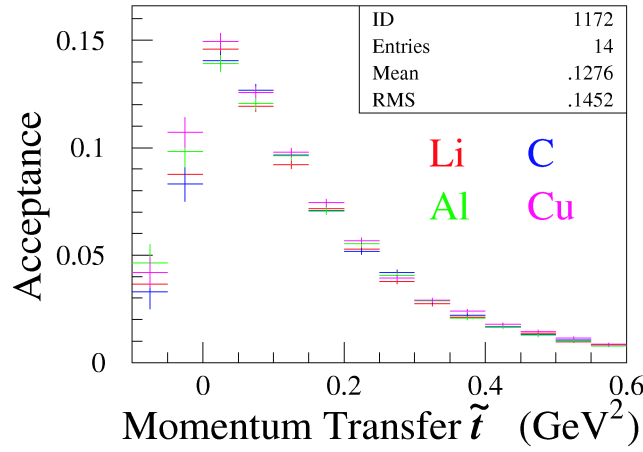


Figure 3.30: Acceptance as a function of \tilde{t}

corrected \tilde{t} distribution for the combined data of all the targets. The slope $b = 3.4 \pm 0.5 \text{ GeV}^{-2}$ is obtained for the combined data. The smallest \tilde{t} region may have larger contribution of the coherent production, thus the fitting with same function is also made in the \tilde{t} region between 0.05 and 0.50.

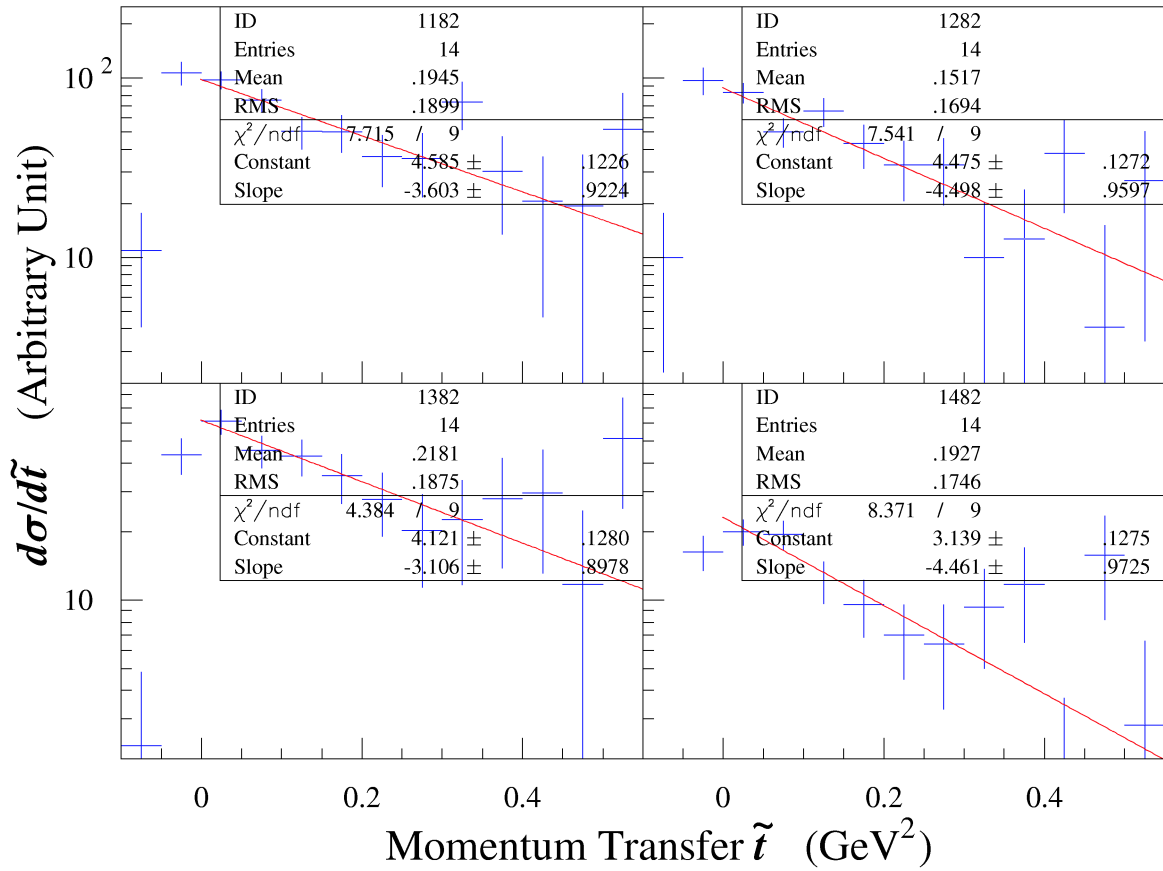
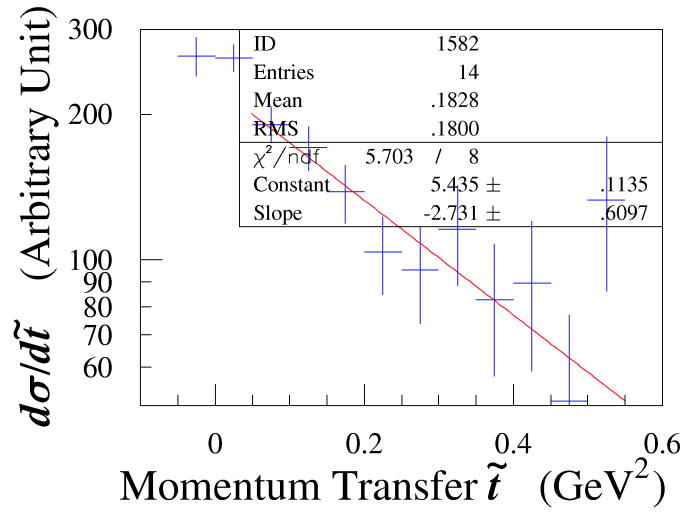


Figure 3.31: Acceptance corrected yield as a function of \tilde{t} . The yield is fitted with an exponential function as shown in the red lines.

Figure 3.32: Acceptance corrected yield as a function of \tilde{t}

In this case $b = 2.7 \pm 0.6 \text{ GeV}^{-2}$ is obtained. The fitted slope does not significantly change even if small \tilde{t} events are excluded, and contribution of the coherent production in small \tilde{t} region seems small. Table 3.16 shows the summary of the obtained slope parameters b in the \tilde{t} distribution. These slope

Table 3.16: Summary of b parameters in the \tilde{t} distribution

Fitting region \tilde{t} (GeV^2)	0.00–0.50	0.05–0.50
Li	3.6 ± 0.9	2.7 ± 1.2
C	4.5 ± 1.0	4.0 ± 1.2
Al	3.1 ± 0.9	2.5 ± 1.2
Cu	4.5 ± 1.0	4.9 ± 1.7
All	3.4 ± 0.5	2.7 ± 0.6

parameters are consistent with the case of ϕ photo-production on the proton, $b = 2.1 \sim 3.0 \text{ GeV}^{-2}$ at SAPHIR [70] or $b = 3.38 \pm 0.23 \text{ GeV}^{-2}$ at LEPS [57]. This shows incoherent process is dominant in this incident γ energy region even at small scattering angles.

3.5.5 Scattering angle of K^+ in the helicity frame

When a vector meson decays into two spinless particles, angular distribution for one of the decay particle of the vector mesons are expressed as

$$\begin{aligned}
 W(\cos\theta, \phi) = \frac{3}{4\pi} \left\{ \frac{1}{2}(\rho_{-1-1} + \rho_{11}) \sin^2\theta + \rho_{00} \cos^2\theta \right. \\
 + \frac{1}{\sqrt{2}}(-\text{Re}\rho_{10} + \text{Re}\rho_{-10}) \sin 2\theta \cos\phi \\
 + \frac{1}{\sqrt{2}}(-\text{Im}\rho_{10} + \text{Im}\rho_{-10}) \sin 2\theta \sin\phi \\
 \left. - \text{Re}\rho_{1-1} \sin^2\theta \cos\phi + \text{Im}\rho_{1-1} \sin^2\theta \cos 2\phi \right\}, \tag{3.24}
 \end{aligned}$$

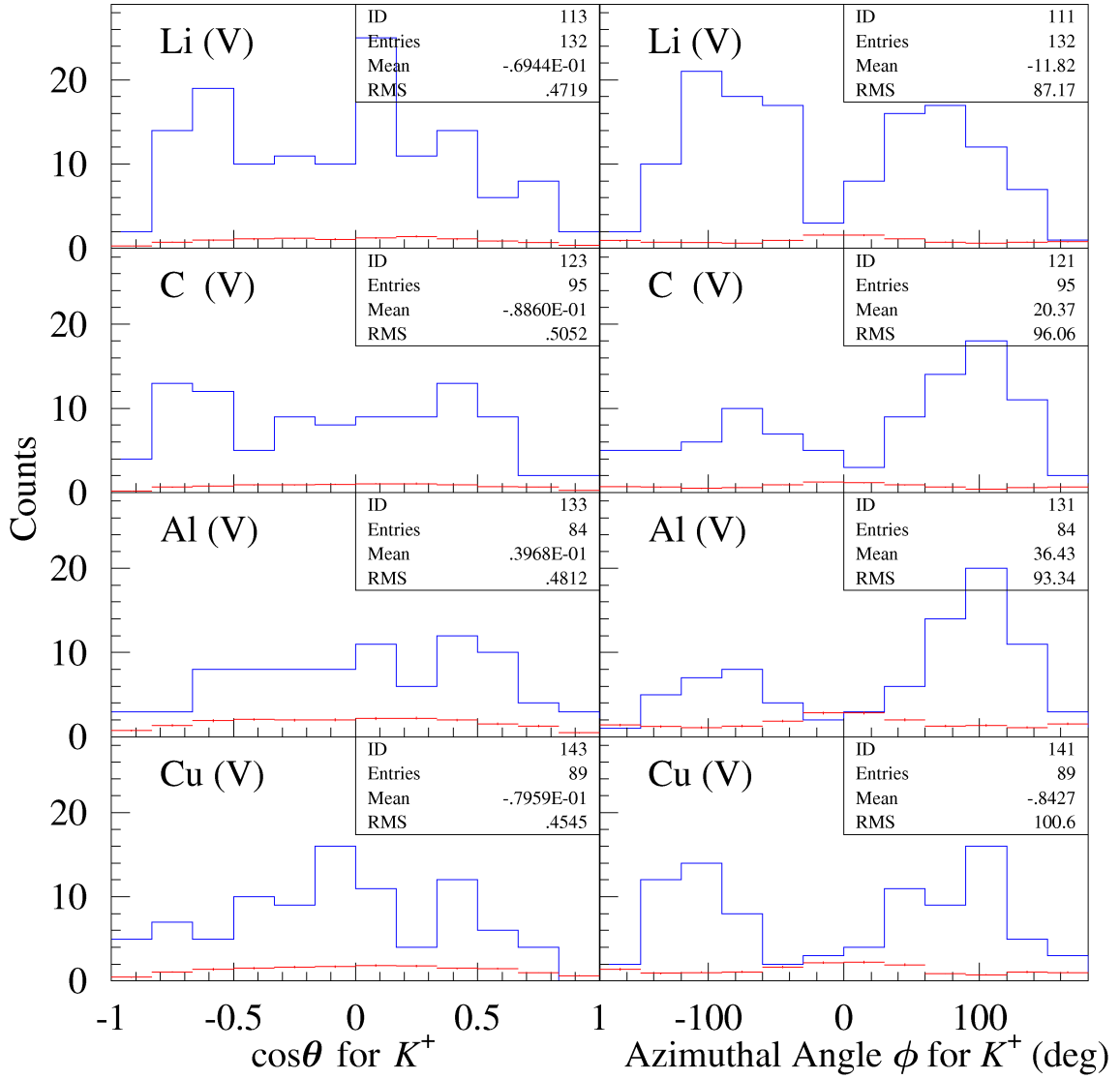


Figure 3.33: Scattering angle of K^+ in the helicity frame for the vertically polarized photon data. The red lines show the estimated non-resonant K^+K^- background events.

where ρ stands for the spin density matrix of the ϕ meson. If s-channel helicity is conserved, non helicity conserving amplitudes are 0. Decay angular distribution for the vector meson production by the linearly polarized photons with the polarization P_γ becomes

$$W(\cos\theta, \phi, \Phi) = \frac{3}{\pi}(1 - \cos^2\theta) \left\{ \frac{1}{2} + P_\gamma \rho_{1-1}^1 \cos 2(\phi - \Phi) \right\}, \quad (3.25)$$

where Φ stands for the polarization vector of the vector meson in the rest frame of the vector meson. Pure natural and unnatural parity exchanges give $\rho_{1-1}^1 = +1/2$ and $-1/2$, respectively.

The helicity frame is basically the rest frame of the ϕ meson (V_{rest}), and the frame velocity in the laboratory frame is described as

$$\vec{\beta} = \vec{P}_\phi / E_\phi. \quad (3.26)$$

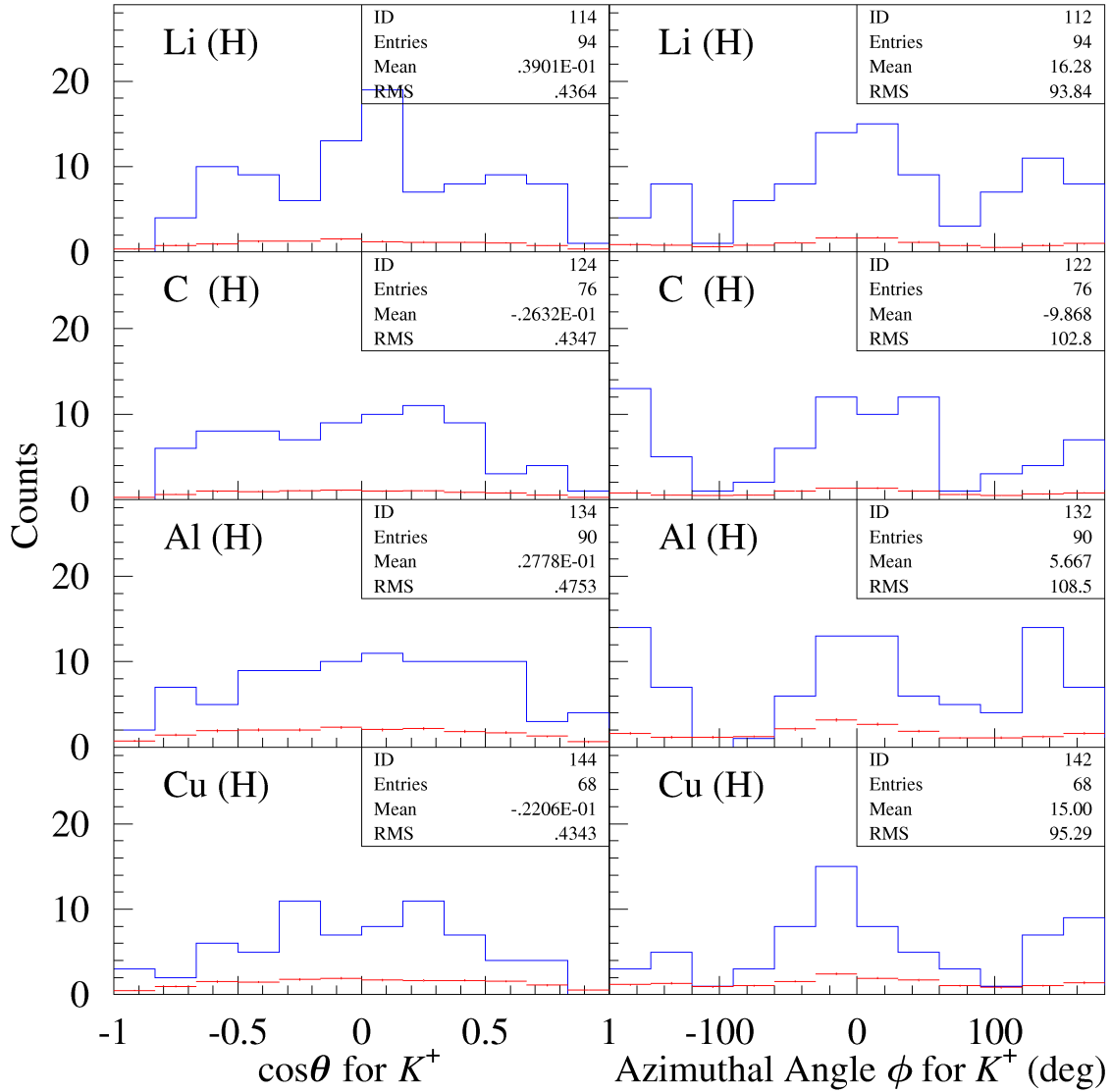


Figure 3.34: Scattering angle of K^+ in the helicity frame for the horizontally polarized photon data. The red lines show the estimated non-resonant K^+K^- background events.

Momenta in the helicity frame can be obtained easily by the Lorentz transform, although the directions of the axes are different from those in the laboratory frame. In the helicity frame, x , y , and z axes are defined so that \vec{z} is opposite to the outgoing recoil nucleon in V_{rest} , and that \vec{y} is normal to the production plane in V_{rest} . The unit vectors of the x -, y -, z -axes \hat{x} , \hat{y} , \hat{z} are described as

$$\begin{cases} \hat{z} \propto -\vec{P}_p, \\ \hat{y} \propto \vec{P}_\gamma \times \hat{z}, \text{ and} \\ \hat{x} \propto \hat{y} \times \hat{z}, \end{cases} \quad (3.27)$$

where \vec{P}_γ and \vec{P}_p are given in the rest frame of the produced ϕ meson. Therefore scattering angle of the decay particle K^+ in the helicity frame is given

$$\begin{cases} \cos \theta = \hat{\pi} \cdot \hat{z}, \\ \cos \phi = \frac{\hat{y}(\hat{z} \cdot \hat{\pi})}{|\hat{z} \cdot \hat{\pi}|}, \\ \sin \phi = \frac{\hat{x}(\hat{z} \cdot \hat{\pi})}{|\hat{z} \cdot \hat{\pi}|}, \end{cases} \quad (3.28)$$

where $\vec{\pi}$ stands for the flight vector of K^+ in V_{rest} . Figure 3.33 and 3.34 shows scattering angles of K^+ in the helicity frame, where the target is assumed to be proton at rest and additional condition $|t| < 0.2 \text{ GeV}^2$ is required because the detector acceptance is not biased so much in this $|t|$ region. Figure 3.35 shows those for the liquid hydrogen target (LH_2) with the same condition except for

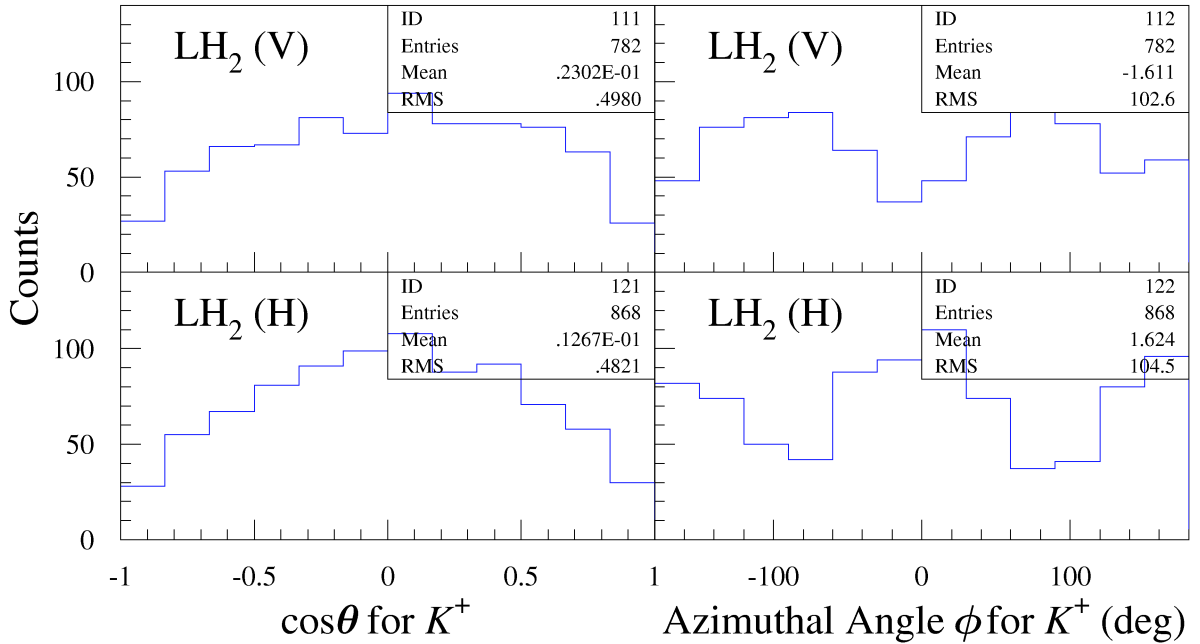


Figure 3.35: Scattering angle of K^+ in the helicity frame for LH_2 . The amplitude of the azimuthal scattering angle of K^+ for LH_2 is smaller than that for the nuclear target.

z -vertex, and which is required as

$$-1000. \leq z < -900, \quad (3.29)$$

where z stands for z -vertex position. The amplitude of the azimuthal angle of K^+ for nuclear target is larger than that for LH_2 . According to the OZI rule, the diffractive Pomeron exchange is dominant in ϕ photo-production on the proton [71, 72, 73, 74]. Diffractive contributions are accompanied

by the non-diffractive channels associated with the unnatural parity exchange [70]. For coherent ϕ photo-production at forward angles, the isovector π -exchange amplitude is strongly suppressed [73]. Figure 3.36 shows the possible reaction mechanisms. The contribution of the unnatural parity ex-

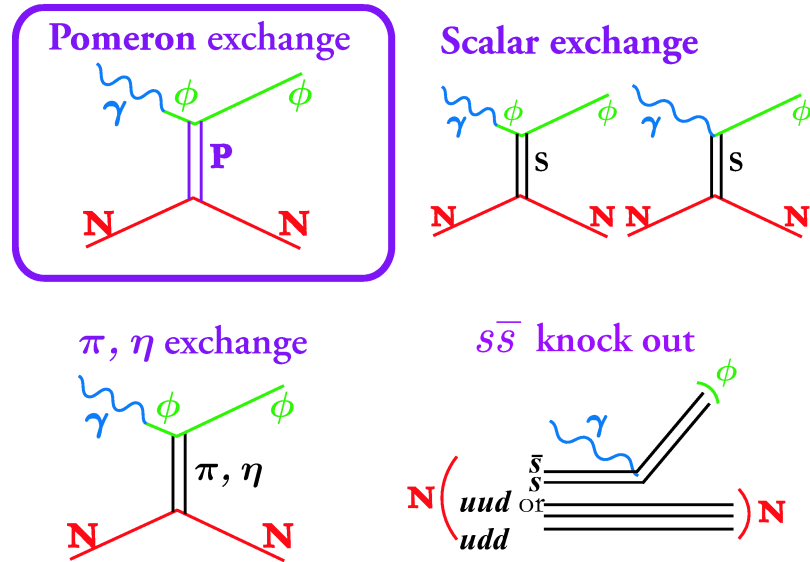


Figure 3.36: Reaction mechanism of the diffractive ϕ photo-production on the nucleon. The diffractive Pomeron exchange is dominant, and are accompanied by the non-diffractive channels associated with the unnatural parity exchange (π/η).

change might be canceled out between production on the proton and that on the neutron in the nucleus. This implies that coherent ϕ photo-production exists.

3.6 Background events

The candidate of the background events are

- contamination of the start counter events,
- contamination of the events with particle mis-identification, and
- non resonant K^+K^- events.

In this section, these background events are discussed.

3.6.1 Contamination of the start counter events

The contamination of the start counter in the z -vertex target region is estimated in this subsection. The z -vertex resolution depends on the opening angle of K^+K^- tracks, which is discussed in Appendix C.1.3. The real numbers of ϕ events in the target and in the start counter regions are defined as n_t , n_s , respectively. The N_t and N_s stand for the measured numbers of ϕ events in the target and in the start counter regions, respectively. The probability that the target ϕ events are measured

Table 3.17: Probabilities of the contamination due to the vertex cut. The R_t and R_s stand for the probability that the target ϕ events are measured within the target region, and that the start counter ϕ events are measured within the start counter region, respectively. The N_t and N_s denote the measured numbers of ϕ events in the target and in the start counter regions, respectively.

Opening Angle θ_{12}	Li				C			
	N_t	N_s	R_t	R_s	N_t	N_s	R_t	R_s
0.00–0.05	1	0	89.29±5.85	69.47±4.02	1	0	88.00±6.50	81.68±3.38
0.05–0.10	6	0	93.75±1.83	85.09±1.46	5	0	95.12±1.68	96.15±0.79
0.10–0.15	20	0	98.49±0.57	93.41±0.73	11	0	99.56±0.31	98.96±0.30
0.15–0.20	55	1	99.52±0.20	96.22±0.45	43	3	99.76±0.14	99.15±0.22
0.20–0.25	150	14	99.63±0.10	99.11±0.16	128	10	99.70±0.10	99.89±0.06
0.25–0.30	137	13	99.68±0.08	99.28±0.14	97	13	99.91±0.05	99.77±0.08
0.30–0.35	39	3	99.57±0.14	99.55±0.17	34	9	99.82±0.09	99.87±0.09
0.35–0.40	10	0	99.23±0.29	99.64±0.26	12	0	99.77±0.16	100.00±0.00
0.40–0.45	2	0	99.41±0.41	99.03±0.68	4	0	100.00±0.00	100.00±0.00
0.45–0.50	3	0	98.36±1.15	98.94±1.06	1	0	100.00±0.00	100.00±0.00
Opening Angle θ_{12}	Al				Cu			
	N_t	N_s	R_t	R_s	N_t	N_s	R_t	R_s
0.00–0.05	1	0	68.18±9.93	81.68±3.38	1	0	69.70±8.00	81.68±3.38
0.05–0.10	5	1	93.55±1.80	96.15±0.79	6	1	98.13±0.93	96.15±0.79
0.10–0.15	25	3	99.17±0.41	98.96±0.30	15	4	99.44±0.32	98.96±0.30
0.15–0.20	39	4	99.70±0.15	99.15±0.22	36	9	99.53±0.19	99.15±0.22
0.20–0.25	113	14	99.94±0.04	99.89±0.06	96	35	99.89±0.06	99.89±0.06
0.25–0.30	108	7	99.88±0.05	99.77±0.08	103	36	99.91±0.04	99.77±0.08
0.30–0.35	42	5	99.87±0.08	99.87±0.09	31	15	99.75±0.10	99.87±0.09
0.35–0.40	10	1	99.77±0.16	100.00±0.00	10	2	99.79±0.15	100.00±0.00
0.40–0.45	3	0	99.11±0.52	100.00±0.00	2	0	99.15±0.49	100.00±0.00
0.45–0.50	1	0	100.00±0.00	100.00±0.00	0	0	99.30±0.70	100.00±0.00

within the target region and that the start counter ϕ events are measured within the start counter region are denoted by R_t and R_s , respectively. Let us assume the probability that the target ϕ events are measured in the start counter region is $1 - R_t$, and that the start counter ϕ events are measured in the target region is $1 - R_s$. The following relations are valid:

$$\begin{aligned} N_t &= R_t n_t + (1 - R_s) n_s, \text{ and} \\ N_s &= (1 - R_t) n_t + R_s n_s. \end{aligned} \quad (3.30)$$

The contamination of the start counter ϕ events in the target region N_c is estimated as

$$N_c = N_t - R_t n_t. \quad (3.31)$$

The number of target ϕ events can be estimated from Eq. (3.30) as

$$n_t = \frac{1}{R_t + R_s - 1} \{R_s(N_t + N_s) - N_s\}. \quad (3.32)$$

The R_t and R_s have been determined by the MC simulation in each K^+K^- opening angle region. The target region is defined as the same as described in Subsection 3.4.6. The start counter z -vertex region is defined as

$$\begin{aligned} -863. &\leq \text{vtz}(\text{ivtx}) < -800. \text{ for Li} \\ -872. &\leq \text{vtz}(\text{ivtx}) < -800. \text{ for C, Al, and Cu.} \end{aligned} \quad (3.33)$$

Table 3.17 shows the variables N_t , N_s , R_t , and R_s for each K^+K^- opening angle region. The number of contaminated start counter events are obtained as

$$\begin{aligned} \text{Li} & 0.10^{+0.96}_{-0.10}, \\ \text{C} & 0.04^{+0.38}_{-0.04}, \\ \text{Al} & 0.01^{+0.45}_{-0.01}, \text{ and} \\ \text{Cu} & 0.19^{+0.37}_{-0.19}. \end{aligned}$$

The contamination of the start counter ϕ events in the target region is negligibly small.

3.6.2 Particle mis-identification

The fraction that pions are identified as kaons has been estimated for each momentum region according to the momentum dependent mass resolution described in Eq. (3.12). Figure 3.37 shows the fraction of particle mis-identification. The fraction of particle mis-identification is 0.032 at maximum since the momentum of charged kaons ranges from 0.6 to 1.2 GeV as shown in Figure C.1 in Appendix C.1.1. The number of π^+K^- events are 137, 126, 154, and 234 for Li, C, Al, and Cu, respectively. The 24, 20, 25, and 57 π^+K^- events appear in the ϕ peak region of the K^+K^- invariant mass distribution if π^+ is identified as K^+ , respectively. Then, the number of π^+K^- events identified as K^+K^- is estimated to be 0.7, 0.6, 0.8, and 1.8 in the ϕ peak region at maximum. The number of $K^+\pi^-$ events are 689, 575, 656, and 848. The 111, 92, 107, and 132 $K^+\pi^-$ events appear in the ϕ peak region of the K^+K^- invariant mass distribution if π^- is identified as K^- , respectively. Then, the number of $K^+\pi^-$ events identified as K^+K^- is estimated to be 3.5, 2.9, 3.4, and 4.2 in the ϕ peak region at maximum. On the other hand, the number of $\pi^+\pi^-$ events are 11339, 10960, 14248, and 22903. The 4078, 4051, 5228, and 8157 $\pi^+\pi^-$ events appear in the ϕ peak region of the K^+K^- invariant mass distribution if π^+ and π^- are identified as K^+ and K^- , respectively. Then, the number of $\pi^+\pi^-$ events identified as K^+K^- is estimated to be 4.0, 4.0, 5.2, and 8.0 in the ϕ peak region at maximum.

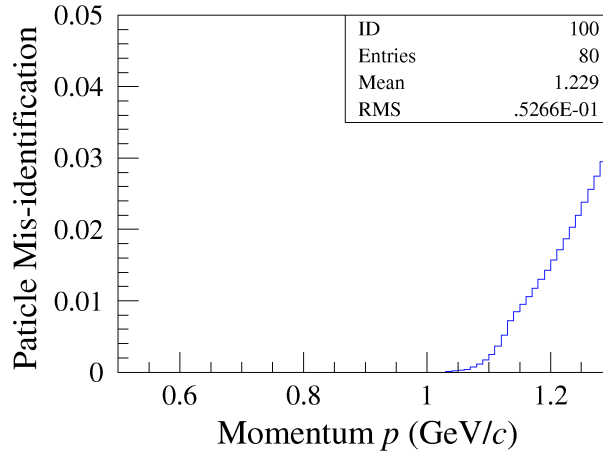


Figure 3.37: Fraction of pions identified as kaon. The fraction increases as the momentum of the pion increases.

The contamination of the $\pi^+\pi^-$, $K^+\pi^-$, or π^+K^- events are negligibly small. because an averaged value for the fraction of particle mis-identification is much smaller than 0.0315, and the estimated contamination should be much smaller (The electron or positron tracks are included for the pion tracks in this subsection. The fraction of particle mis-identification is always smaller for electrons or positrons than that for pions).

Since the time of flight is mis-measured by 1.966 nsec longer or shorter for the accidental coincidence charged particles associate with the successive RF bunches, the mass square of these particles are wrong. The inclined loci in Figure 3.11 in Subsection 3.4.3 show the mis-measured events. When the events with number of tracks are larger than 1 are selected, these loci disappear as shown in Figure 3.12 in Subsection 3.4.3. The proton accidental coincidence tracks are still observed in heavier targets, but contamination of these tracks appear in the higher momentum than that of charged kaons decaying from ϕ mesons as discussed in Appendix C.1.1.

3.6.3 Non resonant K^+K^- events

To estimate the K^+K^- events in the ϕ peak of the invariant mass distributions, the non-resonant K^+K^- events are generated by the MC simulation assuming the three-body phase space of the reaction $\gamma N \rightarrow K^+K^-N$. Figure 3.38 shows the K^+K^- invariant mass distribution for non-resonant K^+K^- production. The contribution of the non-resonant K^+K^- production in the ϕ peak region has been estimated as

$$\begin{aligned} & \#N(1.005 \leq m_{KK} < 1.035)_{\text{real}} \\ &= \#N(1.050 \leq m_{KK} < 1.100)_{\text{real}} \times \frac{\#N(1.005 \leq m_{KK} < 1.035)_{\text{MC}}}{\#N(1.050 \leq m_{KK} < 1.100)_{\text{MC}}}. \end{aligned} \quad (3.34)$$

As a result, number of ϕ mesons has been obtained as

$$N_\phi = N(1.005 \leq m < 1.035) - N(1.005 \leq m_{KK} < 1.035). \quad (3.35)$$

The background K^+K^- contribution has been subtracted for each target for each direction of the polarity.

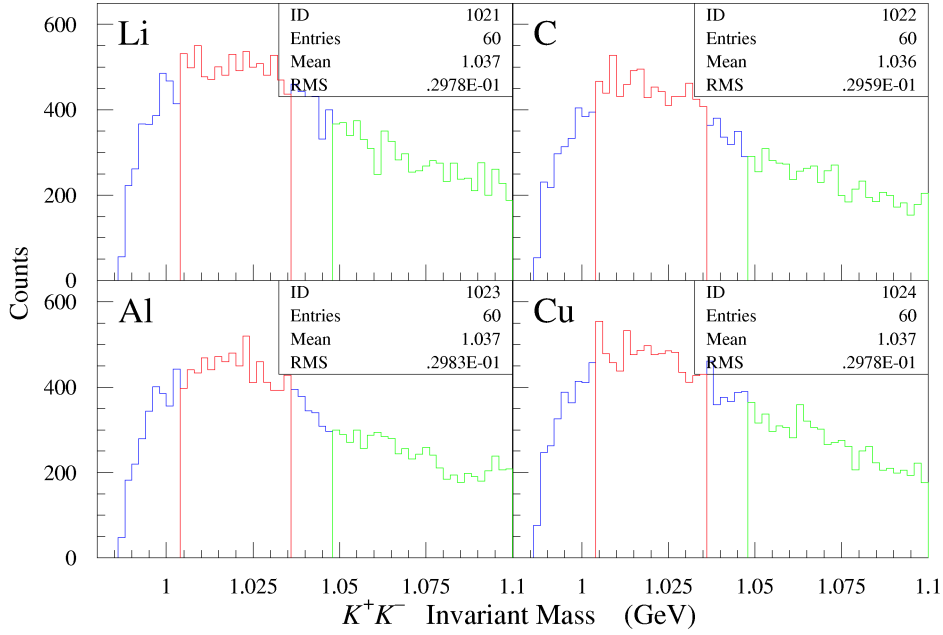


Figure 3.38: K^+K^- invariant mass distribution for non-resonant KK production. The red histograms shows the events which pass the standard ϕ cut ($1.005 \leq m_{KK} < 1.035$ GeV), and the green ones show the events used in the background estimation.

3.7 Normalization

In order to extract ϕ - N total cross section, the mass number dependence of the ϕ meson yields for various target nuclei is needed. The effective number of tagger hits, the number of target nuclei, and other correction factors for the normalization are estimated.

3.7.1 Effective number of tagger hits

The number of tagger hits is counted by a scaler module. But the counting efficiency depends on the tagger rate because of a finite width of the tagger signals to the scaler. Here the correction of the tagger counts by the scaler number is discussed.

The width of a input signal to the scaler module is set to 100 nsec and scaler module needs 5 nsec interval in order to identify two signals. The accidental coincidence rate α_{tagger} is considered to be

$$\alpha_{\text{tagger}} = [\text{Tagger Rate}] \times [\text{Dead Time (105 nsec)}], \quad (3.36)$$

assuming the signals have a Poisson distribution and $\alpha_{\text{tagger}} \ll 1$.

The accidental coincidence rate is also estimated from the TDC distributions of the tagger plastic scintillators [75] shown in Figure 3.39, in which the timing associated with the true events is calibrated to be zero. In order to select clean hits, the following conditions are required.

$$\begin{aligned} A_i^U &> 100, \\ A_i^D &> 100, \\ |T_{ij}^U - [\text{True Timing}]| &< 10, \text{ and} \\ |T_{ij}^D - [\text{True Timing}]| &< 10, \end{aligned} \quad (3.37)$$

where A^U , A^D stand for the ADC and T^U , T^D denote the TDC of the upstream and downstream plastic scintillators, respectively. The subscript i , j means the plastic scintillator number, and the

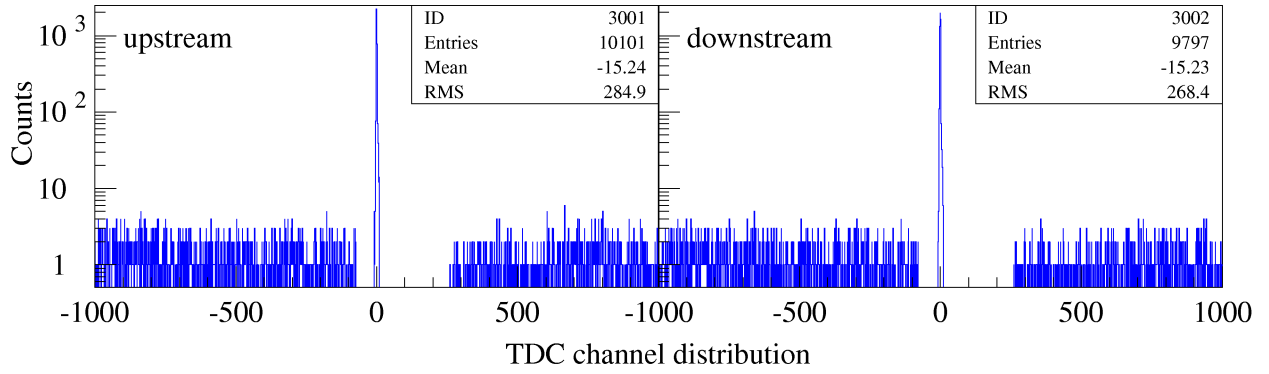


Figure 3.39: TDC distributions of tagger plastic scintillator

index of the hit, respectively. Background seems to be flat except for the region close to the true timing. The accidental coincidence rate $\alpha_{\text{distribution}}$ is estimated from the TDC distribution by

$$\alpha_{\text{distribution}} = \frac{\text{Counts (upstream)}[105 \text{ ns}] + \text{Counts (downstream)}[105 \text{ ns}]}{\text{Counts (true signal)}[-10 \sim +10]}, \quad (3.38)$$

where $\text{Count}[105 \text{ nsec}]$ is estimated as number of counts in the region $-840 \sim -420$ is normalized to the 105 nsec (0.5 nsec/channel).

In the experiment, the storage ring was operated with the two filling patterns, and Table 3.18 shows the information on the filling pattern of the electron injection beam. Figure 3.40 shows the

Table 3.18: Filling pattern of the electron injection beam

Cycle	Period	Filling Pattern
9	Nov 8 10:00–14 10:00	multi-bunch
9	Nov 15 10:00–20 15:00	1 bunch (1.5 mA)+multi-bunch

comparison of the accidental coincidence rate estimated by the tagger rate with that by the TDC distributions for two filling patterns. The slope of the correlation is slightly smaller than 1, which depends on the operated filling patterns.

The accidental coincidence rate estimated by the TDC distributions is adopted since the tagger plastic scintillator signals may not have a Poisson distribution according to the filling pattern. The relation of the accidental coincidence rate by the TDC distributions to that by the tagger rate is assumed as

$$\alpha_{\text{distribution}} = c\alpha_{\text{tagger}} \quad (3.39)$$

The parameter c is determined by fitting the correlation shown in Figure 3.39. The fitting results are summarized in Table 3.19.

Table 3.19: Correction parameter for accidental coincidence rate

Period	c
Nov 8 10:00–14 10:00	0.884 ± 0.012
Nov 15 10:00–20 15:00	0.915 ± 0.013

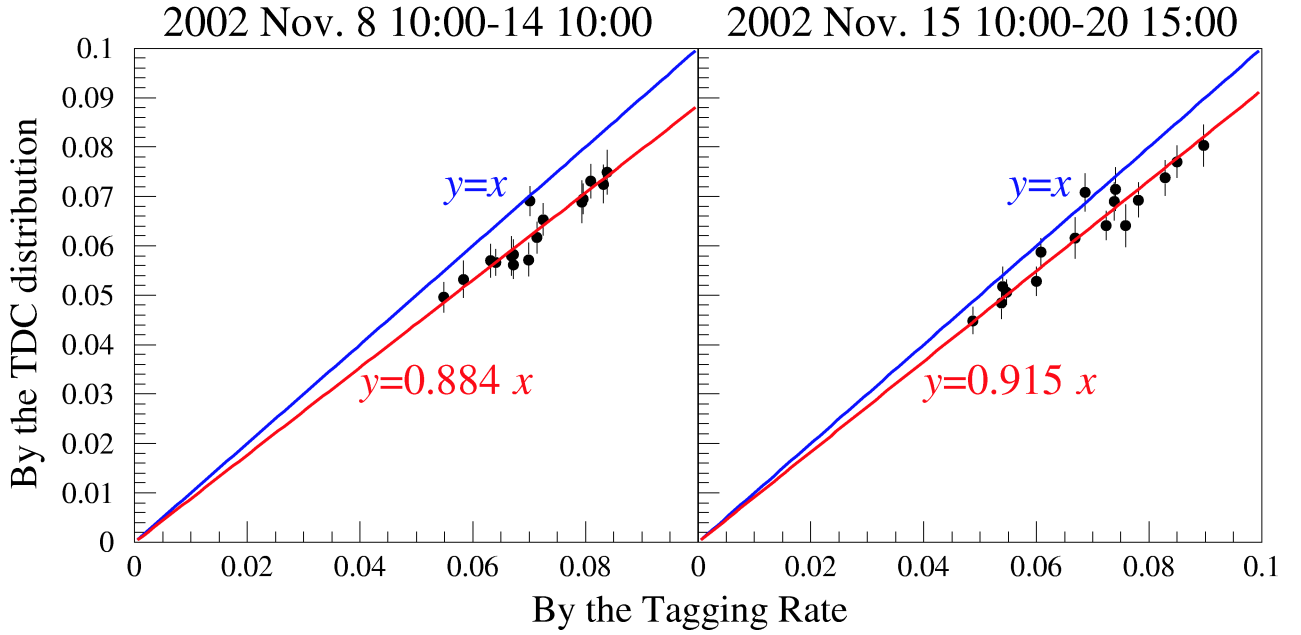


Figure 3.40: Comparison of the accidental coincidence rate by the tagger rate and by the TDC distributions.

The number of tagger counts are corrected by using the accidental coincidence rate as

$$\begin{aligned}
 [\text{True Tag Counts}] &= \frac{[\text{Measured Tag Counts}]}{1 - \alpha_{\text{Distribution}}} \\
 &= \frac{[\text{Measured Tag Counts}]}{1 - c\alpha_{\text{Tagger}}} \\
 &= \frac{[\text{Measured Tag Counts}]}{1 - c \times [\text{Tagger Rate}] \times [\text{Dead Time}]}
 \end{aligned}$$

The correction is made to estimate the effective tagger counts for every ten thousand buffers (C_{10000}) or for every buffer (C_1). The relation of the accidental coincidence rate by the TDC distributions to that by the tagger rate is assumed to be expressed by the quadratic, which gives the correction factor to the tagger counts $R = [\text{true tag count}]/[\text{measured tag count}]$ [75] as

$$\begin{aligned}
 R &= 0.999 + 0.936 \times 10^{-4} \cdot x + 0.238 \times 10^{-7} \cdot x^2 \quad \text{for multi - bunch, and} \\
 R &= 1.000 + 0.110 \times 10^{-3} \cdot x + 0.341 \times 10^{-7} \cdot x^2 \quad \text{for 1 bunch (1.5 mA) + multi - bunch,}
 \end{aligned} \tag{3.40}$$

where x is tagger rate (cps). This correction is also done for every ten thousand buffers (K_{10000}) or for every buffer (K_1).

Table 3.20 shows the effective tagger counts with the tagger rate corrections. The differences between C_1 and C_{10000} , between K_1 and K_{10000} , and between C and K are less than $\sim 0.1\%$, less than $\sim 0.5\%$, and $\sim 1\%$, respectively. All the differences are small. K_1 is adopted for the effective tagger counts.

Table 3.20: Effective photon counts with correction

Target	Polarity	Simple Counts	C_1	C_{10000}	K_1	K_{10000}
Li	Vert.	3.685×10^{10}	3.969×10^{10}	3.968×10^{10}	4.001×10^{10}	4.020×10^{10}
Li	Horz.	2.951×10^{10}	3.130×10^{10}	3.129×10^{10}	3.150×10^{10}	3.156×10^{10}
C	Vert.	3.876×10^{10}	4.171×10^{10}	4.171×10^{10}	4.219×10^{10}	4.237×10^{10}
C	Horz.	2.567×10^{10}	2.726×10^{10}	2.725×10^{10}	2.752×10^{10}	2.757×10^{10}
Al	Vert.	4.628×10^{10}	4.978×10^{10}	4.977×10^{10}	5.037×10^{10}	5.054×10^{10}
Al	Horz.	4.408×10^{10}	4.680×10^{10}	4.679×10^{10}	4.719×10^{10}	4.732×10^{10}
Cu	Vert.	1.184×10^{11}	1.274×10^{11}	1.274×10^{11}	1.288×10^{11}	1.293×10^{11}
Cu	Horz.	9.737×10^{11}	1.034×10^{11}	1.033×10^{11}	1.043×10^{11}	1.046×10^{11}

3.7.2 Number of target nuclei

The number of target nuclei in a unit area is calculated as

$$\frac{\xi [\text{cm}] \times \rho [\text{g/cm}^3]}{A [\text{g/mol}]} \times N_A [\text{mol}^{-1}] = \frac{N_A \rho \xi}{A} [\text{cm}^{-2}]. \quad (3.41)$$

where A , ξ [cm], and ρ [g/cm³] is mass number, thickness, and density, respectively, and $N_A = 6.0221367(36) \times 10^{23}$ [mol⁻¹] stands for the Avogadro number. Table 3.21 shows the properties of nuclear targets used and the number of nuclei in a unit area².

Table 3.21: Properties of the nuclear targets used. The Li target was a block, and each of the other three targets was divided into three pieces.

Target	Mass Number A	Thickness ξ [cm]	Density ρ [g/cm ³]	#Nuclei in a Unit Area [cm ⁻²]
Li	6.941	10.0	0.534	4.63×10^{23}
C	12.011	3×1.20	1.730	3.12×10^{23}
Al	26.982	3×0.80	2.702	1.45×10^{23}
Cu	63.546	3×0.10	8.92	2.54×10^{22}

3.7.3 Attenuation of the photon flux in the target material

The number of effective tagger counts discussed in Subsection 3.7.1 is that of induced photon counts by backward Compton scattering. Some induced photons are lost by converting e^+e^- pairs and so on until they reach the target, and some are lost during the flight in the target material itself. The former is common for all the nuclear targets, thus only the latter is discussed in this subsection.

The photon flux is attenuated during passing through the material, and the attenuation of photon flux is described as

$$N_\gamma = N_\gamma^0 \exp\{-(\mu/\rho)x\} = \exp\{-\mu t\}, \quad (3.42)$$

where x is a travel distance defined as mass per a unit area, and μ/ρ stands for the mass attenuation coefficient. The length x is obtained from the density ρ and the ordinal length t and described as

²The lithium target used had been thought to be ⁶Li isotope. Its mixture of ⁶Li and ⁷Li has been investigated by means of the accelerator mass spectrometry (AMS) at Tandem van de Graaff accelerator Laboratory at Kyoto University — spattering, accelerating, and analyzing the mass. It has been found to have a natural mixture [76]. Later, it has been found to be natural one by checking the lithium at KEK where it came from [77].

$x = \rho t$. Mass attenuation coefficient μ/ρ can be obtained numerically on the web page [78]. The photon flux at the start counter is obtained by multiplying η_{att} described in the equation (3.43) to the effective nucleon number.

$$\eta_{\text{att}}(\text{StartCounter}) = \exp(-x_0), \quad (3.43)$$

where $x_0 = (\mu/\rho)x$ is the target thickness in the unit length through which the photon intensity becomes $1/e$. In order to obtain the averaged photon flux in the target, the averaged attenuation factor should be multiplied:

$$\eta_{\text{att}}(\text{Target}) = \frac{1}{x_0} \int_0^{x_0} \exp(-t) dt = \frac{1}{x_0} (1 - \exp(-x_0)). \quad (3.44)$$

Table 3.22 shows the summary of the mass attenuation coefficient μ/ρ , $\eta_{\text{att}}(\text{StartCounter})$, and $\eta_{\text{att}}(\text{Target})$.

Table 3.22: Attenuation of the photon flux in the target. The Li target was a block, and each of the other three targets was divided into three pieces.

Target	μ/ρ [cm^2/g]	Thickness x_0	$\eta_{\text{att}}(\text{StartCounter})$	$\eta_{\text{att}}(\text{Target})$
Li	9.06×10^{-3}	0.048	0.953	0.976
C	1.74×10^{-2}	0.108	0.897	0.948
Al	3.10×10^{-2}	0.201	0.818	0.906
Cu	5.83×10^{-2}	0.156	0.856	0.926

3.7.4 Efficiency of the data taking system

Efficiency of the data taking system η_{DAQ} (live time) is estimated from the number of ungated triggers (trigger requests) and that of gated triggers (trigger accepts) as

$$\eta_{\text{DAQ}} = \frac{\#\text{gated triggers}}{\#\text{ungated triggers}} \quad (3.45)$$

Figure 3.41 shows the run dependence of η_{DAQ} . One run is divided into lumps of every 10,000 buffers. The η_{DAQ} is very stable for all the lumps. Table 3.23 shows the averaged efficiency η_{DAQ} of all for each target and each polarity.

Table 3.23: Averaged efficiency of the data taking system.

target	polarity	η_{DAQ}
Li	Vert.	0.91243 ± 0.00012
Li	Horz.	0.93048 ± 0.00012
C	Vert.	0.88923 ± 0.00011
C	Horz.	0.90854 ± 0.00013
Al	Vert.	0.86201 ± 0.00010
Al	Horz.	0.88497 ± 0.00010
Cu	Vert.	0.90245 ± 0.00007
Cu	Horz.	0.91928 ± 0.00007

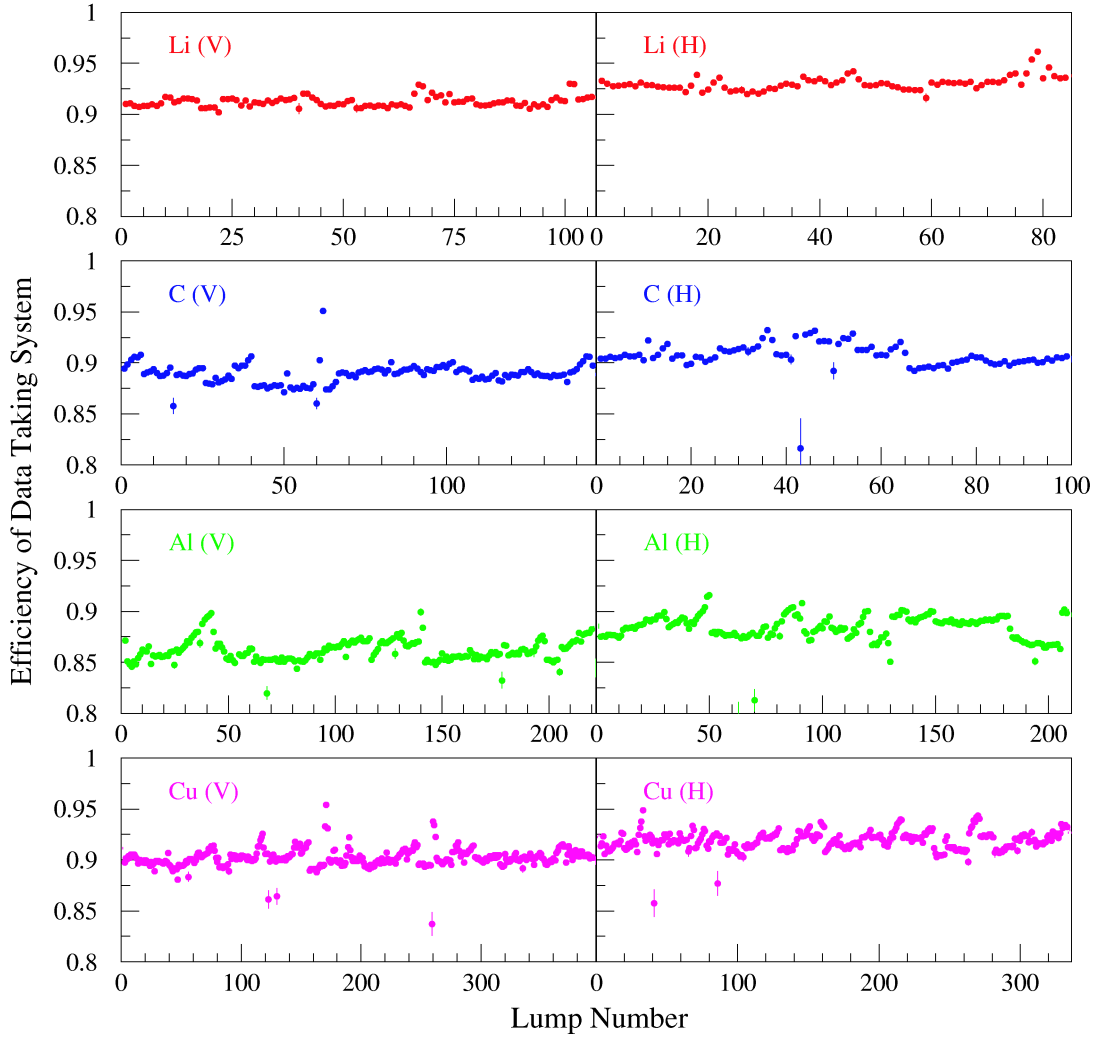


Figure 3.41: Efficiency of data taking system. The V denotes the efficiencies for the vertically polarized photon data, and the H denotes those for the horizontally polarized photon data.

3.7.5 Efficiency of the analyzer

The LEPSana stops analyzing the events when the number of SVTX clusters, DC clusters, or track candidates exceeds maximum set in it. The hits due to the accidental coincidence events or the δ -rays enlarge these numbers and make them exceed maximum. These hits are considered to happen at random. Figure 3.42 shows the run dependence of the fraction of the events that can not be analyzed. One run is also divided into lumps of every 10,000 buffers. The fraction is very stable and almost constant for all the lumps. Since the fraction is very small, the rejection of the events that cannot be analyzed does not affect final results even if those hits do not happen at random. The efficiency of the analyzer η_{ana} is defined as

$$\eta_{\text{ana}} = 1 - \frac{\text{\#Events That Can Not Be Analyzed}}{\text{\#Events}} \quad (3.46)$$

Table 3.24 summarizes the averaged efficiency η_{ana} of all for each target each polarity.

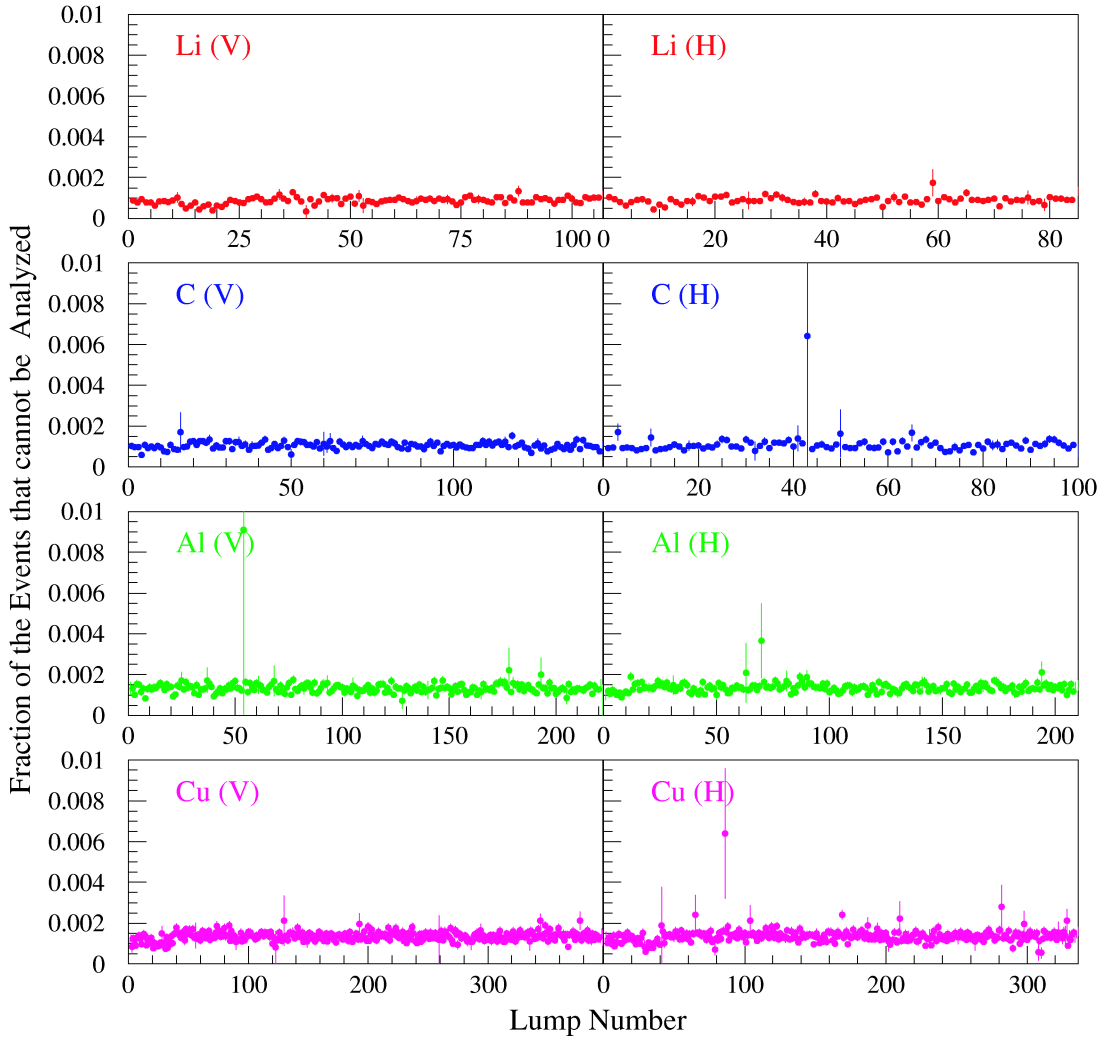


Figure 3.42: Fraction of the events that cannot be analyzed. The V denotes the efficiencies for the vertically polarized photon data, and the H denotes those for the horizontally polarized photon data.

Table 3.24: Averaged efficiency of the analyzer

target	polarity	η_{ana}
Li	Vert.	0.99913 ± 0.00001
Li	Horz.	0.99911 ± 0.00002
C	Vert.	0.99895 ± 0.00001
C	Horz.	0.99896 ± 0.00002
Al	Vert.	0.99867 ± 0.00001
Al	Horz.	0.99864 ± 0.00001
Cu	Vert.	0.99865 ± 0.00001
Cu	Horz.	0.99865 ± 0.00001

3.7.6 Geometrical acceptance

The geometrical acceptance of the LEPS spectrometer has been estimated by the MC simulation as

$$\eta_{\text{geo}} = \frac{\#\text{Observed } \phi}{\#\text{Generated } \phi}. \quad (3.47)$$

Table 3.25 shows the acceptance. The geometrical acceptance is estimated assuming that ϕ mesons

Table 3.25: Geometrical acceptance (η_{geo})

target	Vert.	Horz.
Li	$5.13 \pm 0.08 \times 10^{-2}$	$6.55 \pm 0.09 \times 10^{-2}$
C	$5.02 \pm 0.08 \times 10^{-2}$	$6.46 \pm 0.09 \times 10^{-2}$
Al	$5.02 \pm 0.08 \times 10^{-2}$	$6.55 \pm 0.10 \times 10^{-2}$
Cu	$5.31 \pm 0.09 \times 10^{-2}$	$6.92 \pm 0.10 \times 10^{-2}$

are produced with the natural parity exchange as described in Appendix B since Figures 3.33 and 3.34 in Subsection 3.5.5 seem to suggest that the natural parity exchange dominates. The difference of the geometrical acceptance between vertically and horizontally polarized photon data caused by the assumed decay asymmetry. The attenuation of the charged kaons are included in the geometrical acceptance. The detail of estimation of the geometrical acceptance is discussed in Appendix C.2.1.

3.7.7 Yield for ϕ photo-production from nuclei

The normalized yield for the horizontally polarized photon beam Y_H and that for the vertically one Y_V has been estimated as

$$Y^H(A) = \frac{N_\phi^H}{\eta_{\text{geo}}^H \eta_{\text{DAQ}}^H \eta_{\text{ana}}^H \eta_{\text{att}}^H N_{\text{tag}}^H N_\tau}, \text{ and} \quad (3.48)$$

$$Y^V(A) = \frac{N_\phi^V}{\eta_{\text{geo}}^V \eta_{\text{DAQ}}^V \eta_{\text{ana}}^V \eta_{\text{att}}^V N_{\text{tag}}^V N_\tau},$$

where H and V in the superscript of the variables shows the data for the horizontally or vertically polarized one, and the variables denote:

N_ϕ : number of observed phi events after the background is subtracted,

N_{tag} : effective number of tagger hits,

N_τ : number of target nuclei in unit area,

η_{geo} : geometrical acceptance,

η_{DAQ} : efficiency of data taking system,

η_{ana} : efficiency of the analyzer, and

η_{att} : attenuation of the photon flux in the target material,

which are discussed in this subsection and Subsection 3.6.3. The yield has been obtained by Y^H and Y^V to suppress the difference acceptance due to the different direction of the polarity [57] as

$$Y(A) = \frac{1}{2} \left(Y^H(A) + Y^V(A) \right). \quad (3.49)$$

Figure 3.43 shows the A -dependence of the ϕ photo-production from nuclei. Fitting has been made with the standard parameterization $Y(A) = Y_0 A^\alpha$. The yield of all the ϕ events for each target is found to be proportional to $A^{0.63 \pm 0.05}$. The yield for each target and the fitting parameters are summarized in Table 3.26.

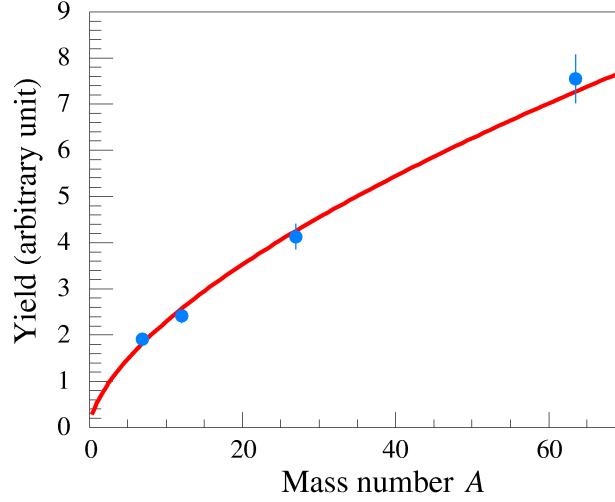


Figure 3.43: A -dependence of the ϕ meson photo-production from nuclei. The data points are fitted with the parameterization $A^{0.63}$. The error bars for the data are statistical only.

Table 3.26: Fitting parameters for A -dependence for all the ϕ mesons. Each yield column shows the yield of ϕ events in the first row, that for the estimated KK background in the second row, The Y_0 , α , and χ^2 columns show the fitting results and χ^2 of the fitting with the function $Y(A) = Y_0 A^\alpha$ in the first row, respectively.

Yield (Li)	Yield (C)	Yield (Al)	Yield (Cu)	Y_0	α	χ^2
1.912 ± 0.112	2.419 ± 0.164	4.134 ± 0.276	7.553 ± 0.526	0.543 ± 0.076	0.625 ± 0.047	1.94
0.122 ± 0.052	0.160 ± 0.081	0.330 ± 0.143	0.371 ± 0.215			

Chapter 4

ϕ - N total cross section

In this chapter, the subtraction of coherent ϕ photo-production and the determination of the ϕ - N total cross section are discussed. The obtained results are compared with some theoretical predictions.

4.1 Determination of the ϕ - N total cross section

In order to determine $\sigma_{\phi N}$ from the A -dependence of the ϕ photo-production yield, an optical model of a Glauber-type multiple scattering theory for incoherent production is applied [48, 47], which is described in Subsection 1.2. In this model, the production cross section from a nucleus, $d\sigma_A^{\text{inc}}/dt$, is described as

$$\frac{d\sigma_A^{\text{inc}}}{dt} = A_{\text{eff}} \frac{d\sigma_N}{dt}, \quad (4.1)$$

where A_{eff} is the effective nucleon number and $d\sigma_N/dt$ is the production cross section on the nucleon. The A_{eff} for ϕ photo-production is expressed as a function of A , $\sigma_{\gamma N}$, and $\sigma_{\phi N}$;

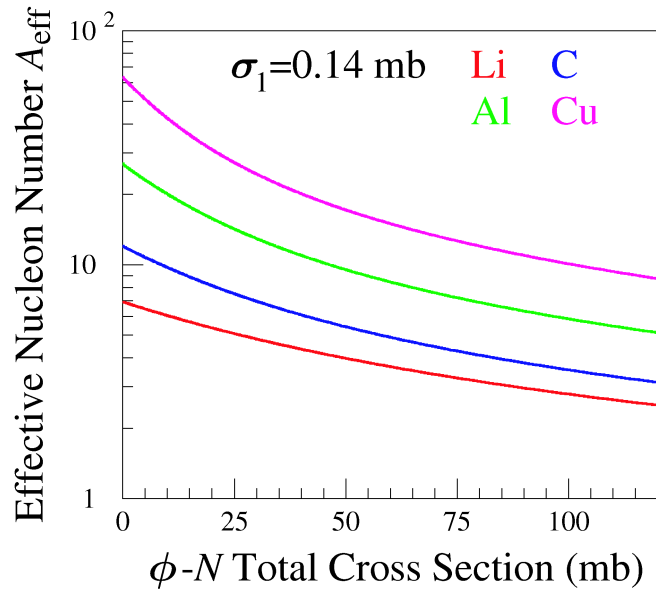
$$A_{\text{eff}}(A, \sigma_{\gamma N}, \sigma_{\phi N}) = \frac{1}{\sigma_{\phi N} - \sigma_{\gamma N}} \int \left(e^{-\sigma_{\gamma N} T(\vec{b})} - e^{-\sigma_{\phi N} T(\vec{b})} \right) d^2b, \quad (4.2)$$

$$T(\vec{b}) = A \int_{-\infty}^{+\infty} \rho(\vec{b}, z) dz,$$

where $\sigma_{\gamma N}$ stands for the total photon-nucleon cross section, \vec{b} denotes the impact vector of the incident photon, and ρ is the nucleon density of the target nucleus. The effect of quasi-elastic collision between a ϕ meson and a nucleon in the nucleus is not included in Equation (4.1) since the direction and energy change of the outgoing ϕ meson is small because of the small direct ϕNN coupling [27]. Assuming the same $d\sigma_N/dt$ for the proton and for the neutron, $\sigma_{\phi N}$ can be derived from the A -dependence of the ϕ photo-production cross sections. In this case, the absolute values of $d\sigma_A^{\text{inc}}/dt$ are not necessary. The normalized number of events for ϕ photo-production from nuclei, defined by Equation (3.49) as $Y(A)$, is described by that for ϕ photo-production on the nucleon, Y_N , and A_{eff} :

$$Y(A) = A_{\text{eff}}(A, \sigma_{\gamma N}, \sigma_{\phi N}) \cdot Y_N, \quad (4.3)$$

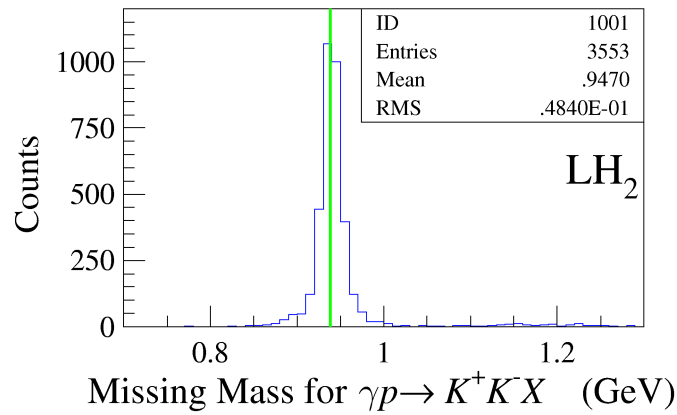
because $Y(A)$ is proportional to the differential cross section $d\sigma_A/dt$ for the fixed t due to the same $|t|$ dependence as described in Subsection 3.5.4. The $\sigma_{\gamma N}$ is fixed to be $140 \mu\text{b}$ in the energy range from 1.5 to 2.4 GeV [49]. The nucleon density is given by normalizing the charge density distribution [81], where the proton and neutron density distributions are assumed to have the same r -dependence, which is described in Appendix F.3. Figure 4.1 shows A_{eff} as a function of $\sigma_{\phi N}$. The same branching ratio of the $\phi \rightarrow K^+ K^-$ process for each target nucleus is used since almost all the ϕ mesons decay outside the nucleus. The measured $Y(A)$ values are fitted by Equation (4.3) with $\sigma_{\phi N}$ and Y_N as free parameters.

Figure 4.1: A_{eff} as a function of $\sigma_{\phi N}$

4.2 Incoherent and coherent ϕ photo-production

Near the threshold of ϕ photo-production, the coherent process is suppressed due to the heavy mass of the ϕ meson. The momentum transfer square $|t|$ is much larger even at forward angles than the momentum transfer square region where the coherent process is dominantly observed ($|t| < 0.01 \text{ GeV}^2/c^2$). The minimum $|t|$ are 0.0537, 0.0528, 0.0522, 0.0519 GeV^2 for Li, C, Al, and Cu at $E_\gamma = 2.4 \text{ GeV}$, respectively. In order to determine the ϕ -N total cross section by Equation (1.6) in Subsection 1.2, the yields for incoherent ϕ photo-production are needed.

Whether the ϕ mesons are produced coherently or incoherently has been investigated by using

Figure 4.2: Missing mass m_X for $\gamma p \rightarrow K^+ K^- X$ in LH_2 . The green line shows the nominal mass of the proton.

missing mass. The missing mass m_X for the reaction $\gamma A \rightarrow K^+ K^- X$ is given by

$$\begin{aligned} m_X^2 &= E_X^2 - (p_X^x)^2 - (p_X^y)^2 - (p_X^z)^2 \\ &= (E_\gamma + m_A - E_{K^+} - E_{K^-})^2 \\ &\quad - \left\{ (-p_{K^+}^x - p_{K^-}^x)^2 + (-p_{K^+}^y - p_{K^-}^y)^2 + (E_\gamma - p_{K^+}^z - p_{K^-}^z)^2 \right\}, \end{aligned} \quad (4.4)$$

where m_A shows the target mass, $(E_X, p_X^x, p_X^y, p_X^z)$, $(E_{K^+}, p_{K^+}^x, p_{K^+}^y, p_{K^+}^z)$, and $(E_{K^-}, p_{K^-}^x, p_{K^-}^y, p_{K^-}^z)$ stand for the four dimensional momenta of missing particle and K^+ , and K^- , respectively. Here, the incident γ beam is assumed to go on a parallel with the z axis. Figure 4.2 shows the missing mass distribution in LH_2 assuming that the reaction should be $\gamma p \rightarrow K^+ K^- X$. The missing mass distribution is fitted with a Gaussian in the region from 0.925 to 0.955 GeV, the mass 0.9378 ± 0.0002 GeV and the width 0.0112 ± 0.0004 GeV are obtained. The ϕ mesons are actually produced on the proton. Figure 4.3 shows the missing mass m_X distributions for the reaction $\gamma A \rightarrow K^+ K^- X$ in

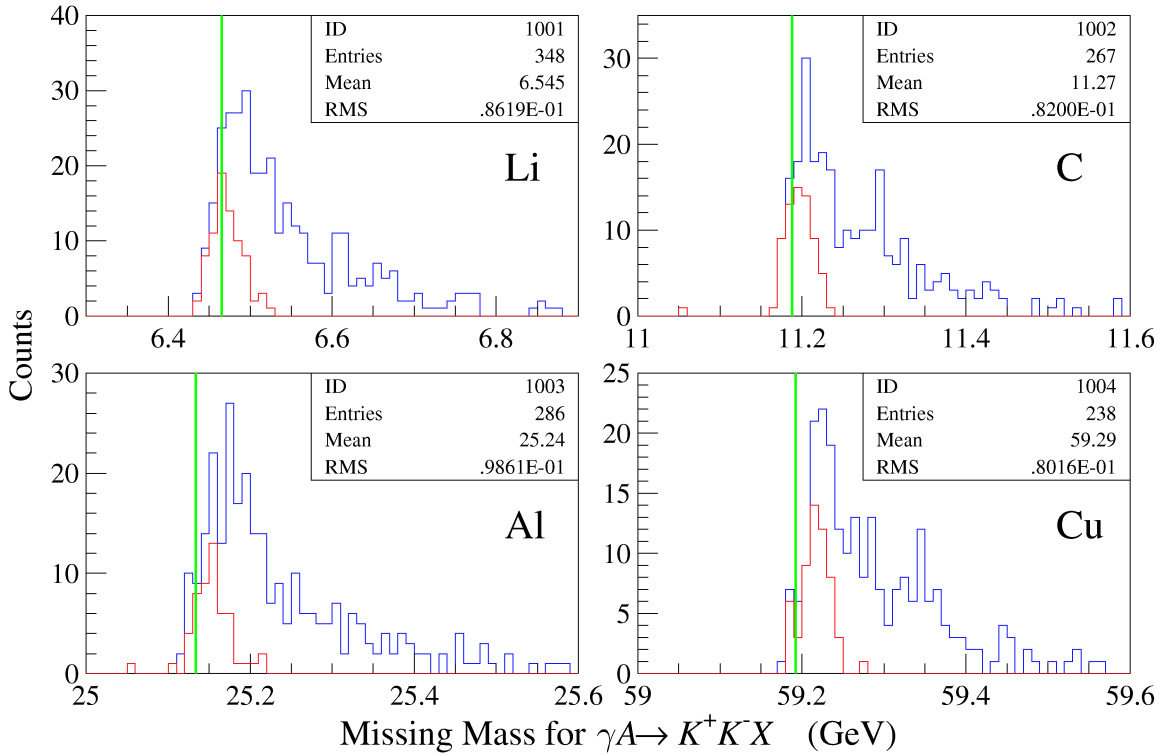


Figure 4.3: Missing mass m_X of $\gamma A \rightarrow K^+ K^- X$ in the real data. The blue lines show all the events, and the red ones show the events with $|t| < 0.1 \text{ GeV}^2$. The green lines show the nominal mass of the nuclei.

the four nuclear targets. These missing mass distributions in nuclear targets have much wider peaks than that in LH_2 . If ϕ mesons are produced only in the coherent process, the width of the peak in the missing mass distribution is widened only by the resolution of the detector system, energy loss and multiple scattering in the target material, and these are in the same order as LH_2 target. The coherent process can not be dominant in the ϕ photo-production from nuclei in this energy range basically. The events with $|t| < 0.1 \text{ GeV}^2$, which are shown by the red lines in Figure 4.3, make the similar narrow peaks to the LH_2 ones, and these positions are close to the masses of the nuclei. The condition $|t| < 0.1 \text{ GeV}^2$ can enhance the coherent process, and this momentum transfer range corresponds to the size of nuclei (3~4 fm).

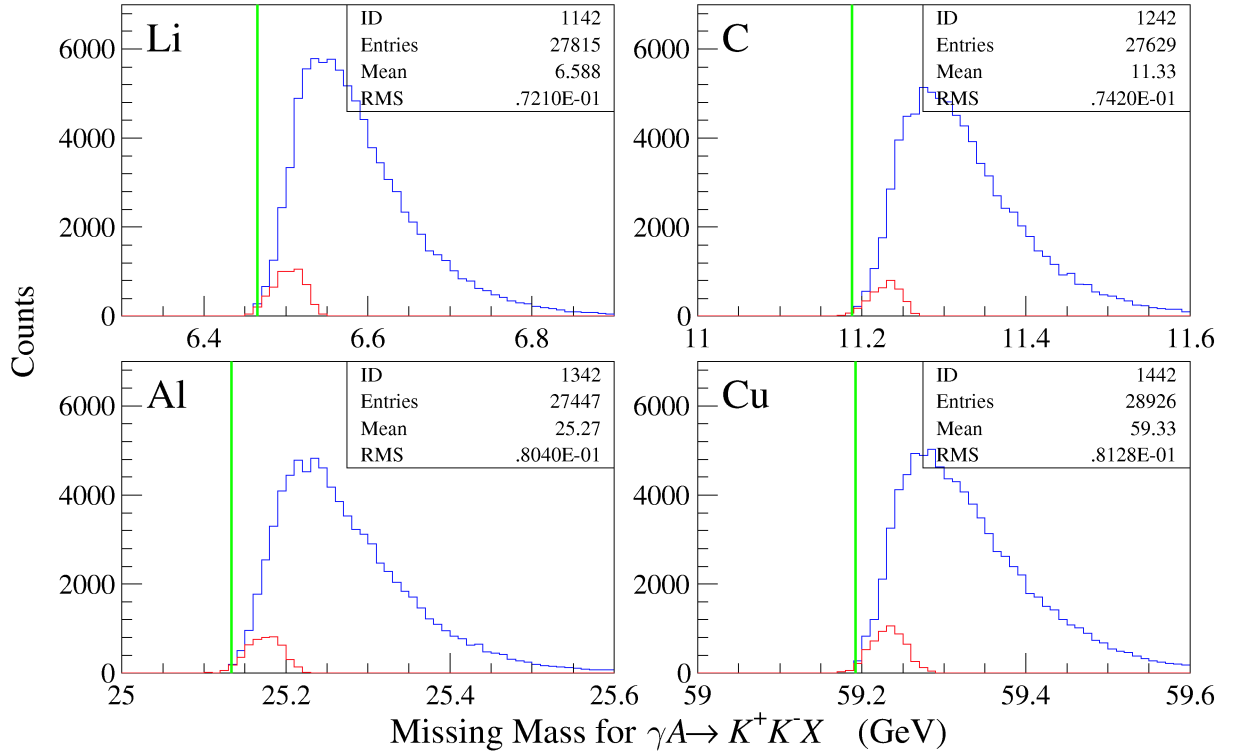


Figure 4.4: Missing mass m_X of $\gamma A \rightarrow K^+ K^- X$ for incoherent production in the MC simulation. The blue lines show all the events, and the red ones show the events with $|t| < 0.1 \text{ GeV}^2$. The green lines show the nominal mass of the nuclei.

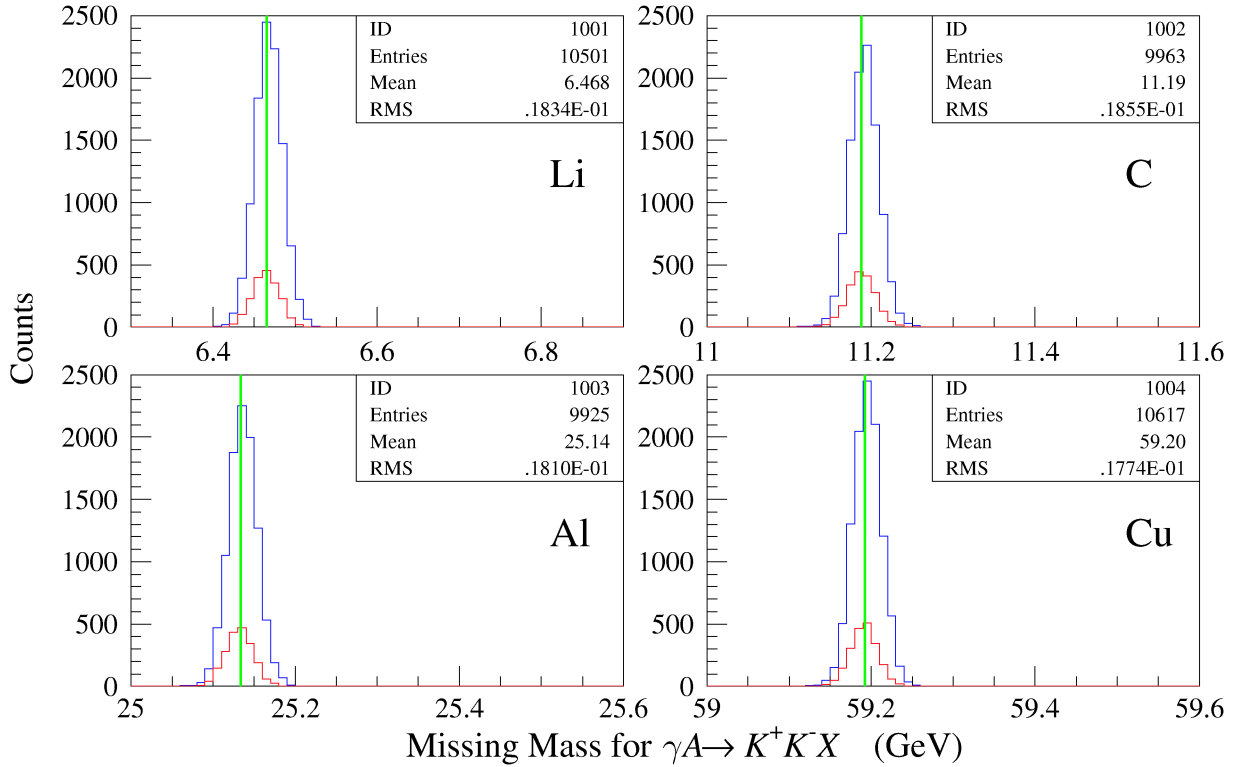


Figure 4.5: Missing mass m_X of $\gamma A \rightarrow K^+ K^- X$ for coherent production in the MC simulation. The blue lines show all the events, and the red ones show the events with $|t| < 0.1 \text{ GeV}^2$. The green lines show the nominal mass of the nuclei.

The missing mass m_X distribution for the reaction $\gamma A \rightarrow K^+ K^- X$ has been investigated for the incoherently and coherently produced ϕ mesons in the MC simulation. Figure 4.4 and 4.5 show the missing mass distributions for the incoherent and coherent processes, respectively. Here, the coherent ϕ events are generated as a two body phase space, and large $|t|$ events are enhanced. The coherent process events concentrate at the mass of the nucleus in these distributions, and a fraction of the events m_X are close to the mass of the nucleus is very small for the incoherent process.

Let us define the missing energy E_x (excitation energy) as

$$E_x = m_X - m_A, \quad (4.5)$$

where m_X stands for the missing mass m_X for the reaction $\gamma A \rightarrow K^+ K^- X$. Figure 4.6 shows the

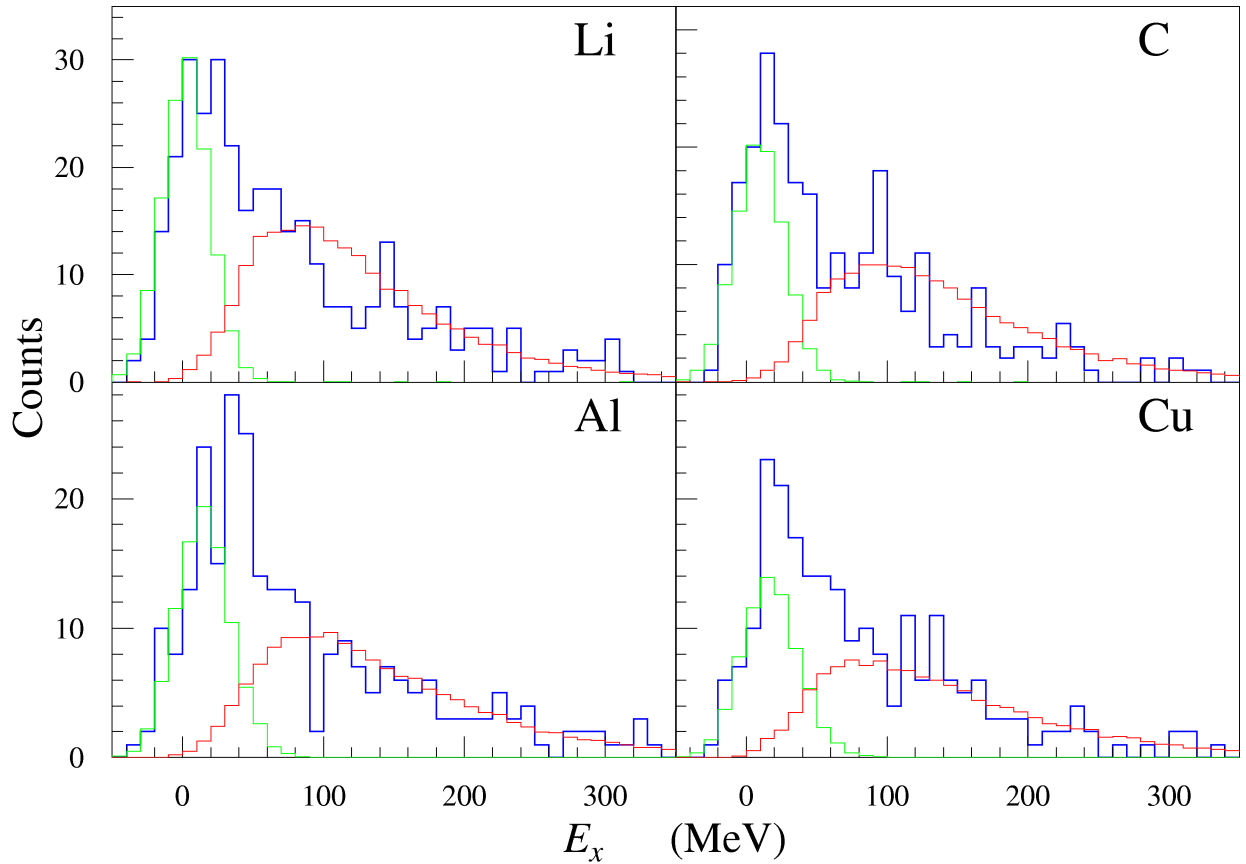


Figure 4.6: The blue histograms show the missing energy distributions for the real data. The green and red ones show the missing energy distributions for the coherent and incoherent processes, respectively. The normalization of both the coherent and incoherent processes are made by eyes.

comparison of the missing energy distributions between the real and MC simulation data. The missing energy distributions of coherent ϕ photo-production concentrate at 0 MeV within the experimental resolution (19 MeV), and those of incoherent production are distributed in the positive E_x region.

4.3 Subtraction of the coherent process contribution

In this subsection, the estimation of the coherent process is determined with a help of theoretical calculations. The amplitude for the $\gamma N \rightarrow \phi N$ elementary process will have a spin-flip (sf) and a non-spin-flip (nsf) parts:

$$T_{\gamma N \rightarrow \phi N} = T_{\text{nsf}} + T_{\text{sf}}. \quad (4.6)$$

To evaluate the cross section of the coherent process in the nucleus, the sum over spin, isospin, and nucleons is performed for the amplitude.

$$\sigma_{\text{coh}} \sim \left| \sum_{\substack{\text{spin, isospin,} \\ \text{nucleons}}} T_{\gamma N \rightarrow \phi N} \right|^2 \sim |T_{\text{nsf}}|^2 \quad (4.7)$$

The spin-flip part vanishes when summing over spin when the target is spin-saturated. The cross section of the coherent process is affected only by the non-spin-flip part, thus differential cross section can be expressed by the nuclear form factor $F(q)$,

$$\frac{d\sigma_{\text{coh}}}{d\Omega} = |A F(q)|^2 \quad (4.8)$$

The nuclear form factor $F(q)$ is evaluated by the Fourier transform of the nucleon density distribution,

$$A F(q) = \int d\vec{r} e^{i\vec{q}\cdot\vec{r}} \rho(\vec{r}) = \frac{4\pi}{q} \int_0^\infty dr r \rho(r) \sin(qr). \quad (4.9)$$

The density nuclear profiles are obtained from the experimental parameterization of the charge distributions [81], where the nucleon density is normalized assuming the same radial dependence of the proton and neutron density distribution so that $\int \vec{r} \rho(r) = A$.

On the contrary, in the incoherent process, the square of the amplitude should be performed before the sum over spin, isospin, and nucleons:

$$\sigma_{\text{inc}} \sim \sum_{\substack{\text{spin, isospin,} \\ \text{nucleons}}} |T_{\gamma N \rightarrow \phi N}|^2 \sim |T_{\text{nsf}}|^2 + |T_{\text{sf}}|^2 \quad (4.10)$$

Therefore, the ratio between the coherent and incoherent process can be expressed as:

$$\frac{d\sigma_{\text{coh}}/dt}{d\sigma_{\text{inh}}/dt} \sim \frac{|A F(q)|^2}{A} \frac{|T_{\text{nsf}}|^2}{|T_{\text{nsf}}|^2 + |T_{\text{sf}}|^2} \leq A |F(q)|^2 \quad (4.11)$$

Figure 4.7 shows the ratio of the coherent to incoherent cross sections as a function of the incident γ energy, where the integration in the kinematical region $|t|_{\text{min}} < |t| < |t|_{\text{max}}$ is also performed for each process. The ratio does not increase monotonically as a consequence of the oscillatory behaviors of the nuclear form factor. The relation between q^2 and t is described for the target mass m_A ,

$$q^2 = \frac{t}{4m_A^2} (t - 4m_A^2). \quad (4.12)$$

Figure 4.8 shows the relation between q^2 and t . The differential cross section $d\sigma/dt$ can be expressed by using the initial and final momenta in the center of mass frame p_i, p_f ,

$$\frac{d\sigma_{\text{coh}}}{dt} = \frac{\pi |A F(q)|^2}{p_i p_f} \quad (4.13)$$

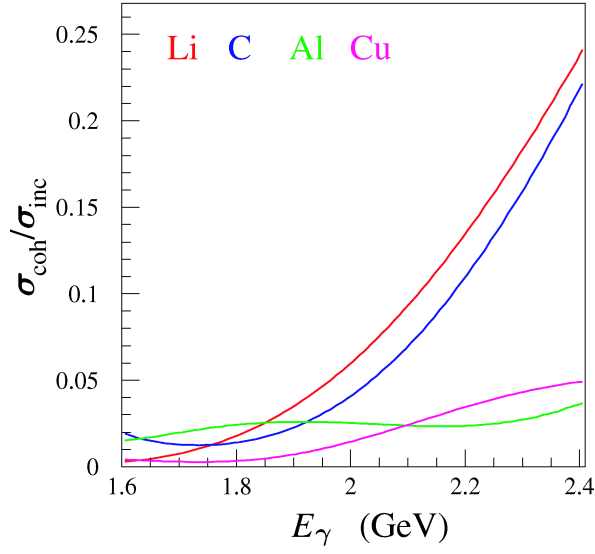


Figure 4.7: Coherent to incoherent ratio

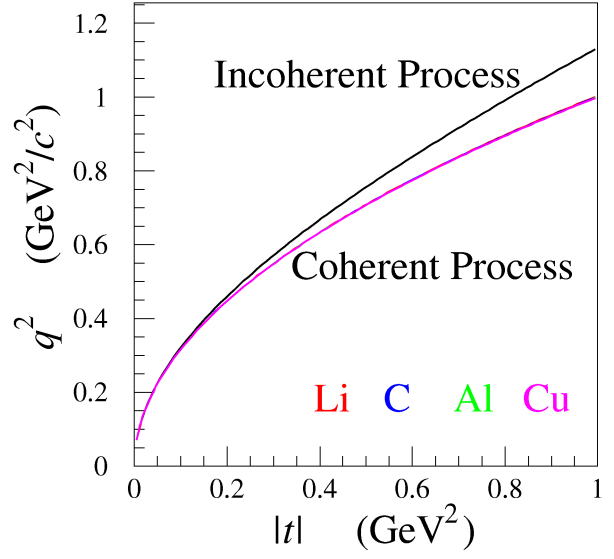
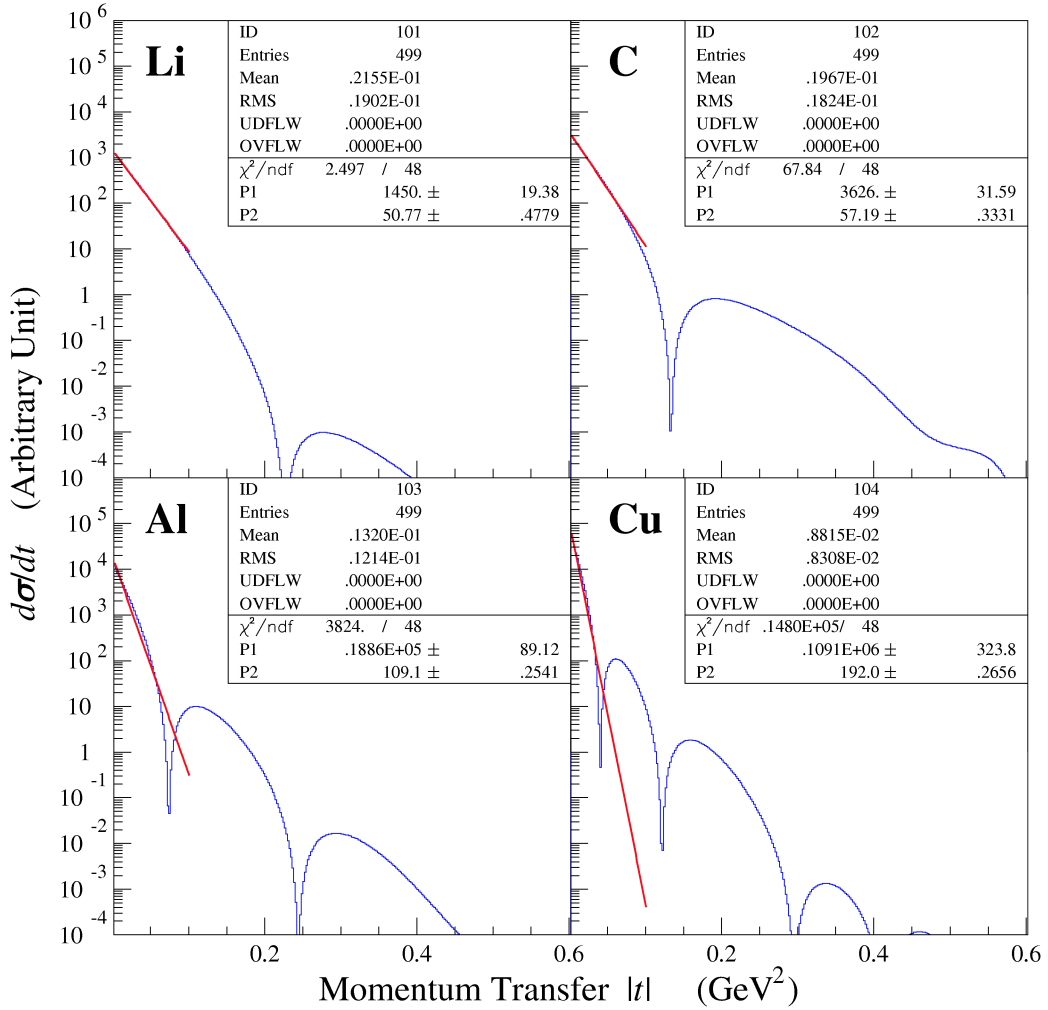

 Figure 4.8: Relation between q^2 and t

 Figure 4.9: Coherent differential cross section $d\sigma_{\text{coh}}/dt$. The red lines show the fitting results with a function $d\sigma_{\text{coh}}/dt = C \exp(-bt)$ in the region $|t|=0.0-0.1$ GeV².

Table 4.1: Fitting results for the low $|t|$ coherent differential cross section

Target	$d\sigma_{\text{coh}}/dt _{t=0}$ (Arbitrary Unit)	b (GeV^{-2}/c^{-2})
Li	$1.450 \pm 0.019 \times 10^3$	50.8 ± 0.5
C	$3.626 \pm 0.032 \times 10^3$	57.2 ± 0.3
Al	$1.886 \pm 0.009 \times 10^4$	109.2 ± 0.3
Cu	$1.091 \pm 0.003 \times 10^5$	192.0 ± 0.3

Figure 4.9 shows the differential cross section in an arbitrary unit. The differential cross section is fitted with the function $d\sigma_{\text{coh}}/dt|_{t=0} \exp(-b|t|)$ in the low $|t|$ region ($|t| = 0.0\text{--}0.1 \text{ GeV}^2$), and fitting results are summarized in Table 4.3. Target mass number dependence of the differential cross section at optical point $d\sigma_{\text{coh}}/dt(A)|_{t=0}$, and the slope of the exponential function for the differential cross section $b(A)$ is fitted with the function $C A^\alpha$. The fitting results for the $d\sigma_{\text{coh}}/dt(A)|_{t=0}$ are

$$\begin{aligned} C &= 26.4 \pm 0.4, \text{ and} \\ \alpha &= 1.998 \pm 0.003, \end{aligned} \quad (4.14)$$

and those for $b(A)$ are

$$\begin{aligned} C &= 11.6 \pm 0.2, \text{ and} \\ \alpha &= 0.674 \pm 0.005. \end{aligned} \quad (4.15)$$

Approximately $d\sigma_{\text{coh}}/dt(A)|_{t=0} \propto A^2$, and $b(A) \propto R^2 \sim A^{2/3}$ can be valid.

The number of coherent production ϕ events for each nuclear target is assumed to be proportional to the integration of the coherent differential cross section $d\sigma_{\text{coh}}/dt$ from $|t|_{\text{min}}$ to $|t|_{\text{max}}$ for each incident γ energy E_γ . Figure 4.10 shows the cross section of coherent ϕ photo-production from nuclei. Here, no other E_γ dependence is not taken into account than the integration region $|t|_{\text{min}}$ and $|t|_{\text{max}}$.

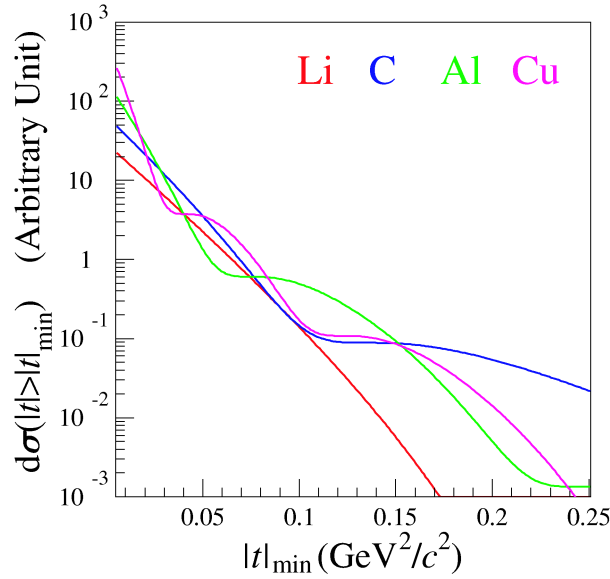


Figure 4.10: Cross sections for coherent production $\sigma_{\text{coh}}(|t| > |t|_{\text{min}})$. An integration over $|t|$ larger than $|t|_{\text{min}}$ has been performed.

The coherent cross section is larger for the larger mass number target when all the $|t|$ region is allowed ($|t|_{\min} = 0$ is assumed). The $|t| > |t|_{\min}$ cross section of the coherent process has a similar value for each target under the condition $|t|_{\min} \sim 0.05 \text{ GeV}^2$ for $E_\gamma \sim 2.4 \text{ GeV}$.

The number of the coherent ϕ events are estimated to be proportional to be 11.2, 16.2, 10.2, and 24.3 in a unit number of target nuclei (N_{tgt}) in an effective number of incident γ rays ($N_\gamma C_{\text{att}}$) for Li, C, Al, and Cu, respectively, where only the integration cut point t_{\min} depends on the incident γ energy E_γ . The number of the coherent ϕ events are estimated for each target nuclei, each polarization assuming that the missing energy for $\gamma A \rightarrow \phi A$ have a symmetric shape, and that all the negative missing energy events for Li are produced in the coherent process. Figure 4.11 shows $\gamma A \rightarrow \phi A$ missing energy distribution for Li. The number of negative missing energy events are 14 and 27 for

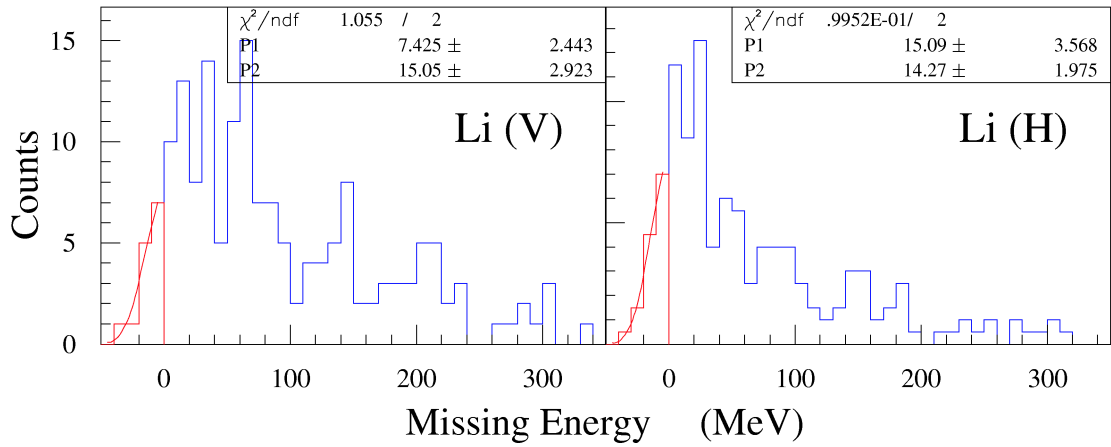


Figure 4.11: Missing energy distribution in Li. The red histograms show the events with the negative missing energy.

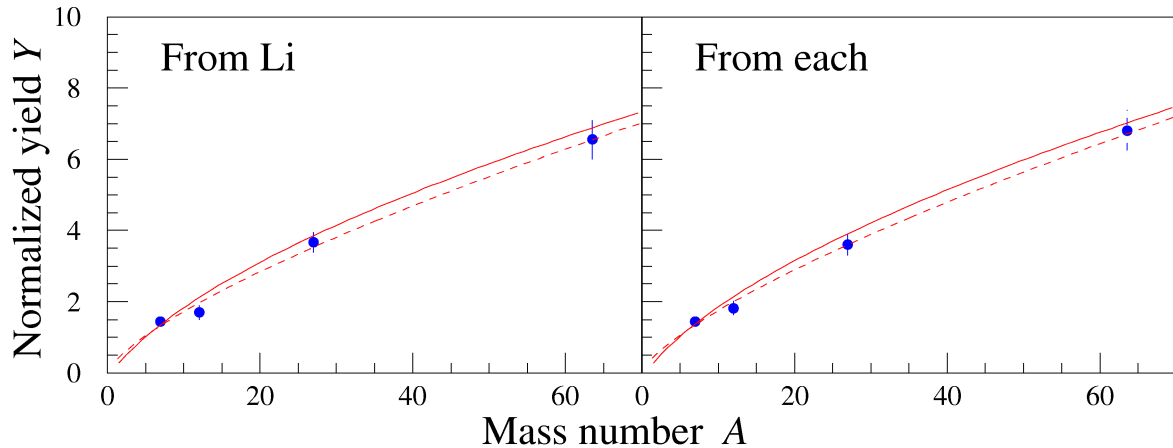


Figure 4.12: A -dependence with subtraction of the coherent ϕ events. The left panel shows the A -dependence where each yield is evaluated subtracting the estimated coherent ϕ events from the negative missing energy events in Li as an input, and the right one shows that where each yield is evaluated subtracting twice number of negative missing energy events. The solid and dashed curves show the fitting results with the functions $Y(A) = Y_N A_{\text{eff}}(A)$ and $Y(A) = Y_0 A^\alpha$, respectively. The fitting results are summarized in Table 4.3.

vertically and horizontally polarized beam, respectively. The estimated number of coherent ϕ events

Table 4.2: Estimated number of coherent ϕ events

polarization	Li	C	Al	Cu
Vert.	28.0 ± 7.5 (14)	28.1 ± 7.5 (10)	9.4 ± 2.5 (9)	10.2 ± 2.7 (7)
Horz.	54.0 ± 10.4 (27)	44.8 ± 8.6 (20)	21.5 ± 4.1 (8)	20.2 ± 3.9 (4)

for each nuclear target for each polarization is summarized in Table 4.3 together with the number of negative missing energy events in parentheses. Each yield for the incoherent process has been evaluated subtracting the estimated coherent ϕ events ("From Li") or subtracting twice number of negative missing energy events ("From Each"). The yields are fitted with the function $Y(A) = Y_0 A^\alpha$ and $Y(A) = A_{\text{eff}}(A, \sigma_{\gamma N}, \sigma_{\phi N}) \cdot Y_N$. The yields $Y(A)$ as a function of mass number A and fitting results are shown in Figure 4.12 and are summarized in Table 4.3.

Table 4.3: Fitting results of the yield after the coherent ϕ events are subtracted with the "From Li" and From "Each" methods. Both methods have two rows. Each yield column shows the yield of ϕ events in the first row, and that of the non-resonant KK background in the second row. The Y_N/Y_0 , $\sigma_{\phi N}/\alpha$, and χ^2 columns show the fitting results and χ^2 of the fitting with the functions $Y(A) = Y_N A_{\text{eff}}(A)$, $Y(A) = Y_0 A^\alpha$ in the first and second rows, respectively.

Method	Yield (Li)	Yield (C)	Yield (Al)	Yield (Cu)	Y_A/Y_0	$\sigma_{\phi N} \text{ (mb)}/\alpha$	χ^2
From Li	1.435 ± 0.135	1.698 ± 0.199	3.670 ± 0.285	6.554 ± 0.529	0.298 ± 0.055	$35.1^{+17.1}_{-11.3}$	1.35
	0.122 ± 0.052	0.160 ± 0.081	0.330 ± 0.143	0.371 ± 0.215	0.327 ± 0.073	0.722 ± 0.069	2.74
From Each	1.435 ± 0.135	1.821 ± 0.197	3.597 ± 0.305	6.815 ± 0.572	0.298 ± 0.055	$34.1^{+16.5}_{-11.1}$	0.77
	0.122 ± 0.052	0.160 ± 0.081	0.330 ± 0.143	0.371 ± 0.215	0.328 ± 0.072	0.727 ± 0.068	1.33

4.4 Selection of the kinematical region for incoherent production

As a cross check, the coherent process contribution is removed by selecting the kinematical region for incoherent production. The missing energy E_x distributions of coherent ϕ photo-production concentrate at 0 MeV, and the events with E_x close to 0 MeV are few for incoherent ϕ production. Thus, E_x is required to be larger than the threshold E_x^{thr} to select the incoherent events. Figure 4.13

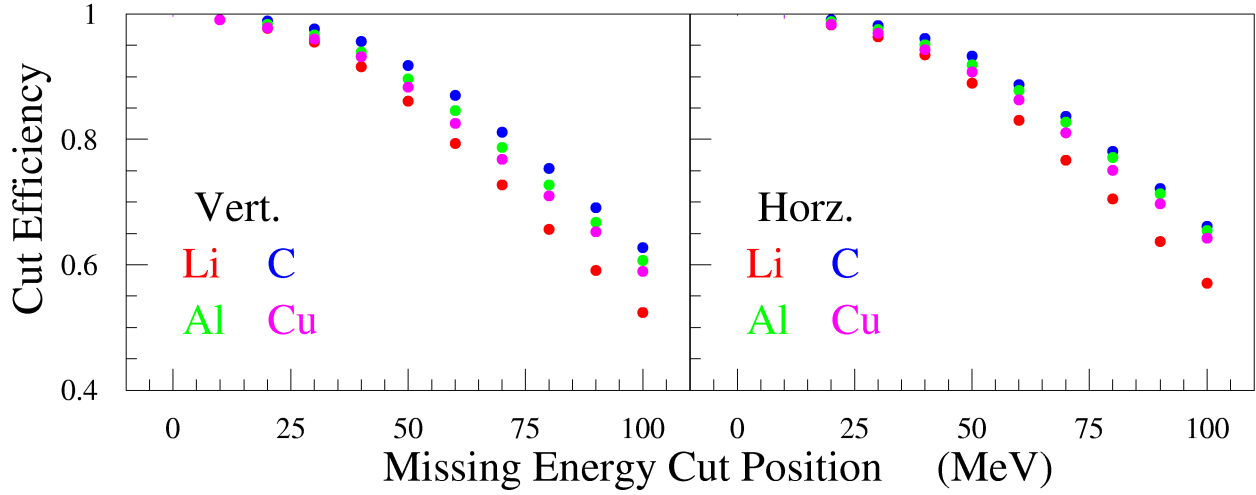


Figure 4.13: Efficiency of the missing energy cut. The left panel shows the efficiency for the vertically polarized photon data, and the right one shows that for the horizontally polarized ones.

shows the efficiency of this cut for incoherent ϕ photo-production estimated by the MC simulation. The difference of the efficiencies among the four targets are somewhat large if E_x^{thr} is larger than 60

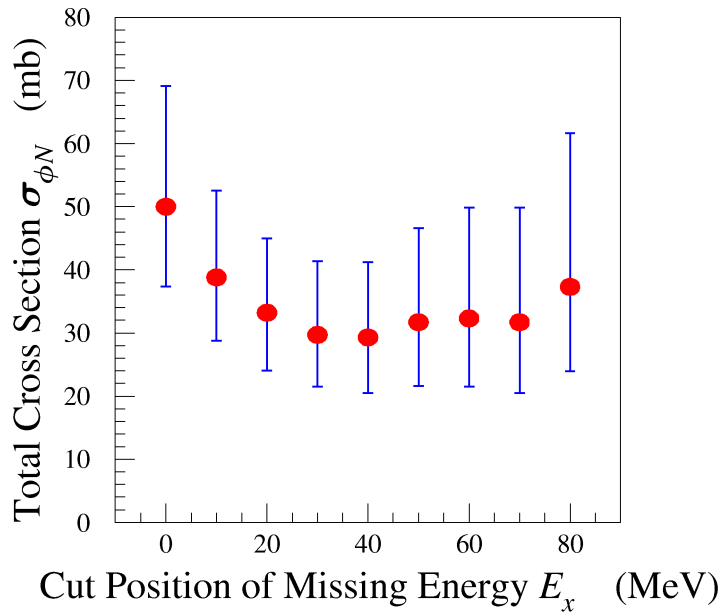


Figure 4.14: ϕ - N total cross section $\sigma_{\phi N}$ according to the E_x cut

Table 4.4: Fitting results of the yield with $E_x \geq E_x^{\text{thr}}$. Every cut condition has three rows, where each yield column shows the yield of ϕ events in the first row, those of the non-resonant KK background in the second row, used number of KK events in the standard ϕ cut in the third row. The Y_N/Y_0 , $\sigma_{\phi N}/\alpha$, and χ^2 columns show the fitting results and χ^2 of the fitting with the functions $Y(A) = Y_N A_{\text{eff}}(A)$, $Y(A) = Y_0 A^\alpha$ in the first and second rows, respectively.

E_x^{thr} (MeV)	Yield (Li)	Yield (C)	Yield (Al)	Yield (Cu)	Y_N / Y_0	$\sigma_{\phi N}$ (mb) / α	χ^2
No Cut	1.912 ± 0.112	2.419 ± 0.164	4.134 ± 0.276	7.553 ± 0.526	0.558 ± 0.067	$70.8^{+31.7}_{-19.0}$	0.44
	0.122 ± 0.052	0.160 ± 0.081	0.330 ± 0.143	0.371 ± 0.215	0.543 ± 0.076	0.625 ± 0.047	1.94
	188,160	145,122	137,149	123,115			
0	1.675 ± 0.106	2.217 ± 0.157	3.900 ± 0.269	7.273 ± 0.517	0.416 ± 0.059	$50.0^{+19.1}_{-12.7}$	0.23
	0.122 ± 0.052	0.149 ± 0.078	0.314 ± 0.139	0.340 ± 0.206	0.441 ± 0.066	0.668 ± 0.049	1.09
	161,146	128,116	131,138	119,109			
10	1.512 ± 0.102	2.039 ± 0.152	3.773 ± 0.265	7.037 ± 0.511	0.339 ± 0.052	$38.8^{+13.7}_{-10.0}$	0.21
	0.117 ± 0.051	0.150 ± 0.078	0.301 ± 0.137	0.341 ± 0.207	0.373 ± 0.058	0.704 ± 0.051	0.81
	139,138	117,108	126,133	114,106			
20	1.388 ± 0.098	1.780 ± 0.143	3.590 ± 0.258	6.666 ± 0.500	0.288 ± 0.046	$33.2^{+11.8}_{-9.2}$	1.30
	0.112 ± 0.051	0.141 ± 0.076	0.263 ± 0.130	0.317 ± 0.202	0.317 ± 0.053	0.731 ± 0.054	2.20
	126,126	101,95	118,125	104,102			
30	1.235 ± 0.095	1.634 ± 0.138	3.371 ± 0.250	6.061 ± 0.484	0.249 ± 0.040	$29.7^{+11.7}_{-8.2}$	1.06
	0.116 ± 0.052	0.131 ± 0.074	0.214 ± 0.117	0.326 ± 0.208	0.281 ± 0.049	0.742 ± 0.057	1.66
	104,118	90,88	110,112	95,90			
40	1.141 ± 0.094	1.500 ± 0.134	3.180 ± 0.247	5.591 ± 0.474	0.229 ± 0.038	$29.3^{+11.9}_{-8.8}$	1.40
	0.120 ± 0.054	0.123 ± 0.072	0.204 ± 0.116	0.335 ± 0.214	0.257 ± 0.048	0.745 ± 0.060	1.96
	96,104	80,80	101,103	84,83			
50	1.099 ± 0.096	1.342 ± 0.131	2.929 ± 0.243	5.171 ± 0.468	0.221 ± 0.039	$31.7^{+14.9}_{-10.1}$	2.28
	0.127 ± 0.058	0.128 ± 0.075	0.195 ± 0.115	0.322 ± 0.217	0.244 ± 0.051	0.737 ± 0.067	3.10
	85,99	70,70	89,92	72,76			
60	1.068 ± 0.098	1.313 ± 0.134	2.667 ± 0.240	5.124 ± 0.483	0.214 ± 0.039	$32.3^{+17.5}_{-10.8}$	1.47
	0.123 ± 0.059	0.136 ± 0.080	0.195 ± 0.121	0.345 ± 0.234	0.235 ± 0.053	0.736 ± 0.073	2.20
	76,90	65,66	75,83	67,72			
70	1.029 ± 0.101	1.292 ± 0.137	2.594 ± 0.244	4.982 ± 0.498	0.206 ± 0.039	$31.7^{+18.1}_{-11.2}$	1.02
	0.128 ± 0.063	0.133 ± 0.082	0.185 ± 0.121	0.372 ± 0.252	0.227 ± 0.054	0.738 ± 0.076	1.59
	72,76	61,60	67,77	62,65			
80	1.014 ± 0.106	1.303 ± 0.142	2.509 ± 0.252	4.689 ± 0.508	0.219 ± 0.041	$37.3^{+24.3}_{-13.4}$	0.44
	0.134 ± 0.069	0.128 ± 0.083	0.201 ± 0.131	0.407 ± 0.277	0.240 ± 0.059	0.712 ± 0.080	0.90
	64,70	56,57	61,69	54,58			

MeV. The yields $Y^{\text{H}}(A)$ and $Y^{\text{V}}(A)$ in Eq. (3.48) are divided also by the efficiency, and are given by

$$\begin{aligned}
 Y^{\text{H}}(A) &= \frac{N_{\phi}^{\text{H}}}{\eta_{\text{ME}}^{\text{H}} \eta_{\text{geo}}^{\text{H}} \eta_{\text{DAQ}}^{\text{H}} \eta_{\text{ana}}^{\text{H}} \eta_{\text{att}}^{\text{H}} N_{\text{tag}}^{\text{H}} N_{\tau}}, \text{ and} \\
 Y^{\text{V}}(A) &= \frac{N_{\phi}^{\text{V}}}{\eta_{\text{ME}}^{\text{V}} \eta_{\text{geo}}^{\text{V}} \eta_{\text{DAQ}}^{\text{V}} \eta_{\text{ana}}^{\text{V}} \eta_{\text{att}}^{\text{V}} N_{\text{tag}}^{\text{V}} N_{\tau}},
 \end{aligned} \tag{4.16}$$

where η_{ME} shows the efficiency of the missing energy cut.

The yield are fitted with the function $Y(A) = Y_0 A^\alpha$ and $Y(A) = A_{\text{eff}}(A, \sigma_{\gamma N}, \sigma_{\phi N}) \cdot Y_N$ for various E_x^{thr} values. Table 4.4 shows the yields of the ϕ events, those of the estimated non-resonant $K^+ K^-$ contribution, used $K^+ K^-$ events in the standard ϕ cut together with the fitting parameters for various E_x^{thr} values. Figure 4.14 shows $\sigma_{\phi N}$ as a function of E_x^{thr} . Fitting results are stable from $E_x^{\text{thr}} = 30$

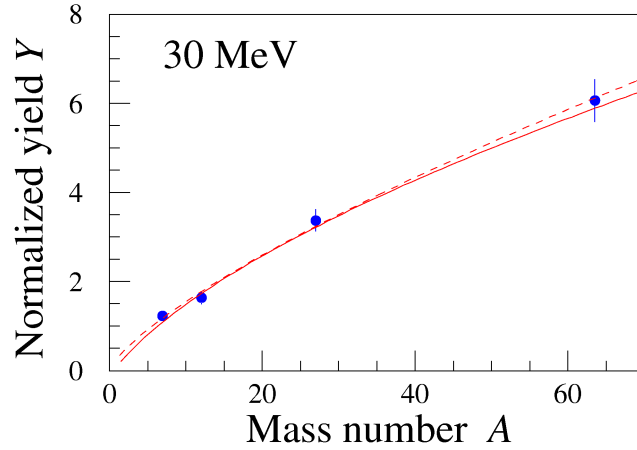


Figure 4.15: A -dependence with the 30 MeV missing energy cut. The solid and dashed curves show the fitting results with the functions $Y(A) = Y_N A_{\text{eff}}(A)$ ($\sigma_{\phi N} = 29.7_{-8.2}^{+11.7}$ mb) and $Y(A) = Y_0 A^\alpha$ ($\alpha = 0.742 \pm 0.057$), respectively. The fitting results are summarized in Table 4.4.

up to 80 MeV. The cuts with the smaller E_x^{thr} than 20 MeV make $\sigma_{\phi N}$ larger, this implies the lighter target has more coherent ϕ events. When the coherent events are more contaminated in the lighter target, the yield is enhanced in the lighter target, and it makes $\sigma_{\phi N}$ larger and α smaller.

The $\sigma_{\phi N}$ is $29.7_{-8.2}^{+11.7}$ mb for the 30 MeV cut, in which the statistics are highest. This value is consistent with the values for the yields after the coherent contributions are subtracted as discussed in Subsection 4.3. Figure 4.15 shows the yields as a function of mass number A together with the fitting results.

4.5 Comparison with the theoretical calculations

A quark model [29] gives a prediction of 13.0 ± 1.5 mb for $\sigma_{\phi N} = \sigma_{\phi p}$ [28]. This value is deduced from the total $\pi^\pm p$ and $K^+ p$ cross sections obtained at high energy limit as

$$\sigma_{\phi p} = 2(\sigma_{K^+ p} - \sigma_{\pi^+ p} + \sigma_{\pi^- p}). \quad (4.17)$$

The vector meson dominance model (VDM) indicates $\sigma_{\phi N} = 7.7\text{--}8.7$ mb at $E_\gamma = 4.6\text{--}6.7$ GeV [28], which is obtained from the relation between $\sigma_{\phi N}$ and $d\sigma/dt|_{t=0}$:

$$\left. \frac{d\sigma_{\gamma p \rightarrow \phi p}}{dt} \right|_{t=0} = \frac{\alpha}{64\pi} \frac{1 + \alpha_{\phi p}^2}{\gamma_\phi^2/4\pi} \sigma_{\phi p}, \quad (4.18)$$

where α stands for the fine structure constant, $\alpha_{\phi p}$ denotes the the real-imaginary ratio of ϕ -proton scattering amplitude, $\gamma^2/4\pi$ shows the γ - ϕ coupling constant, and the measured differential cross section $d\sigma_{\gamma p \rightarrow \phi p}/dt$ for ϕ photo-production on the proton has been used. Both the two values are $\sigma_{\phi N}$ in free space, which are smaller than the present results (about 35 mb), indicating the modification of the ϕ - N scattering amplitude in the nuclear medium.

Cabrera *et al.* [27] calculated the A -dependence of the ϕ photo-production cross section from nuclei in terms of the variable $P_{\text{out}} = \sigma_A/(A\sigma_N)$, which represents the probability of a photo-produced ϕ meson going out the nucleus. The P_{out} was deduced from the yields for incoherent ϕ photo-production as

$$P_{\text{out}} = \frac{\sigma_A}{A\sigma_N} = \frac{A_{\text{eff}}}{A} = \frac{Y(A)}{Y_N A}, \quad (4.19)$$

where $Y(A)$ and Y_N stand for the yield and coefficients of the fitting results with the function of $Y(A) = Y_N A_{\text{eff}}$, respectively.

The probabilities P_{out} are obtained for the yields after the estimated coherent ϕ contributions are subtracted as described in Subsection 4.3, and are summarized in Table 4.5. Figure 4.16 shows P_{out} as a function of A together with the theoretical calculations given by Cabrera *et al.* [27]. The probabilities

Table 4.5: Probability P_{out} with subtraction of the coherent ϕ events

Method	Li	C	Al	Cu
From Li	0.694 ± 0.065	0.474 ± 0.056	0.456 ± 0.038	0.347 ± 0.029
From Each	0.694 ± 0.065	0.509 ± 0.055	0.447 ± 0.038	0.360 ± 0.030

P_{out} are smaller than the theoretical predictions. The reduction of the ϕ meson flux obtained in the present experiment is almost twice as much as the theoretical predictions. The absolute value of P_{out} depends on the applied model to deduce $\sigma_{\phi N}$. However, the ratio of P_{out} for different targets is model-independent. The ratios $P_{\text{out}}(\text{C})/P_{\text{out}}(\text{Li})$, $P_{\text{out}}(\text{Al})/P_{\text{out}}(\text{Li})$, and $P_{\text{out}}(\text{Cu})/P_{\text{out}}(\text{Li})$ are 0.683 ± 0.103 , 0.657 ± 0.082 , and 0.500 ± 0.063 , respectively, for the yields after the coherent ϕ events estimated from the negative missing energy events in Li are subtracted. Note that the average momentum of the detected ϕ mesons are $\langle P_\phi \rangle = 1.8$ GeV/ c as described in Subsection 3.5.3. The ratios are 0.733 ± 0.105 , 0.644 ± 0.081 , and 0.519 ± 0.065 for the yields after the coherent ϕ events estimated from the negative missing energy events in each target are subtracted, respectively. Figure 4.17 shows the ratios. These ratios are 0.97–0.98, 0.91–0.94, and 0.85–0.88, respectively, for $P_\phi = 2.0$ GeV/ c regardless of the Pauli-blocking effect in the theoretical calculations [27]. The ratios are smaller than the theoretical predictions. The theoretical calculations underestimate the decrease of photo-produced ϕ meson flux in the nucleus.

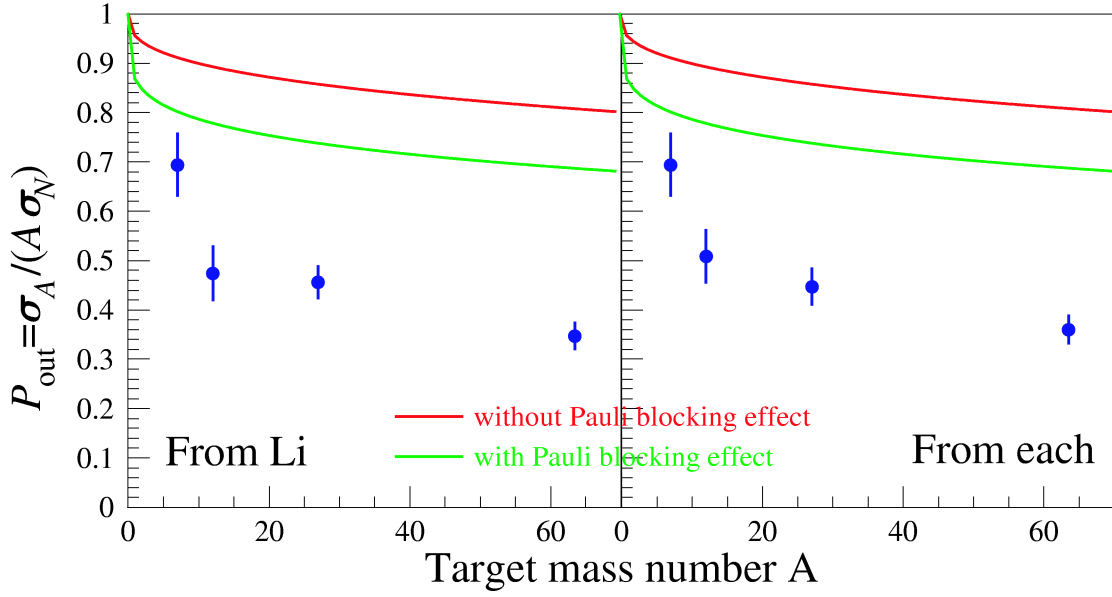


Figure 4.16: Comparison of P_{out} for the yields after the coherent ϕ events are subtracted. The left panel shows P_{out} where each yield is evaluated subtracting the estimated coherent ϕ events from the negative missing energy events in Li as an input, and the right one shows that where each yield is evaluated subtracting twice number of negative missing energy events. The red and green curves show the theoretical calculations given by Cabrera *et al.* [27] without and with Pauli-blocking correction for the ϕ meson scattering angle in the laboratory frame of 0° , respectively. The overall normalization errors ($\sim 19\%$) are not included in this figure.

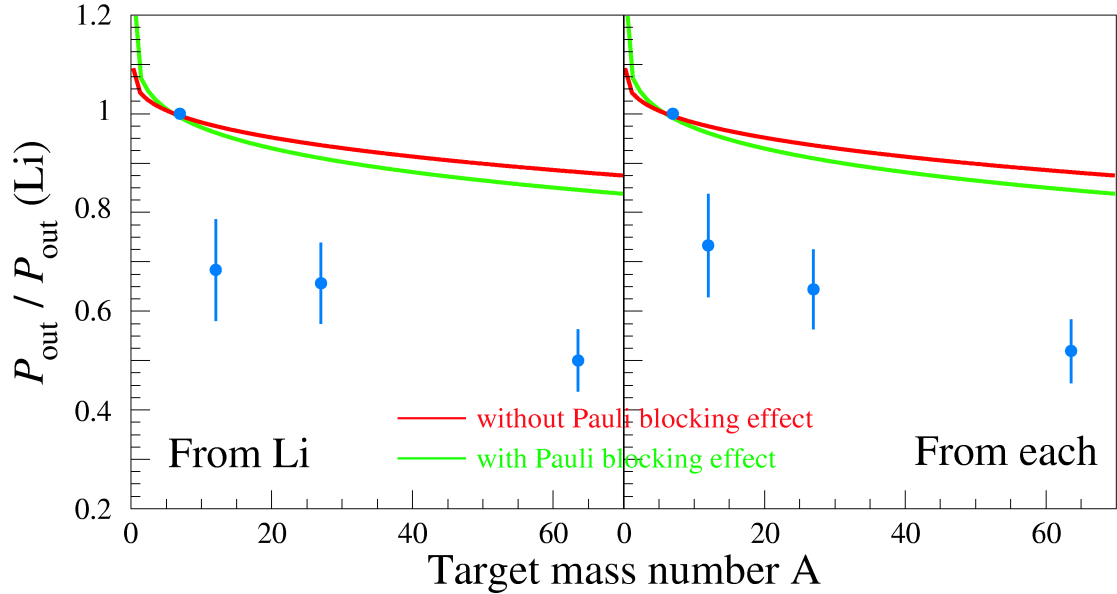


Figure 4.17: Comparison of $P_{\text{out}}/P_{\text{out}}(\text{Li})$ for the yields after the coherent ϕ events are subtracted. The red and green curves show the theoretical calculations given by Cabrera *et al.* [27] without and with Pauli-blocking correction for the ϕ meson scattering angle in the laboratory frame of 0° , respectively.

As a cross check, the probabilities P_{out} are estimated for the yields in the kinematical region of the incoherent process (30 MeV missing energy cut) as described in Subsection 4.4, and are summarized in Table 4.5. Figure 4.18 shows the probability P_{out} as a function of A . The probabilities P_{out} are

Table 4.6: Probability P_{out} in the kinematical region of the incoherent process

	Li	C	Al	Cu
P_{out}	0.715 ± 0.055	0.546 ± 0.046	0.501 ± 0.037	0.384 ± 0.031

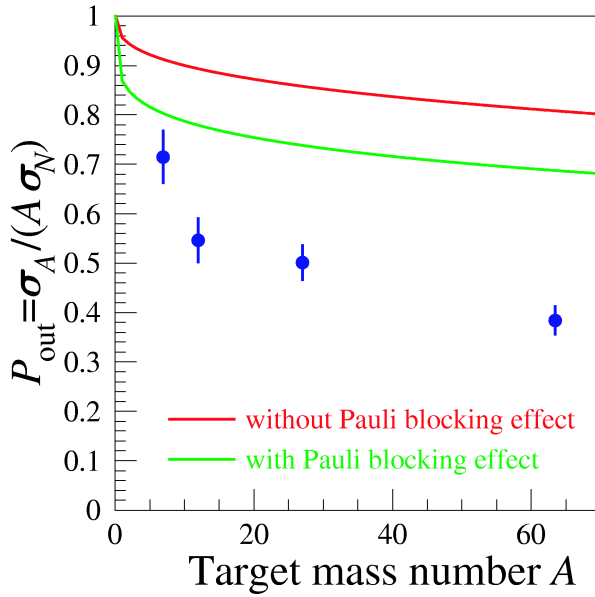


Figure 4.18: Comparison of P_{out} in the kinematical region of the incoherent process. The red and green curves show the theoretical calculations as same as Figure 4.16. The overall normalization error (18%) is not included in this figure.

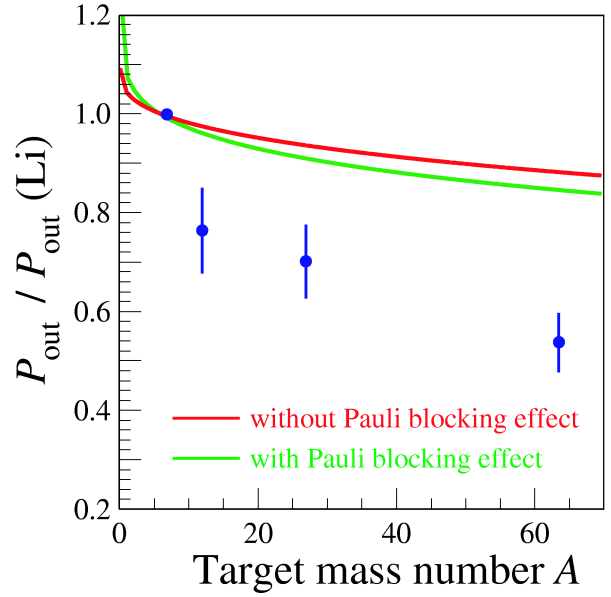


Figure 4.19: Comparison of $P_{\text{out}}/P_{\text{out}}(\text{Li})$ for the yields in the kinematical region of the incoherent process. The red and green curves show the same theoretical calculations as Figure 4.17.

also smaller than the theoretical predictions. The ratios $P_{\text{out}}(\text{Li})/P_{\text{out}}(\text{Cu})$, $P_{\text{out}}(\text{C})/P_{\text{out}}(\text{Cu})$, and $P_{\text{out}}(\text{Al})/P_{\text{out}}(\text{Cu})$ are 0.764 ± 0.087 , 0.701 ± 0.075 , and 0.537 ± 0.060 , respectively. The ratios are also smaller than the theoretical predictions.

The discrepancy in the probabilities P_{out} and the ratios $P_{\text{out}}/P_{\text{out}}(\text{Li})$ implies that the ϕ - N interaction is stronger than theoretical estimations due to the modification of the ϕ properties in the nuclear medium.

4.6 Why large $\sigma_{\phi N}$ is obtained?

The reasons why large $\sigma_{\phi N}$ is obtained would be attributed to

- $\sigma_{\phi N}$ is actually enlarged in the nuclear medium,
- difference of ϕ photo-production cross sections σ_p and σ_n and difference of total ϕ - p and ϕ - n cross sections,

- the Glauber-type multiple scattering theory can not be applicable in this energy range,
- the ϕ - N interaction at low energies is strong, and
- the subtraction ambiguity of the coherent ϕ contribution.

$\sigma_{\phi N}$ is actually enlarged in the nuclear medium:

It has been expected to be observed that $\sigma_{\phi N}$ is enlarged in the nuclear medium due to the change of the ϕ properties. Cabrera *et al.* calculate the A -dependence from the ϕ self-energy in the nuclear medium. However, Cabrera's calculations do not include the modification of nucleons in the nuclear medium. It is difficult to determine whether $\sigma_{\phi N}$ is enlarged due to the modification of nucleons or due to that of the ϕ meson.

Difference of ϕ photo-production cross sections σ_p and σ_n and difference of total $\phi - p$ and $\phi - n$ cross sections:

In the determination of $\sigma_{\phi N}$, the ϕ photo-production cross sections on the proton σ_p and the neutron σ_n are assumed to be the same in the present work. For the photo-production of ρ mesons, a theoretical calculation has predicted that the ratio of the production cross sections between $\sigma(\gamma p \rightarrow \rho p)$ and $\sigma(\gamma n \rightarrow \rho n)$ is not unity [88]. The ratio of ϕ photo-production cross sections between σ_p and σ_n can not be unity. The total ϕ - p and ϕ - n cross sections $\sigma_{\phi p}$ and $\sigma_{\phi n}$ are also assumed to be the same. Basically, the targets used are the $N \simeq Z$ nuclei. These differences between σ_p and σ_n and between $\sigma_{\phi p}$ and $\sigma_{\phi n}$ do not affect the average value of σ_N and $\sigma_{\phi N}$. It is needed to investigate the ϕ photo-production cross sections from various nuclei including $N \neq Z$ nuclei.

Applicability of the Glauber-type multiple scattering theory:

The Glauber-type multiple scattering theory is applied in a wide energy range. The $\sigma_{\eta N}$ has been determined by using the theory with a large scattering angle correction at low energies where the kinetic energy of the η meson ranges $T_\eta < 200$ MeV [32]. Applicability of the theory can be tested by comparing the PDG value of the $\sigma_{K^+ N}$ and $\sigma_{K^- N}$ determined by applying the theory to single K^+ photo-production in the present data. The applicability of the theory for ρ photo-production is also important in this energy range. In the present experimental setup, however, produced charged π 's from ρ mesons are vetoed online by the silica aerogel Čerenkov counter.

ϕ - N interaction at low energies is strong:

If the ϕ - N interaction at low energies is strong, the enlargement of $\sigma_{\phi N}$ in the nuclear medium is not attributed to the effect of the medium modification. It is reported that the $|t| = |t|_{\min}$ limit values of the differential cross section as a function of E_γ show a bump around $E_\gamma = 2$ GeV [57]. This is incompatible with the interpretation by Pomeron and pseudo scalar exchanges only. The scalar exchange and existence of a ϕ - N resonance can account for the the bump.

Subtraction ambiguity of the coherent ϕ contributions:

In the present work, the ϕ photo-production cross section has been assumed to be the sum of the coherent and incoherent ones. If this assumption is not valid, the different value of $\sigma_{\phi N}$ will be obtained. The semi-coherent ϕ production in which only a few nucleons are involved is discussed in Subsection E.2.

Chapter 5

Conclusion

The photo-production of ϕ mesons from nuclear targets were measured at SPring-8/LEPS (“ ϕ photo-production off nuclei”, C01BL33LEP-6002N, Spokesperson: T. Ishikawa) in order to deduce the ϕ - N total cross section $\sigma_{\phi N}$ and to investigate the modification of the ϕ properties in the nuclear medium. Photons were produced by backward Compton scattering with an ultra-violet Ar laser from 8 GeV electrons in the storage ring, and ranged from 1.5 to 2.4 GeV. The targets used in the experiment were Li, C, Al, and Cu with thicknesses of 100 mm, 36 mm, 24 mm, and 3 mm, respectively. Charged kaons decayed from ϕ mesons were detected at forward angles with the LEPS spectrometer. The ϕ mesons were observed in the K^+K^- invariant mass distributions. The measured mass and width were consistent with those of the free ϕ meson. This is because the almost all the ϕ mesons decay outside a nucleus ($\gtrsim 95\%$) in the momentum range from 1.0 to 2.2 GeV. The measured momentum transfer $|t|$ ranged up to 0.6 GeV². The differential cross section for each target was fitted with a function of $d\sigma/d\tilde{t} = C \exp(-b\tilde{t})$, where $\tilde{t} = |t| - |t|_{\min}$, and $|t|_{\min}$ is the minimum $|t|$ given under the assumption that the target is a proton at rest. The obtained slope parameters b were 3.6 ± 0.9 , 4.5 ± 1.0 , 3.1 ± 0.9 , and 4.5 ± 1.0 GeV⁻², respectively. These parameters were consistent with that for ϕ photo-production on the proton $b = 2.1 \sim 3.0$ GeV⁻² at SAPHIR [70], or $b = 3.38 \pm 0.23$ GeV⁻² at LEPS [57] within the errors. The cross section of all the ϕ events for each target was found to be proportional to $A^{0.63 \pm 0.05}$.

The contribution of the coherent process could not be negligibly small especially for light nuclear targets even at low energies ($E_\gamma \sim 2$ GeV). The missing energy E_x was defined as $E_x = m_X - m_A$, where m_X was the missing mass for the reaction $\gamma A \rightarrow \phi X$, and m_A stands for the mass of the target nucleus. The E_x for the coherent process concentrated at 0 MeV within the experimental resolution, and that for the incoherent process was distributed in the positive E_x region. The obtained E_x distribution had not only incoherent but also small coherent contributions. The coherent contribution in Li was evaluated in the E_x distribution. Assuming that there were no ϕ events produced incoherently in the negative E_x region, the total coherent events were estimated to be twice the number of events in the negative E_x region. Since the coherent contribution was relatively small for the heavier target, the coherent ϕ contributions in the other targets were evaluated theoretically using the estimated one in Li as an input. The contribution of the coherent process is proportional to the square of the nuclear form factor $d\sigma/dq \propto |AF(q)|^2$, where q was the three dimensional momentum transfer. After subtracting the coherent contribution as the background, the cross sections gave a relation $\sigma_A \propto A^{0.72 \pm 0.07}$.

In order to determine $\sigma_{\phi N}$ from the A -dependence of the ϕ photo-production cross section, an optical model of a Glauber-type multiple scattering theory for incoherent production was applied. In this model, the production cross section from a nucleus is described as $d\sigma_A^{\text{inc}}/dt = A_{\text{eff}} d\sigma_N/dt$, where A_{eff} is the effective nucleon number and $d\sigma_N/dt$ is the production cross section on the nucleon. The

A_{eff} is a function of A , $\sigma_{\gamma N}$, and $\sigma_{\phi N}$, where $\sigma_{\gamma N}$ stands for the total photon-nucleon cross section. The $\sigma_{\gamma N}$ was fixed to be $140 \mu\text{b}$ in the energy range from 1.5 to 2.4 GeV. The measured photo-production cross sections were fitted by a function $\sigma_A = A_{\text{eff}} \sigma_N$ with $\sigma_{\phi N}$ and σ_N as free parameters. The value of $\sigma_{\phi N}$ was estimated to be 35_{-11}^{+17} mb [89, 90].

As a cross check, the coherent contributions for the other targets were estimated using the exactly same technique as in the case of Li. In this case, σ_A was proportional to $A^{0.73 \pm 0.07}$, and $\sigma_{\phi N}$ was estimated to be 34_{-11}^{+17} mb. It was consistent with the former results. Similar results were also obtained by selecting the kinematical region for the incoherent process instead of subtracting the coherent contribution. When the events with E_x larger than 30 MeV were selected $\sigma_A \propto A^{0.74 \pm 0.06}$ and $\sigma_{\phi N} = 30_{-8}^{+12}$ mb were obtained. The results were stable even if the missing energy cut was tightened up to 80 MeV. These values obtained in this experiment were much larger than $\sigma_{\phi N}$ in free space (7.7–8.7 mb) [28].

Although it is difficult to separate the incoherent and coherent ϕ photo-productions near the threshold, the estimated $\sigma_{\phi N}$ was always about 35 mb in any case from the A -dependence of incoherent ϕ photo-production. The values were much larger than $\sigma_{\phi N}$ in free space, indicating the modification of the ϕ - N scattering amplitude in the nuclear medium. The A -dependence of the yields for incoherent ϕ photo-production was compared with the theoretical calculations given by Cabrela *et al.* in terms of the probability $P_{\text{out}} = \sigma_A / (A \sigma_N)$. The obtained P_{out} were smaller than the theoretical predictions. The absolute value of P_{out} obtained in the experiment depends on an applied model to deduce $\sigma_{\phi N}$. The model-independent ratios $P_{\text{out}} / P_{\text{out}}(\text{Li})$ were estimated, and were also smaller than the theoretical predictions. The theoretical calculations underestimate the decrease of photo-produced ϕ meson flux in the nucleus. This discrepancy implies that the ϕ - N interaction is stronger than theoretical estimations due to the modification of the ϕ properties in the nuclear medium.

In summary, the A -dependence of the ϕ photo-production cross section suggests that the ϕ properties might change in the nuclear medium although the change of the mass and width is not observed in the K^+K^- invariant mass distribution. The ratio $P_{\text{out}} / P_{\text{out}}(\text{Li})$ is smaller than the theoretical predictions, which implies that the in-medium modification might be larger than the predictions. It should be noted that the $\sigma_{\phi N}$ value in free space is still ambiguous at low energies. It is important to establish the production mechanism for ϕ photo-production on the proton near the threshold and to confirm the $\sigma_{\phi N}$ value in free space at low energies.

Acknowledgement

I would like to express my sincere gratitude to Prof. Ken'ichi Imai. He has encouraged, advised, and supported me at every stage of this work: planning of the experiment, carrying out the experiment, analysis, and publication.

I am gratefully acknowledge Prof. Hajime Shimizu. He has continuously encouraged me to complete the doctoral dissertation. He has been always available for discussion, has taken remarkable care of me, and has made to improve this thesis.

I deeply appreciate Prof. Takashi Nakano for the invaluable discussions with him. He has given me many suggestions and advices for the analysis from the beginning. He taught me a great deal with his great insight and passion for hadron physics.

I express many thanks to Prof. Mamoru Fujiwara. He gave me many suggestions and discussions on the experiment. Especially, a lot of his advices has polished up the manuscript of the publication.

I am grateful to Prof. Masaru Yosoi. He has instructed me experiments on nuclear physics since I was an undergraduate student. I have had the great opportunity to work on experiments at SPring-8/LEPS facility under the guidance of him. I have been also deeply influenced from his attitude to the study of science and physics.

I would like to thank Prof. Jirota Kasagi, the director of Laboratory of Nuclear Science, Tohoku University. He has given a log of supports.

I am indebted to the members of the SPring-8/LEPS collaboration. Without their efforts, this work would never finished. I would like to particularly thank Dr. Tomoaki Hotta, Dr. Tetsuhiko Yorita, Dr. Norihito Muramatsu, Dr. Hideki Kohri, Dr. Mizuki Sumihama, Dr. Tsutomu Mibe, Dr. Toru Matsumura, Mr. Manabu Miyabe, Mr. Yuki Shiino, Prof. Remco G.T. Zegers, Prof. Jung Keun Ahn, Prof. Wen-Cheng Chang, and Dr. Dmitry S. Oshuev for their tireless involvement in the experiments and data analysis, and their endless push for the perfection. Without their help, this thesis would have taken significantly longer. My special thanks also go to Prof. Kenneth Hicks, Prof. Chilakamarri Rangacharyulu, Prof. Hidetoshi Akimune, Dr. Hisako Fujimura, Prof. Tetsuya Murakami, Prof. Masanobu Nakamura, Mr. Masayuki Niiyama, Prof. Masaharu Nomachi, Prof. Atsushi Sakaguchi, Dr. Yorihito Sugaya, and Dr. Hidenori Toyokawa for their many suggestions and advices to me. I would also like to thank Dr. Schin Daté and Dr. Yuji Ohashi for the important roles that they played in preparation and running of the SPring-8/LEPS experiments. I deeply acknowledge Dr. Atsushi Wakai, Prof. Takahiro Iwata, and Dr. Katsuya Yonehara for the development of the laser injection system. Without their help, the photon beam with high quality cannot be obtained. I would like to thank my collaborators Ms. Deuk Soon Ahn, Prof. Hideyuki Kawai, Prof. Chang Wan Wang, Mr. Koji Miwa, Mr. Masataka Morita, Mr. Hidehito Nakamura, Dr. Takahito Ooba, Prof. Yasuhiro Sakemi, Dr. Koichi Kino, and Mr. Yuya Toi.

I wish to thank the SPring-8 staff for their dedicated efforts of providing a high quality beam. I also thank all the people who contributed to the construction of the LEPS facility. I gratefully acknowledge Dr. Takashi Hasegawa (Honjo Metal Co. Ltd.) for making the Li target suitable for the experiment.

I have had the good fortune of working closely with talented colleagues: Prof. Atsushi Tamii, Dr. Takahiro Kawabata, and Mr. Naohiko Tsukahara. They have sparked my interest in physics research and given me a lot of supports.

I have also joined in the experiments in the ring cyclotron facility at Research Center for Nuclear Physics (RCNP), Osaka University. I want to thank all the members I have collaborated in the RCNP experiments: Prof. Harutaka Sakaguchi, Prof. Yoshitaka Fujita, Prof. Testuo Noro, Prof. Kichiji Hatanaka, Prof. Tomotsugu Wakasa, Dr. Masato Yoshimura. Dr. Izuru Daito, Dr. Hidetomo P. Yoshida, Dr. Makoto Uchida, Dr. Hiroyuki Takeda, Dr. Masashi Itoh, Ms. Tomoko Taki, Ms. Emi Obayashi, Mr. Yuusuke Yasuda, Dr. Jun'ichiro Kamiya, Dr. Keigo Hara, and Mr. Satoru Terashima. They helped me a great deal in many physics discussions and in all the aspects of the experiments.

I have spent enjoyable years in the graduate school. I wish to thank all the members of Experimental Nuclear Physics Laboratory, and Experimental Nuclear and Hadronic Physics Laboratory in Kyoto University: Prof. Hideto En'yo, Prof. Naohito Saito, Prof. Haruhiko Funahashi, Dr. Hiroki Kanda, Dr. Shuichi Kuwamoto, Dr. Masaya Ishino, Dr. Kyoichiro Ozawa, Dr. Kazuhiro Yamamoto, Dr. Tsuguchika Tabaru, Dr. Atsuko Ichikawa-Kondo, Prof. Jiro Murata, Dr. Yasuhiro Kondo, Mr. Ryosaku Muramatsu, Dr. Hisashi Akikawa, Dr. Hisayuki Torii, Dr. Hitoshi Takahashi, Dr. Junji Tojo, Mr. Yuji Tanaka, Ms. Megumi Naruki, Mr. Takuya Miyashita, Mr. Takahiro Sasaki, Mr. Kenji Miyazaki, Mr. Daisuke Seki, Mr. Yasushi Hirai, Mr. Choong Jae Yoon, Mr. Fuminori Sakuma, Dr. Masaaki Kitaguchi, Mr. Yoshinori Fukao, Mr. Shinsuke Ota, and Mr. Manabu Togawa. I would like to express my thanks to Ms. Yuka Nakakoji-Sasaki, Ms. Terue Kiyosawa-Ishino, Ms. Ayako Furumori-Nagaoka, and Ms. Ayami Nakao for their secretarial support and hospitality.

I have spent invaluable and enjoyable years in Laboratory of Nuclear Science. I wish to thank all the professors, doctors, and students in or associate with Laboratory of Nuclear Science, Tohoku University: Prof. Hiroyuki Hama, Prof. Kazushige Maeda, Prof. Toshiyuki Takahashi, Prof. Tatsuo Terasawa, Prof. Tadaaki Tamae, Prof. Tsutomu Ohtsuki, Prof. Hiroshi Y. Yoshida, Dr. Katsuhiko Shinto, Dr. Hirohito Yamazaki, Dr. Hideyuki Yuki, Dr. Fujio Hinode, Dr. Tadashi Kinoshita, Dr. Yasushi Tajima, Mr. Itaru Nishikawa, Mr. Yoshiyuki Satoh, Mr. Atsushi Miyamoto, Mr. Tadashi Nakabayashi, Mr. Fusashi Miyahara, Mr. Takumi Tanaka, Mr. Takahide Shimizu, Ms. Mari Inoue, Mr. Mitsuhiro Sengoku, Mr. Katsunori Satou, Ms. Yukie Hayashi, Mr. Takayuki Hayakawa, Mr. Shinya Suzuki, Mr. Koutaku Suzuki, Mr. Yutaka Saitoh, Mr. Ken'yu Okamura, Mr. Hiroki Yonemura, Mr. Ryo Hashimoto, Mr. Hiroshi Fukasawa, Mr. Ken'ichi Nawa, Mr. Masashi Honmo, Mr. Yusuke Noguchi, and Mr. Makoto Okano.

Appendix A

A-dependence of the production cross section

The production cross sections of the coherent and incoherent processes are reviewed [47, 48], some typographic errors in the references are corrected, and omitted intermediate formulae are added.

The reaction $1 + N \rightarrow 2 + N$ is considered, and the assumptions in the kinematics are the same as in Subsection 1.2. The vector \vec{k} denotes the momentum of the incident photon. The vector \vec{b} stands for the impact parameter of particles 1 and 2. A set of A nucleons is assumed to occupy fixed positions $\vec{s}_1, \dots, \vec{s}_A$ relative to the axis of a collision, and the vectors $\vec{s}_1, \dots, \vec{s}_A$ are perpendicular to \vec{k} . Figure A.1 shows definition of the kinematics for the estimation of the production cross sections.

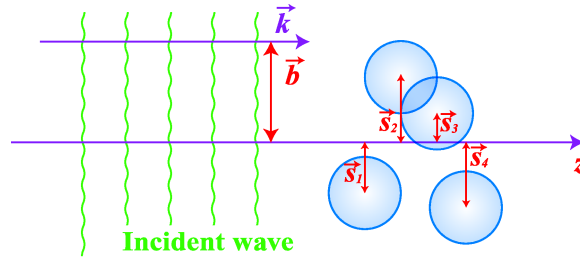


Figure A.1: Definition of the kinematics for the estimation of the production cross sections. The \vec{k} denotes the momentum of the incident photon, and the \vec{b} stands for the impact vector. The \vec{s}_j shows the transverse component for the position of the nucleon j .

The profile function $\Gamma_{ij}(\vec{b})$ is defined as

$$\Gamma_{ij}(\vec{b}) = \frac{1}{2\pi ik} \int f_{ij}(\vec{q}) \exp(-i\vec{q} \cdot \vec{b}) d^2q, \quad (\text{A.1})$$

where f_{ij} is the two-body scattering or production amplitude, and \vec{q} is the momentum transfer. The inverse relations are obtained by the Fourier transformation.

$$f_{ij}(\vec{q}) = \frac{ik}{2\pi} \int \Gamma_{ij}(\vec{b}) \exp(i\vec{q} \cdot \vec{b}) d^2b. \quad (\text{A.2})$$

The production amplitude at small angles is given by

$$F_{FI}(\vec{q}) = \frac{ik}{2\pi} \sum_{j=1}^A \int \exp(i\vec{q} \cdot \vec{b}) d^2b \int u_F^*(r_1, \dots, r_A) \Gamma(\vec{b} - \vec{s}_j)$$

$$\times \prod_{z_i < z_j}^i \left(1 - \Gamma_{11}(\vec{b} - \vec{s}_i)\right) \prod_{z_k > z_j}^k \left(1 - \Gamma_{22}(\vec{b} - \vec{s}_k)\right) u_I(\vec{r}_1, \dots, \vec{r}_A) d\vec{r}_1 \cdots d\vec{r}_A, \quad (\text{A.3})$$

where $u_I(\vec{r}_1, \dots, \vec{r}_A)$ and $u_F(\vec{r}_1, \dots, \vec{r}_A)$ are the target wave functions for the initial and final states, respectively.

A.1 Production cross section for the coherent process

The final state is the same as initial one for the coherent process:

$$u_F(\vec{r}_1, \dots, \vec{r}_A)^* u_I(\vec{r}_1, \dots, \vec{r}_A) = |u_I(\vec{r}_1, \dots, \vec{r}_A)|^2. \quad (\text{A.4})$$

A simple approximation for the nuclear wave function without any correlations among nucleons are applied following Glauber [46]:

$$|u_I(\vec{r}_1, \dots, \vec{r}_A)|^2 = \prod_{i=1}^A \rho(\vec{r}_i), \quad (\text{A.5})$$

where $\rho(\vec{r}_j)$ describes the single particle density function of the nucleus, and which satisfies

$$\int \rho(\vec{r}_j) d\vec{r}_j = 1. \quad (\text{A.6})$$

The approximation (A.7) can hold under the condition that the range of the two body interactions is much less than the nuclear radius, and in that case $\rho(\vec{s}_j, z)$ varies slowly compared to $\Gamma(\vec{b} - \vec{s}_j)$ as a function of \vec{s}_j .

$$\int \Gamma_{ij}(\vec{b} - \vec{s}_j) \rho(\vec{s}_j, z) d^2 s_j dz \cong \int \Gamma_{ij}(\vec{b} - \vec{s}_j) d^2 s_j \int \rho(\vec{b}, z) dz = -\frac{2\pi i}{k} \frac{f_{ij}(0)T(\vec{b})}{A}, \quad (\text{A.7})$$

where

$$T(\vec{b}) = A \int \rho(\vec{b}, z) dz, \quad (\text{A.8})$$

and Eq. (A.2) has been used. Substituting the production wave functions in Eq. (A.3), the coherent production amplitude F_{FI} becomes

$$\begin{aligned} F_{FI}(\vec{q}) &= \frac{ik}{2\pi} \sum_{j=1}^A \int \exp(i\vec{q} \cdot \vec{b}) d^2 b \int \Gamma_{12}(\vec{b} - \vec{s}_j) \rho(\vec{r}_j) d\vec{r}_j \\ &\quad \times \prod_{z_i < z_j}^i \int \left(1 - \Gamma_{11}(\vec{b} - \vec{s}_i)\right) \rho(\vec{r}_i) d\vec{r}_i \prod_{z_k > z_j}^k \int \left(1 - \Gamma_{22}(\vec{b} - \vec{s}_k)\right) \rho(\vec{r}_k) d\vec{r}_k \\ &= \frac{ik}{2\pi} \int \exp(i\vec{q} \cdot \vec{b}) d^2 b \left(-\frac{2\pi i}{k} \frac{f_{12}(0)T(\vec{b})}{A}\right) \sum_{j=1}^A \left(1 + \frac{2\pi i}{k} \frac{f_{11}(0)T(\vec{b})}{A}\right)^{j-1} \left(1 + \frac{2\pi i}{k} \frac{f_{22}(0)T(\vec{b})}{A}\right)^{A-j} \\ &= \frac{ik}{2\pi} \int \exp(i\vec{q} \cdot \vec{b}) d^2 b \left(-\frac{2\pi i}{k} \frac{f_{12}(0)T(\vec{b})}{A}\right) \frac{\left(1 + \frac{2\pi i}{k} \frac{f_{11}(0)T(\vec{b})}{A}\right)^A - \left(1 + \frac{2\pi i}{k} \frac{f_{22}(0)T(\vec{b})}{A}\right)^A}{\left(1 + \frac{2\pi i}{k} \frac{f_{11}(0)T(\vec{b})}{A}\right) - \left(1 + \frac{2\pi i}{k} \frac{f_{22}(0)T(\vec{b})}{A}\right)} \\ &= \frac{ik}{2\pi} \frac{-f_{12}(0)}{f_{11}(0) - f_{22}(0)} \int \exp(i\vec{q} \cdot \vec{b}) d^2 b \left\{ \left(1 + \frac{2\pi i}{k} \frac{f_{11}(0)T(\vec{b})}{A}\right)^A - \left(1 + \frac{2\pi i}{k} \frac{f_{22}(0)T(\vec{b})}{A}\right)^A \right\} \\ &= \frac{ik}{2\pi} \frac{-f_{12}(0)}{f_{11}(0) - f_{22}(0)} \int \exp(i\vec{q} \cdot \vec{b}) d^2 b \\ &\quad \times \left\{ \exp\left(\frac{2\pi i}{k} f_{11}(0)T(\vec{b})\right) - \exp\left(\frac{2\pi i}{k} f_{22}(0)T(\vec{b})\right) \right\} \end{aligned} \quad (\text{A.9})$$

The approximation

$$\left(1 + \frac{2\pi i}{k} \frac{f_{ij}(0)T(\vec{b})}{A}\right)^A \cong \exp\left(\frac{2\pi i}{k} f_{ij}(0)T(\vec{b})\right) \quad (\text{A.10})$$

has been used in the transformation of the equation (A.9). Using the optical theorem

$$\text{Im}f_{ii}(0) = \frac{k}{4\pi}\sigma_{iN}, \quad (\text{A.11})$$

where σ_{iN} is the total cross section of the particle i in interaction with a nucleon, the coherent production cross section is described by using the cylindrical Bessel function of the first kind of order zero J_0 as

$$\frac{d\sigma^{\text{coh}}}{dt} = \left(\frac{d\sigma_N}{dt}\right)_{t=0} \frac{4}{(\sigma_{1N} - \sigma_{2N})^2 + (\alpha_{1N}\sigma_{1N} - \alpha_{2N}\sigma_{2N})^2} \left| \int J_0(qb) \left\{ \exp\left(-\frac{1}{2}(1 - i\alpha_{1N})\sigma_{1N}T(b)\right) - \exp\left(-\frac{1}{2}(1 - i\alpha_{2N})\sigma_{2N}T(b)\right) \right\} db \right|^2, \quad (\text{A.12})$$

where α_{iN} are the ratio of real to imaginary parts of the scattering amplitudes on a nucleon, and $d\sigma_N/dt$ is the two body cross section corresponding to the reaction $1 + N \rightarrow 2 + N$. For $t = 0$ limit, a simple two body cross section

$$\left(\frac{d\sigma^{\text{coh}}}{dt}\right)_{t=0} = \left(\frac{d\sigma_N}{dt}\right)_{t=0} A_{\text{eff}}^2(A, \sigma_{1N}/2, \sigma_{2N}/2) \quad (\text{A.13})$$

is obtained by using A_{eff} defined in Eq. (1.3) in Subsection 1.2.

A.2 Production cross section for the incoherent process

The production amplitude can be express as

$$F_{FI}(\vec{q}) = \sum_j F_{FIj}(\vec{q}), \quad (\text{A.14})$$

where

$$F_{FIj}(\vec{q}) = \frac{ik}{2\pi} \int \exp(i\vec{q} \cdot \vec{b}) d^2b \int u_F^*(\vec{r}_1, \dots, \vec{r}_A) \Gamma(\vec{b} - \vec{s}_j) \times \prod_{z_i < z_j}^i \left(1 - \Gamma_{11}(\vec{b} - \vec{s}_i)\right) \prod_{z_k > z_j}^k \left(1 - \Gamma_{22}(\vec{b} - \vec{s}_k)\right) u_I(\vec{r}_1, \dots, \vec{r}_A) d\vec{r}_1 \cdots d\vec{r}_A. \quad (\text{A.15})$$

The cross section for the incoherent process can be described as

$$\frac{d\sigma^{\text{inc}}}{d\Omega} = \sum_F \sum_j |F_{FIj}|^2 = \sum_j |F_{IIj}|^2, \quad (\text{A.16})$$

where closure has been used the transformation from the middle side to the right hand side. Using the production wave function (A.5), the incoherent production cross section becomes

$$\frac{d\sigma^{\text{inc}}}{d\Omega} = \frac{k^2}{4\pi^2} \sum_{j=1}^A \int d^2b d^2b' \exp\left(i\vec{q} \cdot (\vec{b} - \vec{b}')\right) u_I^*(\vec{r}_1, \dots, \vec{r}_A) u_I(\vec{r}_1, \dots, \vec{r}_A) \Gamma_{12}^*(\vec{b}' - \vec{s}_j) \Gamma_{12}(\vec{b} - \vec{s}_j)$$

$$\begin{aligned}
& \times \prod_{z_i < z_j}^i \left(1 - \Gamma_{11}^*(\vec{b}' - \vec{s}_i)\right) \left(1 - \Gamma_{11}(\vec{b} - \vec{s}_i)\right) \\
& \times \prod_{z_k > z_j}^k \left(1 - \Gamma_{22}^*(\vec{b}' - \vec{s}_k)\right) \left(1 - \Gamma_{22}(\vec{b} - \vec{s}_k)\right) d\vec{r}_1 \cdots d\vec{r}_A \\
& = \frac{k^2}{4\pi^2} \int d^2b d^2b' \exp\left(i\vec{q} \cdot (\vec{b} - \vec{b}')\right) \int \Gamma_{12}^*(\vec{b}' - \vec{s}_j) \Gamma_{12}(\vec{b} - \vec{s}_j) d\vec{r}_j \\
& \quad \times \frac{\left(\int (1 - \Gamma_{11}^*(\vec{b}' - \vec{s}_i))(1 - \Gamma_{11}(\vec{b} - \vec{s}_i)) d\vec{r}_i\right)^A - \left(\int (1 - \Gamma_{22}^*(\vec{b}' - \vec{s}_k))(1 - \Gamma_{22}(\vec{b} - \vec{s}_k)) d\vec{r}_k\right)^A}{\left(\int (1 - \Gamma_{11}^*(\vec{b}' - \vec{s}_i))(1 - \Gamma_{11}(\vec{b} - \vec{s}_i)) d\vec{r}_i\right) - \left(\int (1 - \Gamma_{22}^*(\vec{b}' - \vec{s}_k))(1 - \Gamma_{22}(\vec{b} - \vec{s}_k)) d\vec{r}_k\right)} \quad (\text{A.17})
\end{aligned}$$

The following relations (A.18) and (A.19) hold.

$$\begin{aligned}
& \int \Gamma_{ij}^*(\vec{b}' - \vec{s}) \Gamma_{ij}(\vec{b} - \vec{s}) d^2s \\
& = \int d^2s \frac{-i}{2\pi k} \int f_{ij}^*(\vec{q}') \exp\left(-i\vec{q}' \cdot (\vec{b}' - \vec{s})\right) d^2q' \frac{i}{2\pi k} \int f_{ij}(\vec{q}) \exp\left(-i\vec{q} \cdot (\vec{b} - \vec{s})\right) d^2q \\
& = \frac{1}{k^2} \iint f_{ij}^*(\vec{q}') f_{ij}(\vec{q}) \exp\left(-i(\vec{q}' \cdot \vec{b} + \vec{q} \cdot \vec{b}')\right) \frac{1}{4\pi} \int \exp\left(i(\vec{q}' + \vec{q}) \cdot \vec{s}\right) d^2s d^2q' d^2q \\
& = \frac{1}{k^2} \iint f_{ij}^*(\vec{q}') f_{ij}(\vec{q}) \exp\left(-i(\vec{q}' \cdot \vec{b} + \vec{q} \cdot \vec{b}')\right) \delta(\vec{q}' + \vec{q}) d^2q' d^2q \\
& = \frac{1}{k^2} \int |f_{ij}(\vec{q})|^2 \exp\left(-i\vec{q} \cdot (\vec{b} - \vec{b}')\right) d^2q, \quad \text{and} \quad (\text{A.18})
\end{aligned}$$

$$\begin{aligned}
& \int \left(1 - \Gamma_{ii}^*(\vec{b}' - \vec{s})\right) \left(1 - \Gamma_{ii}(\vec{b} - \vec{s})\right) \rho(\vec{r}) d^2r \\
& = \int \rho(\vec{r}) - \Gamma_{ii}^*(\vec{b}' - \vec{s}) \rho(\vec{r}) - \Gamma_{ii}(\vec{b} - \vec{s}) \rho(\vec{r}) + \Gamma_{ii}^*(\vec{b}' - \vec{s}) \Gamma_{ii}(\vec{b} - \vec{s}) \rho(\vec{r}) d^2r \\
& = 1 - \frac{2\pi i}{k} f_{ii}^*(0) \frac{T(\vec{b}')}{A} + \frac{2\pi i}{k} f_{ii}(0) \frac{T(\vec{b})}{A} + \int \Gamma_{ii}^*(\vec{b}' - \vec{s}) \Gamma_{ii}(\vec{b} - \vec{s}) \rho(\vec{r}) d^2r \\
& = 1 - \frac{2\pi i}{k} (f_{ii}^*(0) - f_{ii}(0)) \frac{T(\vec{b})}{A} + \int \Gamma_{ii}^*(\vec{b}' - \vec{s}) \Gamma_{ii}(\vec{b} - \vec{s}) d^2s \frac{T(\vec{b})}{A} \\
& = 1 - \frac{\sigma_{iN} T(\vec{b})}{A} + \frac{1}{k^2} \int |f_{ij}(\vec{q})|^2 \exp\left(-i\vec{q} \cdot (\vec{b} - \vec{b}')\right) d^2q \frac{T(\vec{b})}{A}, \quad (\text{A.19})
\end{aligned}$$

where the approximation $T(\vec{b}') \cong T(\vec{b})$ has been used, and also the optical theorem

$$\sigma_{iN} = \frac{4\pi}{k} \text{Im} f_{ii}(0) = -\frac{2\pi i}{k} (f_{ii}^*(0) - f_{ii}(0)) \quad (\text{A.20})$$

has been used.

Substituting $\vec{b} - \vec{b}'$ with β and using the relations (A.18) and (A.19), Eq. (A.17) becomes

$$\begin{aligned}
\frac{d\sigma^{\text{inc}}}{dt} & \cong \frac{k^2}{4\pi^2} \int d^2b d^2\beta \exp(i\vec{q} \cdot \vec{\beta}) \\
& \quad \times \frac{\frac{1}{k^2} \int |f_{12}(\vec{q}')|^2 \exp\left(-i\vec{q}' \cdot \vec{\beta}\right) d^2q' \frac{T(\vec{b})}{A}}{-\left(\sigma_{1N} - \sigma_{2N}\right) \frac{T(\vec{b})}{A} + \frac{1}{k^2} \int \left(|f_{12}(\vec{q}')|^2 - |f_{12}(\vec{q}'')|^2\right) \exp\left(-i\vec{q}' \cdot \vec{\beta}\right) d^2q' \frac{T(\vec{b})}{A}}
\end{aligned}$$

$$\begin{aligned}
& \times \left[\exp(-\sigma_{1N}T(\vec{b})) \left\{ 1 + \frac{1}{k^2} \int |f_{11}(\vec{q}')| \exp(-i\vec{q}' \cdot \beta) d^2q' \frac{T(\vec{b})}{A} \right\} \right. \\
& \quad \left. - \exp(-\sigma_{1N}T(\vec{b})) \left\{ 1 + \frac{1}{k^2} \int |f_{22}(\vec{q}')| \exp(-i\vec{q}' \cdot \beta) d^2q' \frac{T(\vec{b})}{A} \right\} \right] \\
& \cong \frac{k^2}{4\pi^2} \int d^2b d^2\beta \exp(i\vec{q} \cdot \vec{\beta}) \frac{1}{k^2} \int |f_{12}(\vec{q}')|^2 \exp(-i\vec{q}' \cdot \vec{\beta}) d^2q' \\
& \quad \times \frac{\exp(-\sigma_{1N}T(\vec{b})) - \exp(-\sigma_{2N}T(\vec{b}))}{-(\sigma_{1N} - \sigma_{2N})} \left\{ 1 \right. \\
& \quad + \frac{\frac{1}{k^2} \int (|f_{11}(\vec{q}'')|^2 - |f_{22}(\vec{q}'')|^2) \exp(-i\vec{q}'' \cdot \beta) d^2q''}{\sigma_{1N} - \sigma_{2N}} \\
& \quad + \frac{\int (\exp(-\sigma_{1N}T(\vec{b})) |f_{11}(\vec{q}'')|^2 - \exp(-\sigma_{2N}T(\vec{b})) |f_{22}(\vec{q}'')|^2) \exp(-i\vec{q}'' \cdot \beta) d^2q''}{\exp(-\sigma_{1N}T(\vec{b})) - \exp(-\sigma_{2N}T(\vec{b}))} \\
& \quad \left. \times T(\vec{b}) \right\} \\
& = \int d^2b \frac{\exp(-\sigma_{1N}T(\vec{b})) - \exp(-\sigma_{2N}T(\vec{b}))}{-(\sigma_{1N} - \sigma_{2N})} \\
& \quad \times \int |f_{12}(\vec{q}')|^2 \left\{ \frac{1}{4\pi^2} \int \exp(i(\vec{q} - \vec{q}') \cdot \beta) d^2\beta \right\} d^2\vec{q}' \\
& \quad + \int d^2b \frac{\exp(-\sigma_{1N}T(\vec{b})) - \exp(-\sigma_{2N}T(\vec{b}))}{-(\sigma_{1N} - \sigma_{2N})} \int |f_{12}(\vec{q}')|^2 \left\{ \frac{1}{k^2} \right. \\
& \quad \times \frac{\int (|f_{11}(\vec{q}'')|^2 - |f_{22}(\vec{q}'')|^2) \left\{ \frac{1}{4\pi^2} \int \exp(i(\vec{q} - \vec{q}' - \vec{q}'') \cdot \beta) d^2\beta \right\} d^2q''}{\sigma_{1N} - \sigma_{2N}} \left. \right\} d^2q'' \\
& \quad + \int d^2b \left\{ |f_{11}(\vec{q}'')|^2 \exp(-\sigma_{1N}T(\vec{b})) - |f_{22}(\vec{q}'')|^2 \exp(-\sigma_{2N}T(\vec{b})) \right\} \\
& \quad \times \left\{ \frac{1}{4\pi^2} \int \exp(i(\vec{q} - \vec{q}' - \vec{q}'') \cdot \beta) d^2\beta \right\} T(\vec{b}) d^2q'' \\
& = \frac{d\sigma_N}{dt} A_{\text{eff}}(A, \sigma_{1N}, \sigma_{2N}) + \int \frac{d\sigma_N(\vec{q}')}{d\Omega'} G(\vec{q}, \vec{q}'; A, \sigma_{1N}, \sigma_{2N}) d^2q', \tag{A.21}
\end{aligned}$$

where the Dirac's delta functions

$$\begin{aligned}
& \frac{1}{4\pi^2} \int \exp(i\vec{\beta} \cdot (\vec{q} - \vec{q}')) d^2\beta = \delta(\vec{q} - \vec{q}') \\
& \frac{1}{4\pi^2} \int \exp(i\vec{\beta} \cdot (\vec{q} - \vec{q}' - \vec{q}'')) d^2\beta = \delta(\vec{q} - \vec{q}' - \vec{q}'') \tag{A.22}
\end{aligned}$$

have been used, and A_{eff} and G are defined in Eqs. (1.5) and (1.3) in Subsection 1.2, respectively. The same equation as Eq. (1.2) is obtained.

Appendix B

Decay angular distribution of the vector meson

In this appendix, the decay angular distribution of the ϕ meson that has been used in the Monte Carlo (MC) simulation g3leps is reviewed [82, 83].

B.1 General decay angular distribution of the vector meson

The decay angular distribution of the vector meson into spinless mesons in its rest frame is described as

$$W(\cos \theta, \phi) = M\rho(V)M^\dagger = \sum_{\lambda_V, \lambda'_V} \langle \theta, \phi | M | \lambda_V \rangle \rho_{\lambda_V, \lambda'_V} \langle \lambda'_V | M^\dagger | \theta, \phi \rangle, \quad (\text{B.1})$$

where M is the decay amplitude, and $\rho(V)$ is the density matrix of the vector meson. The M is expressed as

$$\langle \theta, \phi | M | \lambda_V \rangle = \sqrt{\frac{3}{4\pi}} D_{\lambda_V 0}^{1*}(\phi, \theta, -\phi), \quad (\text{B.2})$$

where D is the Wigner rotating functions given by

$$\begin{aligned} D_{10}^1(\phi, \theta, -\phi) &= -\frac{1}{2} \sin \theta e^{-i\phi}, \\ D_{00}^1(\phi, \theta, -\phi) &= \cos \theta, \text{ and} \\ D_{-10}^1(\phi, \theta, -\phi) &= \frac{1}{2} \sin \theta e^{i\phi}. \end{aligned} \quad (\text{B.3})$$

Because the density matrix $\rho(V)$ is hermitian, the angular distribution is obtained as

$$\begin{aligned} W(\cos \theta, \phi) &= \frac{3}{4\pi} \left\{ \frac{1}{2} (\rho(V)_{11} + \rho(V)_{-1-1}) \sin^2 \theta + \rho(V)_{00} \cos^2 \theta \right. \\ &\quad + \frac{1}{\sqrt{2}} \left(-\text{Re}\rho(V)_{10} + \text{Re}\rho(V)_{-10} \right) \sin 2\theta \cos \phi \\ &\quad + \frac{1}{\sqrt{2}} \left(\text{Im}\rho(V)_{10} + \text{Im}\rho(V)_{-10} \right) \sin 2\theta \cos \phi \\ &\quad \left. - \text{Re}\rho(V)_{1-1} \sin^2 \theta \cos 2\phi + \text{Im}\rho(V)_{1-1} \sin^2 \theta \sin 2\phi \right\}. \end{aligned} \quad (\text{B.4})$$

B.2 Density matrix of linearly polarized photons

The wave function of linearly polarized photons is described as

$$|\gamma\rangle = -\frac{1}{\sqrt{2}} \left(e^{-i\Phi} |\lambda_\gamma = +1\rangle - e^{-i\Phi} |\lambda_\gamma = -1\rangle \right), \quad (\text{B.5})$$

where Φ is an angle between the polarization vector of the photon and the production plane (x - z plane) in the helicity frame as defined in Subsection 3.5.5. Then, the density matrix of linearly polarized pure photon states is constructed as

$$\rho(\gamma) = \frac{1}{2} \begin{pmatrix} 1 & -e^{-2i\Phi} \\ -e^{2i\Phi} & 1 \end{pmatrix}. \quad (\text{B.6})$$

As for partially polarized photons, the density matrix is written as a combination of the unit matrix I , and the Pauli matrices σ_i ($i = 1, 2, 3$):

$$\rho(\gamma) = \frac{1}{2} \left(I + \vec{P}_\gamma \cdot \vec{\sigma} \right), \quad (\text{B.7})$$

where \vec{P}_γ is the vector of the polarity, which is described as

$$\vec{P}_\gamma = P_\gamma (-\cos 2\Phi, -\sin 2\Phi, 0) \quad (\text{B.8})$$

for linear polarized photons.

B.3 Decomposition of the density matrix $\rho(V)$

The polarization states of the photon and the vector meson are connected by the production amplitude T as

$$\rho(V) = T \rho(\gamma) T^\dagger. \quad (\text{B.9})$$

Then, elements of the density matrix $\rho(V)$ can be written as

$$\left(\rho^0(V), \rho^\alpha(V) \right) = T \left(\frac{1}{2} I, \frac{1}{2} \sigma^\alpha \right) T^\dagger, \quad (\text{B.10})$$

and $\rho(V)$ is transformed from Eq. (B.7):

$$\rho(V) = \rho^0(V) + \sum_{i=1}^3 P_\gamma^\alpha \rho(V)^\alpha. \quad (\text{B.11})$$

The four hermitian matrices ρ^α ($\alpha = 0, 1, 2, 3$) are described as

$$\begin{aligned} \rho_{\lambda_V \lambda_{V'}}^0 &= \frac{1}{2N} \sum_{\lambda_\gamma, \lambda'_N, \lambda_N} T_{\lambda_V \lambda'_N, \lambda_\gamma \lambda_N} T_{\lambda_{V'} \lambda'_N, \lambda_\gamma \lambda_N}^*, \\ \rho_{\lambda_V \lambda_{V'}}^1 &= \frac{1}{2N} \sum_{\lambda_\gamma, \lambda'_N, \lambda_N} T_{\lambda_V \lambda'_N, -\lambda_\gamma \lambda_N} T_{\lambda_{V'} \lambda'_N, \lambda_\gamma \lambda_N}^*, \\ \rho_{\lambda_V \lambda_{V'}}^2 &= \frac{1}{2N} \sum_{\lambda_\gamma, \lambda'_N, \lambda_N} \lambda_\gamma T_{\lambda_V \lambda'_N, -\lambda_\gamma \lambda_N} T_{\lambda_{V'} \lambda'_N, \lambda_\gamma \lambda_N}^*, \text{ and} \\ \rho_{\lambda_V \lambda_{V'}}^3 &= \frac{1}{2N} \sum_{\lambda_\gamma, \lambda'_N, \lambda_N} \lambda_\gamma T_{\lambda_V \lambda'_N, \lambda_\gamma \lambda_N} T_{\lambda_{V'} \lambda'_N, \lambda_\gamma \lambda_N}^*, \end{aligned} \quad (\text{B.12})$$

where the label V is omitted from $\rho(V)_{ik}$. The parity conservation gives relations between the elements in the matrix as

$$\begin{aligned}\rho_{\lambda\lambda'}^\alpha &= (-1)^{\lambda-\lambda'} \rho_{-\lambda-\lambda'}^\alpha \text{ for } \alpha = 0, 1, \text{ and} \\ \rho_{\lambda\lambda'}^\alpha &= -(-1)^{\lambda-\lambda'} \rho_{-\lambda-\lambda'}^\alpha \text{ for } \alpha = 2, 3.\end{aligned}\tag{B.13}$$

From Eq (B.4), the decay angular distribution $W(\cos\theta, \phi)$ is expressed as

$$W(\cos\theta, \phi) = W^0(\cos\theta, \phi) + \sum_{\alpha=1}^3 P_\gamma W^\alpha(\cos\theta, \phi),\tag{B.14}$$

where

$$\begin{aligned}W^0(\cos\theta, \phi) &= \frac{3}{4\pi} \left(\frac{1}{2}(1 - \rho_{00}^0) + \frac{1}{2}(3\rho_{00}^0 - 1) \cos^2\theta \right. \\ &\quad \left. - \sqrt{2}\text{Re}\rho_{10}^0 \sin 2\theta \cos\phi - \rho_{1-1}^0 \sin^2\theta \cos 2\phi \right), \\ W^1(\cos\theta, \phi) &= \frac{3}{4\pi} \left(\rho_{11}^1 \sin^2\theta + \rho_{00}^1 \cos^2\theta - \sqrt{2}\rho_{10}^1 \sin 2\theta \cos\phi - \rho_{1-1}^1 \sin^2\theta \cos 2\phi \right), \\ W^2(\cos\theta, \phi) &= \frac{3}{4\pi} \left(+\sqrt{2}\text{Im}\rho_{10}^2 \sin 2\theta \sin\phi + \text{Im}\rho_{1-1}^2 \sin^2\theta \sin 2\phi \right), \text{ and} \\ W^3(\cos\theta, \phi) &= \frac{3}{4\pi} \left(+\sqrt{2}\text{Im}\rho_{10}^3 \sin 2\theta \sin\phi + \text{Im}\rho_{1-1}^3 \sin^2\theta \sin 2\phi \right).\end{aligned}\tag{B.15}$$

The decay angular distribution for linearly polarized photons with the vector of the polarization in Eq. (B.8) becomes

$$W(\cos\theta, \phi, \Phi) = W^0(\cos\theta, \phi) - P_\gamma \cos 2\Phi W^1(\cos\theta, \phi) - P_\gamma \sin 2\Phi W^2(\cos\theta, \phi).\tag{B.16}$$

B.4 Density matrix for the s -channel helicity conserving model

The production amplitude in the center of mass frame is described as

$$T_{\lambda_V \lambda'_N, \lambda_\gamma \lambda_N} = t_{\lambda_N \lambda_\gamma} \delta_{\lambda'_N \lambda_N} \delta_{\lambda_V \lambda_\gamma}.\tag{B.17}$$

The s -channel helicity conserving model with $J^\pi = 0^+, 0^-$ exchange have in the helicity frame the characteristics: 1) the matrices ρ^α ($\alpha = 0, 1, 2, 3$) are independent of photon energy and production angle, and 2) ρ^0, ρ^3 are diagonal and ρ^1, ρ^2 are antidiagonal. Then, the density matrices in the helicity system of the vector meson for the s -channel helicity conserving model are written as

$$\begin{aligned}\rho^0 &= \begin{pmatrix} +1/2 & 0 & 0 \\ 0 & 0 & 0 \\ 0 & 0 & +1/2 \end{pmatrix}, \quad \rho^1 = \begin{pmatrix} 0 & 0 & +a \\ 0 & 0 & 0 \\ +a & 0 & 0 \end{pmatrix}, \\ \rho^2 &= \begin{pmatrix} 0 & 0 & -ia \\ 0 & 0 & 0 \\ +ia & 0 & 0 \end{pmatrix}, \text{ and } \rho^3 = \begin{pmatrix} +1/2 & 0 & 0 \\ 0 & 0 & 0 \\ 0 & 0 & -1/2 \end{pmatrix},\end{aligned}\tag{B.18}$$

where $a = +1/2, -1/2$ for $J^\pi = 0^+, 0^-$ exchange, respectively. In the MC simulation, incoherent ϕ photo-production on a nucleon is generated by the spin density matrix of the natural parity exchange ($J^\pi = 0^+$).

Appendix C

Systematic uncertainty

C.1 Different responses of the detector system

C.1.1 Acceptance of the particle identification

The difference of the detector system for the various targets is only the target material itself, and the energy loss and multiple scattering in it can affect the acceptance of the particle identification. Since effects of energy loss and multiple scattering in the target materials to the particle identification are considered to be small, the acceptance of the particle identification is thought to be the same for all the targets. This is confirmed by the Monte Carlo (MC) simulation. Figure C.1 shows the momentum distribution of K^+ and K^- particles for the ϕ events in the real data. Because the momenta of these concentrates between $p = 0.6 \sim 1.2$ GeV, the acceptance is checked only in the momentum region $p = 0.5\text{--}1.3$ GeV.

At first, how many particles pass the particle identification and the good track cuts for the K^+

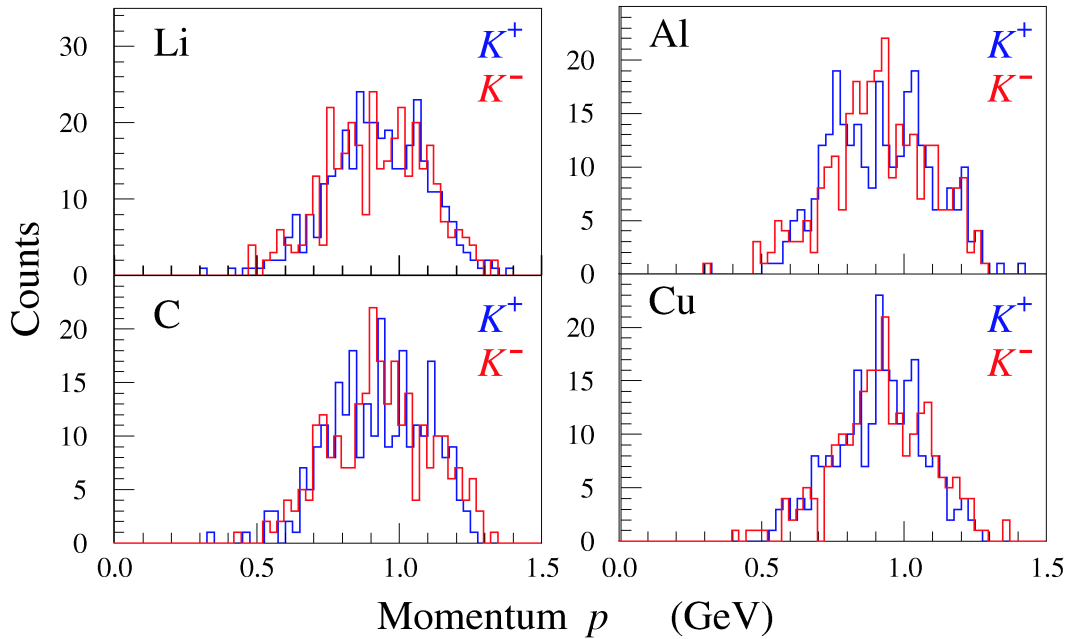


Figure C.1: Momentum distribution of K^+ and K^- . The blue lines show the momentum distributions of K^+ , and the red ones show those of K^- .

and K^- particles which come to the TOF wall without decaying are examined in each momentum bin. Figure C.2 and Table C.1 shows the passing ratio of the cuts. The very high acceptance (more than

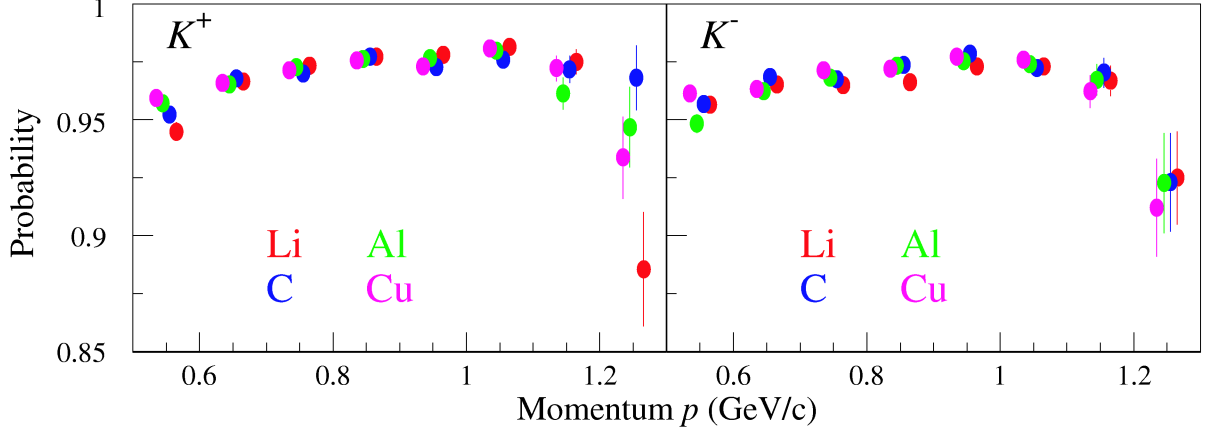


Figure C.2: Passing ratio of the particle identification and the good track cuts. The ratios that K^+ and K^- are detected as K^+ and K^- are shown in each momentum region.

Table C.1: Passing ratio of the particle identification and decay in flight cuts

p (GeV/c)	Li	C	Al	Cu
K^+				
0.5–0.6	0.9450 ± 0.0039	0.9524 ± 0.0037	0.9570 ± 0.0035	0.9595 ± 0.0034
0.6–0.7	0.9665 ± 0.0024	0.9680 ± 0.0024	0.9653 ± 0.0025	0.9660 ± 0.0025
0.7–0.8	0.9732 ± 0.0021	0.9700 ± 0.0022	0.9726 ± 0.0021	0.9714 ± 0.0021
0.8–0.9	0.9773 ± 0.0021	0.9774 ± 0.0021	0.9764 ± 0.0021	0.9758 ± 0.0021
0.9–1.0	0.9781 ± 0.0025	0.9726 ± 0.0027	0.9766 ± 0.0025	0.9728 ± 0.0026
1.0–1.1	0.9815 ± 0.0030	0.9760 ± 0.0034	0.9797 ± 0.0031	0.9808 ± 0.0029
1.1–1.2	0.9749 ± 0.0055	0.9717 ± 0.0058	0.9613 ± 0.0068	0.9721 ± 0.0056
1.2–1.3	0.8855 ± 0.0247	0.9682 ± 0.0140	0.9467 ± 0.0173	0.9337 ± 0.0178
K^-				
0.5–0.6	0.9564 ± 0.0036	0.9566 ± 0.0037	0.9483 ± 0.0040	0.9614 ± 0.0034
0.6–0.7	0.9652 ± 0.0026	0.9685 ± 0.0025	0.9623 ± 0.0027	0.9632 ± 0.0026
0.7–0.8	0.9649 ± 0.0025	0.9675 ± 0.0024	0.9681 ± 0.0024	0.9714 ± 0.0022
0.8–0.9	0.9663 ± 0.0026	0.9736 ± 0.0023	0.9733 ± 0.0023	0.9719 ± 0.0023
0.9–1.0	0.9731 ± 0.0028	0.9782 ± 0.0025	0.9752 ± 0.0027	0.9773 ± 0.0025
1.0–1.1	0.9731 ± 0.0038	0.9721 ± 0.0040	0.9738 ± 0.0036	0.9760 ± 0.0034
1.1–1.2	0.9667 ± 0.0065	0.9703 ± 0.0064	0.9671 ± 0.0067	0.9621 ± 0.0070
1.2–1.3	0.9249 ± 0.0200	0.9231 ± 0.0213	0.9226 ± 0.0215	0.9121 ± 0.0210

98 % for $p = 0.6\text{--}1.2$ GeV/c) is obtained for each momentum region, and any significant difference among the different target nuclei is not observed.

Next, how many particles other than K^+ and K^- particles are detected as K^+ and K^- , or which pass the particle identification and the good track cut, is discussed in each momentum region. Figure C.3 and Table C.2 shows the contamination of the other than K^+ and K^- in the particles detected as K^+ and K^- , and Figure C.4 and Table C.3 shows the probabilities that μ^+ and μ^- are

detected as K^+ and K^- , respectively. Note that the branching ratio of the $K^\pm \rightarrow \mu^\pm \nu_\mu$ mode is $64.43 \pm 0.17 \%$, and the information of K^+ and K^- particles on time of flight and momentum can be extracted from the μ^\pm tracks if the decay happens at downstream of the LEPS spectrometer. No significant difference can be seen among the different targets.

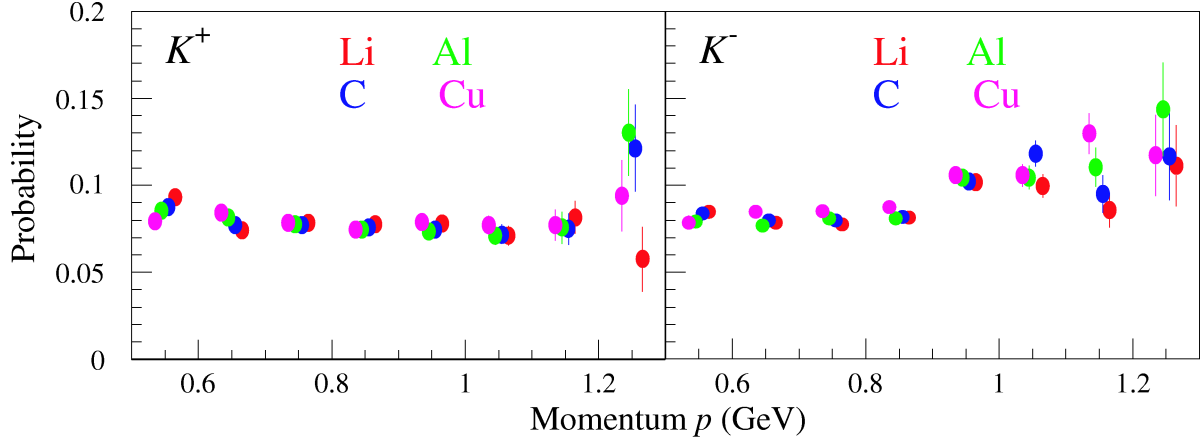
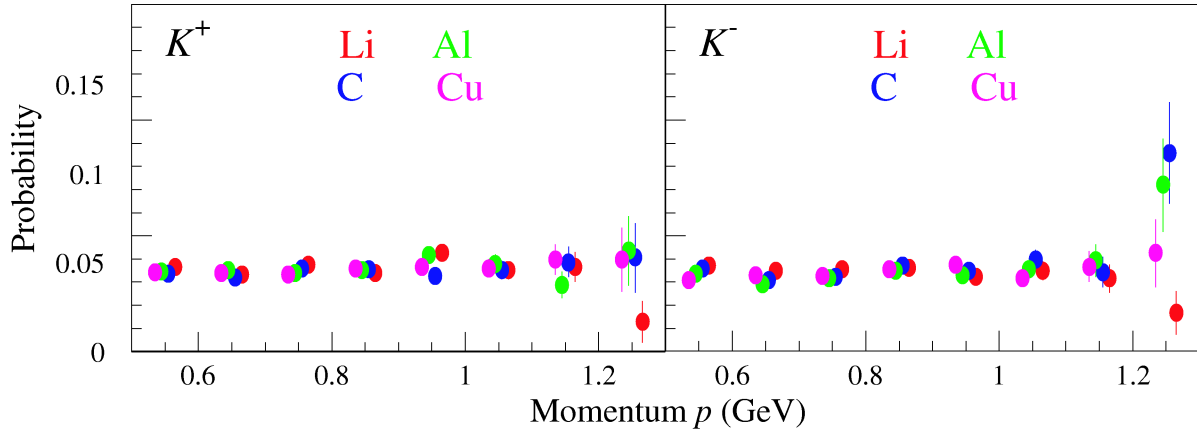


Figure C.3: The probabilities that other than K^+ and K^- particles are detected as K^+ and K^- are shown.

Table C.2: Contamination in the particles detected as K^+ and K^-

p (GeV/c)	Li	C	Al	Cu
K^+				
0.5–0.6	0.0931 ± 0.0048	0.0876 ± 0.0048	0.0854 ± 0.0047	0.0794 ± 0.0045
0.6–0.7	0.0740 ± 0.0035	0.0769 ± 0.0036	0.0818 ± 0.0037	0.0845 ± 0.0038
0.7–0.8	0.0786 ± 0.0034	0.0770 ± 0.0034	0.0775 ± 0.0034	0.0785 ± 0.0033
0.8–0.9	0.0774 ± 0.0036	0.0757 ± 0.0036	0.0744 ± 0.0035	0.0744 ± 0.0035
0.9–1.0	0.0779 ± 0.0044	0.0743 ± 0.0043	0.0736 ± 0.0042	0.0790 ± 0.0042
1.0–1.1	0.0711 ± 0.0056	0.0718 ± 0.0056	0.0713 ± 0.0056	0.0771 ± 0.0055
1.1–1.2	0.0815 ± 0.0094	0.0750 ± 0.0090	0.0756 ± 0.0092	0.0772 ± 0.0089
1.2–1.3	0.0577 ± 0.0187	0.1214 ± 0.0248	0.1304 ± 0.0248	0.0941 ± 0.0205
K^-				
0.5–0.6	0.1107 ± 0.0053	0.1097 ± 0.0054	0.1035 ± 0.0053	0.1028 ± 0.0052
0.6–0.7	0.1026 ± 0.0041	0.1047 ± 0.0042	0.1007 ± 0.0041	0.1108 ± 0.0042
0.7–0.8	0.1015 ± 0.0039	0.1046 ± 0.0040	0.1059 ± 0.0040	0.1115 ± 0.0040
0.8–0.9	0.1064 ± 0.0043	0.1069 ± 0.0042	0.1061 ± 0.0043	0.1143 ± 0.0043
0.9–1.0	0.1019 ± 0.0051	0.1021 ± 0.0051	0.1045 ± 0.0051	0.1060 ± 0.0049
1.0–1.1	0.0995 ± 0.0067	0.1182 ± 0.0074	0.1044 ± 0.0067	0.1058 ± 0.0066
1.1–1.2	0.0856 ± 0.0099	0.0951 ± 0.0107	0.1104 ± 0.0114	0.1297 ± 0.0118
1.2–1.3	0.1111 ± 0.0234	0.1166 ± 0.0251	0.1437 ± 0.0271	0.1170 ± 0.0234

Figure C.4: Probabilities that μ^+ and μ^- are detected as K^+ and K^- Table C.3: Probabilities that μ^+ and μ^- are detected as K^+ and K^-

p (GeV/ c)	Li	C	Al	Cu
K^+				
0.5–0.6	0.0365 ± 0.0031	0.0335 ± 0.0030	0.0344 ± 0.0031	0.0341 ± 0.0030
0.6–0.7	0.0333 ± 0.0024	0.0320 ± 0.0024	0.0351 ± 0.0025	0.0339 ± 0.0024
0.7–0.8	0.0377 ± 0.0024	0.0359 ± 0.0024	0.0338 ± 0.0023	0.0332 ± 0.0022
0.8–0.9	0.0339 ± 0.0024	0.0354 ± 0.0025	0.0352 ± 0.0025	0.0360 ± 0.0025
0.9–1.0	0.0426 ± 0.0033	0.0324 ± 0.0029	0.0416 ± 0.0032	0.0367 ± 0.0030
1.0–1.1	0.0351 ± 0.0040	0.0352 ± 0.0040	0.0380 ± 0.0041	0.0360 ± 0.0038
1.1–1.2	0.0366 ± 0.0065	0.0387 ± 0.0066	0.0288 ± 0.0058	0.0397 ± 0.0065
1.2–1.3	0.0128 ± 0.0090	0.0405 ± 0.0150	0.0435 ± 0.0150	0.0396 ± 0.0137
K^-				
0.5–0.6	0.0374 ± 0.0032	0.0358 ± 0.0032	0.0335 ± 0.0031	0.0308 ± 0.0030
0.6–0.7	0.0348 ± 0.0025	0.0310 ± 0.0024	0.0290 ± 0.0023	0.0327 ± 0.0024
0.7–0.8	0.0354 ± 0.0024	0.0322 ± 0.0023	0.0315 ± 0.0023	0.0326 ± 0.0022
0.8–0.9	0.0363 ± 0.0026	0.0373 ± 0.0026	0.0349 ± 0.0025	0.0357 ± 0.0025
0.9–1.0	0.0322 ± 0.0030	0.0348 ± 0.0031	0.0330 ± 0.0030	0.0377 ± 0.0030
1.0–1.1	0.0350 ± 0.0041	0.0396 ± 0.0045	0.0356 ± 0.0041	0.0316 ± 0.0037
1.1–1.2	0.0315 ± 0.0062	0.0343 ± 0.0066	0.0394 ± 0.0071	0.0367 ± 0.0066
1.2–1.3	0.0167 ± 0.0095	0.0859 ± 0.0219	0.0719 ± 0.0200	0.0426 ± 0.0147

C.1.2 χ^2 probability in the good track cut

The tightest cut in the good track cut is χ^2 probability cut. As is discussed in Appendix C.1.5, the efficiency of drift chamber in the nuclear target run period is much lower than that in the LH2 target run periods. Thus, χ^2 probability cut can be too tight. Number of ϕ events is investigated changing the χ^2 probability limit (default: 0.02) under the condition that the cuts discussed in Section 3.4 except for the χ^2 probability cut is applied. Table C.4 summarizes the number of ϕ events with these ratios to those without any χ^2 probability cut. There is little change in the number of ϕ events by loosening the χ^2 probability cut from the default value though exclusion of χ^2 probability cut make $\sim 15\%$ increase in the number of ϕ events. Figure C.5 shows K^+K^- invariant mass distribution

Table C.4: Number of ϕ events as a function of the χ^2 probability limit

χ^2 probability	Li	C	Al	Cu
0.100	234 (56.4±2.4%)	186 (60.6±2.8%)	195 (58.9±2.7%)	166 (59.5±2.9%)
0.050	292 (70.4±2.2%)	222 (72.3±2.6%)	238 (71.9±2.5%)	197 (70.6±2.7%)
0.040	301 (72.5±2.2%)	233 (75.9±2.4%)	248 (74.9±2.4%)	211 (75.6±2.6%)
0.030	320 (77.1±2.1%)	246 (80.1±2.3%)	263 (79.5±2.2%)	227 (81.4±2.3%)
0.020	348 (83.9±1.8%)	267 (87.0±1.9%)	286 (86.4±1.9%)	238 (85.3±2.1%)
0.010	348 (83.9±1.8%)	267 (87.0±1.9%)	287 (86.7±1.9%)	238 (85.3±2.1%)
0.001	349 (84.1±1.8%)	268 (87.3±1.9%)	288 (87.0±1.8%)	239 (85.7±2.1%)
—	415	307	331	279

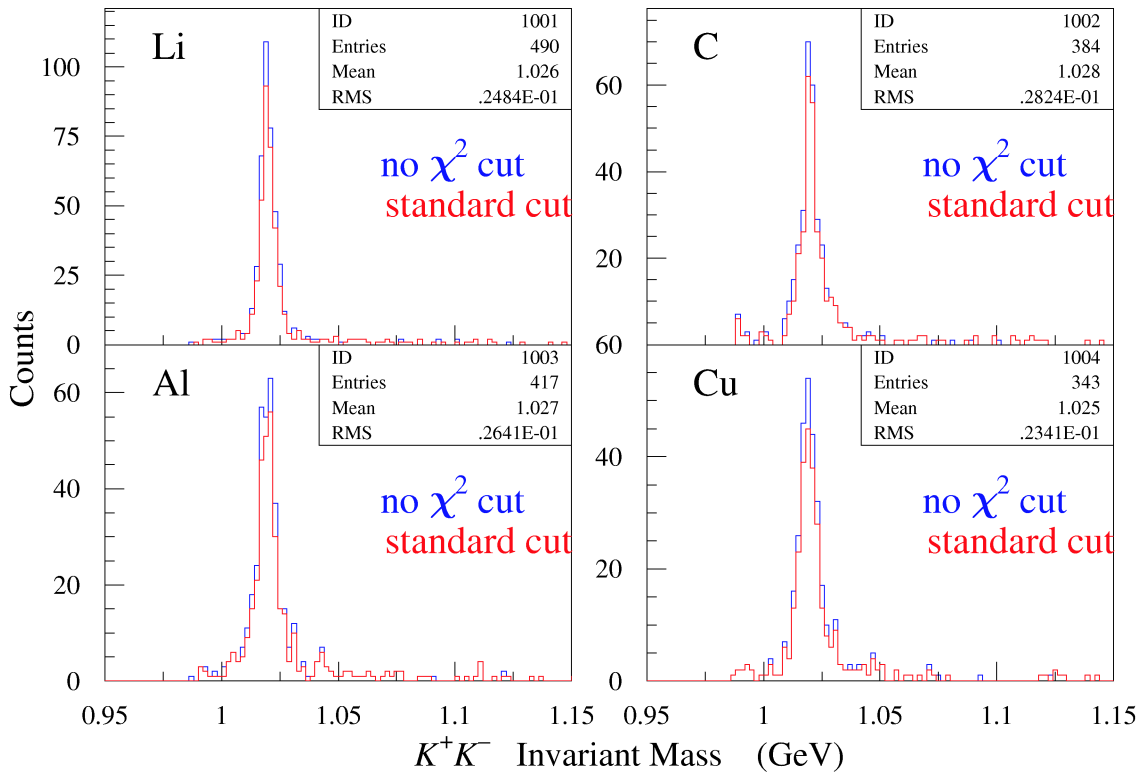
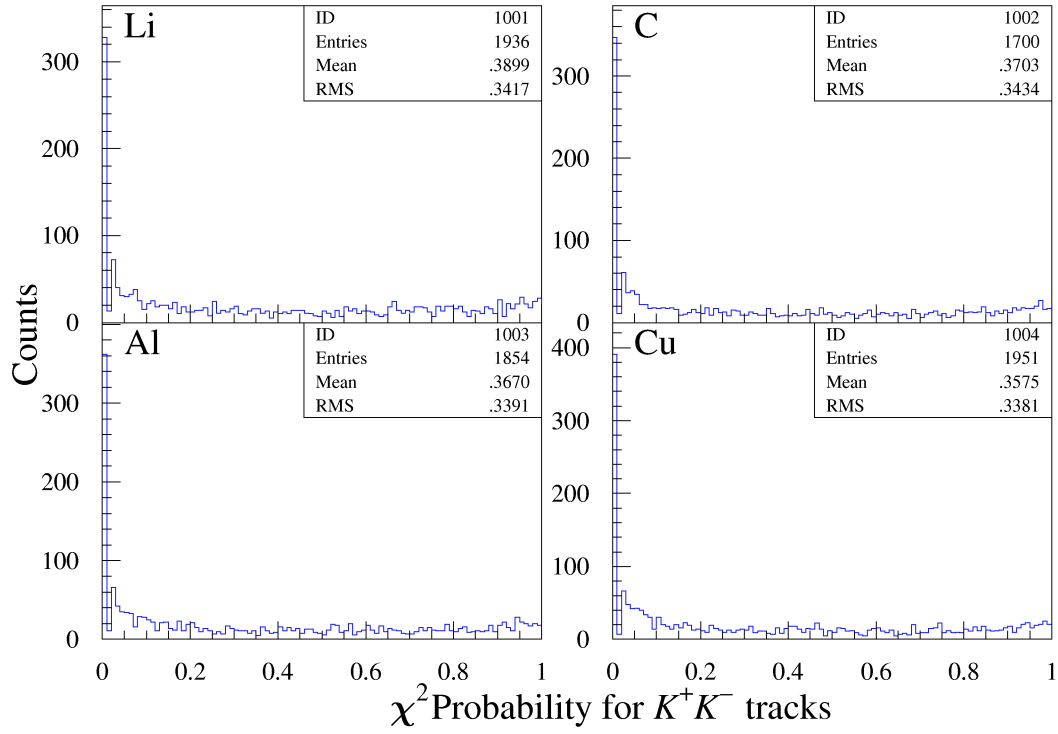


Figure C.5: K^+K^- invariant mass distributions with/without the χ^2 probability cut. The blue lines show the K^+K^- invariant mass distributions without the χ^2 probability cut, and the red lines show those with the χ^2 probability cut.

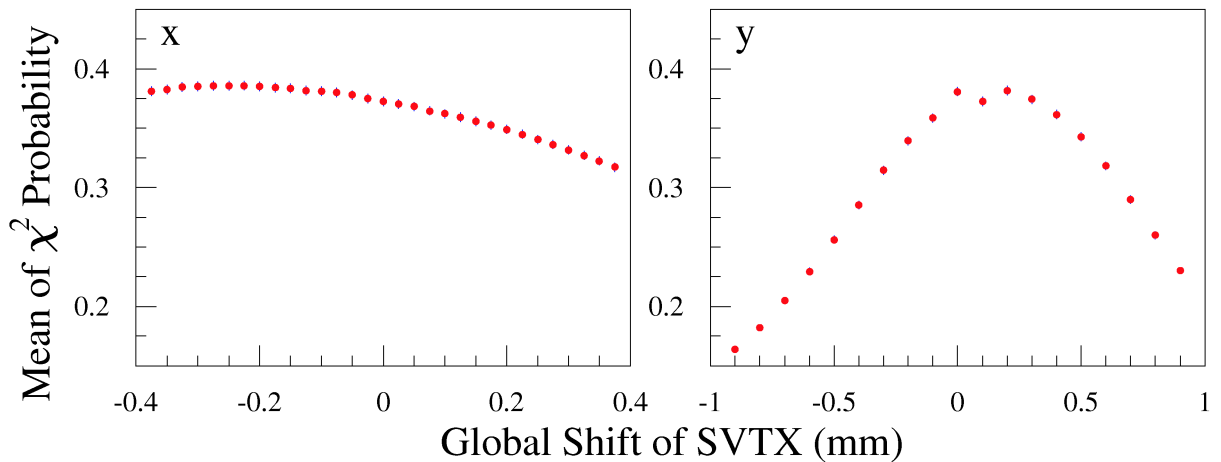
with/without the χ^2 probability cut.

The K^+K^- tracks that does not pass the χ^2 probability cut also makes the ϕ meson peaks in the K^+K^- invariant mass distributions as shown in Figure C.5, and these can be actually associate with the ϕ mesons. The good track cut can be too tight. Figure C.6 shows χ^2 probability distributions for K^+K^- tracks, and the mean of each distribution (0.36~0.39) is smaller than that of LH₂ target (~0.41).

Worse χ^2 probability distribution in the nuclear target run periods can be due to a bad software SVTX alignment. The SVTX detector has been replaced before and after the nuclear target run period. A

Figure C.6: χ^2 probability distribution for K^+K^- tracks

precise software SVTX alignment is needed, but the method by using the reaction $\gamma + p \rightarrow K^+ + \Lambda$ can not be used for the nuclear target runs like LH₂ target since the reacted nucleon is not at rest. Instead a crossing two tracks at a point method has been used for a precise shift and rotation alignment of the SVTX module by module. In this method, the modules are aligned so that the closest distance of the two tracks are minimum.

Figure C.7: χ^2 probability distributions for the K^+K^- tracks as a function of the x , y -global SVTX shifts. The left panel shows the x -global SVTX shift, and the right one shows the y -global SVTX shift.

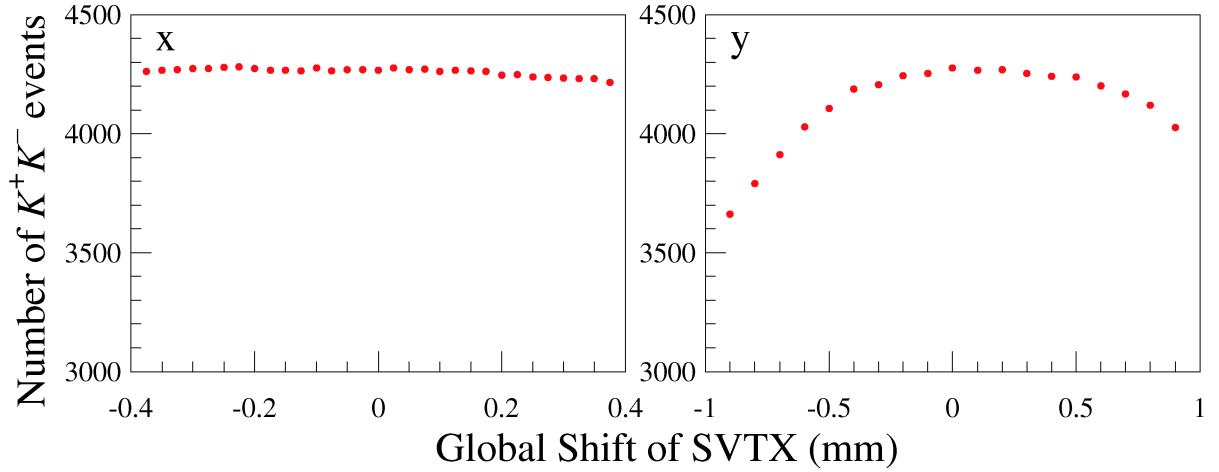


Figure C.8: Number of K^+K^- tracks passing the good track cut as a function of the x , y -global SVTX shifts. The left panel shows the x -global SVTX shift, and the right one shows the y -global SVTX shift.

The mean of χ^2 probability distribution is comparably sensitive to the x , y -global shift of SVTX, thus all the K^+K^- events are re-analyzed with applying x , y -global SVTX shift to check how well the crossing two tracks at a point method works. Figure C.7 shows the mean of χ^2 probability distributions as a function of the x , y -global SVTX shifts. Figure C.8 shows the number of K^+K^- events which pass the good track cut as a function of the x , y -global SVTX shifts. Although the current setting (0 mm x , y -global shift) does not have the largest mean of χ^2 probability distribution, the setting seems to be in the optimum region. Also the global shift does not affect the number of

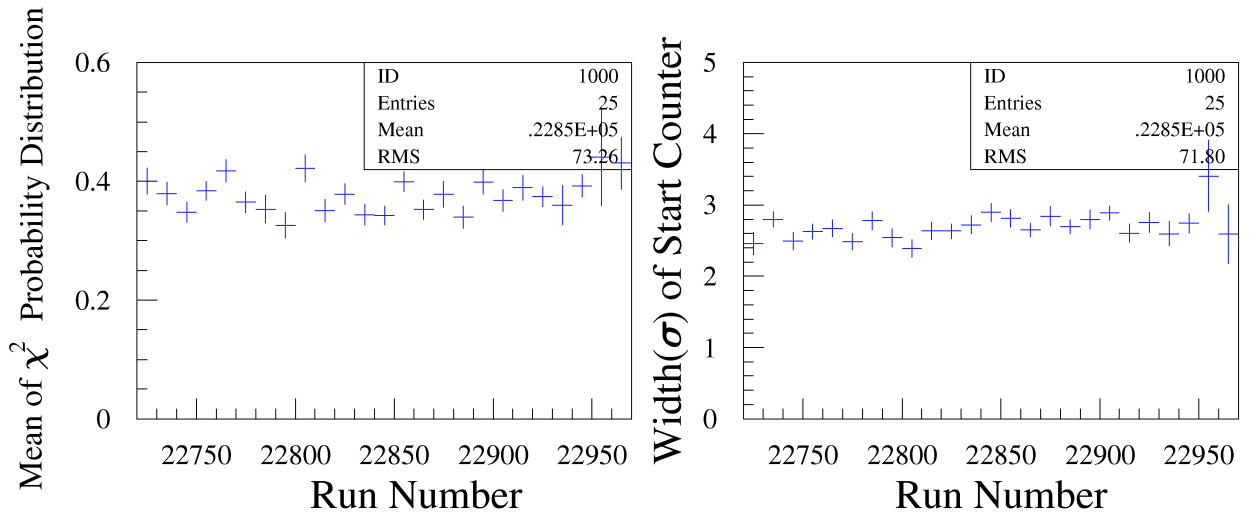


Figure C.9: Run dependence of the mean of the χ^2 distributions and the width of z vertex distributions for the start counter. The left panel shows run dependence of the mean of the χ^2 probability distributions for the K^+K^- tracks, and the right one shows the run dependence of the z -vertex width (σ) of the start counter for the two track events.

K^+K^- tracks so much which pass the good track cut.

Inappropriate threshold values for the DC width can make mean of χ^2 probability distribution smaller. The relation of the drift time to the drift length for the drift chamber would change drastically run by run if this threshold values were too small. In order to check that the threshold is proper or not, the relation of the drift time to the drift length is re-calibrated under the condition that the threshold is 100 channels (about 50 nsec). The difference of the estimated resolutions between current and re-calibrated ones is less than 0.001 mm, and the difference of the drift lengths is 0.003 mm at maximum.

Mean of χ^2 probability distribution is also very stable in the nuclear target run period. The left panel of Figure C.9 shows the run dependence of the mean of the χ^2 probability distributions for the K^+K^- tracks, the right one shows the run dependence of the z -vertex width (σ) of the start counter for two track events, where the fitting function is a sum of a Gaussian and one dimensional polynomial, and no drops or no changes are observed in both run dependences.

C.1.3 z -vertex resolution

The events produced at the target are selected by the z -coordinate of the vertex point. the contamination of the start counter events is estimated by the z -vertex resolution. The z -vertex resolution depends on the opening angle of K^+K^- tracks, which is checked in the MC simulation. Because one sheet of the Cu target is thinnest (1 mm thick), the comparison of the z -vertex distributions between the real and MC simulation data for Cu is the best way to check the resolution. Figure C.11 shows z -vertex distributions of the $\phi \rightarrow K^+K^-$ events for Cu in each opening angle region, where the invariant mass cut discussed in Subsection 3.4.7 has been used. These distributions are fitted with a function

$$F_z(x) = \sum_{i=1}^3 \frac{c_i}{\sqrt{2\pi}\sigma_i} \exp\left(-\frac{(x - m_i)^2}{2\sigma_i^2}\right) + C^2, \quad (\text{C.1})$$

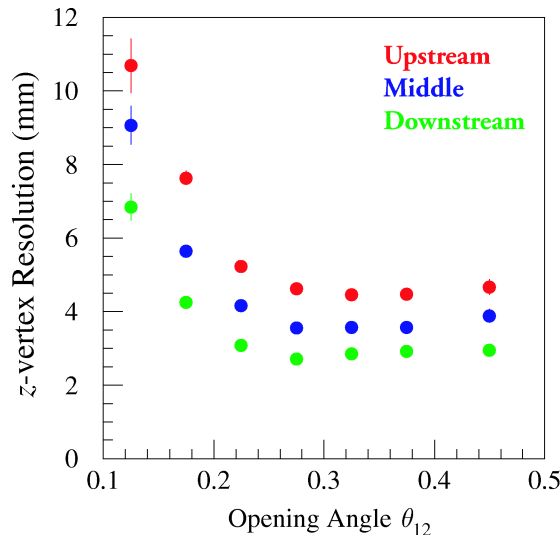


Figure C.10: Opening angle dependence of z -vertex resolutions for $\phi \rightarrow K^+K^-$ events in the MC simulation. The red, blue, and green points show the z -vertex resolutions for the upstream, middle, and downstream Cu sheets.

Table C.5: Fitting results of z -vertex resolutions in the MC simulation

Opening Angle	c	m	σ	C	χ^2/n
0.10–0.15					
upstream	324.5 ± 20.5	-961.65 ± 0.62	10.682 ± 0.741		
middle	329.0 ± 16.3	-925.15 ± 0.53	9.066 ± 0.524		
downstream	317.8 ± 15.8	-890.00 ± 0.33	6.845 ± 0.377		
				0.623 ± 0.143	$263.5/390$
0.15–0.20					
upstream	842.0 ± 22.6	-960.44 ± 0.21	7.637 ± 0.195		
middle	829.9 ± 22.1	-925.55 ± 0.16	5.637 ± 0.157		
downstream	835.3 ± 21.8	-890.12 ± 0.11	4.248 ± 0.115		
				1.057 ± 0.077	$341.5/390$
0.20–0.25					
upstream	2277.9 ± 35.4	-960.43 ± 0.08	5.226 ± 0.080		
middle	2278.9 ± 34.9	-925.29 ± 0.07	4.157 ± 0.059		
downstream	2295.6 ± 34.8	-890.12 ± 0.05	3.083 ± 0.045		
				1.452 ± 0.063	$538.8/390$
0.25–0.30					
upstream	2771.1 ± 38.1	-959.58 ± 0.07	4.620 ± 0.056		
middle	2917.9 ± 38.9	-924.62 ± 0.05	3.566 ± 0.042		
downstream	2989.6 ± 39.2	-889.76 ± 0.04	2.708 ± 0.031		
				1.359 ± 0.055	$561.8/390$
0.30–0.35					
upstream	1317.8 ± 26.4	-959.09 ± 0.09	4.455 ± 0.081		
middle	1381.9 ± 26.9	-924.38 ± 0.07	3.572 ± 0.063		
downstream	1457.8 ± 27.4	-889.71 ± 0.05	2.848 ± 0.045		
				1.059 ± 0.053	$397.6/390$
0.35–0.40					
upstream	448.8 ± 15.5	-958.55 ± 0.16	4.472 ± 0.135		
middle	499.0 ± 16.2	-924.11 ± 0.12	3.578 ± 0.106		
downstream	539.1 ± 16.7	-889.37 ± 0.09	2.914 ± 0.074		
				0.754 ± 0.049	$302.7/390$
0.40–0.50					
upstream	196.1 ± 10.4	-958.28 ± 0.26	4.669 ± 0.218		
middle	254.9 ± 11.8	-923.79 ± 0.19	3.883 ± 0.183		
downstream	256.5 ± 11.6	-889.29 ± 0.14	2.950 ± 0.116		
				0.613 ± 0.049	$285.9/390$

assuming that each peak corresponding to each sheet of Cu has a Gaussian shape, and fitting is made by the maximum likelihood method [69]. Figure C.11 shows the fitting results, and Table C.1.3 summarizes the fitting results. Figure C.10 shows the z -vertex resolution as a function of the opening angle. The narrower opening angle makes the resolution worse simply due to the geometry of the tracks. The extremely larger opening angle also makes it worse slightly as the opening angle becomes larger. The K^+ and K^- with lower momenta decay from ϕ mesons for the large opening angle events. The effect of multiple scattering in a unit length is larger for the lower momentum, and the path lengths with which these particles penetrate in the target materials are longer because these

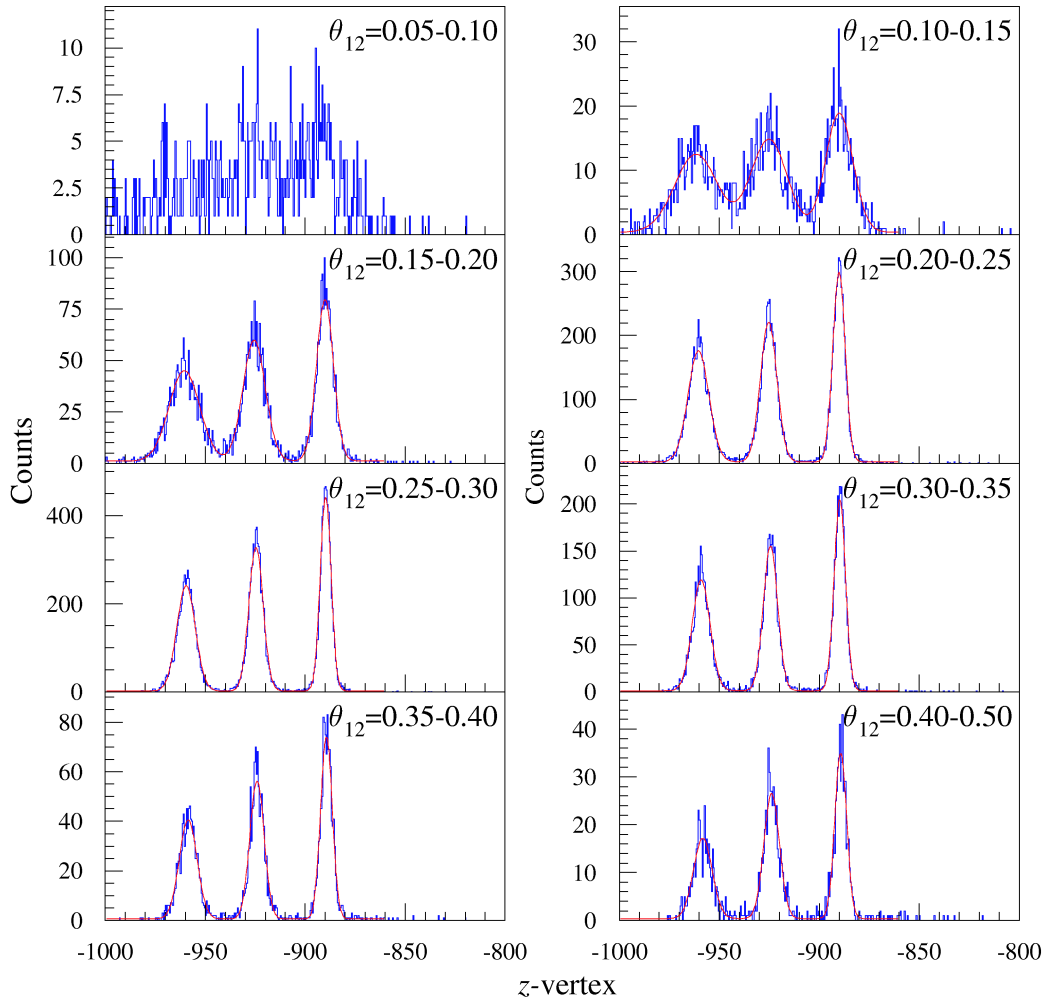


Figure C.11: z -vertex distributions for $\phi \rightarrow K^+K^-$ events in the MC simulation. Clearly, the resolution of the z -vertex is poorer for the smaller opening angles.

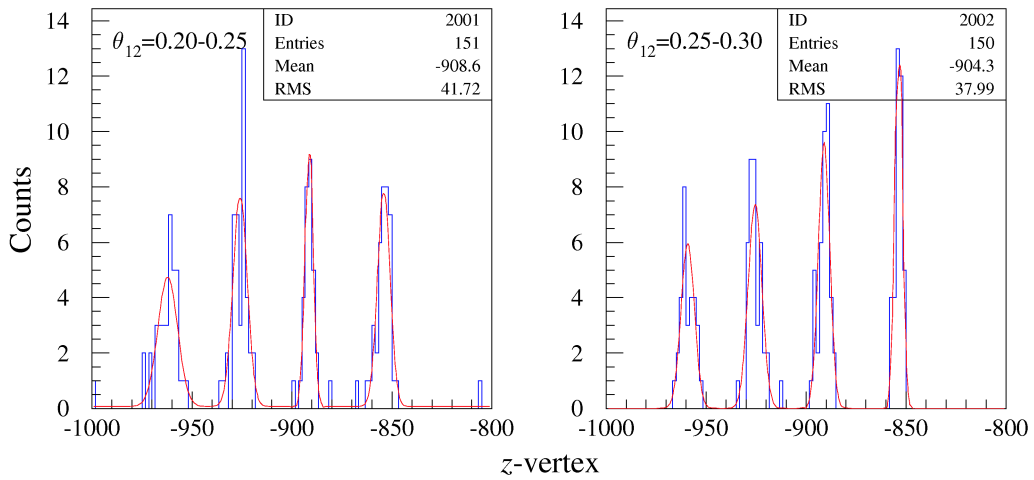


Figure C.12: z -vertex distributions for $\phi \rightarrow K^+K^-$ events in the real data. The left and right panels show the z -vertex distributions for the events with the opening angle from 0.20 to 0.25 and for those with the opening angle from 0.25 to 0.30, respectively.

tracks have comparably larger angles to z -axis.

Figure C.12 shows z -vertex distribution of K^+K^- tracks for Cu in the real data, where the invariant mass cut discussed in Subsection 3.4.7 has been also applied here. In the real data, the peak corresponding to the start counter is also assumed to have a Gaussian shape and the fitting function is

$$F_z(x) = \sum_{i=1}^4 \frac{c_i}{\sqrt{2\pi}\sigma_i} \exp\left(-\frac{(x-m_i)^2}{2\sigma_i^2}\right) + C^2. \quad (\text{C.2})$$

Table C.6: Fitting results of z -vertex resolutions in the real data

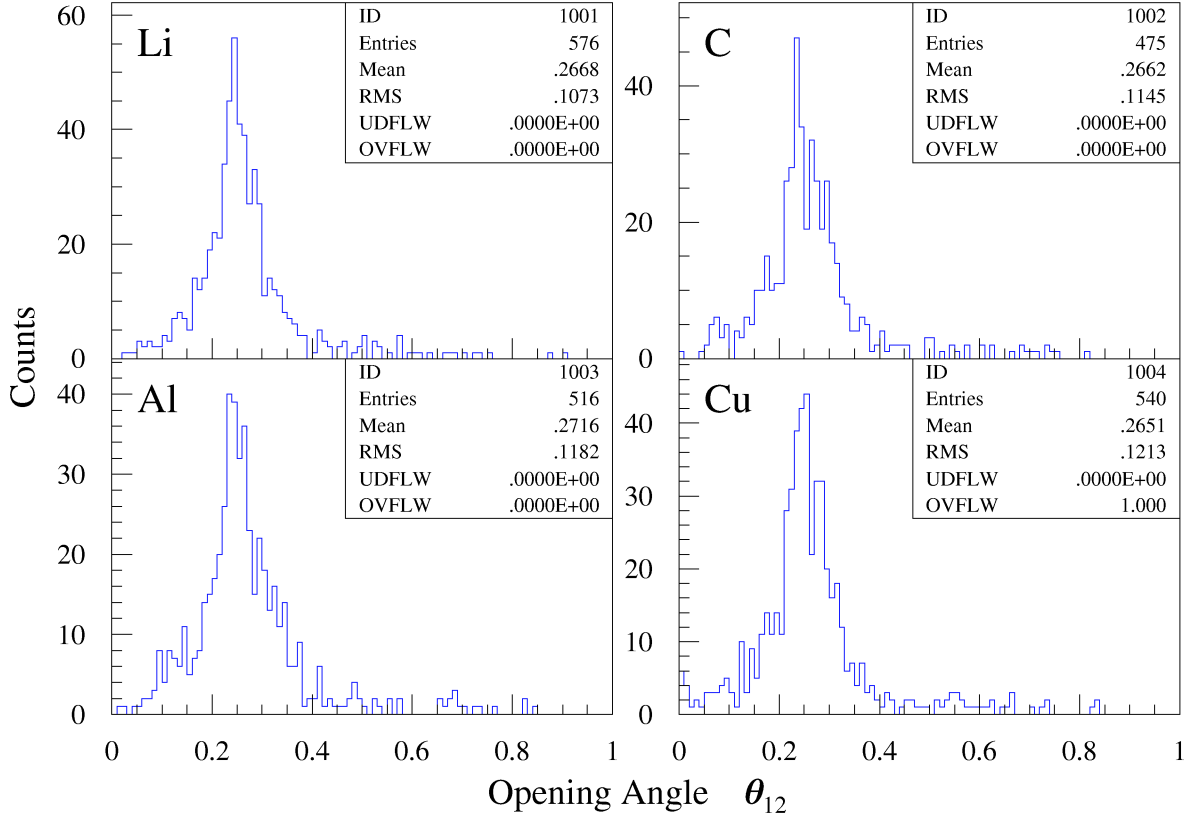
Opening Angle	c	m	σ	C	χ^2/n
0.20–0.25					
Upstream	57.8±10.1	-962.13±0.90	4.929±0.622		
Middle	68.2±10.8	-925.95±0.59	3.576±0.431		
Downstream	47.7±9.0	-891.43±0.41	2.046±0.361		
Start Counter	61.9±10.3	-854.07±0.55	3.156±0.408		
				0.269±0.062	68.6/107
0.25–0.30					
Upstream	49.9±9.1	-959.22±0.61	3.344±0.423		
Middle	64.0±11.7	-925.53±1.10	3.446±1.812		
Downstream	68.2±10.7	-890.99±0.44	2.844±0.310		
Start Counter	63.3±10.3	-853.73±0.31	1.899±0.215		
				-0.078±0.208	42.4/107

Table C.1.3 shows the fitting results. Table C.7 summarizes the comparison of the z -vertex resolutions for $\phi \rightarrow K^+K^-$ events between the real and MC simulation data. No significant difference is observed

Table C.7: Comparison of the z -vertex distribution between the real and MC simulation data

Opening Angle	Real data	MC simulation
0.20–0.25		
upstream	4.929±0.622	5.226±0.080
middle	3.576±0.431	4.157±0.059
downstream	2.046±0.361	3.083±0.045
0.25–0.30		
upstream	3.344±0.423	4.620±0.056
middle	3.446±1.812	3.566±0.042
downstream	2.844±0.310	2.708±0.031

though the results of the real data have a little bit smaller values (better resolutions). Thus, the estimation of z -vertex resolution in the MC simulation is reliable. The z -vertex resolution at downstream is important to separate the start counter events from the target events by the z -vertex cut. The closest distance between the target and start counter is 10 mm for Li, and which is the minimum. When the opening angle were required as $\theta_{12} = 0.10 \sim 0.15$, the events from the target and the start counter would be separated more clearly. Figure C.13 shows the opening angle distribution for each target. The small opening angle events which have a poor z -vertex resolution are a small fraction in the total, and the contamination of the start counter events are negligibly small as discussed in Subsection 3.6.1.

Figure C.13: Opening angle distribution for $\phi \rightarrow K^+K^-$ events

C.1.4 Momentum resolution

The performance of the spectrometer itself is common for all the targets, and only the energy loss and multiple scattering in the target material can affect the momentum resolution.

The mass square resolution for the proton is well reproduced from the resolution of each detector system in the wide momentum range for each target as shown in Figure 3.8 in Subsection 3.4.3. This indicates the momentum resolution is well understood and is included in the geometrical acceptance correction.

C.1.5 Efficiency of drift chambers

The ratio of e^+e^- events to hadron events are higher for the heavier nuclear target, thus the efficiency of the drift chamber may drop for heavy nuclear target. The efficiency of the drift chamber for each target is checked. The procedure of the estimation is as follows:

1. The single proton track events are selected to avoid the decay in flight events.
2. Tracking is performed under the condition that the information of the plane is not used in which efficiency of the wire is wanted to know.
3. Straight line fitting is made using fitting points in the drift chamber that has the plane of interest.

4. The position that the charged particle goes through the plane of interest is determined by interpolating or extrapolating the straight line.
5. Whether the wire is efficient or not is determined by whether the hit exists or not within the two cell size (12 mm for DC1 and 20 mm for DC2) from the predicted position.

Figure C.14 shows the efficiency wire by wire.

The efficiencies for the wires of the DC2, DC3, and DC1X'' are lower, especially they are only about ~70% for DC1X''. The threshold for the DC amplifier/discriminator cards, and the operating high voltages were not optimized in the nuclear target run periods. The supplied high voltage can be too low. Another guess that the software threshold for the TDC width should be too high has been abandoned because the efficiencies are not improved even if the TDC width cut is not applied.

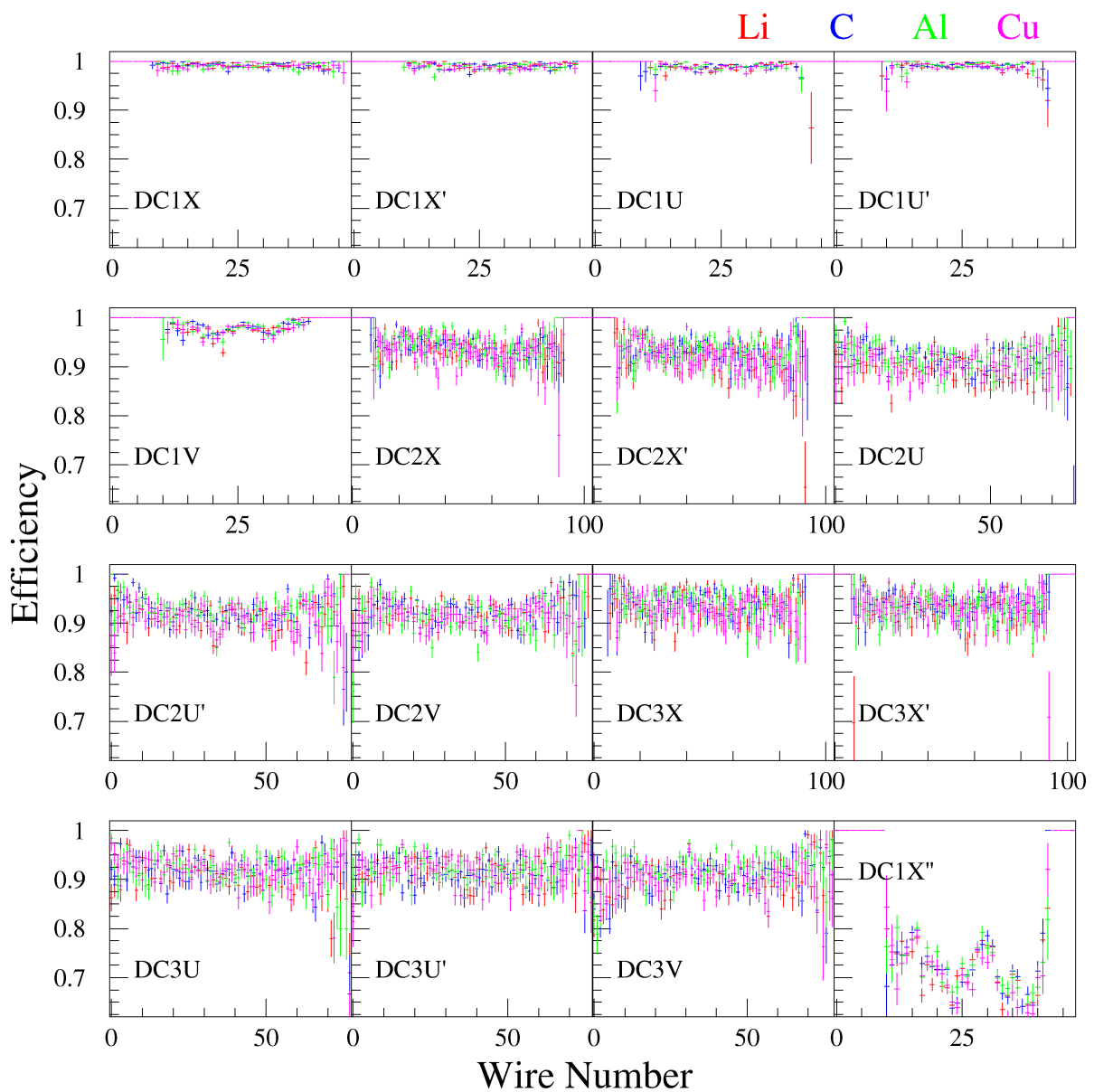


Figure C.14: Efficiency of drift chambers

Figure C.15 shows the efficiencies for the DC1" wires with and without the DC TDC width cut. No significant difference is observed between both the conditions.

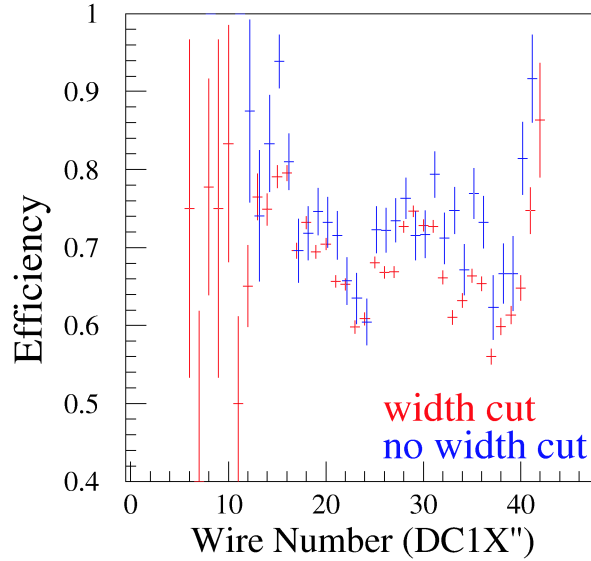


Figure C.15: Comparison of the efficiencies with/without the DC TDC width cut. No significant difference is observed.

As a result, any significant difference of the efficiencies is not observed among the different targets, these low efficiencies do not affect A -dependence.

C.1.6 Yield from the start counter

The yields from the start counter are investigated to confirm the normalization by the tagger hits, by the live time, by the efficiency of the analyzer, and by the attenuation of the photon flux. The yields should be the same for all the nuclear targets because the start counter and its downstream is common. The yield Y_{sta} is defined as

$$Y_{\text{sta}} = \frac{N}{N_{\gamma}\eta_{\text{DAQ}}\eta_{\text{ana}}\eta_{\text{att}}(\text{StartCounter})}, \quad (\text{C.3})$$

where N is the number of events. Note that the geometrical acceptance for the start counter events is common. The Y_{sta} is estimated for $\pi^+\pi^-$ events and $\phi \rightarrow K^+K^-$ events. The $\pi^+\pi^-$, π^+p , π^-p , and K^+K^- events from the start counter are selected as

- number of tracks should be 2,
- number of tagger hits should be 1,
- closest distance should be less than 5 mm,
- particles associated with tracks should $\pi^+\pi^-$, π^+p , π^-p , and K^+K^- ,
- both the two tracks should pass the good track cut,
- opening angle of the two tracks should be less than 0.15, and
- z -vertex should be $-863 \leq z < -840$.

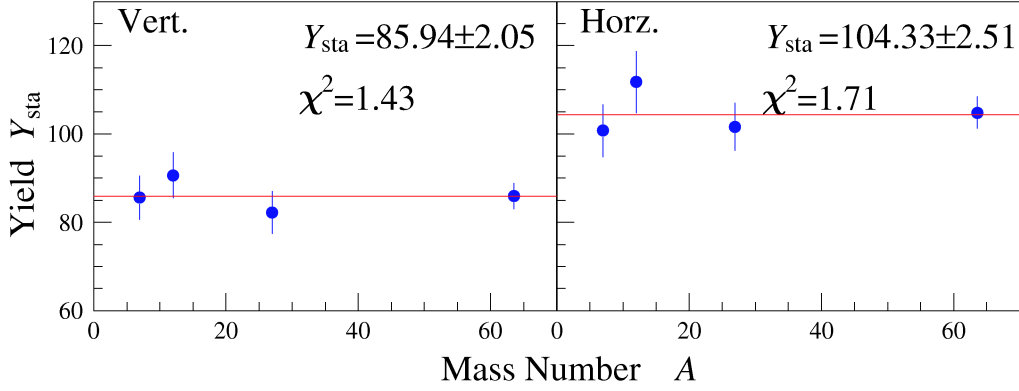


Figure C.16: $\pi^+\pi^-$ yield for the start counter. The left panel shows the yields for the vertically polarized data, and the right ones shows those for the horizontally polarized data.

Table C.8: $\pi^+\pi^-$ yield for the start counter

	Li	C	Al	Cu
#Events (Vert.)	297	307	292	855
Y (Vert.)	85.5 ± 5.0	90.7 ± 5.2	82.3 ± 4.8	85.9 ± 2.9
#Events (Horz.)	281	250	347	857
Y (Horz.)	100.8 ± 6.0	111.7 ± 7.1	101.7 ± 5.5	104.9 ± 3.6

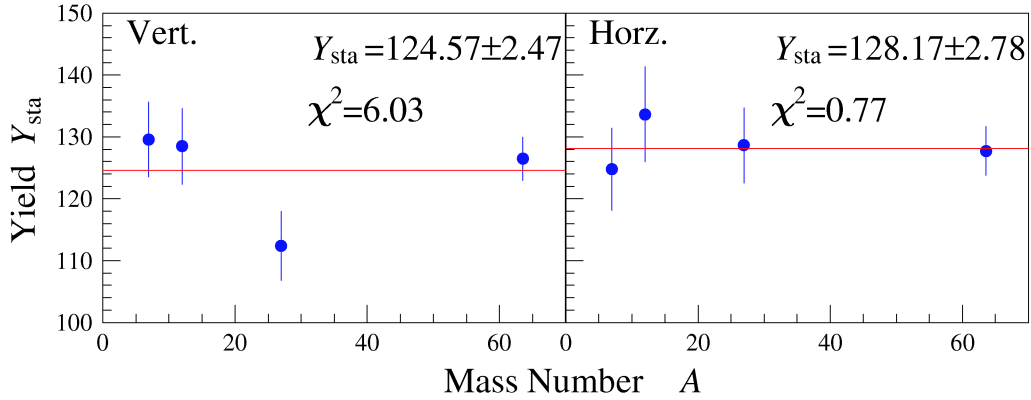


Figure C.17: π^+p yield for the start counter. The left panel shows the yields for the vertically polarized data, and the right ones shows those for the horizontally polarized data.

Table C.9: π^+p yield for the start counter

	Li	C	Al	Cu
#Events (Vert.)	450	435	399	1258
Y (Vert.)	129.6 ± 6.1	128.5 ± 6.2	112.4 ± 5.6	126.4 ± 3.6
#Events (Horz.)	348	299	439	1044
Y (Horz.)	124.8 ± 6.7	133.6 ± 7.7	128.6 ± 6.1	127.7 ± 4.0

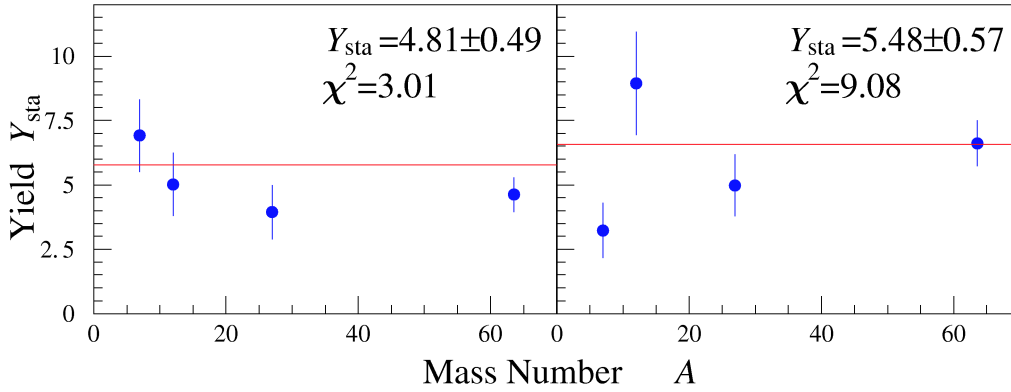


Figure C.18: K^+K^- yield for the start counter. The left panel shows the yields for the vertically polarized data, and the right ones shows those for the horizontally polarized data.

Table C.10: K^+K^- yield for the start counter

	Li	C	Al	Cu
#Events (Vert.)	31	20	18	59
Y (Vert.)	8.9 ± 1.6	5.9 ± 1.3	5.1 ± 1.2	5.9 ± 0.8
#Events (Horz.)	14	22	20	64
Y (Horz.)	5.0 ± 1.3	9.8 ± 2.1	5.3 ± 1.2	7.2 ± 0.9

Tables C.8, C.9, and C.10 summarize the number and the yield of $\pi^+\pi^-$, π^+p , and K^+K^- events, and Figure C.16, C.17, and C.18 show A -dependence of the yields. The yields are constant independently of A for the various reactions, thus it can be concluded that the normalization factors discussed in Section 3.7 do not have a serious problem.

C.2 Different kinematical conditions

C.2.1 z -vertex dependence of the geometrical acceptance

The target positions and thicknesses are different among the four nuclear targets although the center of z positions and their standard deviations have been aimed to be set the same. Because the attenuation of the photon flux in the target material is not implemented in the MC simulation, the number of generated ϕ events are corrected according to z coordinate of the produced points according to the mass attenuation length discussed in Subsection 3.7.3. Figure C.19 shows z distributions of the produced points in the MC simulation with the correction of the photon flux attenuation.

In order to check how precise z dependence of the yield is estimated in the MC simulation, the yield ratios between the real and MC simulation data are investigated in the following three z -vertex regions.

$$\begin{aligned}
 & -965.0 \leq z < -925.0, \quad -925.0 \leq z < -895.0, \quad \text{and} \quad -895.0 \leq z < -864.0 \quad \text{for Li} \\
 & -980.0 \leq z < -942.5, \quad -942.5 \leq z < -907.5, \quad \text{and} \quad -907.5 \leq z < -864.0 \quad \text{for C, Al, and Cu}
 \end{aligned}$$

The attenuation of the photon flux in the target material is also corrected in the MC simulation.

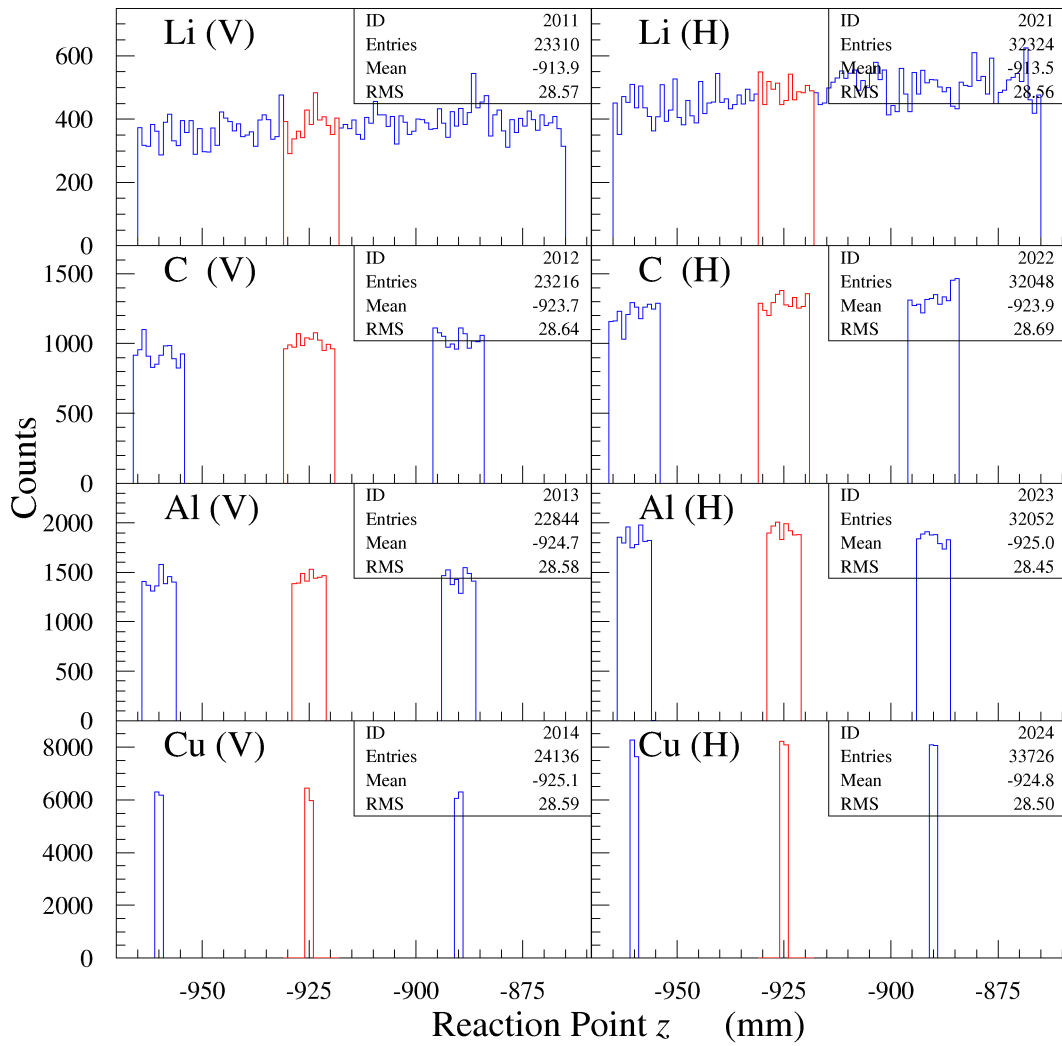


Figure C.19: Yield as a function of z -vertex in the MC simulation.

Figures C.20, and C.21 show these ratios in the various conditions. The ratios are constant, thus z vertex distributions are reproduced in the MC simulation, and this implies the geometrical acceptance of the detector system is well understood.

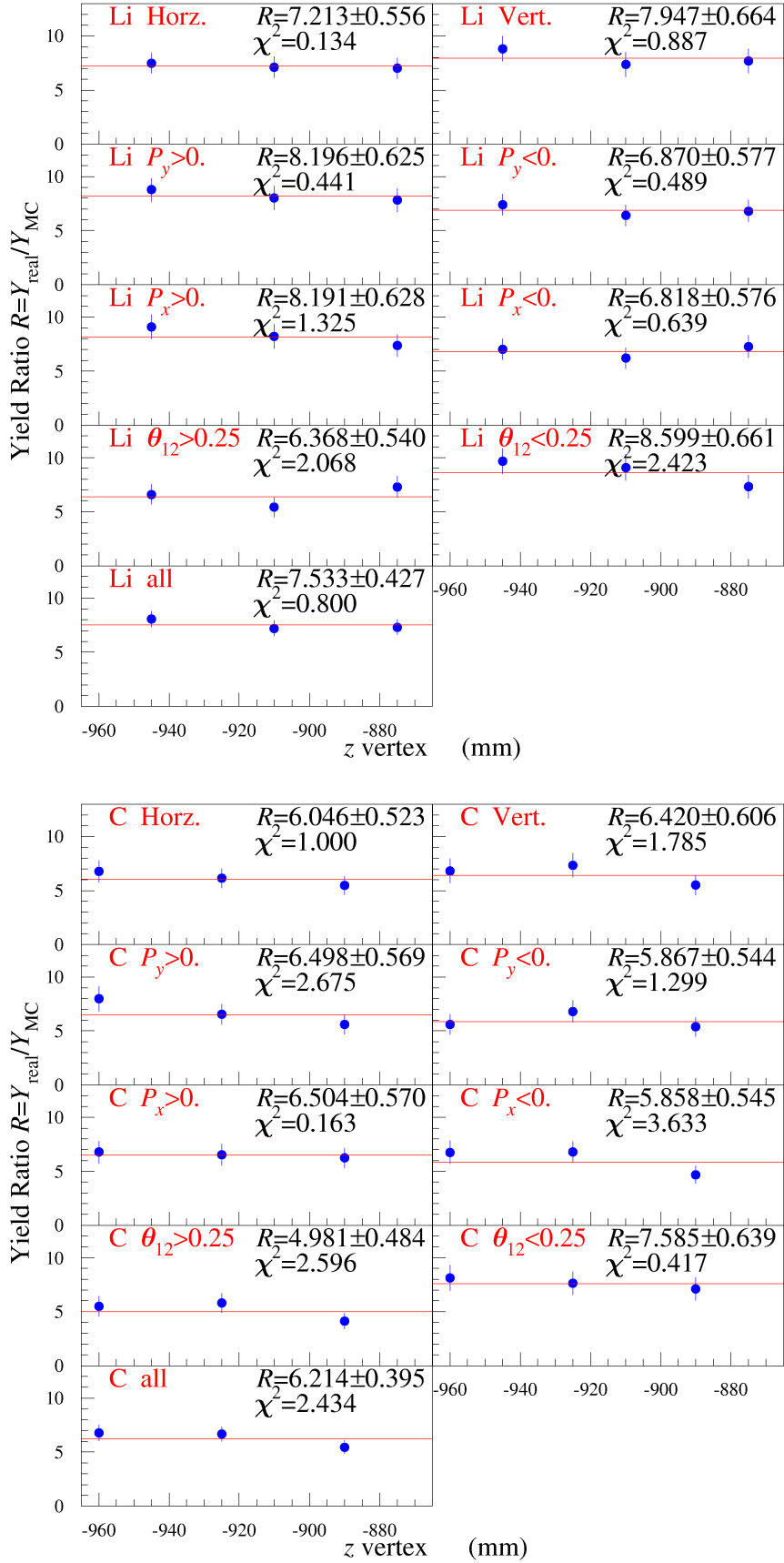


Figure C.20: Yield ratio between the real and MC simulation data (1). Figures show the yield ratios as a function of z -vertex for Li and C.

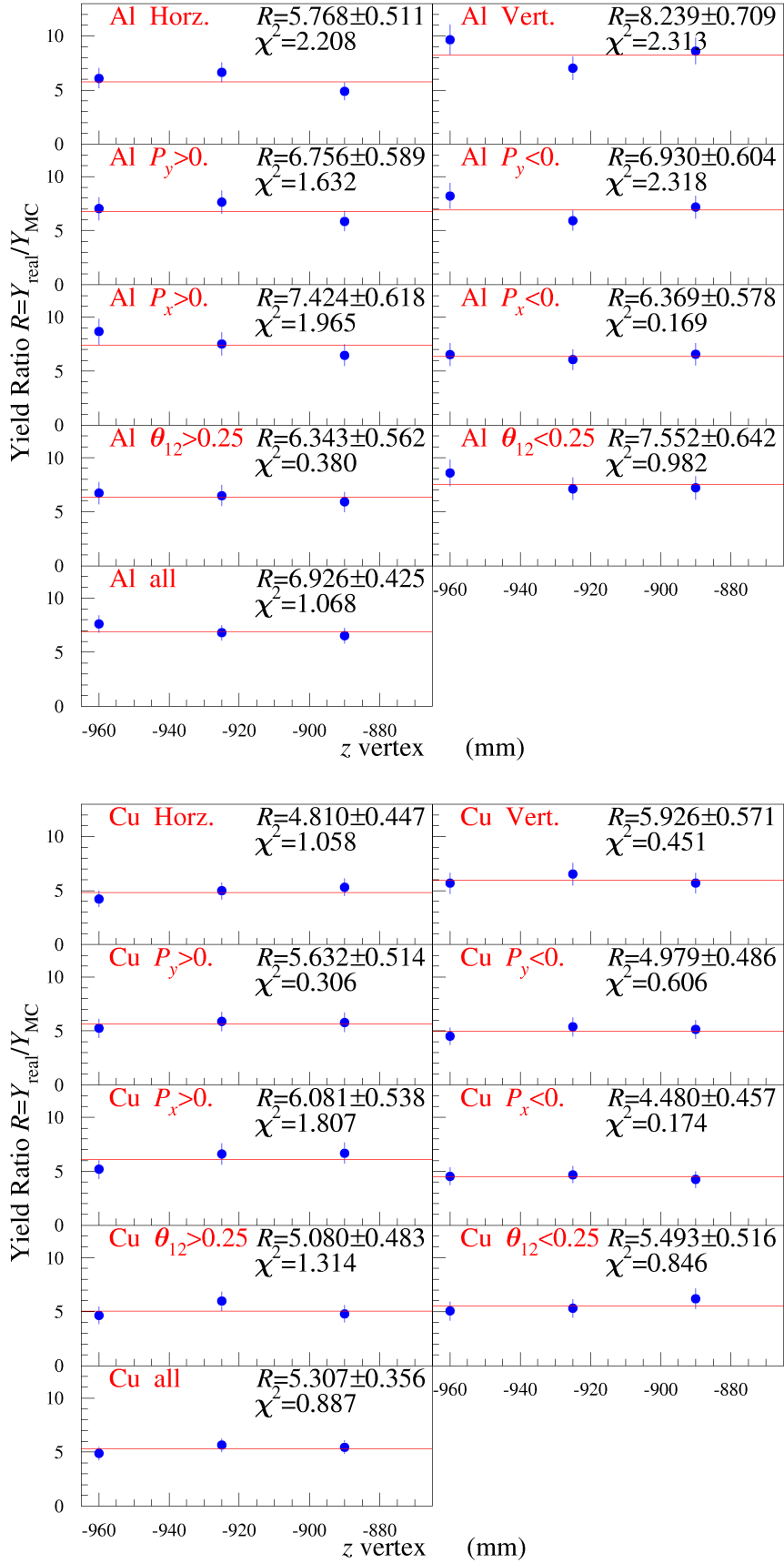


Figure C.21: Yield ratio between the real and MC simulation data (2). Figures show the yield ratios as a function of z -vertex for Al and Cu.

C.2.2 Center of mass energy

The incident γ energy distributions are common among the different targets, while the effective ones to the nucleon differ due to the difference of the Fermi momentum distributions. The E_γ dependence of the cross section near the threshold region can change drastically [79]. This can affect the A -dependence of the yields. Figure C.22 shows the Fermi motion that ϕ mesons are produced

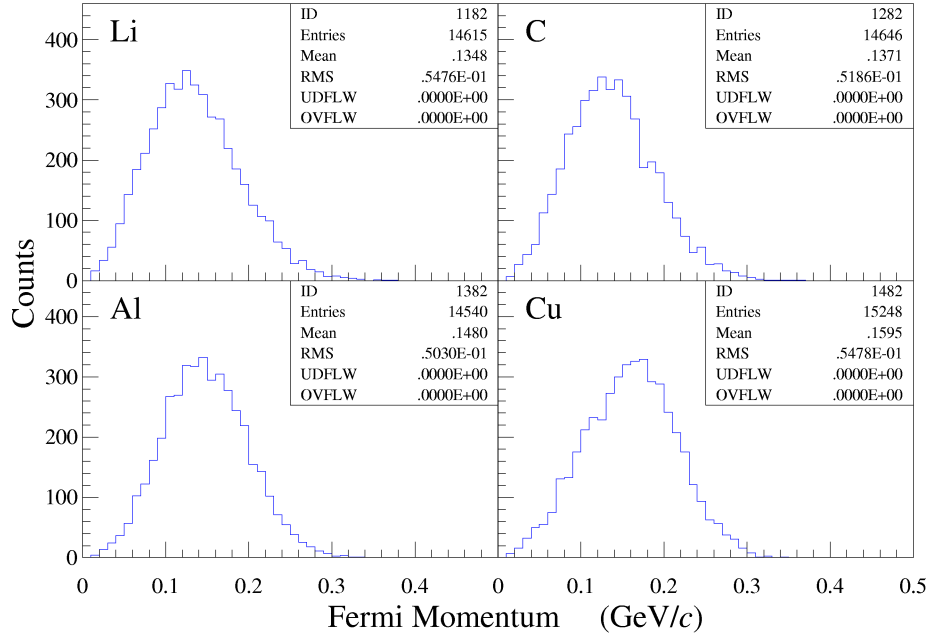


Figure C.22: Fermi momentum distribution for the detected ϕ mesons

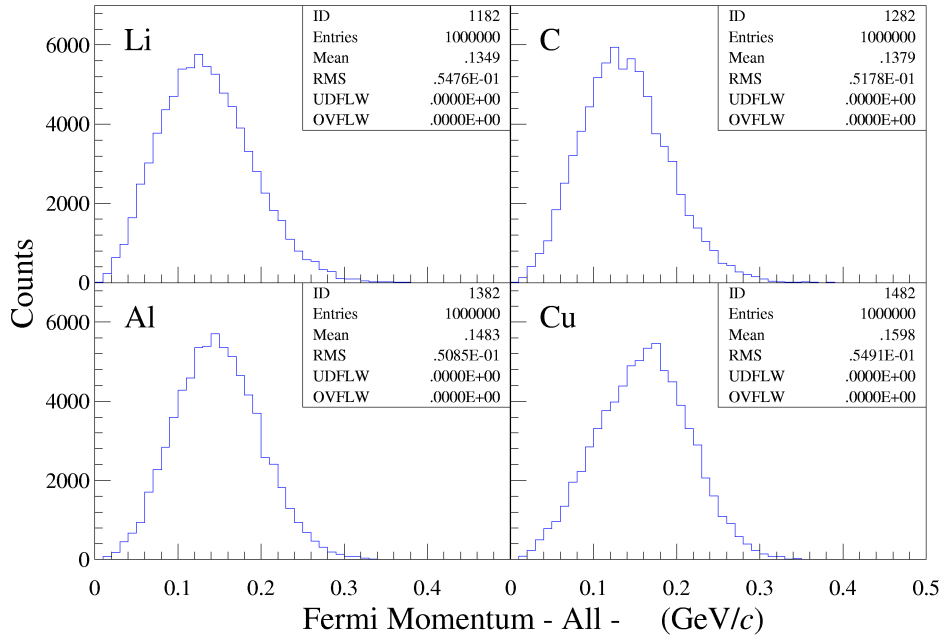


Figure C.23: Fermi momentum distribution for the produced ϕ mesons

and detected in the MC simulation, and Figure C.23 shows that for the produced ones. The heavier target has a larger momentum. As an estimation of the effective incident γ energy, the distributions of center of mass energy between ϕ meson and reacted nucleon $W = \sqrt{s}$ are investigated for the different targets. Figure C.24, C.25 shows these for the detected, and the produced ϕ mesons, respectively.

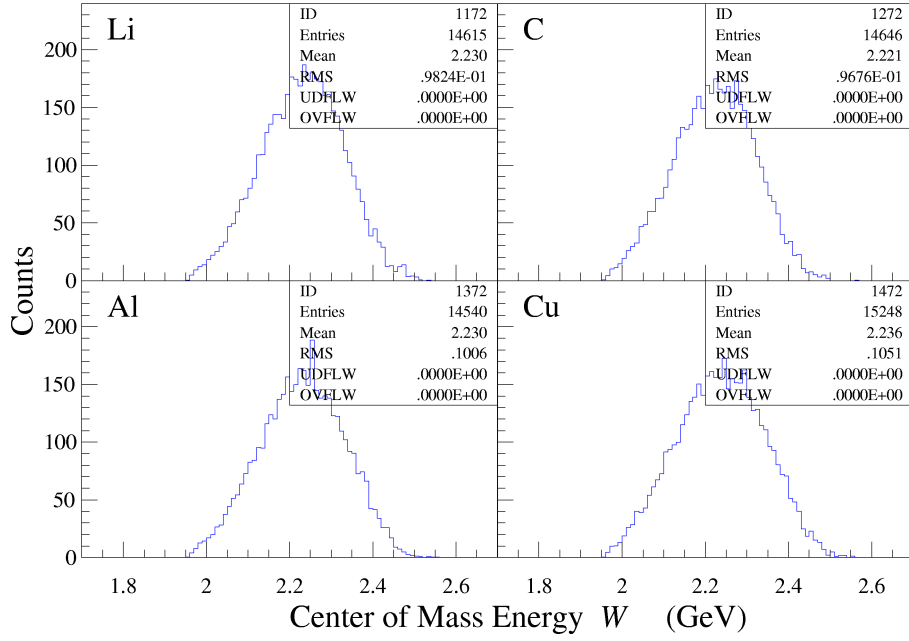


Figure C.24: Center of mass distribution for the detected ϕ mesons

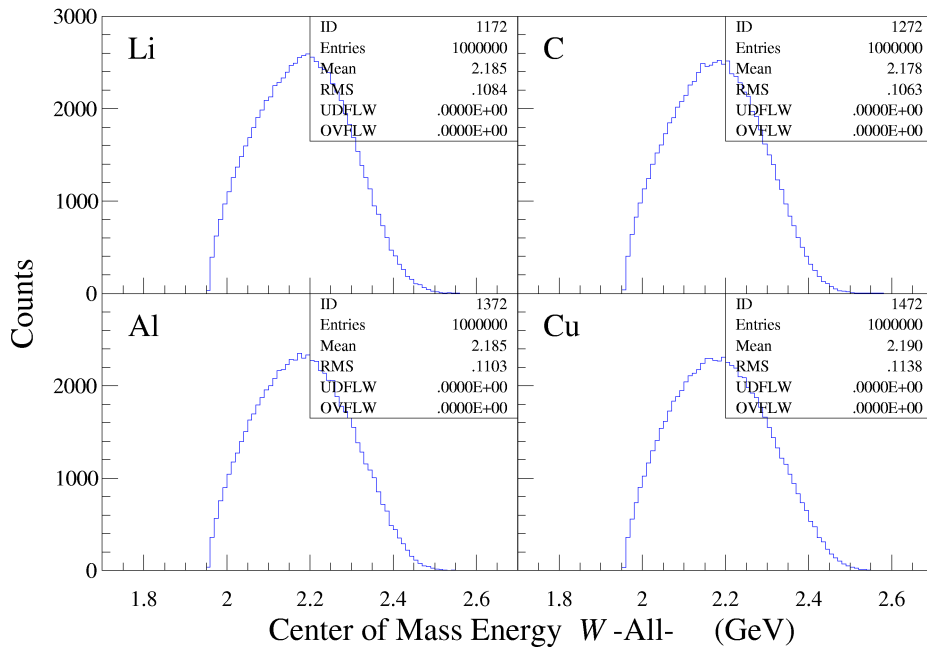
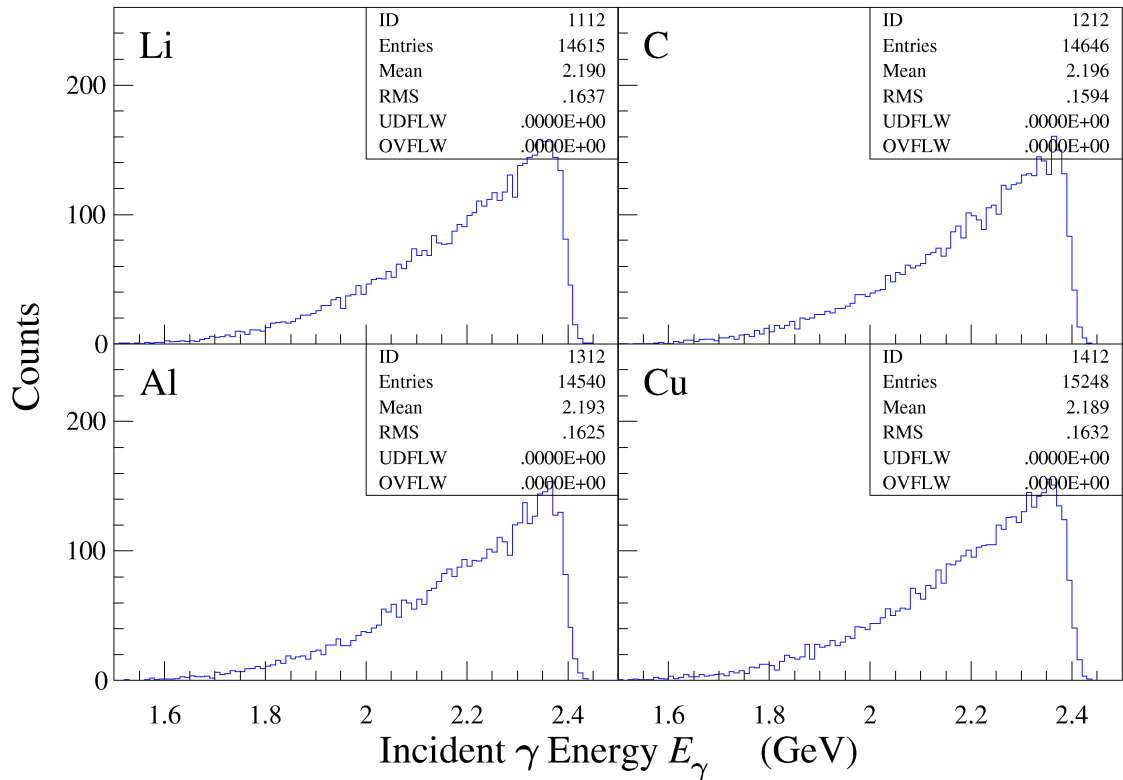
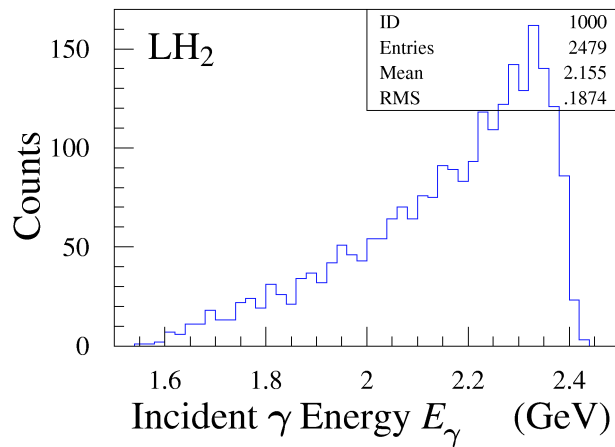


Figure C.25: Center of mass distribution for all the produced ϕ mesons

Figure C.26: Incident γ energy distribution for the detected ϕ meson (MC)Figure C.27: Incident γ energy distribution for the detected ϕ meson for LH₂ (MC)

There is little difference in the W distributions, and the effect of the Fermi motion to the effective γ energy can be negligible. Figure 3.25 in Subsection 3.5.2 shows the γ energy distribution that ϕ mesons are detected in the real data. These also differ little among the different targets. Figures C.26 and C.27 show those in the MC simulation.

C.3 Momentum mis-calibration

If the momentum calibration is wrong due to some reason such as wrong energy loss correction and so on, the missing energy distributions change. In this section, the correction of the momentum is discussed.

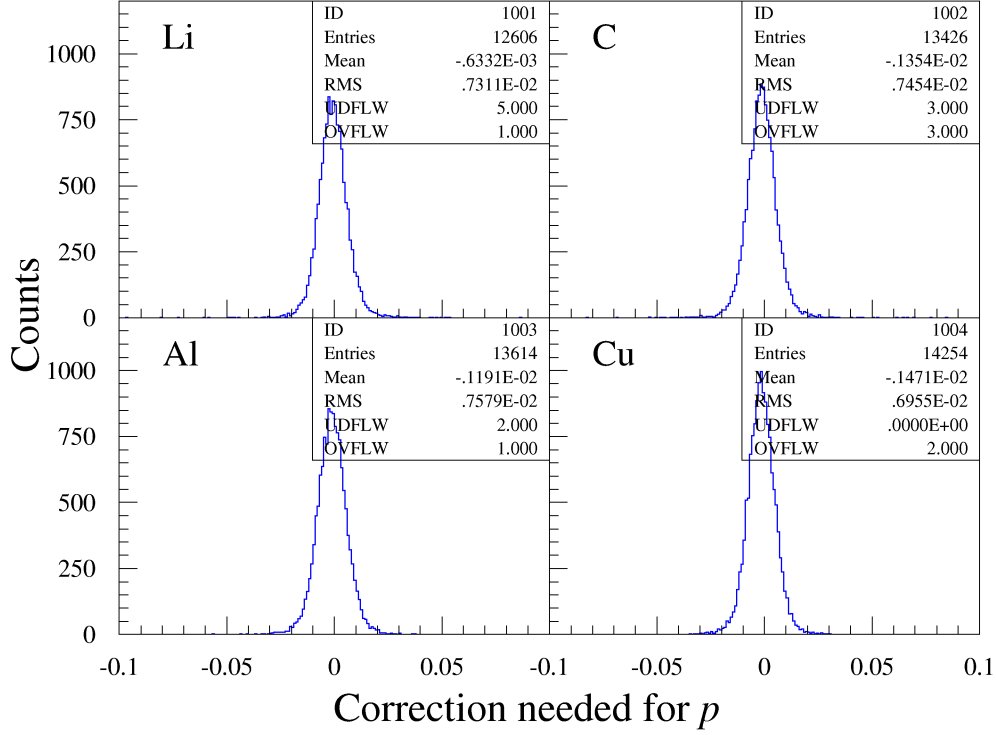


Figure C.28: Correction factor C_p to the measured momentum

The deviation of the KK invariant mass centroid can imply the momentum mis-calibration. The correction C_p needed for p_{meas} is investigated, and C_p is defined as

$$C_p = \frac{p_{\text{meas}}}{p_K} - 1, \quad (\text{C.4})$$

where p_{meas} stands for the measured momentum by the spectrometer, Figure C.28 shows C_p distributions in the MC simulation. The peaks are positioned at zero. The energy loss correction applied to the momentum is reasonable. Figure C.29 shows the relation of the momentum correction (%) to the centroid of the KK invariant mass distribution, where the centroid is obtained by fitting with the Breit-Wigner function between 1000 and 1060 MeV. In order to adjust the centroid to the nominal ϕ meson mass (1019.456 MeV) [49], the momentum corrections of -0.317%, -1.138%, -0.047%, and +0.176% are needed for each target. Figure C.30 shows the comparison of the missing energy distributions with and without this additional momentum correction. The momentum correction makes the missing energy larger especially for the C target.

Figures C.31 show the excess distributions of the measured momentum when the energy loss is estimated under the condition that the target is placed at 1 mm upstream/downstream of the actual target position. The events with the z -vertex between the target sheets concentrate at zero in the excess distributions because the path lengths in the target material do not change. The 1 mm mis-measurement of the target z position makes 0.02%, 0.04%, 0.05%, and 0.02% momentum

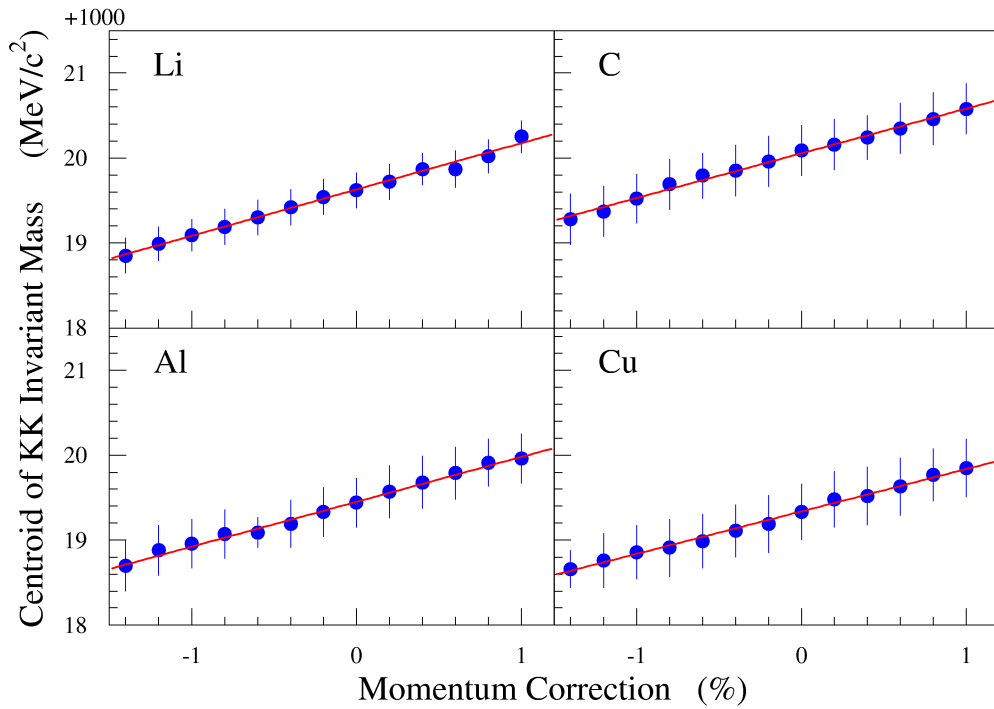


Figure C.29: Relation of the momentum correction to the centroid of the KK invariant mass distribution

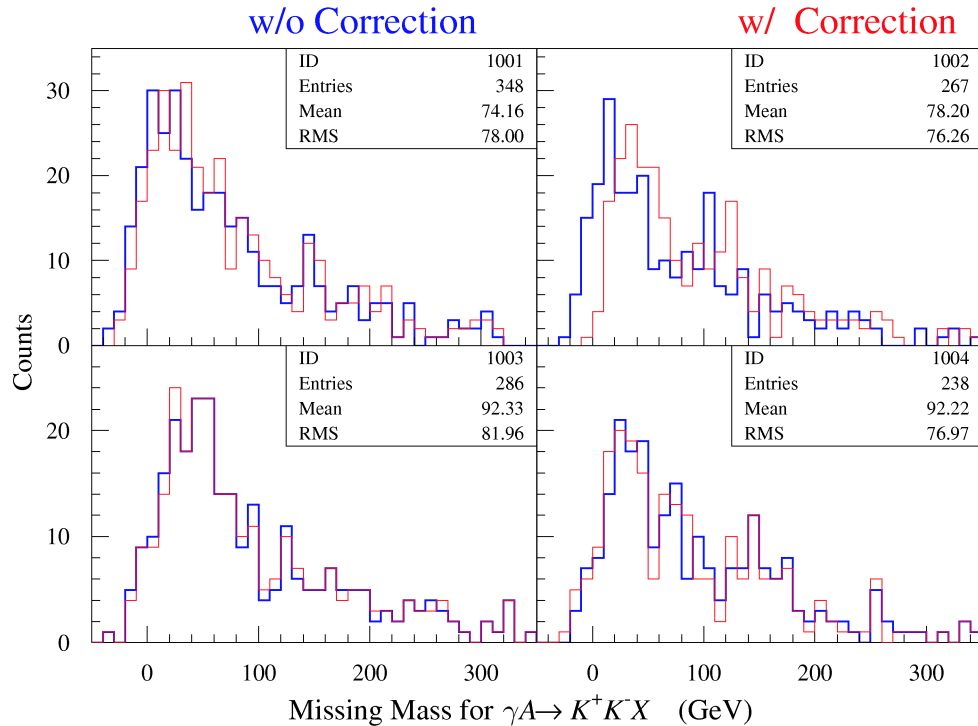


Figure C.30: Comparison of the missing energy distributions with/without momentum correction

mis-measurement. It is difficult to reproduce the 1% momentum correction in the C target by the ambiguity of the z position of the target. The ambiguity of target thickness, which includes the target

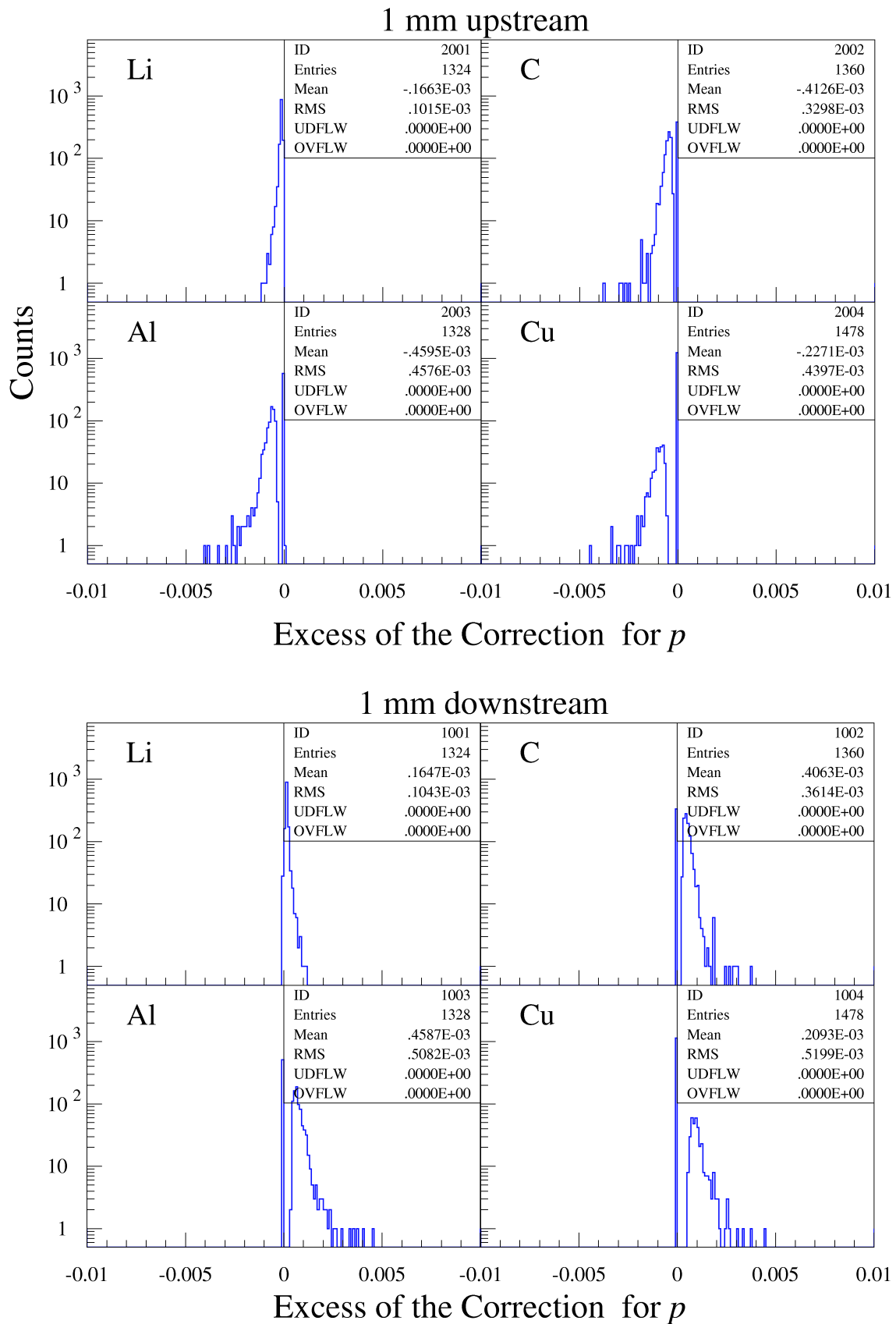


Figure C.31: Excess of the measured momentum. The upper and lower panels show the excess under the condition that the target is placed at 1 mm upstream and 1 mm downstream of the actual target position.

thickness itself and the effective target thickness due to the tilt, is much less than 1 mm, which can not explain 1% momentum correction in C, either. Then, the observed deviation of the K^+K^- peak positions are made by the statistical effects.

C.4 KK background from $\Lambda(1520)$ photo-production

The background candidates in the KK invariant mass distribution are non-resonant KK photo-production, and $\Lambda(1520)$ photo-production on the proton in the nucleus as

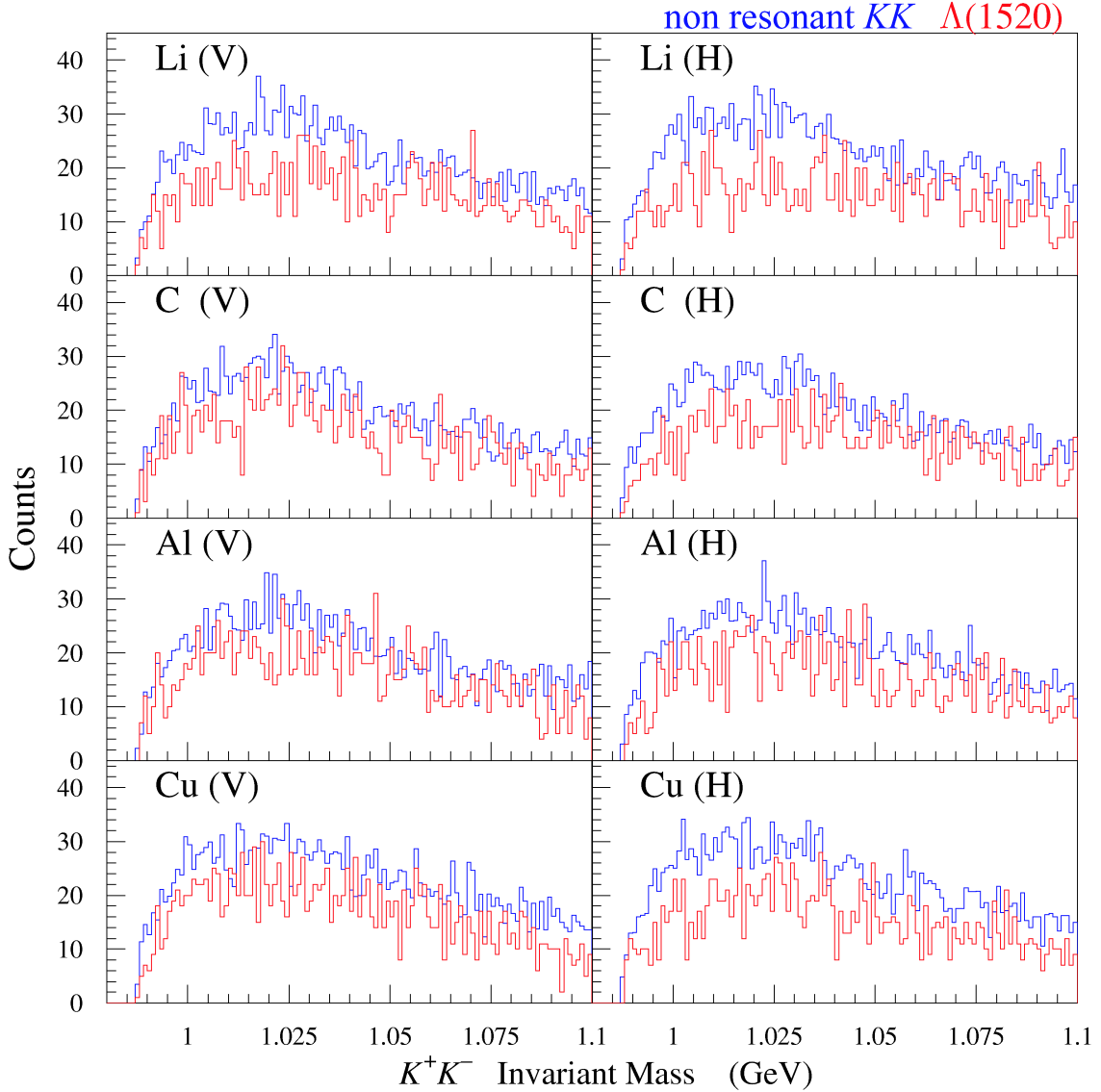
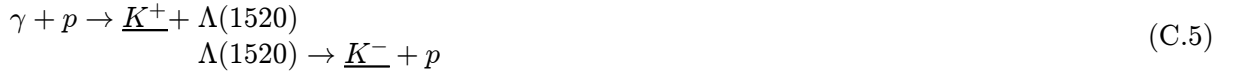


Figure C.32: Comparison between non resonant KK and KK from $\Lambda(1520)$

Non-resonant KK background is discussed in Subsection 3.6.3. Figure C.32 shows K^+K^- invariant mass distributions for non-resonant KK photo-production and those for $\Lambda(1520)$ photo-production on the proton in the nucleus. Energy dependence of the cross section is assumed to be proportional to the phase volume in both the reactions. Similar distributions are obtained especially for the heavy nuclear targets.

Table C.11: Each cut condition has two rows, each yield column shows the yield of ϕ events in the first row, the KK background contribution due to $\Lambda(1520)$ photo-production in the second row. The Y_N/Y_0 , $\sigma_\phi N/\alpha$, and χ^2 columns show the fitting results and χ^2 of the fitting with the function $Y(A) = Y_N A_{\text{eff}}(A, \sigma_{\phi N})$ and $Y(A) = Y_0 A^\alpha$ in the first and second rows, respectively.

Cut	Yield (Li)	Yield (C)	Yield (Al)	Yield (Cu)	Y_N / Y_0	$\sigma_{\phi N} \text{ (mb)} / \alpha$	χ^2
30 MeV Cut	1.256 ± 0.094	1.641 ± 0.138	3.375 ± 0.250	6.045 ± 0.485	0.259 ± 0.041	$31.7^{+12.2}_{-8.8}$	1.16
	0.094 ± 0.022	0.124 ± 0.035	0.210 ± 0.057	0.342 ± 0.110	0.289 ± 0.050	0.733 ± 0.057	1.84
From Li	1.459 ± 0.134	1.711 ± 0.198	3.684 ± 0.285	6.534 ± 0.551	0.310 ± 0.055	$37.3^{+18.5}_{-11.8}$	2.09
	0.099 ± 0.022	0.146 ± 0.037	0.317 ± 0.070	0.390 ± 0.114	0.338 ± 0.074	0.714 ± 0.069	2.94
From Each	1.459 ± 0.134	1.834 ± 0.197	3.610 ± 0.305	6.795 ± 0.573	0.310 ± 0.056	$36.3^{+17.9}_{-11.6}$	0.82
	0.099 ± 0.022	0.146 ± 0.037	0.317 ± 0.070	0.390 ± 0.114	0.339 ± 0.072	0.718 ± 0.067	1.84

The fittings are made for the yields of 30 MeV missing energy cut, and those with the coherent contributions are subtracted assuming the shape of the background KK invariant mass distribution is the same as that of Λ - KK photo-production. Table C.4 summarizes the fitting results with the functions $Y(A) = Y_N A_{\text{eff}}(A, \sigma_{\phi N})$, and $Y(A) = Y_0 A^\alpha$. The obtained A -dependence and $\sigma_{\phi N}$ with the KK background as $\Lambda(1520)$ photo-production is the same as those with the KK background as non-resonant KK photo-production discussed in Subsection 3.6.3.

Appendix D

Incoherent and coherent ϕ photo-production

D.1 Missing mass

The missing mass m_X distributions for the reaction $\gamma p \rightarrow K^+ K^- X$ have been also investigated assuming that the target is a proton (nucleon) at rest. Figure D.1, D.2 show the missing mass m_X

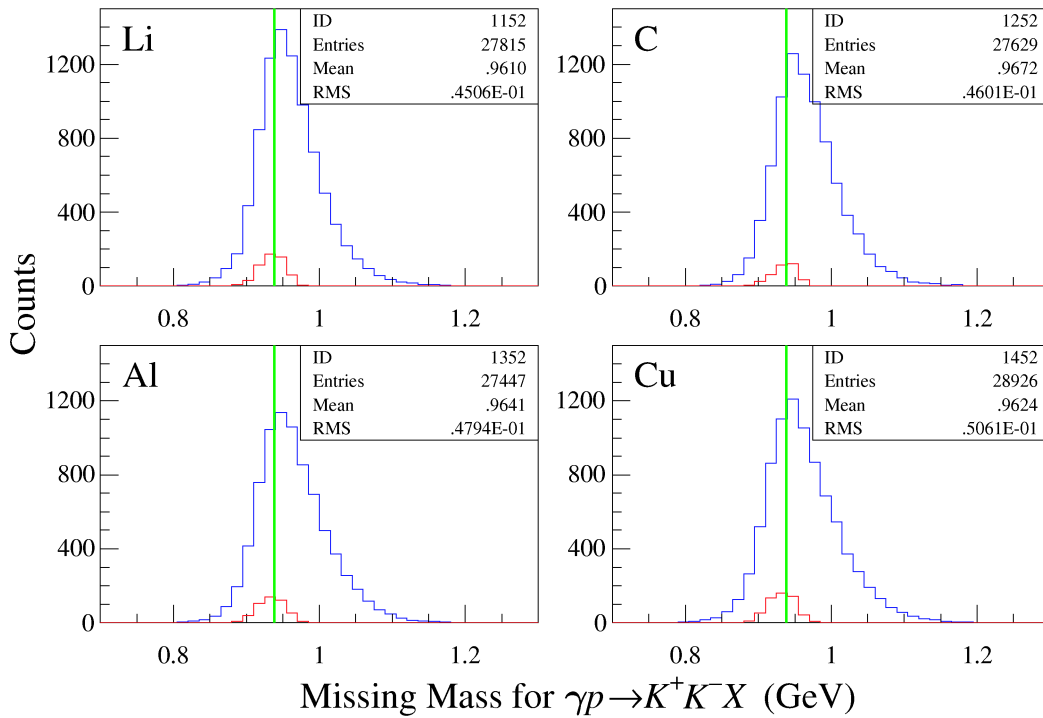


Figure D.1: Missing mass m_X of $\gamma p \rightarrow K^+ K^- X$ for the incoherent process in the MC simulation data. The blue lines show all the events, and the red ones show the events with $|t| < 0.1 \text{ GeV}^2$. The green lines show the nominal mass of the proton.

of $\gamma p \rightarrow K^+ K^- X$ for the incoherent, coherent processes obtained by the MC simulation, respectively. The peak position of the missing mass m_X for $\gamma p \rightarrow K^+ K^- X$ for the incoherent process is positioned at the proton mass smeared out by the experimental resolution and Fermi motion, and it is independent

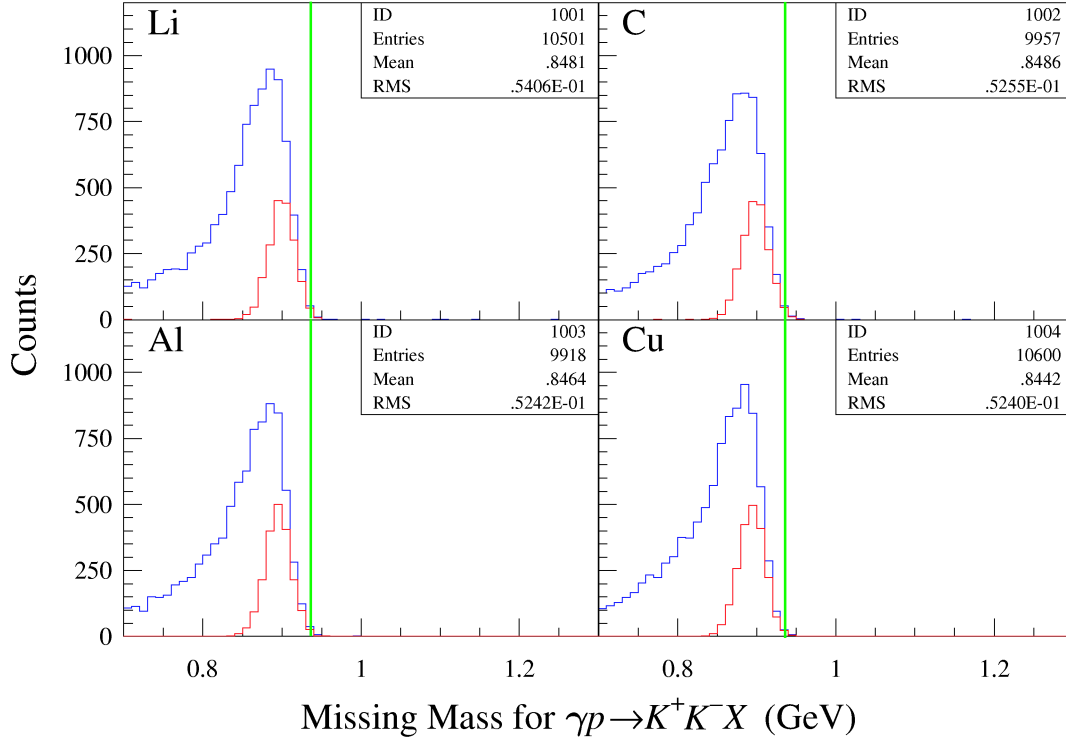


Figure D.2: Missing mass m_X of $\gamma p \rightarrow K^+ K^- X$ for the coherent process in the MC simulation data. The blue lines show all the events, and the red ones show the events with $|t| < 0.1 \text{ GeV}^2$. The green lines show the nominal mass of the proton.

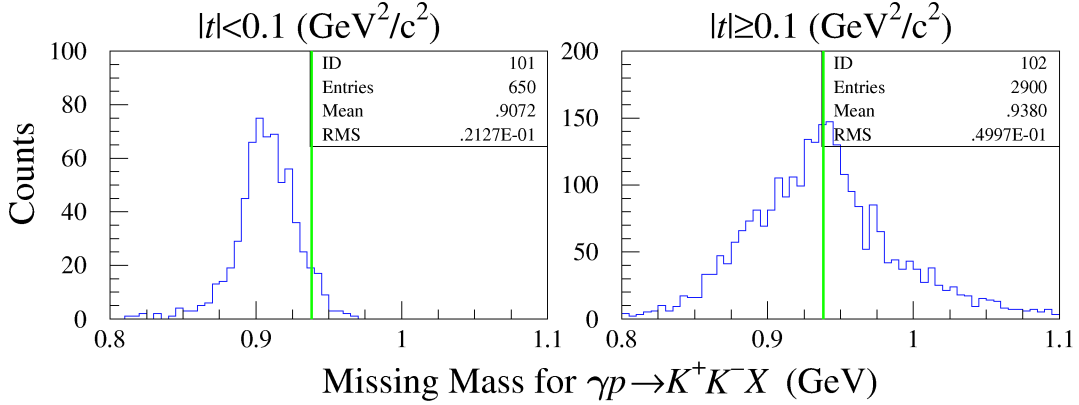


Figure D.3: Missing mass m_X of $\gamma p \rightarrow K^+ K^- X$ for the start counter. The left panel shows the events with $|t| < 0.1 \text{ GeV}^2$, and the right one shows those with $|t| \geq 0.1 \text{ GeV}^2$. The red lines show the nominal mass of the proton.

of the momentum transfer square t . On the other hand, the missing mass m_X for the coherent process is lower than the proton mass. Thus, the enhancement at the missing mass m_X lower than than the proton mass can show the existence of the coherent process.

Figure D.3 shows the missing mass m_X for the reaction $\gamma p \rightarrow K^+ K^- X$ in the start counter for $|t| < 0.1$ GeV, and $|t| \geq 0.1$ GeV. The condition $|t| < 0.1$ GeV makes the peak position lower, this can imply the small $|t|$ events mainly come from coherent process [80]. Although the incoherent process is expected to be dominant due to the kinematical condition in the incident γ energy range 1.5–2.4 GeV, the contribution of the coherent process can not be neglected.

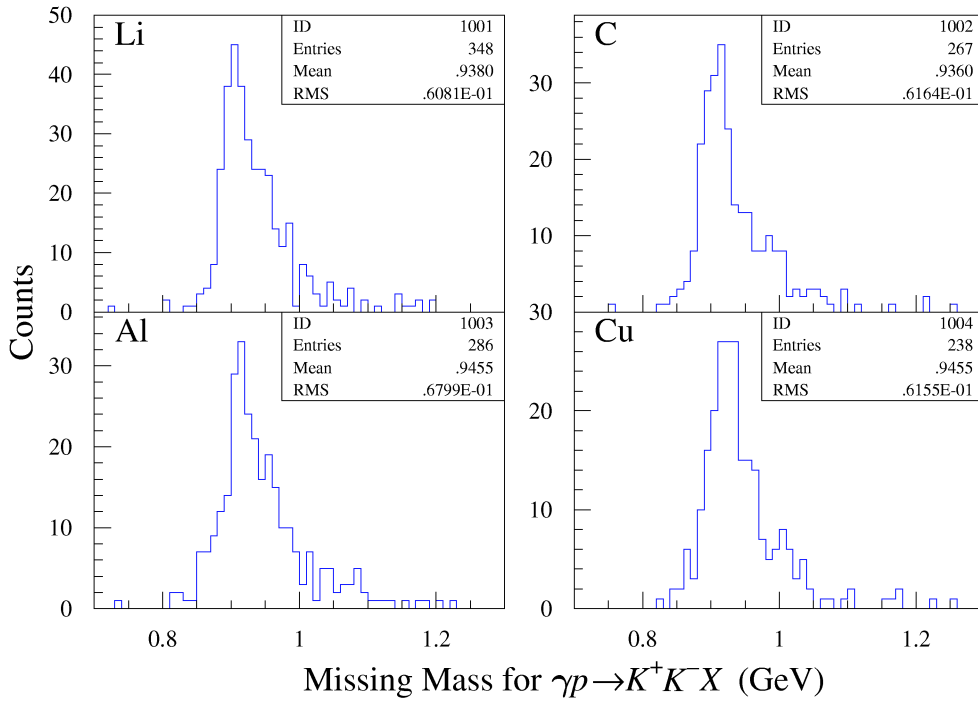


Figure D.4: Missing mass distributions M_X for $\gamma p \rightarrow K^+ K^- X$

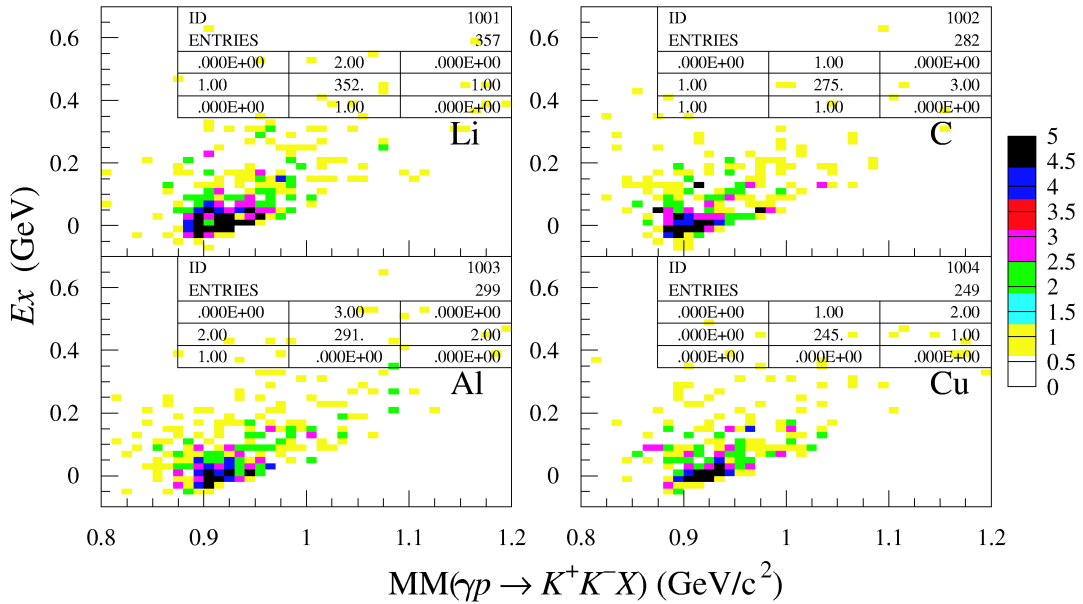


Figure D.5: Correlation between missing energy and missing mass m_X of $\gamma p \rightarrow \phi + X$

Figure D.4 shows the missing mass distributions for the reaction $\gamma p \rightarrow K^+ K^- X$. It seems also difficult to separate the coherent and incoherent processes by means of the missing mass distributions for the reaction $\gamma p \rightarrow K^+ K^- X$.

Figure D.5 shows the correlation between missing energy and missing mass m_X of $\gamma p \rightarrow K^+ K^- X$, and more events concentrate in the lower missing energy and lower missing mass region for the lighter target, this also implies lighter targets have more coherent process events.

D.2 ν - q^2 correlation

In order to separate incoherent and coherent processes, the correlation between energy transfer ν and three dimensional momentum transfer q^2 was investigated, where $\nu = E_\phi - E_\gamma$, and $q^2 = |\vec{p}_\phi - \vec{p}_\gamma|^2$. The correlation is described as

$$\begin{cases} \nu = \sqrt{m_N^2 + q^2} - m_N & \text{for incoherent process, and} \\ \nu = \sqrt{m_A^2 + q^2} - m_A & \text{for coherent process,} \end{cases} \quad (\text{D.1})$$

where nucleon is assumed to be at rest for the incoherent process, and m_N and m_A stand for the nucleon and nucleus mass, respectively. Figures D.6 and D.7 show the correlations for incoherent and coherent processes obtained by the MC simulation, respectively. The MC simulation data shows the equation (D.1) are valid for each process. Figure D.8 shows the correlation in the real data. It can be concluded that there is few coherent process events in large q^2 region, but two processes cannot be separated by means of this correlation in small q^2 region. In order to confirm the equation (D.1) in the real data, the correlation between energy transfer ν and momentum transfer q^2 for the LH₂

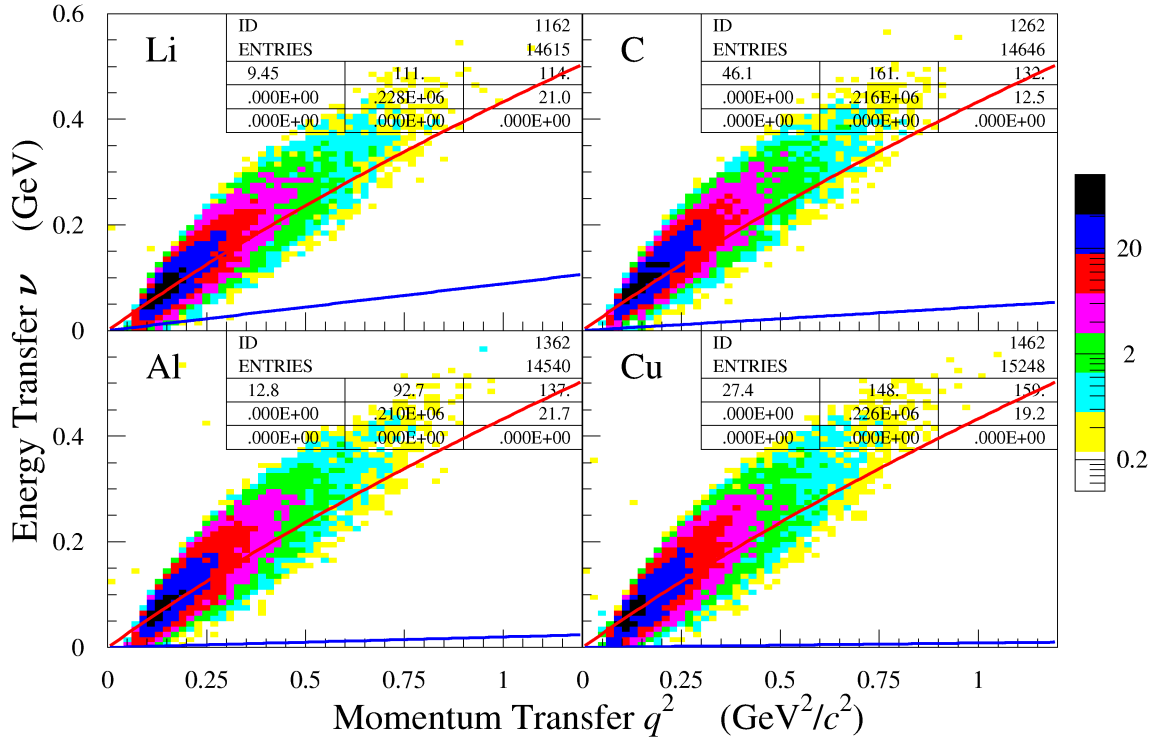


Figure D.6: ν - q^2 correlation for the incoherent process in the MC simulation. The red lines show the predicted lines for incoherent production, and the blue ones show those for coherent production.

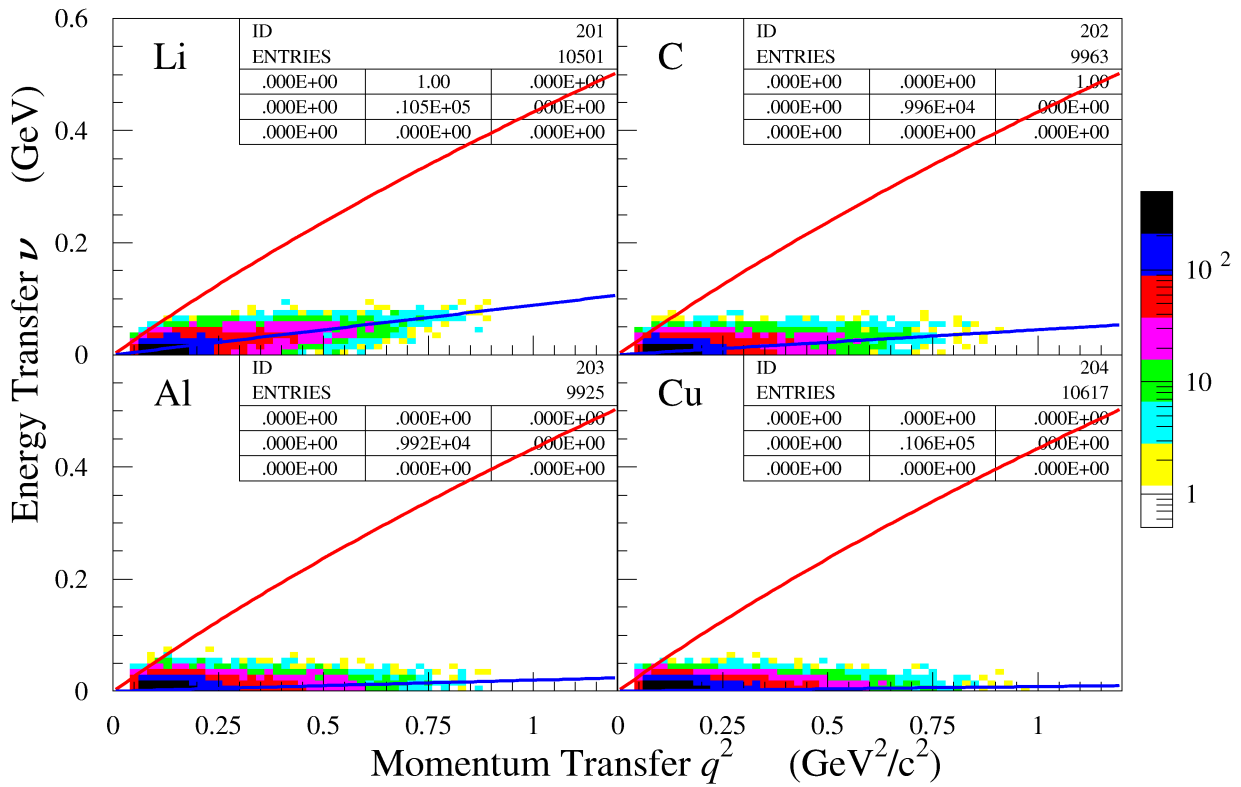


Figure D.7: ν - q^2 correlation for the coherent process in the MC simulation. The red lines show the predicted lines for incoherent production, and the blue ones show those for coherent production.

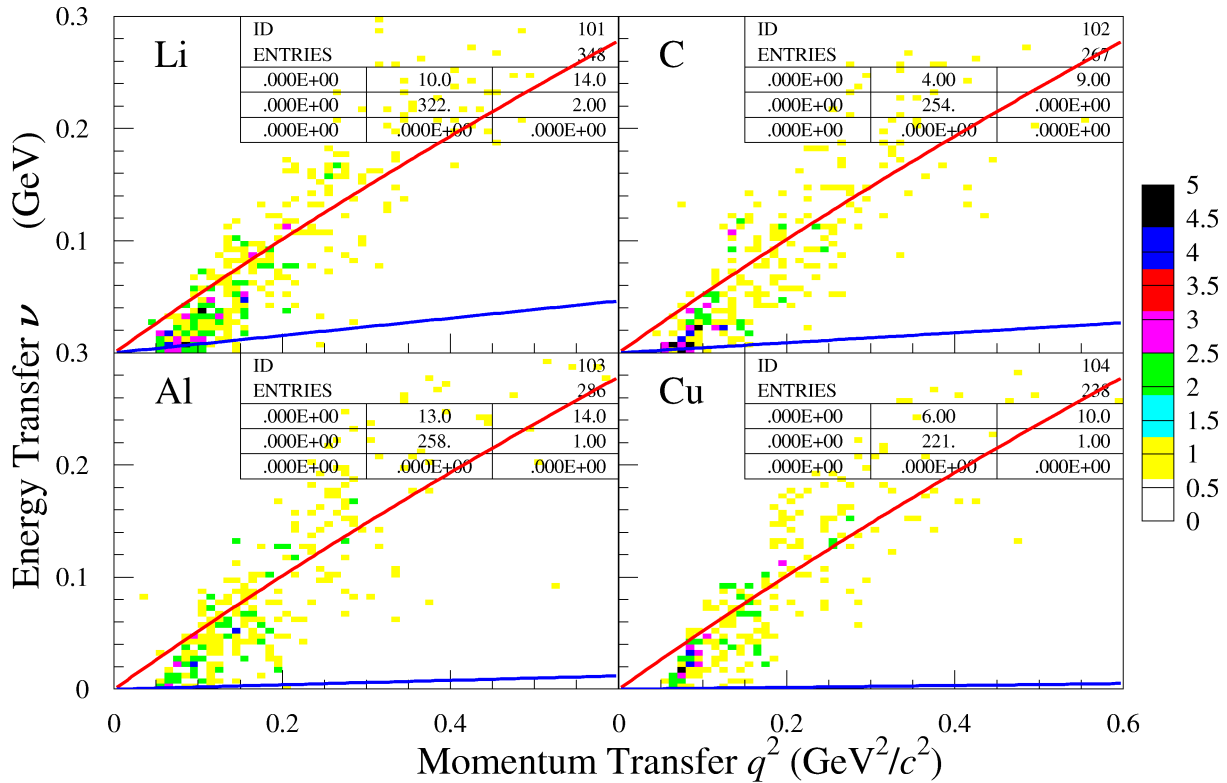


Figure D.8: ν - q^2 correlation in the real data. The red lines show the predicted lines for incoherent production, and the blue ones show those for coherent production.

target was investigated. Figures D.9 and D.10 show the correlations for the LH₂ target in the MC and the real data, respectively. Left panels show the ν^2 - q^2 correlations and right ones show the ν - q^2 correlations together with the expected correlation curves. Both the loci in the MC simulation and

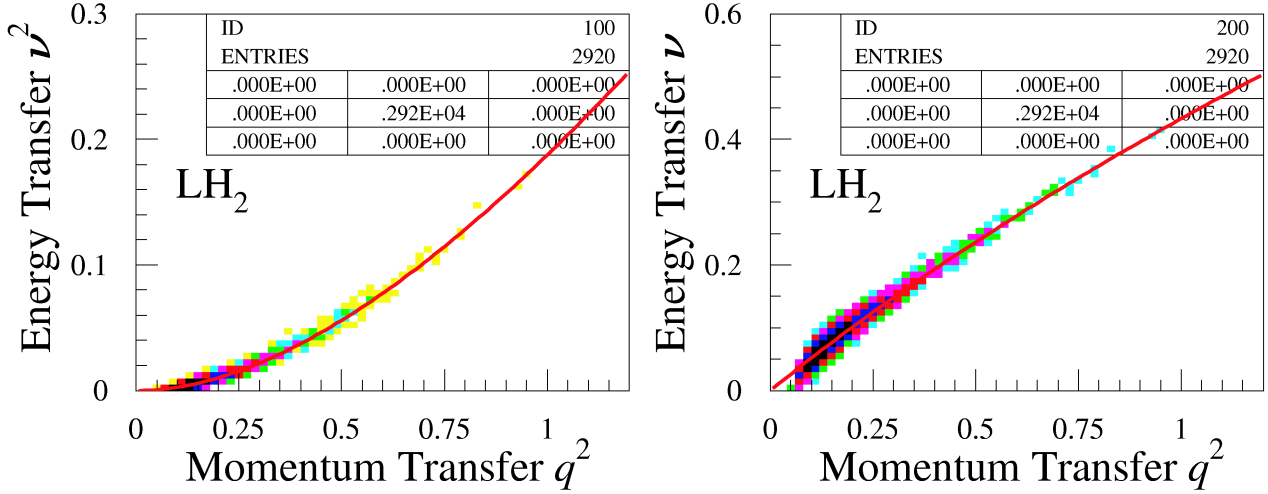


Figure D.9: ν^2 - q^2 and ν - q^2 correlation for the LH₂ target in the MC simulation. The red lines show the predicted lines for the proton target.

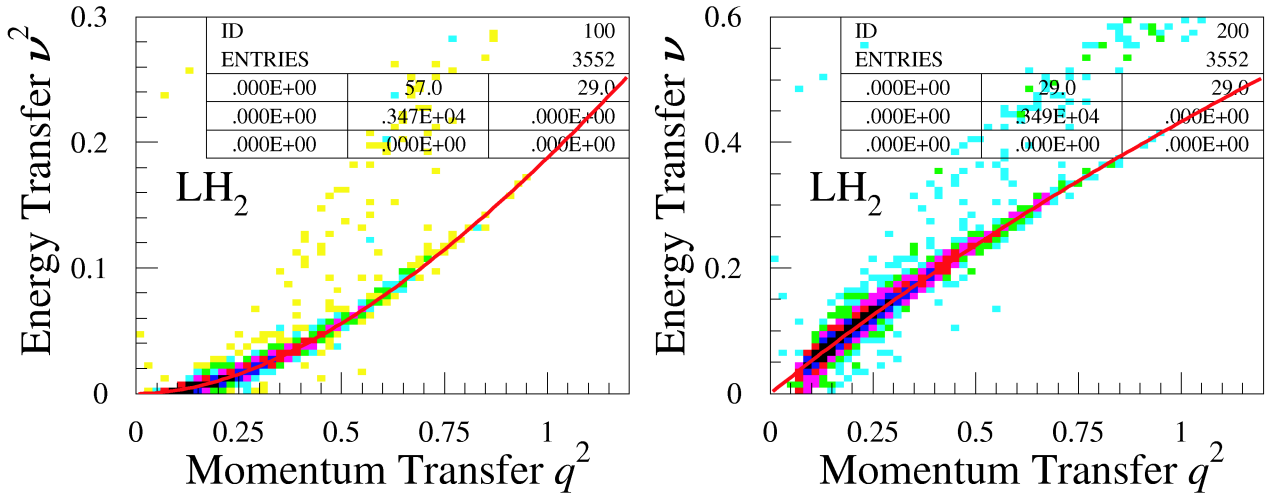


Figure D.10: ν^2 - q^2 and ν - q^2 correlation for the LH₂ target in the real data. The red lines show the predicted lines for the proton target.

real data for the proton target are consistent with the expected correlation curves. The events for coherent production from a nucleus and those for production on the proton at rest are expected to make clear loci in the ν - q^2 correlation, while the events for incoherent production from a nucleus are expected to spread in the wide area due to the Fermi motion. It is difficult to separate the coherent and incoherent processes especially for low $|t|$ events.

Appendix E

ϕ - N total cross section with various cuts

E.1 Selecting kinematical region for the incoherent process

The 30 MeV missing energy cut has been adopted as discussed in Subsection 4.4 for selecting the kinematical region for the incoherent process, and $\sigma_{\phi N}$ is obtained to be $29.7^{+11.7}_{-8.2}$ mb. In this section, the $\sigma_{\phi N}$ is estimated with various cuts to the yield for the kinematical region for the incoherent process.

E.1.1 Excluding one of the four targets for the 30 MeV cut

In order to investigate the stability of $\sigma_{\phi N}$, the fitting has been made by excluding one of the four targets. Table E.1 shows the fitting results. When the lightest or heaviest target Li, Cu was excluded, the change of $\sigma_{\phi N}$ is slightly large but it is still within the errors.

Table E.1: Fitting parameters excluding one of the four targets

	Y_N	$\sigma_{\phi N}$ (mb)	χ^2
All	0.249 ± 0.040	$29.7^{+11.7}_{-8.2}$	1.06
w/o Li	0.219 ± 0.050	$23.4^{+15.5}_{-10.0}$	0.66
w/o C	0.264 ± 0.045	$32.1^{+12.3}_{-8.9}$	0.16
w/o Al	0.253 ± 0.042	$31.7^{+14.1}_{-9.2}$	0.63
w/o Cu	0.243 ± 0.044	$27.7^{+18.2}_{-11.6}$	1.03

E.1.2 Invariant mass

The $\sigma_{\phi N}$ has been also estimated by changing the invariant mass cut. Since the cut points of the invariant mass cut has been fixed independently of the target, a tight cut is not even for different targets due to the different invariant mass resolution. The number of non-resonant K^+K^- events between m_{\min} and m_{\max} is estimated as

$$\begin{aligned} & \#N(m_{\min} \leq \text{IM}_{KK} < m_{\max})_{\text{real}} \\ &= \#N(1050 \leq \text{IM}_{KK} < 1100 \text{ MeV})_{\text{real}} \times \frac{\#N(m_{\min} \leq \text{IM}_{KK} < m_{\max})_{\text{MC}}}{\#N(1050 \leq \text{IM}_{KK} < 1100 \text{ MeV})_{\text{MC}}}. \end{aligned} \quad (\text{E.1})$$

Table E.2: Fitting parameters tightening the invariant mass cut. The asterisk shows the standard ϕ cut. Each cut condition has three rows, each yield column shows the yield of ϕ events in the first row, the non-resonant KK background contribution in the second row, used number of KK events in the third row. The Y_N/Y_0 , $\sigma_{\phi N}/\alpha$, and χ^2 columns show the fitting results and χ^2 of the fitting with the function $Y(A) = Y_N A_{\text{eff}}(A, \sigma_{\phi N})$, $Y(A) = Y_0 A^\alpha$ in the first and second rows, respectively.

Cut	Yield (Li)	Yield (C)	Yield (Al)	Yield (Cu)	C	$\sigma_{\phi N}$ (mb)	χ^2
1010-1030	1.205 ± 0.091	1.531 ± 0.130	3.159 ± 0.237	5.569 ± 0.455	0.255 ± 0.042	$35.1^{+14.7}_{-9.6}$	1.50
	0.078 ± 0.018	0.088 ± 0.025	0.145 ± 0.040	0.219 ± 0.070	0.283 ± 0.050	0.719 ± 0.057	2.34
	98,113	81,82	100,105	82,86			
1005-1035*	1.235 ± 0.095	1.634 ± 0.138	3.371 ± 0.250	6.061 ± 0.484	0.249 ± 0.040	$29.7^{+11.7}_{-8.2}$	1.06
	0.116 ± 0.026	0.131 ± 0.037	0.214 ± 0.058	0.326 ± 0.104	0.281 ± 0.049	0.742 ± 0.057	1.66
	104,118	90,88	110,112	95,90			
1000-1040	1.223 ± 0.098	1.663 ± 0.144	3.445 ± 0.259	6.271 ± 0.503	0.240 ± 0.039	$26.4^{+10.2}_{-7.7}$	0.82
	0.240 ± 0.034	0.171 ± 0.048	0.276 ± 0.075	0.431 ± 0.137	0.271 ± 0.039	0.759 ± 0.058	1.26
	106,120	94,91	112,119	101,93			
995-1045	1.234 ± 0.102	1.677 ± 0.149	3.503 ± 0.268	6.420 ± 0.520	0.238 ± 0.038	$25.2^{+10.0}_{-7.6}$	0.85
	0.238 ± 0.038	0.205 ± 0.058	0.333 ± 0.091	0.521 ± 0.166	0.269 ± 0.050	0.767 ± 0.060	1.27
	109,124	97,93	116,122	104,97			

Table E.3: Fitting parameters tightening the χ^2 probability cut. The asterisk shows the standard ϕ cut. Each cut condition has three rows, and the format is as same as Table E.2.

Cut	Yield (Li)	Yield (C)	Yield (Al)	Yield (Cu)	Y_N/Y_0	$\sigma_{\phi N}$ (mb)/ α	χ^2
$P(\chi^2) \geq 0.02$	1.235 ± 0.095	1.634 ± 0.138	3.371 ± 0.250	6.061 ± 0.484	0.249 ± 0.040	$29.7^{+11.7}_{-8.2}$	1.06
	0.116 ± 0.052	0.131 ± 0.074	0.214 ± 0.117	0.326 ± 0.208	0.281 ± 0.049	0.742 ± 0.057	1.66
	104,118	90,88	110,112	95,90			
$P(\chi^2) \geq 0.03$	1.125 ± 0.091	1.515 ± 0.133	3.116 ± 0.240	5.752 ± 0.470	0.220 ± 0.036	$26.7^{+10.8}_{-7.9}$	0.77
	0.110 ± 0.025	0.122 ± 0.035	0.184 ± 0.054	0.290 ± 0.097	0.248 ± 0.046	0.758 ± 0.060	1.23
	104,108	90,88	110,112	95,90			
$P(\chi^2) \geq 0.04$	1.076 ± 0.088	1.439 ± 0.129	2.947 ± 0.233	5.368 ± 0.450	0.216 ± 0.036	$28.9^{+11.8}_{-8.6}$	0.77
	0.098 ± 0.024	0.110 ± 0.034	0.171 ± 0.052	0.225 ± 0.086	0.243 ± 0.045	0.747 ± 0.061	1.24
	97,106	83,82	99,106	90,85			
$P(\chi^2) \geq 0.05$	1.063 ± 0.087	1.376 ± 0.127	2.795 ± 0.227	5.017 ± 0.434	0.224 ± 0.038	$34.1^{+14.7}_{-10.3}$	0.92
	0.087 ± 0.023	0.111 ± 0.034	0.171 ± 0.052	0.194 ± 0.080	0.249 ± 0.047	0.724 ± 0.061	1.54
	90,103	77,79	92,102	83,79			
$P(\chi^2) \geq 0.06$	0.996 ± 0.085	1.345 ± 0.125	2.666 ± 0.222	4.813 ± 0.426	0.208 ± 0.036	$32.3^{+14.3}_{-9.7}$	0.42
	0.087 ± 0.023	0.101 ± 0.032	0.171 ± 0.053	0.194 ± 0.080	0.234 ± 0.045	0.729 ± 0.063	0.80
	87,102	76,74	86,99	77,74			
$P(\chi^2) \geq 0.07$	0.947 ± 0.083	1.263 ± 0.121	2.513 ± 0.215	4.607 ± 0.418	0.196 ± 0.035	$31.7^{+14.5}_{-10.0}$	0.47
	0.081 ± 0.022	0.101 ± 0.032	0.152 ± 0.049	0.196 ± 0.081	0.219 ± 0.044	0.733 ± 0.065	0.90
	84,94	75,71	82,95	75,70			
$P(\chi^2) \geq 0.08$	0.905 ± 0.080	1.224 ± 0.119	2.466 ± 0.213	4.504 ± 0.414	0.183 ± 0.032	$29.3^{+13.5}_{-9.2}$	0.47
	0.075 ± 0.021	0.091 ± 0.031	0.152 ± 0.049	0.197 ± 0.081	0.207 ± 0.042	0.743 ± 0.066	0.82
	75,86	70,63	77,86	72,64			
$P(\chi^2) \geq 0.09$	0.868 ± 0.079	1.172 ± 0.117	2.420 ± 0.212	4.404 ± 0.409	0.171 ± 0.031	$27.2^{+12.7}_{-8.8}$	0.63
	0.069 ± 0.020	0.090 ± 0.030	0.152 ± 0.049	0.195 ± 0.080	0.194 ± 0.040	0.754 ± 0.067	0.98
	72,82	69,59	76,84	71,62			

Table E.2 shows the fitting results. No significant changes of $\sigma_{\phi N}$ are observed even if the invariant mass cut is tightened.

E.1.3 χ^2 probability cut

The $\sigma_{\phi N}$ has been also checked tightening the χ^2 probability cut of each track. Table E.3 shows the fitting results. Any significant changes of the ϕ -N total cross section also cannot be observed even if the χ^2 probability cut for each track is tightened.

E.1.4 Incident γ energy

Table E.4 shows the fitting parameters under the condition that the incident γ energy is required as $E_\gamma \geq 2.2$ GeV and $E_\gamma < 2.2$ GeV, namely the averaged incident γ energy is $\langle E_\gamma \rangle = 2.3$ and 2.0 GeV, respectively. Figure E.1 shows the yields as a function of mass number A together with fitting results.

Table E.4: Fitting parameters for different incident γ energies. Each cut condition has three rows, and the format is the same as Table E.2.

Cut	Yield (Li)	Yield (C)	Yield (Al)	Yield (Cu)	Y_N/Y_0	$\sigma_{\phi N}$ (mb)/ α	χ^2
$\langle E_\gamma \rangle = 2.3$ GeV	0.719 ± 0.074	0.965 ± 0.104	2.090 ± 0.199	3.551 ± 0.366	0.144 ± 0.027	$28.0^{+14.4}_{-9.8}$	1.21
	0.091 ± 0.022	0.055 ± 0.023	0.156 ± 0.048	0.146 ± 0.066	0.163 ± 0.037	0.750 ± 0.074	1.53
	66,67	53,50	74,65	56,51			
$\langle E_\gamma \rangle = 2.0$ GeV	0.518 ± 0.059	0.649 ± 0.094	1.280 ± 0.152	2.476 ± 0.322	0.109 ± 0.022	$35.0^{+27.0}_{-14.4}$	0.58
	0.022 ± 0.013	0.096 ± 0.037	0.059 ± 0.035	0.214 ± 0.098	0.120 ± 0.034	0.722 ± 0.095	0.96
	38,51	37,38	37,47	39,39			

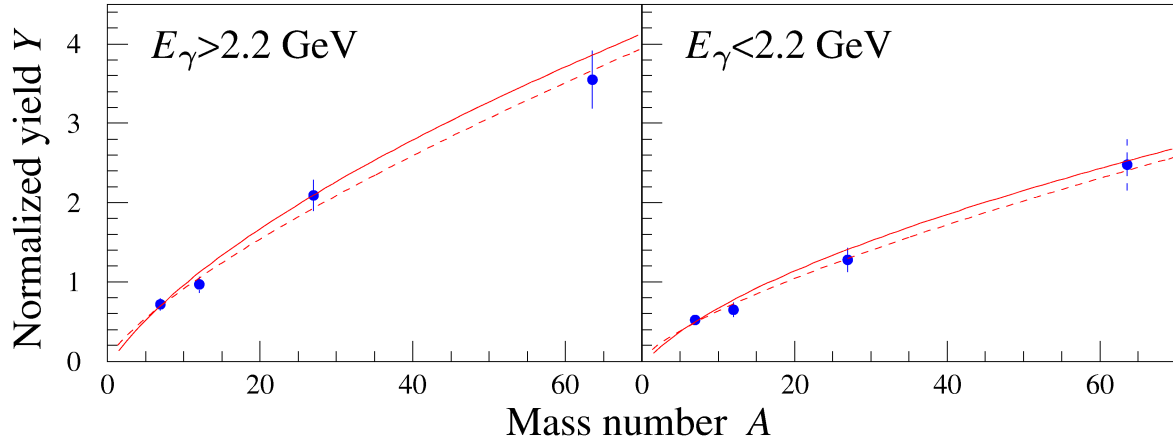


Figure E.1: A -dependence for different incident γ energy regions. The solid and dashed curves show the fitting results with the functions $Y(A) = Y_N A_{\text{eff}}(A)$ and $Y(A) = Y_0 A^\alpha$, respectively.

E.1.5 Momentum of ϕ meson

Table E.5 shows the fitting parameters under the condition that the momentum of the measured ϕ mesons is required as $P_\phi \geq 1.8$ GeV and $P_\phi < 1.8$ GeV, namely the averaged momentum of the

Table E.5: Fitting parameters different ϕ meson momentum regions. Each cut condition has three rows, and the format is as same as Table E.2.

Cut	Yield (Li)	Yield (C)	Yield (Al)	Yield (Cu)	Y_N/Y_0	$\sigma_{\phi N}$ (mb)/ α	χ^2
$\langle P_\phi \rangle = 2.0$ GeV	0.631 ± 0.067	0.913 ± 0.100	1.892 ± 0.185	3.122 ± 0.337	0.132 ± 0.025	$28.9_{-10.0}^{+14.9}$	1.02
	0.051 ± 0.017	0.038 ± 0.019	0.088 ± 0.036	0.060 ± 0.042	0.151 ± 0.034	0.740 ± 0.073	1.08
	56,56	49,47	63,59	49,43			
$\langle P_\phi \rangle = 1.6$ GeV	0.600 ± 0.067	0.715 ± 0.097	1.474 ± 0.169	2.916 ± 0.350	0.118 ± 0.024	$30.5_{-13.1}^{+23.4}$	1.39
	0.068 ± 0.021	0.099 ± 0.034	0.132 ± 0.048	0.289 ± 0.104	0.129 ± 0.037	0.741 ± 0.093	1.90
	48,62	41,41	47,53	46,47			

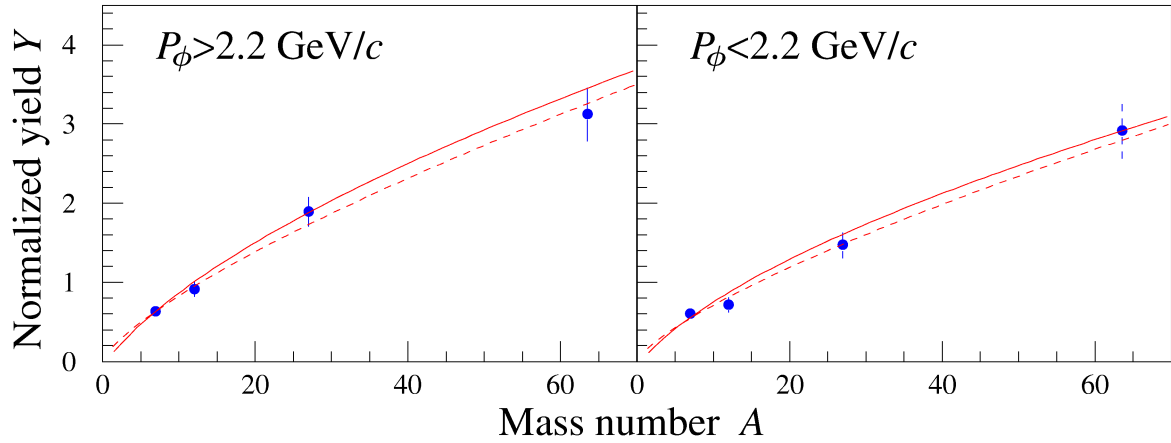


Figure E.2: A -dependence for different ϕ meson momentum regions. The solid and dashed curves show the fitting results with the functions $Y(A) = Y_N A_{\text{eff}}(A)$ and $Y(A) = Y_0 A^\alpha$, respectively.

ϕ mesons is $\langle P_\phi \rangle = 2.0$ and 1.6 GeV/c, respectively. In the larger momentum or larger γ energy condition, $\sigma_{\phi N}$ becomes smaller although the statistical significance is poor.

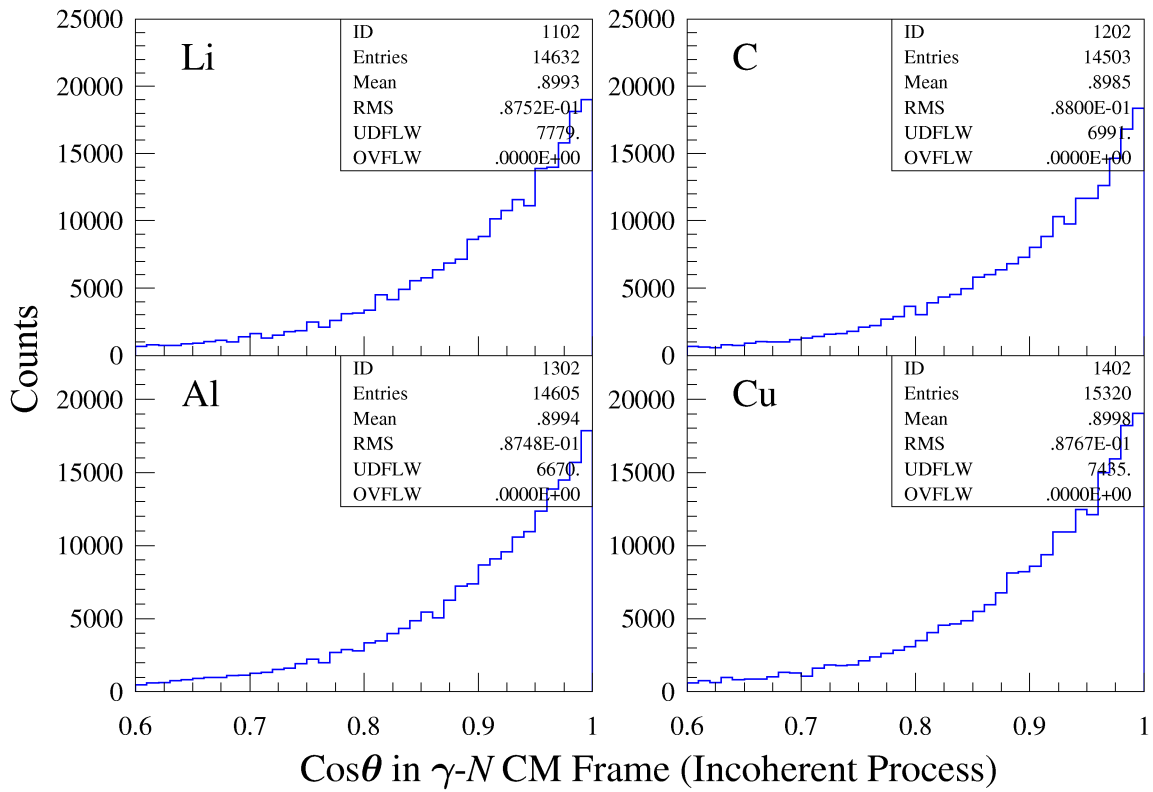
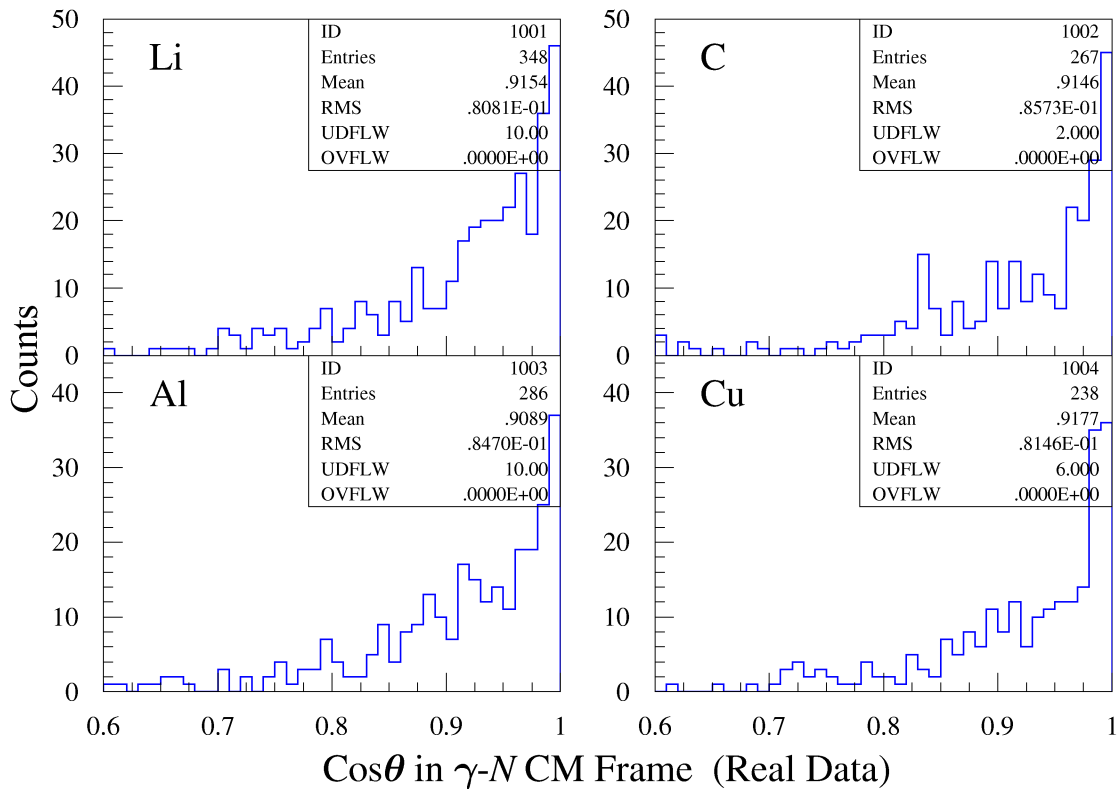
E.1.6 Scattering angle in the γ - N center of mass system

If the momentum calibration is wrong due to some reason such as wrong energy loss correction and so on, the missing energy distributions change. In order to suppress the mis-calibration effect of the momentum measurement in separating coherent and incoherent processes, the scattering angle in the γ - N center of mass frame $\cos \theta^*$ is considered.

The scattering angle $\cos \theta^*$ is obtained assuming that the target is nucleon at rest, and that γ beam goes in a parallel direction with z -axis. Momenta of the kaons in γ - N center of mass frame is described with given incident γ energy E_γ as,

$$\begin{cases} p_x^{\text{CM}} = p_x^{\text{LAB}} \\ p_y^{\text{CM}} = p_y^{\text{LAB}} \\ p_z^{\text{CM}} = \gamma_f (p_z^{\text{LAB}} - \beta_f E) = \gamma_f p^{\text{LAB}} \left\{ \frac{p_z^{\text{LAB}}}{p^{\text{LAB}}} - \beta_f \left(1 + \left(\frac{m_K}{p^{\text{LAB}}} \right)^2 \right)^{1/2} \right\} \end{cases}, \quad (\text{E.2})$$

where β_f is the velocity of the γ - N center of mass frame, and $\gamma_f = 1/\sqrt{1 - \beta_f^2}$. The incident γ energy ranges from 1.5 to 2.4 GeV, thus β_f varies from 0.62 to 0.72. The scattering angle $\cos \theta^*$ is expressed

Figure E.3: Scattering angle in the γ - N CM frame $\cos\theta$ for the incoherent processFigure E.4: Scattering angle in the γ - N CM frame $\cos\theta$ for the real data

as

$$\cos \theta^* = \frac{p_z^{\text{CM}}}{\sqrt{\left(p_x^{\text{CM}}\right)^2 + \left(p_y^{\text{CM}}\right)^2 + \left(p_z^{\text{CM}}\right)^2}}. \quad (\text{E.3})$$

Even if absolute value of each kaon momentum is wrong, the difference is canceled out between numerator and denominator in $\cos \theta^*$ when the directions of the momenta in γ - N center of mass frame are correct. This is approximately valid if the directions of the momenta in laboratory frame are correct, and if the deviation of

$$\frac{p_z^{\text{LAB}}}{p^{\text{LAB}}} - \beta_f \left(1 + \left(\frac{m_K}{p^{\text{LAB}}}\right)^2\right)^{1/2} \quad (\text{E.4})$$

is small comparing to its mean value. Since the observed kaon momentum decaying from ϕ meson ranges 0.5–1.3 GeV and the value of equation (E.4) ranges from -0.01 to 0.33 because $p_z^{\text{LAB}}/p^{\text{LAB}} \simeq 1$. Although using $\cos \theta^*$ does not suppress the mis-calibration effect of the momentum measurement in separating coherent and incoherent processes, it can be still useful to separate the coherent and incoherent processes. Figure E.3 shows the expected $\cos \theta^*$ distribution for the incoherent processes

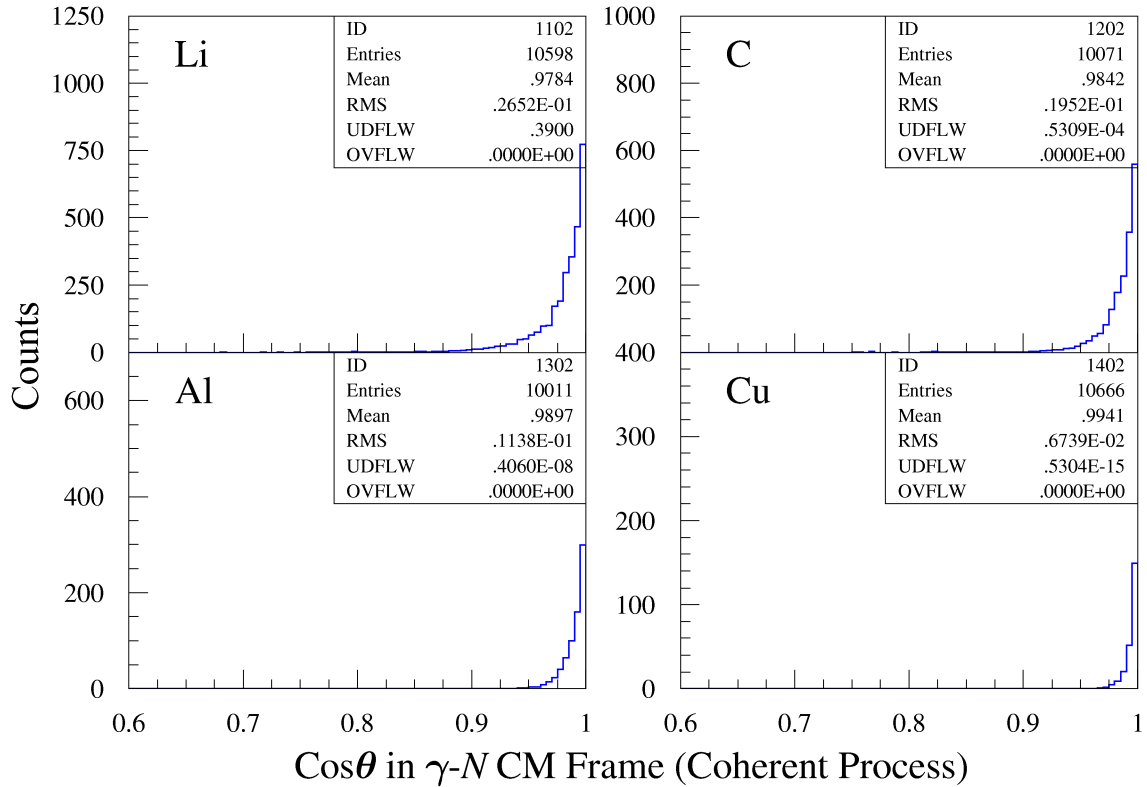


Figure E.5: Scattering angle in the γ - N CM frame $\cos \theta$ for the coherent process

obtained by the Monte Carlo simulation, and Figure E.4 shows measured one. The prominent peaks at $\cos \theta^* = 1$ in the real data are the events which ϕ mesons were scattered at very small angles and are thought to be the contribution of the coherent process. Figure E.5 shows the scattering angle for the coherent process obtained by the MC simulation, where the slope of $|t|$ distribution for the generated

Table E.6: Fitting parameters for different $\cos\theta^*$ cuts. Each cut condition has three rows, and the format is as same as Table E.2.

$\cos\theta^* _{\max}$	Yield (Li)	Yield (C)	Yield (Al)	Yield (Cu)	Y_N/Y_0	$\sigma_{\phi N} \text{ (mb)}/\alpha$	χ^2
No Cut	1.912 ± 0.112	2.419 ± 0.164	4.134 ± 0.276	7.553 ± 0.526	0.558 ± 0.067	$70.8^{+31.7}_{-19.0}$	0.44
	0.122 ± 0.052	0.160 ± 0.081	0.330 ± 0.143	0.371 ± 0.215	0.543 ± 0.076	0.625 ± 0.047	1.94
	188,160	145,122	137,149	123,115			
0.94	1.189 ± 0.092	1.556 ± 0.138	2.886 ± 0.233	4.846 ± 0.434	0.311 ± 0.045	$55.2^{+28.8}_{-16.5}$	0.38
	0.089 ± 0.023	0.150 ± 0.041	0.208 ± 0.059	0.293 ± 0.099	0.328 ± 0.058	0.650 ± 0.059	0.33
	98,112	79,92	86,108	63,87			
0.92	0.960 ± 0.085	1.345 ± 0.129	2.468 ± 0.218	4.238 ± 0.413	0.230 ± 0.038	$43.6^{+22.2}_{-13.5}$	0.22
	0.081 ± 0.023	0.121 ± 0.037	0.179 ± 0.056	0.273 ± 0.098	0.255 ± 0.050	0.680 ± 0.065	0.26
	80,85	68,76	70,92	54,74			
0.90	0.813 ± 0.080	1.148 ± 0.121	2.105 ± 0.209	3.609 ± 0.396	0.194 ± 0.033	$42.9^{+25.0}_{-14.5}$	0.19
	0.065 ± 0.021	0.103 ± 0.035	0.189 ± 0.059	0.292 ± 0.105	0.216 ± 0.047	0.682 ± 0.072	0.16
	58,74	58,61	58,77	43,63			

ϕ events in the simulation were fixed to be $b = 11.6 \times A^{0.674} \text{ GeV}^{-2}$ obtained in Subsection 4.3. Almost all the events are concentrated at $\cos\theta^* = 1$ especially for the heavy targets. Although the requirement $\cos\theta^* < \cos\theta^*_{\max}$ may suppress coherent ϕ events, it is difficult to distinguish the coherent process from the incoherent one with good statistics for the light target nucleus (Li) by using $\cos\theta^*$. Table E.1.6 shows normalized yield and fitting results.

E.2 Semi-coherent process

The missing energy distribution in the real data discussed in Subsection 4.4 has not been reproduced by the linear sum of the missing energy distributions for coherent and incoherent productions. An enhancement at 20–30 MeV from the sum of the incoherent and coherent missing energy distributions exists in the missing energy distribution for all the nuclear targets in the real data. This may imply the reaction mechanism contributes other than the coherent and incoherent processes. The reaction process has been considered that the coherent condition satisfies in a part of nucleus when ϕ mesons are produced. Let us call this mechanism as semi-coherent process. In this section, the missing energy distributions for the semi-coherent process, where only a few nucleons satisfy the coherent condition when ϕ mesons are produced, are discussed.

Figures E.6, E.7 and E.8 show the missing energy distributions for each target when the ϕ mesons are produced on the $A = 2-4$ cluster in a nucleus, where binding energy and Fermi motion is not taken into account. These distributions have a peak between the 0 MeV coherent one and about 80 MeV incoherent one. The missing energy distributions in the real data seem to be reproduced by the coherent, incoherent, and semi-coherent processes. When the missing energy was calculated for the proton target at rest ($\gamma p \rightarrow K^+ K^- p$), the coherent process contributes the negative missing energy area as shown in Figure E.9. Figure E.10 shows the missing energy distribution for the proton at rest as a target when the ϕ mesons are produced on the $A = 2-4$ cluster in a nucleus. All the distributions of coherent and semi-coherent processes obtained by the Monte Carlo (MC) simulation contributes to the negative $\gamma p \rightarrow K^+ K^- p$ missing energy region. On the other hand, the peaks of the incoherent process in the MC simulation are positioned at 0 MeV rather symmetrically in the $\gamma p \rightarrow K^+ K^- p$ missing energy distribution as shown in Figure E.11. Figure E.12 shows the $\gamma p \rightarrow K^+ K^- p$ missing energy distribution in real data. An enhancement of the negative $\gamma p \rightarrow K^+ K^- p$ missing energy events actually exists for all the target, and this comes from the coherent or the semi-coherent processes. The

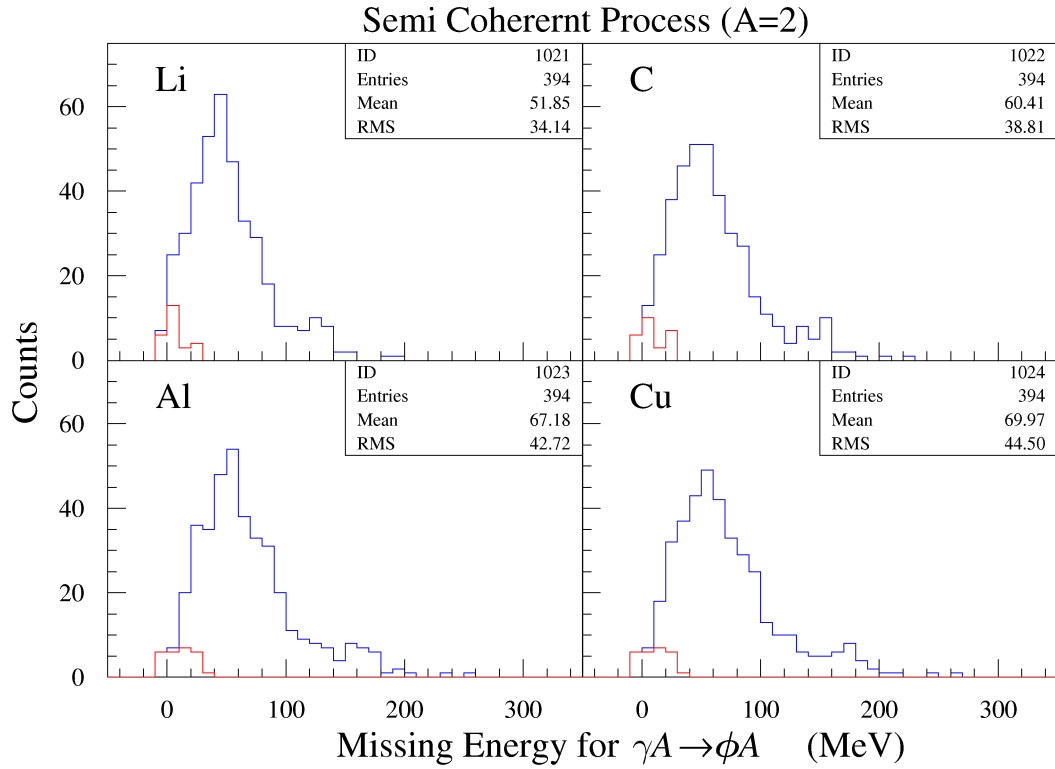


Figure E.6: Missing energy distributions for the $A=2$ semi-coherent process. The blue lines show all the events, and the red ones show the events with $|t| < 0.1 \text{ GeV}^2$.

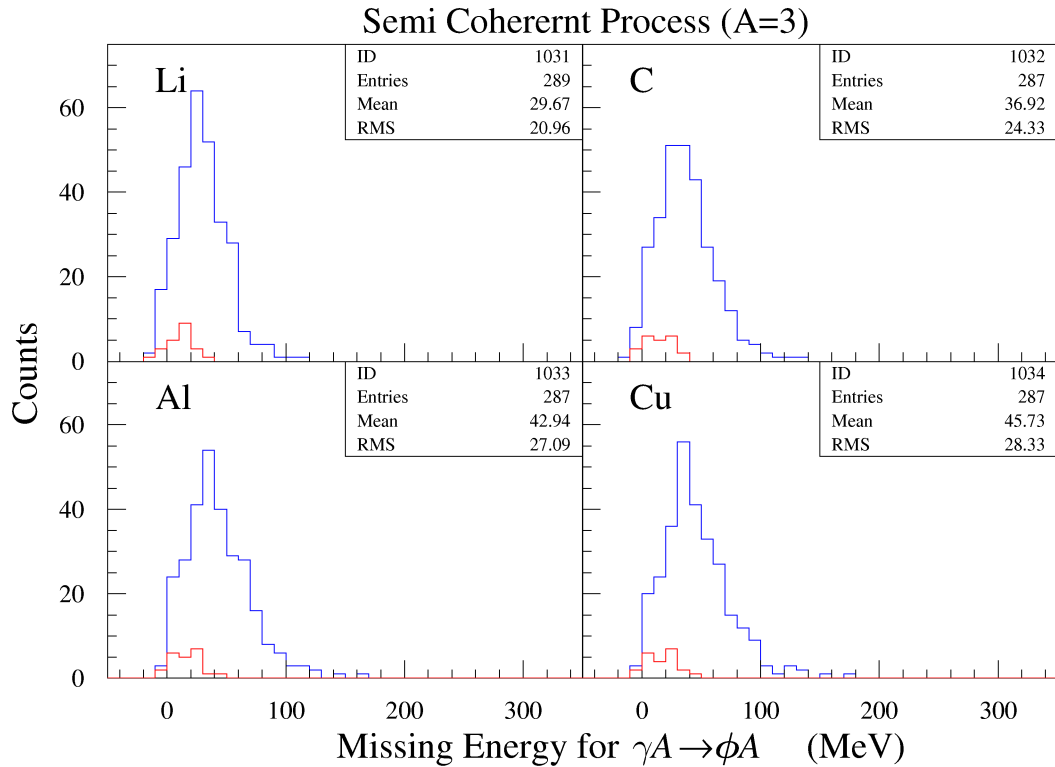


Figure E.7: Missing energy distributions for the $A=3$ semi-coherent process. The blue lines show all the events, and the red ones show the events with $|t| < 0.1 \text{ GeV}^2$.

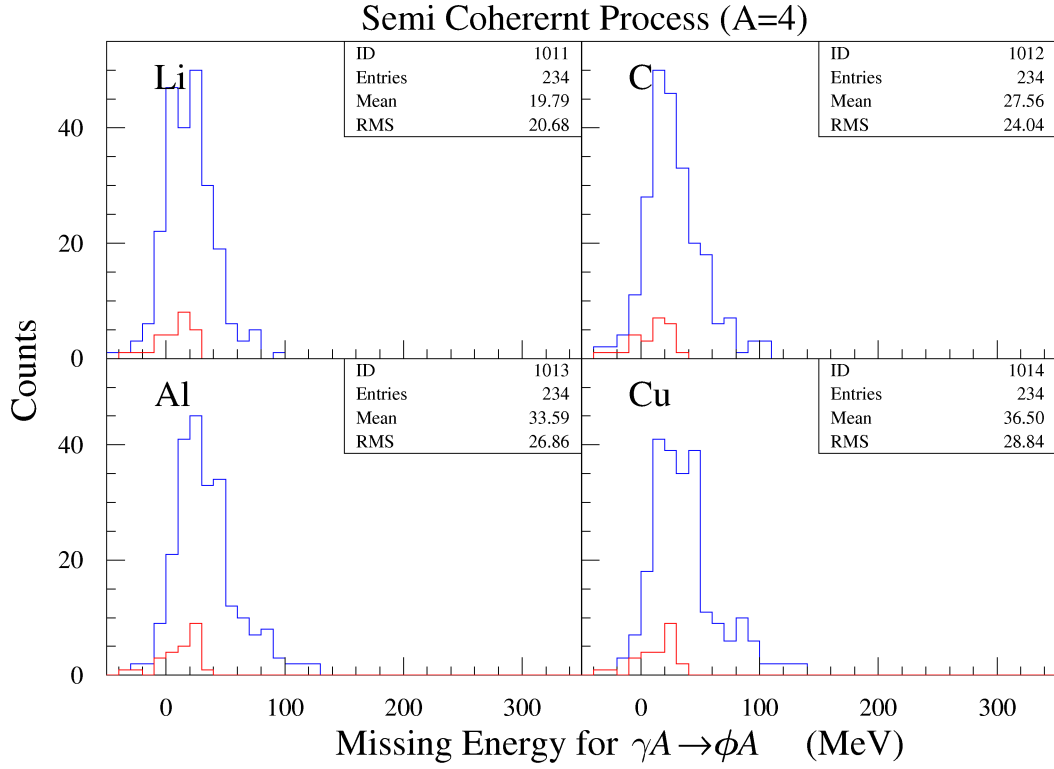


Figure E.8: Missing energy distribution of the $A=4$ semi-coherent process. The blue lines show all the events, and the red ones show the events with $|t| < 0.1 \text{ GeV}^2$.

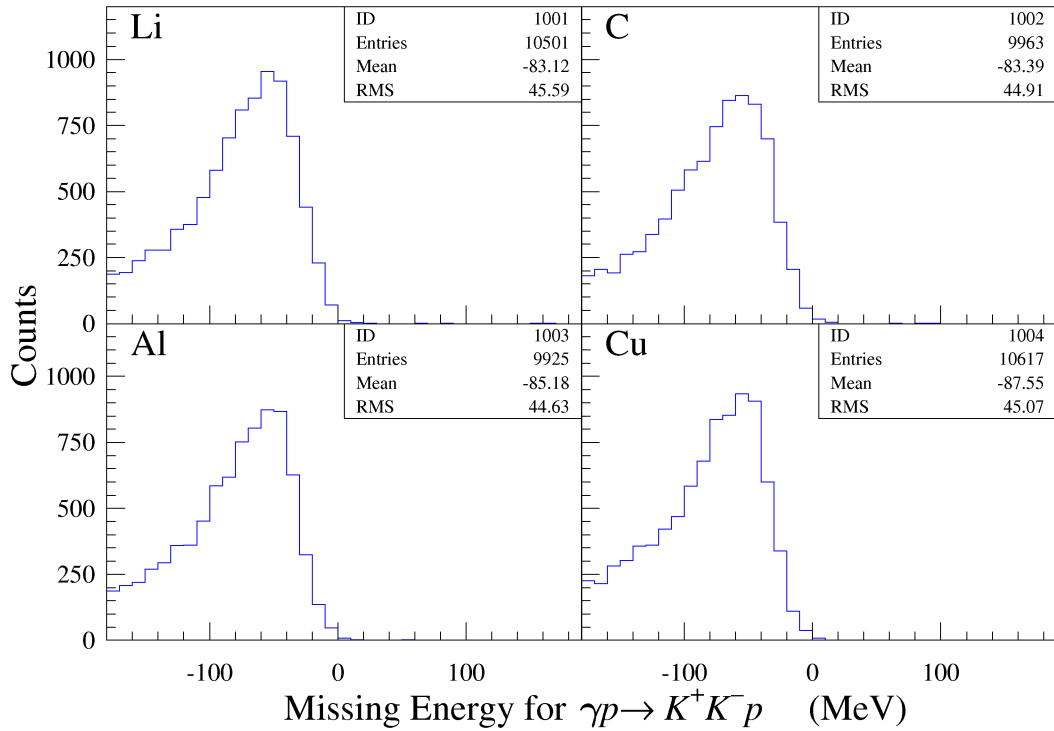
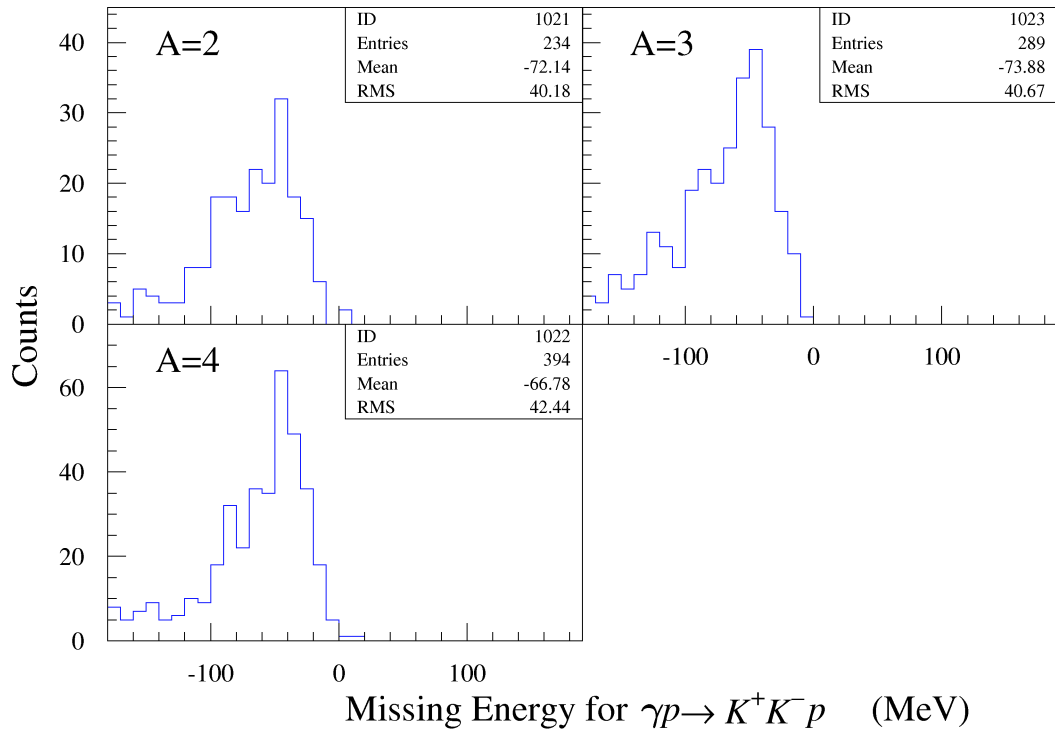
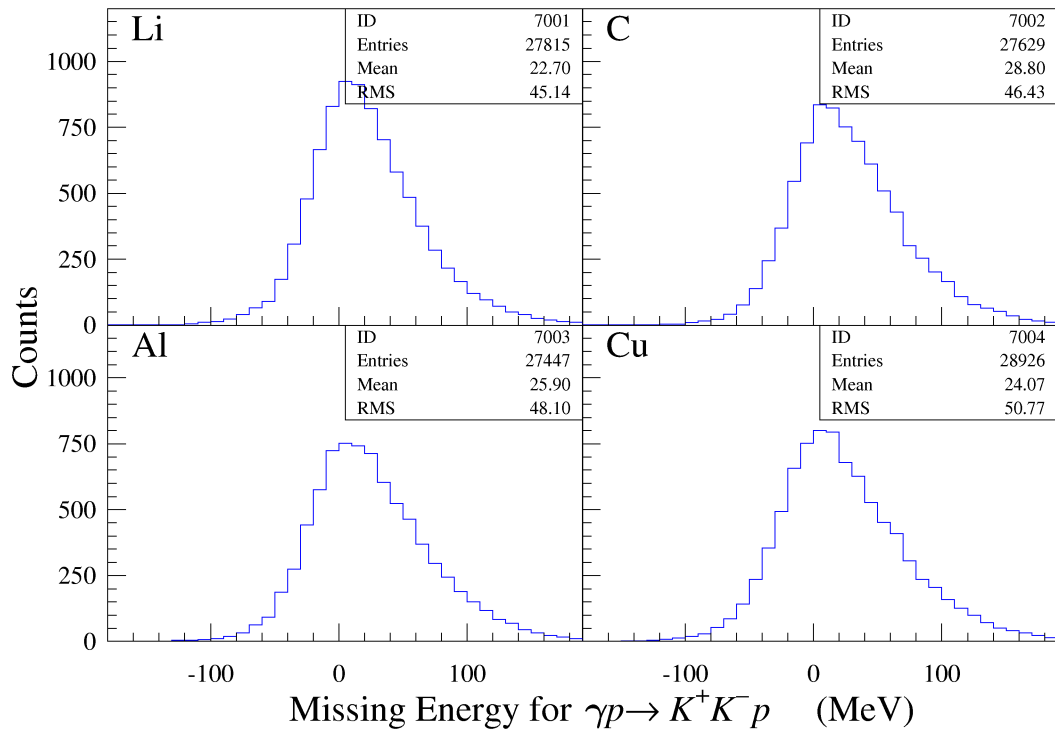
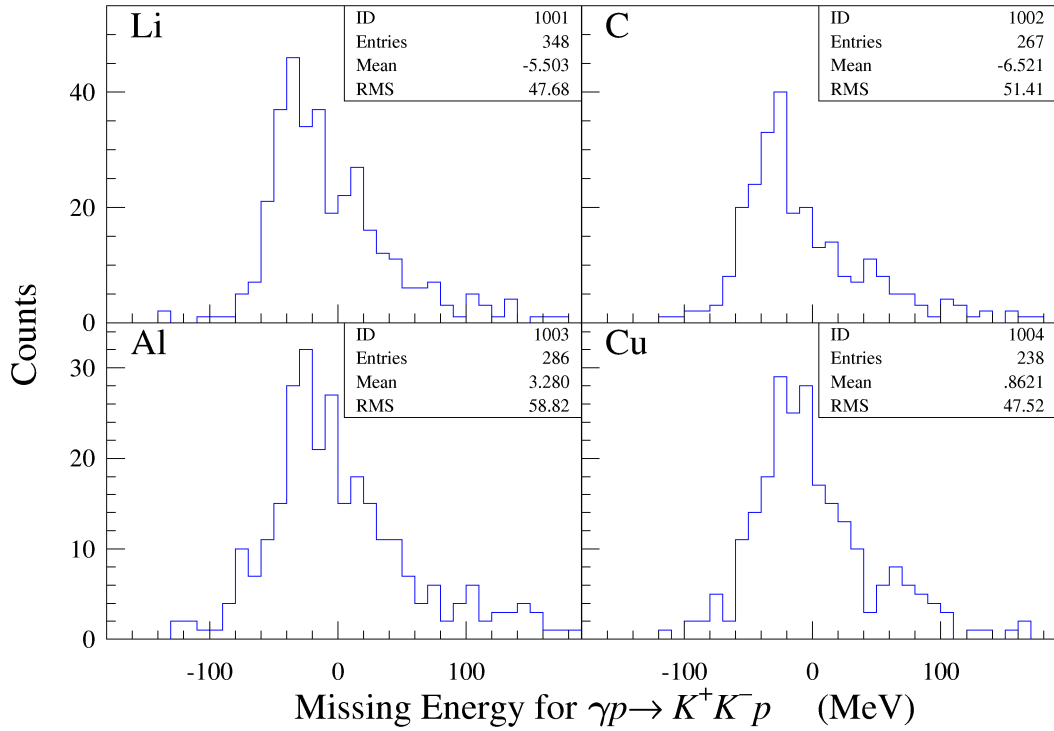
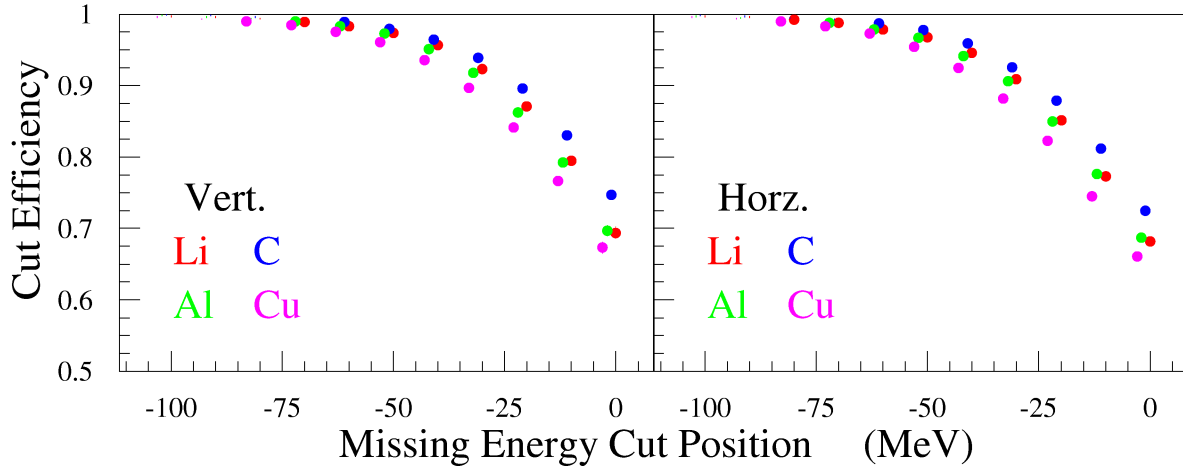


Figure E.9: Missing energy distribution of $\gamma p \rightarrow K^+ K^- p$ for the coherent process.

Figure E.10: Missing energy distribution of $\gamma p \rightarrow K^+ K^- p$ for the $A=2-4$ semi-coherent processFigure E.11: Missing energy distributions of $\gamma p \rightarrow K^+ K^- p$ for the incoherent process

Figure E.12: Missing energy distributions of $\gamma p \rightarrow K^+ K^- p$ in the real data

enhancement at 20–30 MeV in the $\gamma A \rightarrow K^+ K^- A$ missing energy distribution can be attributed to be the semi-coherent process because the coherent process makes a peak at 0 MeV in the distribution. The missing energy for $\gamma p \rightarrow K^+ K^- p$ is also effective since both the coherent and semi-coherent

Figure E.13: Efficiency of the missing energy cut for $\gamma p \rightarrow K^+ K^- p$. The left panel shows the efficiency for the vertically polarized photon data, and the right one shows that for the horizontally polarized ones.

processes are distributed in the negative $\gamma p \rightarrow K^+ K^- p$ missing energy region as show in Figure E.10. Figure E.13 shows the efficiency of the missing energy cut for the reaction $\gamma p \rightarrow K^+ K^- p$. The yield

$Y^H(A)$ and $Y^V(A)$ in Eq. (3.48) is divided also by this efficiency instead of the efficiency for the missing energy E_x cut, and is given by

$$Y^H(A) = \frac{N_\phi^H}{\eta_{\text{MEP}}^H \eta_{\text{geo}}^H \eta_{\text{DAQ}}^H \eta_{\text{ana}}^H \eta_{\text{att}} N_{\text{tag}}^H N_\tau}, \text{ and} \quad (\text{E.5})$$

$$Y^V(A) = \frac{N_\phi^V}{\eta_{\text{MEP}}^V \eta_{\text{geo}}^V \eta_{\text{DAQ}}^V \eta_{\text{ana}}^V \eta_{\text{att}} N_{\text{tag}}^V N_\tau},$$

where η_{MEP} shows the efficiency of the missing energy cut for the reaction $\gamma p \rightarrow K^+ K^- p$. Table E.7 shows the fitting parameters together with the normalized yields by the missing energy cut for $\gamma p \rightarrow K^+ K^- p$, and the $-30-0$ MeV cut which can reject the almost all the coherent and semi-coherent processes. The fitting results are consistent with those of 30 MeV missing energy E_x cut.

Table E.7: Fitting parameters for various missing energy cuts for the reaction $\gamma p \rightarrow K^+ K^- p$. Each cut condition has three rows, and the format is as same as Table E.2.

Cut	Yield (Li)	Yield (C)	Yield (Al)	Yield (Cu)	Y_N/Y_0	$\sigma_{\phi N} \text{ (mb)}/\alpha$	χ^2
-30 MeV	1.217 ± 0.093	1.591 ± 0.132	3.008 ± 0.236	5.930 ± 0.472	$0. \pm 0.043$	$33.2_{-9.3}^{+14.4}$	0.91
	0.251 ± 0.041	0.086 ± 0.029	0.215 ± 0.058	0.282 ± 0.100	0.279 ± 0.051	0.728 ± 0.059	1.62
	114,112	91,81	103,100	103,80			
-20 MeV	1.017 ± 0.086	1.210 ± 0.116	2.554 ± 0.215	4.890 ± 0.434	0.198 ± 0.036	$31.0_{-9.9}^{+15.5}$	2.62
	0.112 ± 0.026	0.079 ± 0.028	0.158 ± 0.051	0.300 ± 0.107	0.217 ± 0.046	0.744 ± 0.069	3.59
	92,100	66,66	89,82	84,70			
-10 MeV	0.804 ± 0.078	1.027 ± 0.109	2.204 ± 0.202	4.012 ± 0.399	0.155 ± 0.029	$27.2_{-9.4}^{+14.4}$	1.26
	0.104 ± 0.026	0.080 ± 0.028	0.162 ± 0.052	0.317 ± 0.113	0.174 ± 0.040	0.757 ± 0.074	1.75
	76,79	53,60	76,74	69,60			
0 MeV	0.707 ± 0.073	0.822 ± 0.099	1.770 ± 0.182	3.048 ± 0.358	0.155 ± 0.028	$41.3_{-15.4}^{+29.9}$	1.83
	0.090 ± 0.024	0.084 ± 0.030	0.147 ± 0.050	0.331 ± 0.119	0.166 ± 0.043	0.700 ± 0.085	2.62
	67,69	46,47	57,66	53,48			

Appendix F

Description of nuclei

F.1 Fermi motion in a nucleus

The treatment of the Fermi motion in the MC simulation g3leps is discussed in this section [84].

F.1.1 Harmonic oscillator model

The harmonic oscillator model is discussed, which is implemented in g3leps for calculating the Fermi motion.

A phenomenological shell model based on the Schrödinger equation for the single particle level is

$$\left\{ -\frac{\hbar^2}{2m}\nabla^2 + V(\vec{r}) \right\} \Phi_i(\vec{r}) = \epsilon_i \psi_i(\vec{r}) \quad (\text{F.1})$$

with a prescribed potential $V(\vec{r})$. A harmonic oscillator potential can be described as

$$V(r) = \frac{1}{2}mr\omega^2. \quad (\text{F.2})$$

In a spherical coordinates, the wave function under the potential can be expanded as

$$\psi_{nlm}(r, \Omega) = N_{nl} \left(\frac{r}{b} \right)^l L_{n-1}^{l+\frac{1}{2}} \left(\frac{r^2}{b^2} \right) \exp \left(-\frac{r^2}{2b^2} \right) Y_{lm}(\Omega), \quad (\text{F.3})$$

where L_n^m is generalized Laguerre function and the harmonic oscillator parameter $b = \sqrt{\hbar/m\omega}$. The normalization factor is determined in the following condition.

$$\begin{aligned} 1 &= \int \psi_{nlm}^*(r, \Omega) \psi_{nlm}(r, \Omega) d\vec{r} \\ &= N_{nl}^2 \int Y_{lm}^*(\Omega) Y_{lm}(\Omega) d\Omega \int_0^\infty \left(\frac{r}{b} \right)^{2l} \left\{ L_{n-1}^{l+\frac{1}{2}} \left(\frac{r^2}{b^2} \right) \right\}^2 \exp \left(-\frac{r^2}{b^2} \right) r^2 dr \\ &= N_{nl}^2 \frac{b^3}{2} \int_0^\infty \left(\frac{r^2}{b^2} \right)^{l+\frac{1}{2}} \left\{ L_{n-1}^{l+\frac{1}{2}} \left(\frac{r^2}{b^2} \right) \right\}^2 \exp \left(-\frac{r^2}{b^2} \right) d \left(\frac{r^2}{b^2} \right) \\ &= N_{nl}^2 \frac{b^3}{2} \frac{\Gamma(n+l+\frac{1}{2})}{(n-1)!} \\ &= N_{nl}^2 \frac{b^3}{2} \frac{(2n+2l-1)!! \Gamma(\frac{1}{2})}{2^{n+l}(n-1)!} \\ &= N_{nl}^2 \frac{b^3}{2^{n+l+1}} \frac{(2n+2l-1)!! \sqrt{\pi}}{(n-1)!} \end{aligned} \quad (\text{F.4})$$

Therefore the normalization factor is determined as the equation (F.5).

$$N_{nl} = \sqrt{\frac{2^{n+l+1}(n-1)!}{(2n+2l-1)!!\sqrt{\pi}b^3}} \quad (\text{F.5})$$

The wave function in momentum space is given in the Fourier transform of that in the coordinate space.

$$\begin{aligned} \Psi(\vec{k}) &= \frac{1}{(\sqrt{2\pi})^3} \int \psi(\vec{r}) \exp(-i\vec{k} \cdot \vec{r}) d\vec{r} \\ &= \frac{1}{(\sqrt{2\pi})^3} \int N_{nl} \left(\frac{r}{b}\right)^l L_{n-1}^{l+\frac{1}{2}}\left(\frac{r^2}{b^2}\right) \exp\left(-\frac{r^2}{2b^2}\right) \exp(-i\vec{k} \cdot \vec{r}) d\vec{r} \end{aligned} \quad (\text{F.6})$$

Thus the nucleon density in momentum space $n(\vec{k})$ is described in equation (F.7).

$$\begin{aligned} n(\vec{k}) &= \Psi_{nlm}^*(\vec{k}) \Psi_{nlm}(\vec{k}) \\ &= \frac{N_{nl}^2}{(2\pi)^3} \iint \left(\frac{r'}{b}\right)^l \left(\frac{r}{b}\right)^l L_{n-1}^{l+\frac{1}{2}}\left(\frac{r'^2}{b^2}\right) L_{n-1}^{l+\frac{1}{2}}\left(\frac{r^2}{b^2}\right) \\ &\quad \times \exp\left(-\frac{r'^2+r^2}{2b^2}\right) \exp(-i\vec{k} \cdot (\vec{r}' - \vec{r})) d\vec{r}' d\vec{r} \end{aligned} \quad (\text{F.7})$$

The relation $bk = r/b$ introduce the following rule of the variable transformation.

$$d\vec{k} = k^2 dk d\Omega = \frac{1}{b^6} r^2 dr d\Omega = \frac{d\vec{r}'}{b^6}, \quad \text{and} \quad d\vec{r} = b^6 d\vec{k} \quad (\text{F.8})$$

Thus the equation (F.7) becomes

$$\begin{aligned} n(\vec{k}) &= \frac{N_{nl}^2}{(2\pi)^3} \iint \left(\frac{r'r}{b^2}\right)^l L_{n-1}^{l+\frac{1}{2}}\left(\frac{r'^2}{b^2}\right) L_{n-1}^{l+\frac{1}{2}}\left(\frac{r^2}{b^2}\right) \exp\left(-\frac{r'^2+r^2}{2b^2}\right) \exp(-i\vec{k}' \cdot (\vec{r}' - \vec{r})) b^6 d\vec{k}' d\vec{r} \\ &= N_{nl}^2 b^6 \int \left(\frac{r'r}{b^2}\right)^l L_{n-1}^{l+\frac{1}{2}}\left(\frac{r'^2}{b^2}\right) L_{n-1}^{l+\frac{1}{2}}\left(\frac{r^2}{b^2}\right) \exp\left(-\frac{r'^2+r^2}{2b^2}\right) \delta(\vec{r}' - \vec{r}) d\vec{r} \\ &= N_{nl}^2 b^6 \left(\frac{r^2}{b^2}\right)^l \left\{ L_{n-1}^{l+\frac{1}{2}}\left(\frac{r^2}{b^2}\right) \right\}^2 \exp\left(-\frac{r^2}{b^2}\right) \\ &= N_{nl}^2 b^6 (b^2 k^2)^l \left\{ L_{n-1}^{l+\frac{1}{2}}(b^2 k^2) \right\}^2 \exp(-b^2 k^2), \end{aligned} \quad (\text{F.9})$$

where Dirac's delta function is

$$\delta(\vec{r}) = \frac{1}{(2\pi)^3} \int \exp(i\vec{k} \cdot \vec{r}) d\vec{k}. \quad (\text{F.10})$$

The nucleon density $N(k)$ which has an absolute momentum $p = \hbar k$ is described as equation (F.11).

$$\begin{aligned} N(k) &= 4\pi k^2 n(k) \\ &= 4\pi k^2 N_{nl}^2 b^6 (b^2 k^2)^l \left\{ L_{n-1}^{l+\frac{1}{2}}(b^2 k^2) \right\}^2 \exp(-b^2 k^2) \end{aligned} \quad (\text{F.11})$$

Nucleon density distribution in momentum space for each state is described in Table F.1.1 by using the equation (F.9).

Table F.1: Nucleon density for each state.

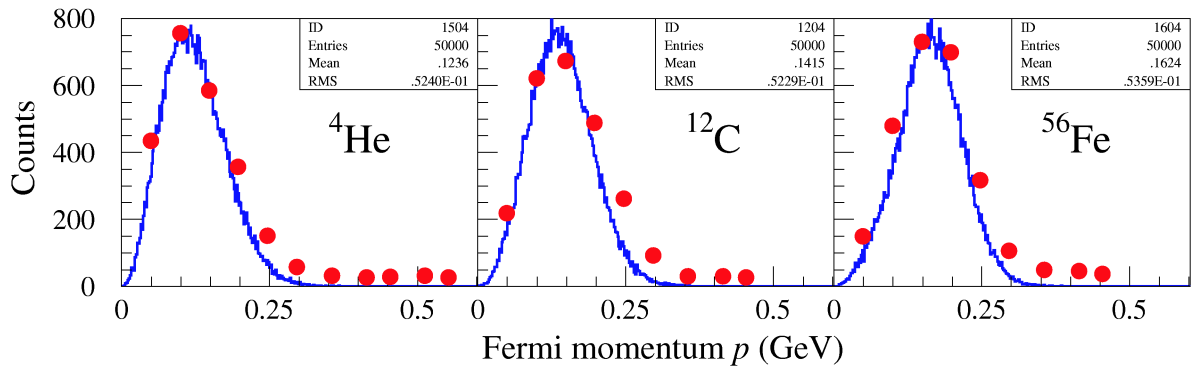
state	n	l	$n(k)$
1s	1	0	$\frac{4b^3}{\sqrt{\pi}} \exp(-b^2k^2)$
1p	1	1	$\frac{8b^3}{3\sqrt{\pi}} b^2k^2 \exp(-b^2k^2)$
1d	1	2	$\frac{16b^3}{15\sqrt{\pi}} b^4k^4 \exp(-b^2k^2)$
2s	2	0	$\frac{8b^3}{3\sqrt{\pi}} \left(\frac{3}{2} - b^2k^2\right)^2 \exp(-b^2k^2)$
1f	1	3	$\frac{32b^3}{105\sqrt{\pi}} b^6k^6 \exp(-b^2k^2)$
2p	2	1	$\frac{16b^3}{15\sqrt{\pi}} b^2k^2 \left(\frac{5}{2} - b^2k^2\right)^2 \exp(-b^2k^2)$

F.1.2 Comparison to the experimental data

The number of nucleons at each state in each target used in g3leps is described in Table F.1.2. The isotopes ^{12}C , ^{27}Al , and ^{64}Cu were assumed for the natural carbon, aluminum, and copper targets, respectively. The harmonic oscillator parameter $b = 1.93$ fm was adopted for C [85], and $A^{-1/15}$ was assumed for the other nuclei to reproduce the Fermi motion for the ^4He and ^{56}Fe nuclei. Figure F.1 shows the comparison of the Fermi momentum distributions $N(k) = 4\pi k^2 n(k)$ between the generated

Table F.2: Number of nucleons at each state.

state	^6Li		C		Al		Cu		^4He		^{56}Fe	
	p	n	p	n	p	n	p	n	p	n	p	n
1s	2	2	2	2	2	2	2	2	2	2	2	2
1p	1	1	4	4	6	6	6	6	0	0	6	6
1d	0	0	0	0	5	6	10	10	0	0	10	10
2s	0	0	0	0	0	0	2	2	0	0	2	2
1f	0	0	0	0	0	0	8	11	0	0	6	8
2p	0	0	0	0	0	0	1	4	0	0	0	0

Figure F.1: Comparison of the Fermi motion with $(e, e'p)$ experimental data.

events in the Monte Carlo simulation code g3leps and the $(e, e'p)$ experiment for ${}^4\text{He}$, C, and ${}^{56}\text{Fe}$ targets [86]. The harmonic oscillator model seems to underestimate the nucleon density in the higher momentum region ($p > 0.2\text{GeV}/c$) comparing to the experimental results for every target.

F.2 Off-shell correction

When ϕ meson is produced on a nucleon in a nucleus, a part of energy is basically used to separate the nucleon from the nucleus. If the separation energy is not used in ϕ photo-production from a nucleus by some reason, the missing energy distribution shifts to the negative side. Figure F.2 shows

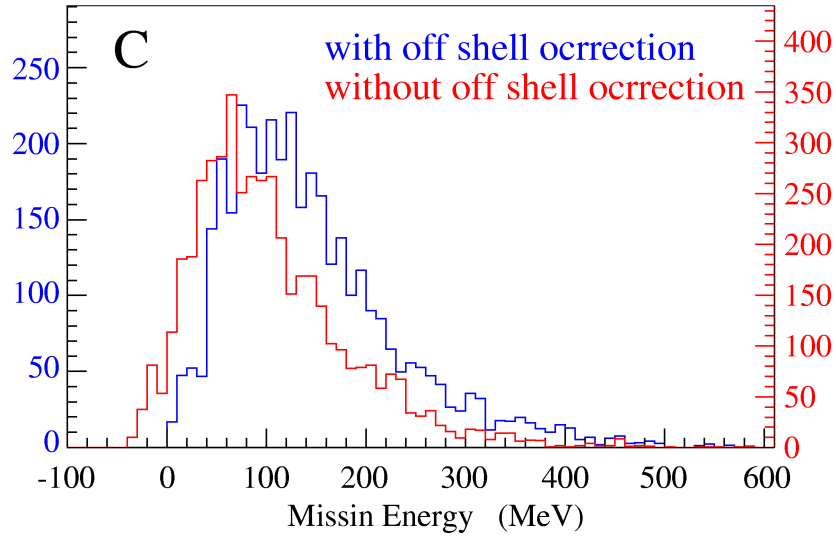


Figure F.2: Missing energy distribution with and without off-shell correction

the missing energy distribution for the incoherent process with and without off-shell correction [87] obtained by the Monte Carlo simulation. The proton, neutron separation energies S_p , S_n are defined as an energy to separate a proton, neutron from a nucleus as

$$\begin{cases} S_p = M_{A-p} + m_p - M_A + m_e, \\ S_n = M_{A-n} + m_n - M_A, \end{cases} \quad (\text{F.12})$$

where M_A and m_e stand for the masses of the nucleus and the electron, M_{A-p} is the mass of the proton and electron separated nuclues, M_{A-n} denotes the mass of the neutron separated nuclei, and m_p , m_n show the proton, neutron masses, respectively. The separation energies of ${}^{12}\text{C}$, for example, are obtained from $M_A = m({}^{12}\text{C})$, $M_{A-p} = m({}^{11}\text{B})$, and $M_{A-n} = m({}^{11}\text{C})$. The proton and neutron separation energies are summarized in Table F.2. Both the proton and neutron separation energies

Table F.3: Proton and neutron separation energy

target	S_p (MeV)	S_n (MeV)
${}^7\text{Li}$	9.98	7.25
${}^{12}\text{C}$	15.96	18.72
${}^{27}\text{Al}$	8.77	13.60
${}^{64}\text{Cu}$	7.20	7.92

of ^{12}C are very large because the $p_{3/2}$ shell of the ^{12}C nucleus is doubly closed.

The efficiency of the missing energy cut has been discussed in Subsection 4.4. The Fermi motion and the binding energy has been taken into account. The considered binding energy is given for the peripheral nucleon. The extra-separation energy is needed for the other than peripheral nucleon. The averaged extra-separation energy (its standard deviation) has been estimated as 6.98 (6.00), 3.68 (5.24), 7.38 (6.98), and 8.44 (8.08) MeV for Li, C, Al, and Cu, respectively. Here the number of nucleons at each shell has been assumed to be in Table F.1.2, the shell energy has been assumed to be $(2n + l)\hbar\omega$. The harmonic oscillator parameter $b = \sqrt{\hbar/m\omega} = 1.84, 1.93, 2.04,$ and 2.15 are adopted for the four nuclear targets. The efficiencies of the missing energy cut is estimated by these additional separation energies, and are $0.955 \pm 0.019, 0.963 \pm 0.014, 0.977 \pm 0.009, 0.982 \pm 0.008, 0.966 \pm 0.016, 0.975 \pm 0.013, 0.960 \pm 0.019,$ and 0.969 ± 0.017 for Li(V), Li(H), C(V), C(H), Al(V), Al(H), Cu(V), and Cu(H), respectively.

The incoherent process with using no separation energy makes the missing energy smaller. However, an enhancement in the small missing energy region is also observed for the nucleus ^{12}C whose separation energy is the largest. The small missing energy events is not incoherent production with using no separation energy but coherent production.

F.3 Nucleon density distributions

Effective nucleon number A_{eff} shown in Subsection 1.2 has been calculated assuming nucleon density has

$$\rho = \rho_0 \{1 + e^{(r-c)/a}\}^{-1}, \quad (\text{F.13})$$

where $c = 1.14A^{1/3}$ fm, and $a = 0.545$ fm according to the Ref. [48]. In order to obtain more realistic nucleon densities, charge density distributions in Ref. [81] have been used. The charge density distributions are described in the harmonic oscillator model for Li, and in the Fourier-Bessel expansion for the others.

In an harmonic oscillator model, charge density distribution is described as

$$\rho(r) = \rho_0 \left\{ 1 + \alpha \left(\frac{r}{a} \right)^2 \right\} \exp \left\{ v - \left(\frac{r}{a} \right)^2 \right\}, \quad (\text{F.14})$$

where the radius r is given in fm. Table F.3 shows the parameters used for Li.

Table F.4: Charge density parameters for Li. The charge density distribution of Li is in the harmonic oscillator model.

target	Li
a	1.77
α	0.327

In a Fourier-Bessel expansion, charge density distribution is described as

$$\rho(r) = \begin{cases} \sum_i a_i J_0 \left(\frac{i\pi r}{R} \right) & \text{for } r \leq R, \\ 0 & \text{for } r > R, \end{cases} \quad (\text{F.15})$$

where J_0 stands for the spherical Bessel function, and the radius r is also given in fm. Table F.3 shows the parameters used for the other targets.

Table F.5: Charge density parameters for C, Al, and Cu. The charge density distributions of C, Al, and Cu are described in the Fourier-Bessel expansion.

target	C	Al	Cu
a_1	+0.15721E-1	+0.43418E-1	+0.45598E-1
a_2	+0.38732E-1	+0.60298E-1	+0.60706E-1
a_3	+0.36808E-1	+0.28950E-2	-0.78616E-2
a_4	+0.14671E-1	-0.23522E-1	-0.31638E-1
a_5	-0.43277E-2	-0.79791E-2	-0.14447E-2
a_6	-0.97752E-2	+0.23010E-2	+0.10953E-1
a_7	-0.68908E-2	+0.10794E-2	+0.42578E-2
a_8	-0.27631E-2	+0.12574E-3	-0.24224E-3
a_9	-0.63568E-3	-0.13021E-3	-0.30067E-3
a_{10}	+0.71809E-4	+0.56563E-4	+0.23903E-3
a_{11}	+0.18441E-3	-0.18011E-4	-0.12910E-3
a_{12}	+0.75066E-4	+0.42869E-5	+0.60195E-4
a_{13}	+0.51069E-4	—	-0.25755E-4
a_{14}	+0.14308E-4	—	+0.10332E-4
a_{15}	+0.23170E-5	—	-0.39330E-5
a_{16}	+0.68465E-6	—	+0.14254E-5
a_{17}	—	—	-0.49221E-6
R	8.0	7.0	9.0

Normalization has been made so that the integral of the nucleon density should be the mass number A :

$$4\pi \int \rho(r)r^2 dr = A, \quad (\text{F.16})$$

where the proton and neutron density have the same r -dependence since the targets used are $N \sim Z$. Figure F.3 shows the nucleon density distribution for each nuclear target in coordinate space.

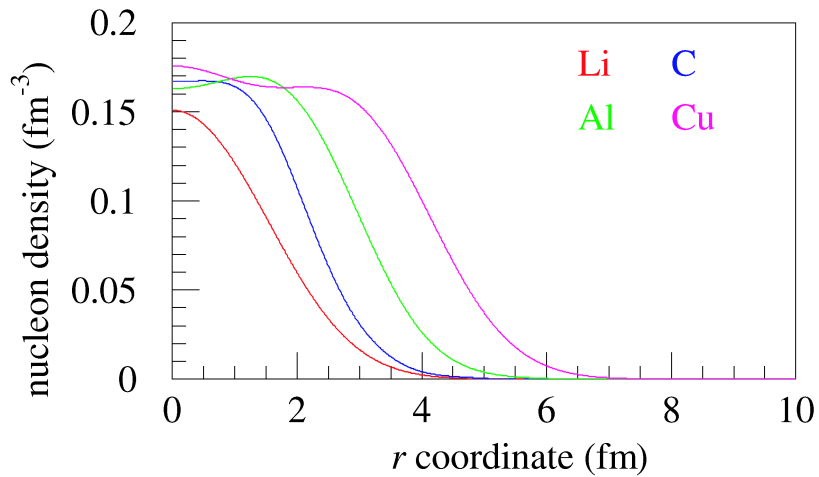


Figure F.3: Nucleon density distributions in coordinate space. The Li has a Gaussian like shape, and the others have Woods-Saxon shapes.

Appendix G

Miscellaneous

G.1 Confirmation of good buffers

In the experiment, some serious troubles of the data taking system have happened. A majority logic unit which summed the TOF wall signals were out of order, and the data before replacing the modules cannot be used. One of the LeCroy TDC1877S modules for DC1U and DC1V sometimes became to return the irregular data suddenly. In case it became to return irregular data, the correlation of the positions between SVTX and DC1 changed. Figure G.1 shows the correlation of the x and y

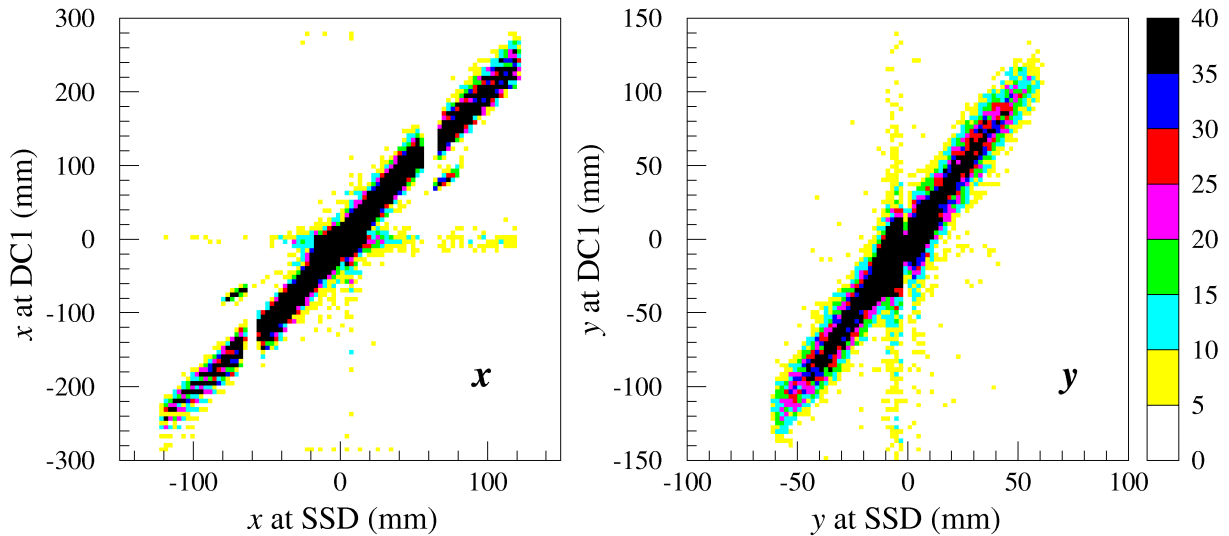


Figure G.1: Correlation of the x/y position between SVTX and DC1. The loci corresponding to the charged particles produced at the target are observed clearly both in the x and y correlation plots, and a locus corresponding to the particles produced far upstream of the target is also observed in the x correlation plot.

positions at SVTX and DC1. A strong correlation can be seen for events of good buffers although different z -positions of the target makes different slopes of the correlation. The x or y correlation does not hold for the events of bad buffers in which the TDC module returned the irregular data.

In order to reject the bad buffers, the ratio of the good events to the number of analyzed events (consistency ratio) was monitored. The condition expressed by the equation (G.1) was required for

Table G.1: Run number used for the analysis and analyzed buffers. The blank cell in the “Buffers” column shows all the buffers in the run are used.

Run	Target	Polarity	Buffers												
22726	C	Horz.	22265	22782	Cu	Vert.		22840	Al	Vert.		22896	Al	Horz.	
22727	C	Vert.	59348	22783	Cu	Horz.		22841	Al	Vert.		22897	Cu	Horz.	
22728	Li	Horz.	68629	22784	Cu	Horz.		22842	Al	Horz.		22898	Cu	Horz.	
27729	Li	Vert.	103646	22785	Al	Horz.		22843	Al	Horz.		22899	C	Horz.	
22730	Cu	Horz.		22786	Al	Horz.		22844	Cu	Horz.		22900	C	Horz.	
22731	Cu	Horz.		22787	Al	Horz.		22845	Cu	Horz.		22901	Cu	Horz.	
22732	Cu	Vert.	22634	22788	Al	Vert.		22846	Cu	Vert.		22902	Cu	Horz.	
22733	Al	Horz.	3494	22789	Al	Vert.		22847	Cu	Vert.		22903	Cu	Vert.	
22734	Al	Horz.		22790	Al	Vert.		22848	C	Vert.		22904	Cu	Vert.	
22735	Al	Vert.	2882	22791	Al	Vert.		22849	C	Horz.		22905	C	Vert.	
22736	Cu	Vert.		22792	Cu	Horz.		22850	Li	Horz.		22906	C	Vert.	
22737	Cu	Horz.		22793	Cu	Horz.		22851	Li	Vert.		22907	Cu	Vert.	
22738	C	Horz.		22794	Cu	Vert.		22852	Cu	Horz.		22908	Cu	Vert.	
22739	C	Vert.		22795	Cu	Vert.		22853	Cu	Horz.		22909	Al	Vert.	
22740	Li	Vert.		22796	Cu	Vert.		22854	Cu	Vert.		22910	Al	Vert.	
22741	Cu	Vert.		22797	C	Horz.		22855	Cu	Vert.		22912	Al	Vert.	
22742	Cu	Vert.		22798	C	Horz.		22856	Al	Horz.		22913	Al	Vert.	
22743	Cu	Horz.		22799	C	Vert.	33772	22857	Al	Horz.		22914	Cu	Vert.	
22744	Cu	Horz.		22800	C	Vert.		22858	Al	Vert.		22915	Cu	Vert.	
22745	Cu	Horz.		22801	Li	Horz.		22859	Al	Vert.		22916	Li	Vert.	
22746	Li	Horz.		22802	Li	Horz.	8176	22860	Cu	Horz.		22917	Li	Horz.	
22747	Al	Horz.		22803	Li	Vert.	53019	22861	Cu	Horz.		22918	Cu	Horz.	
22748	Al	Horz.		22804	Li	Vert.	1055	22862	Cu	Vert.		22919	Cu	Horz.	
22749	Al	Vert.		22805	Cu	Horz.	15950	22863	Cu	Vert.		22920	Al	Horz.	
22750	Al	Vert.		22806	Cu	Horz.		22864	C	Horz.		22921	Al	Horz.	
22751	Cu	Horz.	14078	22807	Cu	Horz.		22865	C	Vert.		22922	Al	Horz.	
22752	Cu	Horz.		22808	Cu	Vert.		22866	Li	Horz.		22923	Cu	Horz.	
22753	Cu	Vert.		22809	Cu	Vert.		22867	Li	Vert.		22924	Cu	Horz.	
22754	Cu	Vert.		22810	Cu	Vert.		22868	Cu	Vert.		22925	Cu	Horz.	
22755	C	Horz.		22811	Al	Vert.		22869	Cu	Vert.		22926	C	Horz.	
22756	C	Vert.	85946	22812	Al	Vert.		22870	Cu	Horz.		22927	C	Horz.	
22757	Li	Vert.		22813	Al	Horz.		22871	Cu	Horz.		22928	C	Horz.	
22758	Li	Horz.		22814	Al	Horz.		22872	Al	Horz.		22929	C	Horz.	
22759	Cu	Horz.	8635	22815	Cu	Horz.		22873	Al	Horz.		22930	Cu	Horz.	
22760	Cu	Vert.		22816	Cu	Horz.		22874	Al	Vert.		22931	Cu	Horz.	
22761	Cu	Vert.		22817	Cu	Vert.		22875	Al	Vert.		22932	Cu	Horz.	
22762	Cu	Vert.		22818	Cu	Vert.		22876	Al	Vert.		22933	Cu	Horz.	
22763	Cu	Horz.		22819	C	Horz.		22877	Cu	Horz.		22935	Cu	Horz.	
22764	Al	Horz.		22820	C	Vert.		22878	Cu	Horz.		22936	Cu	Vert.	
22766	Al	Vert.		22821	Li	Vert.		22879	Cu	Vert.		22937	Cu	Vert.	
22767	Al	Vert.		22822	Li	Horz.		22880	Cu	Vert.		22939	Cu	Vert.	
22768	Al	Horz.		22823	Cu	Horz.		22881	C	Vert.		22940	C	Vert.	
22769	Cu	Horz.		22824	Cu	Vert.		22882	Cu	Vert.		22942	Cu	Vert.	
22770	Cu	Vert.	3405	22825	C	Vert.		22883	Cu	Vert.		22943	Al	Vert.	
22771	Cu	Vert.		22826	C	Vert.		22884	Cu	Vert.		22944	Li	Vert.	
22772	Cu	Horz.	51048	22827	C	Vert.		22885	Cu	Vert.		22945	Li	Horz.	
22773	Cu	Vert.		22830	C	Horz.		22886	Al	Vert.		22946	Cu	Horz.	
22774	C	Vert.		22831	C	Horz.		22887	Al	Vert.		22950	Cu	Horz.	
22775	C	Horz.		22832	C	Vert.		22888	Cu	Vert.		22952	Cu	Horz.	13878
22776	Li	Horz.		22833	Li	Horz.		22889	Cu	Vert.		22954	Cu	Horz.	
22777	Li	Horz.		22834	Li	Vert.		22890	Li	Vert.		22957	Cu	Horz.	1411
22778	Li	Vert.		22835	Cu	Horz.		22891	Li	Horz.		22958	Cu	Horz.	1603
22779	Li	Vert.		22836	Cu	Horz.		22893	Cu	Horz.		22959	Cu	Horz.	11765
22780	Cu	Vert.		22838	Cu	Vert.		22894	Al	Horz.		22960	Cu	Horz.	
22781	Cu	Vert.	48408	22839	Cu	Vert.		22895	Al	Horz.		22961	Al	Horz.	

the good events.

$$\begin{aligned} |x_{\text{DC1}} - 2.2 \times x_{\text{SVTX}}| &< 40 \quad \text{for } x \\ |y_{\text{DC1}} - 2.0 \times y_{\text{SVTX}}| &< 40 \quad \text{for } y \end{aligned} \quad (\text{G.1})$$

Figure G.2 shows the consistency ratio for x and y positions. The sudden drop can be observed in the y consistency ratio, at which the TDC module started to return irregular data.

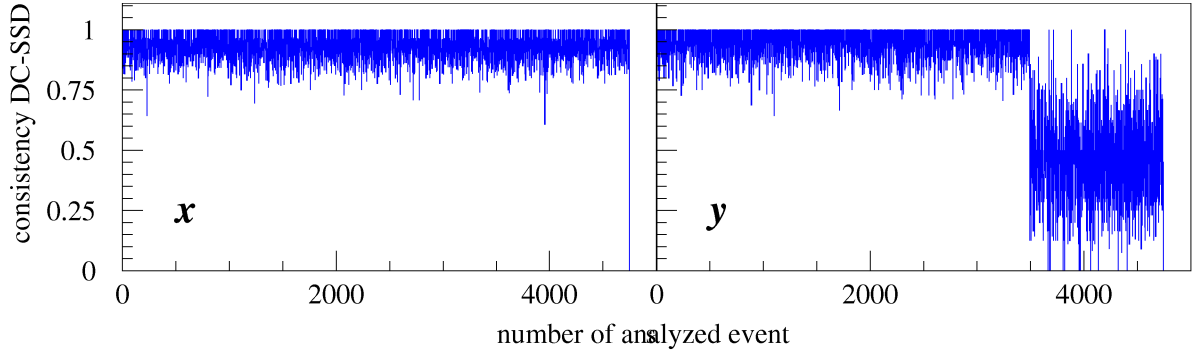


Figure G.2: Consistency ratio for the x and y positions between SVTX and DC1. A sudden drop is observed in the y position after 3405 buffers are analyzed.

The buffers after this kind of sudden drop has been observed are not used for the analysis, and the NTUPLE files have been created only for the good buffers. Table G.1 shows the run numbers used and number of the buffers used in each run for the analysis.

G.2 Voigt function

Voigt function is a Gaussian convoluted Lorentzian (Breit-Wigner function). The characteristic function of the Gaussian and the Lorentzian — Fourier transform of these — are described as

$$F_G(t) = \exp(i\mu_G t - \sigma^2 t^2/2) \text{ for Gaussian, and} \quad (\text{G.2})$$

$$F_L(t) = \exp(i\mu_L t - |t|\Gamma/2) \text{ for Lorentzian,} \quad (\text{G.3})$$

respectively, where μ_G , μ_L and σ , Γ are the centroid and the width of the functions, respectively. The convoluted function is described as

$$\begin{aligned} V(x) &= \frac{1}{2\pi} \int_{-\infty}^{\infty} F_G(t) F_L(t) \exp(-itx) dt \\ &= \frac{1}{2\pi} \int_{-\infty}^{\infty} \{\cos(\mu_G + \mu_L - x)t + i \sin(\mu_G + \mu_L - x)t\} \exp\left(-\sigma^2 t^2/2 - |t|\Gamma/2\right) dt \\ &= \frac{1}{\pi} \int_0^{\infty} \cos(\mu_G + \mu_L - x)t \exp\left(-\frac{\sigma^2 t^2}{2} - \frac{\Gamma}{2}t\right) dt \end{aligned} \quad (\text{G.4})$$

Hyper-geometric function and confluent hyper-geometric one have a recursiveness for the differential and integration described as

$$\begin{cases} \frac{d}{dx} {}_2F_1(\alpha, \beta, \gamma; x) = \frac{\alpha\beta}{\gamma} {}_2F_1(\alpha + 1, \beta + 1, \gamma + 1; x), \text{ and} \\ \frac{d}{dx} {}_1F_1(\alpha, \gamma; x) = \frac{\alpha}{\gamma} {}_1F_1(\alpha + 1, \gamma + 1; x). \end{cases} \quad (\text{G.5})$$

Using the relations (G.5), the following expansion is obtained as

$$\int_0^{\infty} x^{\alpha-1} \exp(-ax^2) \cos cx \, dx = \frac{1}{2a^{\alpha/2}} \Gamma\left(\frac{\alpha}{2}\right) {}_1F_1\left(\frac{\alpha}{2}, \frac{\gamma}{2}; -\frac{c^2}{4a}\right). \quad (\text{G.6})$$

Thus Voigt function is expanded as

$$\begin{aligned}
V(x) &= \int_0^\infty \exp(-at^2 - bt) \cos ct \, dt \\
&= \int_0^\infty \exp(-at^2) \left\{ \sum \frac{(-bt)^k}{k!} \right\} \cos ct \, dt \\
&= \sum \frac{(-b)^k}{k!} \int_0^\infty t^k \exp(-at^2) \cos ct \, dt \\
&= \sum \frac{(-b)^k}{k!} \frac{1}{2a^{(k+1)/2}} \Gamma\left(\frac{k+1}{2}\right) {}_1F_1\left(\frac{k+1}{2}, \frac{1}{2}; -\frac{c^2}{4a}\right), \tag{G.7}
\end{aligned}$$

where $a = \sigma^2/2$, $b = \Gamma/2$, and $c = \mu_G + \mu_L - x$. In order to avoid the column omission in the numerical calculation, the Kummer's transformation

$${}_1F_1(\alpha, \gamma; -x) = e^{-x} {}_1F_1(\gamma - \alpha, \gamma; x) \tag{G.8}$$

was applied, and Voigt function becomes

$$V(x) = \sum \frac{(-b)^k}{k!} \frac{1}{2a^{(k+1)/2}} \Gamma\left(\frac{k+1}{2}\right) \exp\left(-\frac{c^2}{4a}\right) {}_1F_1\left(-\frac{k}{2}, \frac{1}{2}; \frac{c^2}{4a}\right). \tag{G.9}$$

G.3 Finite element method in TOSCA

A simple one space dimension problem is discussed below because the concepts of the method are independent of the number of space dimensions. Consider a Poisson type equation with a potential function ϕ :

$$\nabla \cdot \epsilon \nabla \phi = \rho. \tag{G.10}$$

To solve this equation using a finite element method, the domain is divided into line elements, and the potential ϕ within each line is approximated by a linear polynomial. Because the potential is required to be continuous over the domain, the potential within the line is described by the values of ϕ at the nodes of the line, and the same values are used in other lines that meet at the node. Then, the potential ϕ within the line element is described as

$$\phi(x) = N_1(x)\phi_1 + N_2(x)\phi_2, \tag{G.11}$$

where N_1 and N_2 are the shape functions, and are expressed by a local coordinate system ξ as

$$\begin{aligned}
N_1(x) &= \frac{1}{2}(1 - \xi), \\
N_2(x) &= \frac{1}{2}(1 + \xi), \text{ and} \\
-1 &\leq \xi \leq +1.
\end{aligned} \tag{G.12}$$

Note that the location of $\xi = -1$, and $+1$ expresses the nodes of the line 1, and 2, respectively. The shape function N_i for a particular node is only defined in the elements that used the node and is zero outside these elements.

Weighted residuals are used in TOSCA for the method of approximating the potential ϕ using nodal values ϕ_i and associated shape functions $N_i(x)$. An approximate solution ϕ is determined by requesting to satisfy

$$\int W (\nabla \cdot \epsilon \nabla \phi - \rho) \, dx = 0, \tag{G.13}$$

where W is a weighting function. Integrating Eq. (G.13) by parts to reduce the order of differentiation is applied to ϕ gives

$$\int_a^b (\nabla W \cdot \epsilon \nabla \phi + W \rho) dx - \left[W \epsilon \frac{\partial \phi}{\partial x} \right]_a^b = 0, \quad (\text{G.14})$$

where a and b are the limits of the domain of the equation. In the Eq. (G.14), derivative continuity is not necessary for the W and ϕ functions, and the natural boundary condition on the surface of the domain emerges. In the Galerkin weighted residual method that TOSCA adopts, the shape functions of the nodes are used for each weight function, then the equation for weight function $W_i = N_i$ is obtained by

$$\sum_j \int_a^b (\nabla N_i \cdot \epsilon \nabla N_j \phi_j + N_i \rho) dx - \left[N_i \epsilon \frac{\partial \phi}{\partial x} \right]_a^b = 0 \quad (\text{G.15})$$

for all the elements that contains node i . Taking all the equations for the different weight functions together gives a set of linear equations, which can be written in the matrix form as

$$K \Phi = S, \quad (\text{G.16})$$

where Φ is a vector of unknown nodal potential values ϕ_i , K is a coefficient matrix, of which individual elements are

$$K_{ij} = \int_a^b \nabla N_i \cdot \epsilon \nabla N_j dx, \quad (\text{G.17})$$

and S is a known vector derived from the given line charge densities or assigned boundary conditions.

A Newton-Raphson method is used to solve this type of non-linear equation. Given an initial solution Φ^n , a new solution Φ^{n+1} is found by solving the linearized jacobian system as

$$\Phi^{n+1} = \Phi^n - \alpha J^n R^n, \quad (\text{G.18})$$

where α is a relaxation factor, R^n is a residual matrix described as

$$R^n = K^n \Phi^n - S^n, \quad (\text{G.19})$$

and J is a jacobian described as

$$J^n = \frac{\partial}{\partial \Phi^n} (K^n \Phi^n - S^n). \quad (\text{G.20})$$

The α is chosen to aid convergence, which starts with 1, and in each iteration which is multiplied by 2 if the change in $|R|$ is too small or divided by 2 if the norm of the residual $|R^{n+1}|$ would be greater than $|R^n|$.

Bibliography

- [1] G.E. Brown and M. Rho, Phys. Rept. 269, 333 (1996).
- [2] G.E. Brown and M. Rho, Phys. Rev. Lett. 66, 2720 (1991).
- [3] K. Saito and A.W. Thomas, Phys. Rev. C 51, 2757 (1995).
- [4] CERES Collaboration, G. Agakichiev *et al.*, Phys. Rev. Lett. 75, 1272 (1995)
- [5] G.Q. Li, CM. Ko, G.E. Brown, H. Sorge, Nucl. Phys. A 611, 539 (1996);
- [6] CERES Collaboration, G. Agakichiev *et al.*, Phys. Lett. B 422, 405 (1998).
- [7] H. En'yo *et al.*, Nucl. Phys. A 670, 182c (2000).
- [8] M. Ishino, PhD thesis, Kyoto University (2000).
- [9] K. Ozawa *et al.*, Phys. Rev. Lett. 86, 5019 (2001).
- [10] H. En'yo *et al.*, Prog. Theor. Phys. Suppl. 149, 49 (2003).
- [11] M. Naruki *et al.*, Nucl. Phys. A 721, 297 (2003).
- [12] R. Muto *et al.*, AIP Conf. Proc. 698, 138 (2004).
- [13] R. Muto *et al.*, J. Phys. G 30, S1023 (2004).
- [14] T. Hatsuda and S.H. Lee, Phys. Rev. C 46, 34 (1992).
- [15] C.M. Ko, P. Levai, X.J. Qui, C.T. Li, Phys. Rev. C 45, 1400 (1992).
- [16] T. Hatsuda, H. Shiomi, H. Kuwabara, Prog. Theor. Phys. 95, 1009 (1996).
- [17] F. Klingl, N. Kaiser, W. Weise, Nucl. Phys. A 624, 527 (1997).
- [18] F. Klingl, T. Waas, and W. Weise, Phys. Lett. B 431, 254 (1998).
- [19] H. Kuwabara and T. Hatsuda, Prog. Theor. Phys. 94, 1163 (1995).
- [20] E. Oset, M.J. Vicente Vacas, H. Toki, A. Ramos, Phys. Lett. B 508, 237 (2001).
- [21] E. Oset and A. Ramos, Nucl. Phys. A 679, 616 (2001).
- [22] E. Oset *et al.*, Phys. Lett. B 508, 237 (2001).
- [23] D. Cabrera and M.J. Vicente Vacas, Phys. Rev. C 67, 045203 (2003).
- [24] HADES Collaboration, J. Friese, Nucl. Phys. A 654, 1017c (1999).
- [25] E-802 Collaboration, Y. Akiba *et al.*, Phys. Rev. Lett. 76 (1996) 2021.
- [26] P. Mühlich, T. Falter, C. Greiner, J. Lehr, M. Post, U. Mosel, Phys. Rev. C 67 (2003) 024605.

- [27] D. Cabrera, L. Roca, E. Oset, H. Toki, M.J. Vicente Vacas, Nucl. Phys. A733, 130 (2004).
- [28] H.-J. Behrend et al., Phys. Lett. 56 B, 408 (1975).
- [29] H.J. Lipkin, Phys. Rev. Lett. 16, 1015 (1966).
- [30] T.H. Bauer, R.D. Spital, D.R. Yennie, and F.M. Pipkin, Rev. Mod. Phys. 50, 261 (1978), and references therein.
- [31] L.O. Abrahamian *et al.*, Phys. Lett. B 44, 301 (1973).
- [32] M. Effenberger and A. Sibirtsev, Nucl. Phys. A 632, 99 (1998).
- [33] H. Alvensleben *et al.*, Phys. Rev. Lett. 24, 786 (1970).
- [34] H. Alvensleben *et al.*, Nucl. Phys. B 18, 333 (1970).
- [35] J.G. Asbury *et al.*, Phys. Rev. Lett. 19, 865 (1967).
- [36] H.-J. Behrend *et al.*, Phys. Rev. Lett. 24, 336 (1970).
- [37] F. Bulos *et al.*, Phys. Rev. Lett. 22, 490 (1969).
- [38] P. Coddington *et al.*, Nucl. Phys. B 95, 249 (1975).
- [39] G. McClellan *et al.*, Phys. Rev. Lett. 22, 377 (1969).
- [40] G. McClellan *et al.*, Phys. Rev. D 4, 2683 (1971).
- [41] H.-J. Behrend *et al.*, Phys. Rev. Lett. 24, 1246 (1970).
- [42] H.-J. Behrend *et al.*, Phys. Rev. Lett. 27, 65 (1971).
- [43] P.L. Braccini *et al.*, Nucl. Phys. B 24, 173 (1970).
- [44] T.J. Brodbeck *et al.*, Nucl. Phys. B 136, 95 (1978).
- [45] G. McClellan *et al.*, Phys. Rev. Lett. 26, 1593 (1971).
- [46] R.J. Glauber, in Proc. High energy physics and nuclear structure, 311 (North-Holland, Amsterdam, 1967).
- [47] B. Margolis, Phys. Lett. 26 B, 524 (1968).
- [48] K.S. Kölbig and B. Margolis, Nucl. Phys. B 6, 85 (1968).
- [49] Particle Data Group, K. Hagiwara *et al.*, Phys. Rev. D 66, 010001 (2002).
- [50] Web: <http://www.spring8.or.jp/>
- [51] H. Kamitsubo, Nucl. Inst. Meth. A 303, 421 (1991).
- [52] Web: <http://www.rcnp.osaka-u.ac.jp/Divisions/np1-b/>
- [53] T. Nakano *et al.*, Nucl. Phys. A 684, 71c (2001); T. Nakano, Nucl. Phys. A 721, 112c (2003).
- [54] T. Nakano *et al.*, Phys. Rev. Lett. 91, 012002 (2003).
- [55] R.G.T. Zegers *et al.*, Phys. Rev. Lett. 91, 092001 (2003).
- [56] A. D'Angelo *et al.*, Nucl. Inst. Meth. A 455, 1 (2000).
- [57] T. Mibe, PhD thesis, Osaka University (2004).

- [58] Web: <http://www.vectorfields.com/>
- [59] Y. Sugaya and M. Nomachi, Nucl. Instr. Meth. A437, 68 (1999).
- [60] Y. Sugaya *et al.*, IEEE transactions on nuclear science 48 No.4, 1282 (2001).
- [61] T. Ishikawa, T. Mibe, N. Muramatsu, T. Nakano, M. Sumihama, and R.G.T. Zegers, LEPS Technical Note 1 (unpublished).
- [62] Web: <http://cernlib.web.cern.ch/cernlib/>
- [63] Web: <http://paw.web.cern.ch/paw/>
- [64] Web: <http://wwwasd.web.cern.ch/wwwasd/geant/index.html>
- [65] W.C. Chang, LEPS Technical Note 2 (unpublished).
- [66] M. Sumihama, PhD thesis, Osaka University (2003).
- [67] Web: <http://garfield.web.cern.ch/garfield/>
- [68] T. Mibe, LEPS Technical Note 7 (unpublished).
- [69] S. Baker and R.D. Cousins, Nucl. Instr. Meth. 221, 437 (1984).
- [70] J. Barth, *et al.*, Eur. Phys. J. A 17, 269 (2003).
- [71] Y. Oh and H.C. Bhang, Phys. Rev. C 64, 055207 (2001).
- [72] Q. Zhao, B. Saghai, and J.S. Al-Khalili, Phys. Lett. B 509, 231 (2001).
- [73] A.I. Titov, M. Fujiwara, and T.-S.H. Lee, Phys. Rev. C 66, 022202 (2002).
- [74] A.I. Titov and T.-S.H. Lee, Phys. Rev. C 67, 065205 (2003).
- [75] H. Kohri, Internal LEPS Technical Note 15 (unpublished), and private communication.
- [76] M. Nakamura, private communication.
- [77] H. Noumi and H. Tamura, private communication.
- [78] Web: http://physics.nist.gov/cgi-bin/Xcom/xcom3_1
- [79] T. Nakano and H. Toki, in Proc. Exciting Physics with New Accelerator Facilities, 48 (SPRING-8, Hyogo, Japan 1997)
- [80] T. Nakano, LEPS Technical Note 8 (unpublished), and Amendment of LEPS Technical Note 8 (unpublished).
- [81] H. de Vries *et al.*, Atomic Data and Nuclear Data Tables, 36, 495 (1987).
- [82] K.Schilling, P. Seyboth, and G. Wolf, Nucl. Phys. B 15. 397 (1970).
- [83] R.T. Thews, Phys. Rev. 175, 1749 (1968).
- [84] T. Ishikawa, LEPS Technical Note 13 (unpublished).
- [85] H. de Ruijter, PhD thesis, Lund University (1995).
- [86] A.N. Antonov *et al.*, Phys. Rev. C 65, 024306 (2002).
- [87] M. Nomachi, LEPS Technical Note 6 (unpublished).

- [88] H. Babacan *et al.*, Act. Phys. Polon. B 33, 683 (2002).
- [89] T. Ishikawa and M. Yosoi, in Proc. of Workshop on Quark Nuclear Physics, 27 (Pusan National University, Korea 2002).
- [90] T. Ishikawa *et al.*, Phys. Lett. 608, 215 (2005).